Novel multivariate data analysis techniques to determine functionally connected networks within the brain from EEG or MEG data

vorgelegt von
Diplom-Ingenieur
Arne Ewald

von der Fakultät IV - Elektrotechnik und Informatik
der Technischen Universität Berlin
zur Erlangung des akademischen Grades

Doktor der Naturwissenschaften
- Dr. rer. nat. -

Promotionsausschuss:

Vorsitzender:	Prof. Dr. B. Blankertz
Gutachter:	Prof. Dr. K.-R. Müller
Gutachter:	Dr. G. Nolte
Gutachter:	Prof. Dr. A. Daffertshofer

Berlin 2014
D 83

Abstract

To understand the functionality of the brain, it is crucial to know where sources of ongoing activity are located inside the brain and how they interplay. The synchronization of oscillatory signals generated by large populations of neurons has been identified to serve as a communication mechanism. Due to their excellent temporal resolution in the millisecond range and their non-invasiveness, the electrophysiological measurement modalities Electroencephalography (EEG) and Magnetoencephalography (MEG) are well-suited tools to investigate these synchronization effects. However, due to the mixing of source signals inside the brain into measurement sensors outside the head which is called volume conduction, it is neither possible to uniquely reconstruct the sources nor to study relationships among them. Artifacts of volume conduction impede the interpretation of relationships between sensors as well as between estimated sources.

Within this thesis a novel series of multivariate data analysis methods is introduced that aims at detecting synchronization between large-scale brain sources robust to any volume conduction artifacts. All methods are based upon the concept of an established connectivity measure called the imaginary part of coherency (ImCoh). The ImCoh neglects instantaneous synchronization effects as they are most likely due to source mixing as true source synchronization usually requires some time to evolve.

The computational procedure presented in this thesis is constructed out of four individual methods which can be used sequentially. First, the maximization of the imaginary part of coherency is introduced which leads to an increase of the signal-to-noise ratio for subsequent connectivity analysis and source localization. Furthermore, connectivity measures are derived from this maximization, which are, in contrast to the ImCoh, independent of the particular source mixing. Due to these properties, one of the measures, the Global Interaction Measure (GIM), is used to objectively compare the measurement modalities EEG and MEG. Moreover, the GIM serves as a basis to automatically determine subject specific frequency peaks of synchronization effects. Second, synchronized sources are determined with a novel technique called Self Consistent Multiple Signal Classification (SC Music). It forms an algorithmic improvement over the existing data analysis technique Rap Music

(Recursively Applied Multiple Signal Classification) by diminishing the influence of other sources during the localization procedure. Third, a method called Wedge Music is used to address the question which of the sources, prior determined with SC Music, are actually interacting. Additionally, it is shown that both SC and Wedge Music are, in contrast to measures based on the classical ImCoh, capable of examining differences in interaction between different experimental conditions. Fourth, a method is presented to statistically test the results. This is achieved by generating surrogate data from the real data such that data properties are maintained but all interactions are artificially destroyed. All methods are introduced theoretically and are validated in simulations. Finally, the applicability is demonstrated on real EEG and MEG data.

Zusammenfassung

Die Funktionsweise des Gehirns wird maßgeblich durch das Zusammenspiel von verschiedenen Gehirnregionen bestimmt. Ein Kommunikationsmechanismus ist dabei die Synchronisation von oszillatorischen Signalen, die von großen Neuronenpopulationen erzeugt werden. Mit ihrer hervorragenden zeitlichen Auflösung im Bereich von Millisekunden und ihrer Nicht-Invasivität sind die elektrophysiologischen Messmodalitäten Elektroenzephalografie (EEG) und Magnetoenzephalografie (MEG) gut geeignete Werkzeuge, um diese Synchronisationseffekte zu untersuchen. Die Sensoren an der Kopfoberfläche messen jedoch eine Mischung der im Gehirn generierten Quellsignale. Durch diesen sogenannten Volumenleitungseffekt ist es weder möglich, die Quellen aus den Sensorsignalen eindeutig zu rekonstruieren noch Beziehungen (Konnektivität) zwischen ihnen abzuleiten.

Die vorliegende Arbeit stellt ein Reihe multivariater Datenanalysemethoden vor, um Synchronisation und damit Interaktionen zwischen verschiedenen Gehirnarealen zu erfassen. Alle Methoden basieren auf einem Konzept, dass einem etablierten Konnektivitätsmaß, dem sogenannten Imaginärteil der Kohärenz (englische Abkürzung: ImCoh), zu Grunde liegt. Der ImCoh vernachlässigt gleichzeitig stattfindende Synchronisationseffekte, da sie höchstwahrscheinlich auf Volumenleitungsartefakten beruhen, während echte neuronale Synchronisation im Gegensatz dazu zeitversetzt stattfindet.

Im Wesentlichen werden in dieser Arbeit vier verschiedenen Methoden präsentiert, die nacheinander benutzt werden können. Zunächst wird die Maximierung des ImCohs durch einen optimalen räumlichen Filter beschrieben. Damit wird das Signal-Rausch-Verhältnis der Daten für anschließende Konnektivitätsanalysen und für die Quellrekonstruktion verbessert. Weiterhin werden aus der vorgestellten Theorie dieser Maximierung verschiedene neue Konnektivitätsmaße abgeleitet, auf die die eigentliche Mischung der Quellsignale in die Sensoren keinerlei Einfluss hat. Mit einem dieser Maße, dem Global Interaction Measure (GIM) lassen sich aufgrund dieser Eigenschaften die Messmodalitäten EEG und MEG valide vergleichen. Weiterhin können mit dem GIM versuchspersonenspezifische Frequenzbänder, bei denen eine neuronale Synchronisation stattfindet, automatisch detektiert werden. In einem

zweiten Schritt werden die Gehirnquellen in dem zuvor bestimmten Frequenzband mit einem neuen Analyseverfahren namens Self Consistent Multiple Signal Classification (SC Music) lokalisiert. Dieses stellt eine algorithmische Erweiterung des bereits bestehenden Verfahrens Rap Music (Recursively Applied Multiple Signal Classification) dar. Im Vergleich zu Rap Music verringert SC Music den Einfluss anderer synchroner Quellen und verbessert so die Lokalisation. Drittens adressiert die neu eingeführte Methode Wedge Music die Frage, welche der vorher bestimmten Quellen wirklich interagieren. Es wird gezeigt, dass sowohl SC Music als auch Wedge Music im Gegensatz zu Maßen die auf dem eigentlichen ImCoh basieren in der Lage sind, Interaktionsunterschiede zwischen verschiedenen experimentellen Bedingungen zu ermitteln. Viertens wird eine Methode zur statistischen Validierung der Ergebnisse vorgestellt. Dies geschieht mit Hilfe von Surrogatdaten, die auf Basis gemessener Daten erzeugt werden. Bei den Surrogatdaten werden jegliche zu Grunde liegende Interaktionen künstlich zerstört, während andere statistische Eigenschaften der Daten erhalten bleiben. Alle angesprochenen Methoden werden theoretisch eingeführt und in Simulationen evaluiert. Weiterhin wird die Anwendbarkeit exemplarisch anhand von echten EEG and MEG Daten demonstriert.

Acknowledgments

Forget injuries, never forget kindnesses.

(Confucius)

During the time working on this PhD thesis in different institutions and even beyond, I have encountered so many nice people I would like to thank. Foremost and first, I would like to express my deepest appreciation to my supervisors Guido Nolte and Klaus-Robert Müller. I am extremely grateful for the opportunity to have worked in such close collaboration with Guido Nolte who introduced me into neuroscientific data analysis and into science in general. On the one hand, he provided me with the freedom to explore the field in order to meet my personal interests within this interdisciplinary research landscape. On the other hand, I could come up with any question literally anytime. I benefited a lot from his extraordinary expertise and his great character and I enjoyed all the discussions about science, politics and everything. Similarly, Klaus-Robert Müller supported me in every conceivable way. He always had an open ear and came up with valuable advices. Although never being directly employed at the Berlin Institute of Technology (TUB), it was very important to me being in touch with the lively and scientifically profound Intelligent Data Analysis group, which meanwhile split into the Machine Learning group and the Neurotechnology group. Thank you very much, Benjamin Blankertz, Matthias Treder, Stefan Haufe, Andreas Ziehe, Frank C. Meinecke, Michael Tangermann, Siamac Fazli, Bastian Venthur, Sven Dähne, Johannes Höhne, Martijn Schreuder, Claudia Sannelli, Markus Wenzel, Anne Porbadnigk, Matthias Schultze-Kraft, Felix Bießmann, Carmen Vidaurre, Laura Acqualagna, Kai Görgen, Paul von Bünau, Mikio Braun, Andrea Gerdes, Dominik Kühne and many more! I always felt welcome albeit being only sporadically present and I profited from PhD seminars, long discussions and the nice and active atmosphere in general.

Closely related to the TUB groups and included in the Berlin Brain Computer Interface project was the neurophysics group from the Benjamin Franklin Campus of the Charité. Within the brain@work project and in several Wednesday jour fixes, I could deepen my knowledge in neurophysiology and how to interpret results of the EEG data analysis. Thanks a lot, Gabriel Curio, and moreover Vadim Nikulin,

Manfred Gugler and Tomasso Fedele. Having mentioned the brain@work project, I would also like to thank colleagues of the Daimler AG, namely Andreas Sonnenleitner and Michael Schrauf. It was a fruitful cooperation and a lot of fun making EEG experiments in a driving simulator but also in a real Mercedes-Benz S-Class.

At the beginning of my PhD related studies, I have worked at Fraunhofer FIRST in Berlin where I shared the office with Forooz Shahbazi Avarvand. Next to the great company, I enjoyed a very productive collaboration, which outlived different employments in different cities and is still ongoing. It always has been a great pleasure. Remembering the time at Fraunhofer, I would also like to thank Andreas Ziehe, Steven Lemm, Christian Grozea, Florin Popescu and Jens Kohlmorgen for sharing your knowledge and discussing with a young science greenhorn. I have learned a lot. Equivalently, thanks to Motoaki Kawanabe, Alexander Binder, Wojciech Samek, Tammo Krüger and Konrad Rieck.

After my time at Fraunhofer, I have been employed for almost two years at the NIRx Medizintechnik GmbH where I expanded my neuroscientific horizon with near-infrared spectroscopy and gained insights in industry. A great mentor during this period has been Christoph H. Schmitz. Additionally, I enjoyed working with Thomas Betz, Guilherme A. Zimeo Morais, Arne Krüger and the NIRx team in New York: Randall L. Barbour, Harry L. Graber and Yong Xu. Scientifically associated with the company has been a NIRS research group at Charité. Thank you, Jens Steinbrink, Christina Habermehl and Sophie Piper, for the collaboration and the integration in the informative Friday meetings. Especially, I thank Jan Mehnert, who I met at TUB, NIRx and the NIRS Charité group, for all the support in various projects.

I finally finished this thesis in Hamburg, working at the University Medical Center Hamburg-Eppendorf in the department of Neurophysiology and Pathophysiology. I would like to thank the institute's head Andreas K. Engel for providing me the opportunity to work within this inspiring multidisciplinary research environment which perfectly matches my topic of interest. Furthermore, I thank my office mates Marion Höfle, Thomas Pfeffer, Sarah Bütof, Ina Peiker and Kathrin Müsch for the nice and fruitful atmosphere and interesting scientific and non-scientific discussions. The same applies to the other colleagues in the institute I am grateful to have met and to work with, such as Jonathan Daume, Florian Göschl, Jonas Hollensteiner, Malte Sengelmann, Mohammad Sirous, Stefan Skoruppa, Dorothee Heinrich, Iain Stitt, Mircea Stoica, Anne E. Urai, Gerhard Engler, Alexander Maye, Christian Moll, Till Schneider, Verena N. Buchholz, Nicole David, Ulrich Fickel, Uwe Friese, Edgar Galindo-Leon, Florian Pieper, Johanna Rimmele, Sina Alexa Trautmann-Lengsfeld,

Peng Wang, Alessandro Gulberti, Randolph Helfrich, Hannah Knepper, Hanna Krause, Christine Carl, Gerhard Steinmetz, Roger Zimmermann, Matthias Siemers, Christiane Reißmann, Hilke Petersen, Ute Philipp, Susanne Scheer and more. I really enjoy the atmosphere in the institute, the profound discussions in seminars and various meetings, i.e. journal club, coupling club, beer club, and I am looking forward to continue the investigation of how the brain communicates within this great team here in Hamburg.

For proof reading the first draft of this work, I would like to thank Jan-Hendrik Wülbern, Jochen Oexmann, Jan Mehnert and Forooz Shahbazi Avarvand. I received valuable comments and helpful input. Thanks also to Andreas Daffertshofer from VU Amsterdam who agreed to act as an external examiner and to Benjamin Blankertz for taking the chair of the doctoral committee.

Financially, this work was supported by the BMBF (German Federal Ministry of Education and Research) with the brain@work project ("Development of neurotechnology based man-machine interaction application for industrial environments", Grant 01IB08001E) and the NEUCONN project ("Early detection of neurodegenerative processes in multiple sclerosis", Grant 031A130). Furthermore, I received funding from the NIRx Medizintechnik GmbH.

In the end, I thank my entire family, especially my mother Regina Ewald and my father Klaus Ewald for their unconditional support and love throughout my entire life. Similarly, thanks to my brother Oliver Ewald and his growing little family. Furthermore, I would like to express my deepest gratitude to all my dear friends who partly or even fully accompanied me on my path of life. Without you providing me input, distraction and support, this work would not have been possible and my life would not be half as enjoyable as it is. Thanks to all of you, unfortunately living in so many different parts of the world such as Hamburg, Neukölln, Berlin, Petershagen, Shanghai, Munich, Hildesheim, Duesseldorf, Trondheim, Vienna, Basel and so on. Finally, I thank Lena, who I met pretty much exactly when I started my PhD and who is still a very important part of my life. Thank you for the great time we are having together.

Contents

Notation and list of symbols

$\mathbf{A}$	a matrix - matrices are denoted by bold capital letters
$\mathbf{a}$	a vector - vectors are denoted by bold small letters
A or α	capital Roman or small Greek letters are used as scalar quantities with a specific meaning throughout this thesis, see below
a	small Roman letters are used as matrix or vector indices or as loop variables, except for Euler's constant e and the imaginary unit i, see below
$(.)^\dagger$	complex conjugate transpose of a matrix or vector
$\mathbf{x} \sim \mathcal{N}(\mu, \sigma^2)$	multivariate random variable $\mathbf{x}$, Gaussian distributed with mean μ and variance σ^2
$\Im(.)$ or $(.)^I$	imaginary part of a complex quantity
δ_{pq}	Kronecker delta for two variables p and q
$\Re(.)$ or $(.)^R$	real part of a complex quantity
$(.)^\mathsf{T}$	matrix or vector transpose
$\lvert.\rvert$	absolute value of a quantity
$\mathbb{C}$	set of complex numbers
$(.)^*$	complex conjugate of a scalar quantity
$:=$	is equal by definition to
$\det(.)$	determinant of a square matrix
e	Euler's constant, the base of the natural logarithm; approximately $e = 2.7182$
$\lVert.\rVert_\mathrm{F}$	Frobenius norm

$\hat{.}$	low-rank or subspace representation of a given quantity
i	imaginary unit of a complex number, defined by $i^2 = -1$
$(.)^+$	Moore Penrose pseudoinverse
$\mathbb{R}$	set of real numbers
$\mathrm{tr}(.)$	trace of (.), i.e. the sum over all diagonal elements of a matrix
$\wedge$	Wedge product
$\mathbf{\Sigma}$	covariance matrix
$\mathbf{0}_{NM}$	matrix containing zero elements of size $N \times M$
$\mathbf{I}_N$	quadratic identity matrix of size $N \times N$, i.e. ones on the diagonal, zeros elsewhere
M	number of grid points within the parceled brain
N	number of EEG or MEG measurement channels
P	subspace dimension; for Music algorithms equal to the number of sources to be estimated
T	number of sampling points of a recording
λ	eigenvalue; λ_1 denotes the largest eigenvalue and λ_j the j-th largest eigenvalue
ϑ	principle angle between two spaces
Hz	Hertz, unit of frequency in the International System of Units (SI)
cm	centimeter

1. Introduction

> Men ought to know that from nothing else but the brain come joys, delights, laughter and sports, and sorrows, griefs, despondency, and lamentations.
>
> *(Hippokrates of Kos, 400 B.C.)*

Everything that happens inside the human body is orchestrated by the brain, as well as every interaction with the outside world. The brain is supposed to be the key to cognition, consciousness and to all kinds of emotional responses ranging from depression to euphoria. Trying to understanding the brain is aiming to understand the human being. Furthermore, studying the functioning of the brain intends to learn more about neurodegenerative and mental disorders and to develop therapies and treatments accordingly. Many diseases are linked to pathological brain functioning such as Alzheimer's, Parkinson's, dementia in general, Amyotrophic Lateral Sclerosis (ALS), schizophrenia, autism, depression, and multiple sclerosis.

However, the human brain is likely to be the most complex arrangement of matter in the universe. The largest part of the brain, the cerebral cortex, contains approximately 15-33 billions of neurons (Pelvig et al., 2008). These are connected via approximately 125 trillions of synapses which roughly corresponds to the number of stars in 1500 Milky Ways (Micheva et al., 2010).

The interest in the brain is substantial and, hence, history of neuroscience is long and can be traced back to the Edwin Smith Surgical Papyrus around 1700 B.C. In the 18^{th} century, the idea of functional localization and specialization evolved (Gall and Lewis, 1835). It was derived from observed symptoms following a local brain lesion due to either brain damage or surgical experiments in animals. The most famous lesion example is the story of Phineas Gage in 1848 and can be considered as the cornerstone of cognitive neuroscience. An iron rod destroyed his frontal lobe in an accidental explosion (see Figure 1.1) from which he recovered without significant motor, sensory or cognitive deficits. His behavior, however, altered. This observation heavily supported the hypothesis of functionally specialized brain regions and provided further evidence for linking the brain to behavior (Harlow, 1868). More or less concurrently, in the mid of the 19^{th} century, the German neurologist Karl Wernicke proposed that different behaviors are produced by different brain regions interconnected by specific neural pathways (Wernicke, 1874; Kandel et al., 2012).

The first non-invasive and in-vivo brain measurements have been conducted in the early 20^{th} century. Vladimir Vladimirovich Pravdich-Neminsky recorded electrical fields generated by neuronal sources in animals in 1912 (Pravdich-Neminsky, 1913).

Hans Berger further established Electroencephalography (EEG) by recording the first human EEG in 1924 (Berger, 1929). Magnetic fields produced by the same neuronal sources as EEG have been measured for the first time outside the head by David Cohen in 1968. His experiments formed the basis of Magnetoencephalography (MEG) (Cohen, 1968).

Figure 1.1.: Phineas Gage brain damage. (Harlow, 1868)

Due to technological advances, neuroscience experienced an enormous boost in the past decades. With modern computers, researchers are able to store, process and analyze the large amounts of data generated by the brain. Additionally, imaging techniques such as Computerized Tomography (CT), Single Photon Emission Computed Tomography (SPECT), Positron Emission Tomography (PET) and Magnetic Resonance Imaging (MRI) became available during the 1970s and 1980s. These allowed a first non-invasive glance inside the working brain and the evolution of anatomical and functional brain atlases (Tzourio-Mazoyer et al., 2002; Talairach and Tournoux, 2008). Especially, functional magnetic resonance imaging (fMRI) which evolved in the early 1990s quickly became the most widely-used neuroimaging modality as it is non-invasive and does not expose subjects to radiation. With fMRI it is possible to localize "brain activity" very precisely. To be specific, fMRI does not measure brain activity directly. Changes in blood flow in certain areas are detected, which are related to energy consumption and, finally, to neural activity. These are called the Blood Oxygenation Level Dependent (BOLD) signals. Nevertheless, modern scanners achieve a spatial resolution down to a single millimeter or even below. Many fMRI studies have been conducted localizing a blood flow change in regions of the brain during a specific task (overviews are e.g. given in Berman et al., 2006; Logothetis, 2008). However, not only the location of neuronal activity but also the interplay with other brain regions is crucial to understand cognitive processing and its links to behavior (Brodmann, 1909; Ramón y Cajal, 1909; Horwitz, 2003; Vincent et al., 2006; Dosenbach et al., 2007; Vincent et al., 2008; Swanson, 2011; Siegel et al., 2011). Therefore, increasing interest has recently been directed to the topic of brain connectivity studied with modern imaging techniques. This can also be seen in Figure 1.2 which illustrates the number of publications related to brain connectivity from 1990 to 2013.

The field of brain connectivity is usually divided into three different research directions all investigating links between distinct units within the brain. First, the study of anatomical links which is referred to as anatomical connectivity. Second, the study of statistical dependencies between different time series called functional connectivity. Third, the study of direct causal inferences which is called effective connectivity. A further discrimination is commonly made concerning the size of the brain units under investigation. These range from single neurons up to large populations of neurons (Jirsa and McIntosh, 2007; Friston, 2009). The focus of this thesis lies on functional connectivity between large populations of neurons.

Although statistical dependencies between BOLD signals of different brain regions

have extensively been examined (for an overview and outlook see e.g. Friston, 2011; Smith, 2012), the investigation of functional connectivity with fMRI has some drawbacks. A fast whole brain fMRI scan takes between one and two seconds due to technical reasons and is thereby several magnitudes slower than neural activity. Moreover, the BOLD signal itself is an epiphenomena of neural activity and occurs on the time scale of multiple seconds. Therefore, even a faster fMRI signal acquisition would only lead to a higher sampled BOLD signal, not providing more information about underlying neural activity. In contrast to that, the excellent time resolution of MEG and EEG provides a unique window on the fast dynamics of human brain functions. Using electrophysiological recording techniques such as EEG and MEG, neural activity can be measured directly with sampling frequencies up to 1kHz and faster. Due to these properties, an essential mechanism of functional communication can be captured with EEG and MEG: synchronization of oscillatory signals. As in many other physical and biological systems (see Strogatz, 2003), synchronization plays a key role for communication and interactions between different entities - here, between different brain regions (Singer, 1999; Engel et al., 2001; Varela et al., 2001; Fries, 2005; Hipp et al., 2012; Engel et al., 2013).

Hans Berger already observed oscillatory activity by visual inspection of his EEG data in 1914. Nowadays, with modern computer technology, it is possible to investigate synchronization between multiple of these signal sources inside the brain, although measured at the scalp. However, there exist intrinsic challenges to explore brain sources and even more synchronized brain sources from EEG or MEG data. Due to the propagation of electromagnetic fields inside the head, each signal generated by a single brain source (i.e. a population of neurons) is recorded by multiple measurement sensors placed outside the head (Nunez et al., 1997). Therefore, data observed at scalp level are a mixture of the underlying source activities (Baillet et al., 2001). Unfortunately, the mathematical inversion, i.e. calculating brain sources from EEG or MEG data, is an ill-posed problem (Sarvas, 1987). Assuming a linear superposition of sources, this can be seen from the fact that there are usually much more possible brain sources than there are measurement sensors. This so called inverse problem or problem of source reconstruction gave rise to numerous approaches incorporating different assumptions about the underlying sources (e.g. Jeffs et al., 1987; Ioannides et al., 1990; Hämäläinen et al., 1993; Cardoso and Souloumiac, 1993; Van Veen et al., 1997; Hämäläinen and Ilmoniemi, 1994; Mosher et al., 1999b; Mosher and Leahy, 1999; Gross et al., 2001; Lin et al., 2006; Pascual-Marqui et al., 2002; Pascual-Marqui, 2002; Pascual-Marqui et al., 2011; Haufe et al., 2011). In the context of synchronization between brain sources another problem arises due to

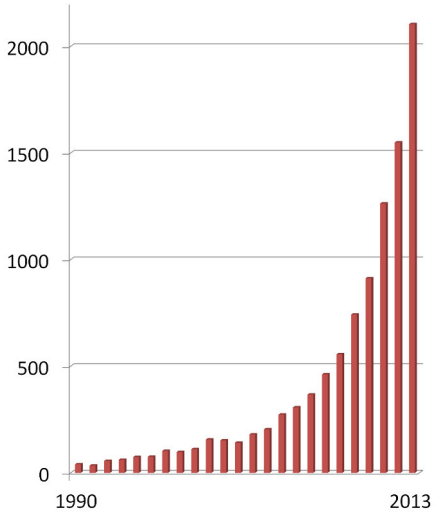

Figure 1.2.: Brain connectivity paper since 1990. PubMed search with keywords 'brain connectivity'.

volume conduction. As a single source signal is captured by many sensors, any connectivity metric, e.g. a measure of correlation, would detect a relationship between these sensors. Although this issue has been addressed methodologically more and more over the past years (Nolte et al., 2004, 2006; Pascual-Marqui, 2007b; Stam et al., 2007; Schoffelen and J.Gross, 2009; Nolte and Müller, 2010; Vinck et al., 2011; Gonzalez et al., 2011; Ewald et al., 2012; Avarvand et al., 2012; Haufe et al., 2012; Marzetti et al., 2013; Ewald et al., 2013), it is still common practice to estimate source activity first and, then, to apply connectivity metrics in source space. Nonetheless, the problem of volume conduction does not seem to be unraveled by solving the inverse problem. For example, Haufe et al. (2012) showed that also on source level spurious interactions can arise due to remaining artifacts of volume conduction.

1.1. Scope of this work

The scope of this thesis is to introduce, evaluate and prove the applicability of a new data analysis methodology that aims at detecting synchronized and, hence, interacting neuronal sources. A special focus lies on the robustness of the novel methodology towards any artifacts of volume conduction. This is achieved by employing the concept behind the imaginary part of coherency (ImCoh) first published by Nolte et al. (2004). Coherence, in general, has been shown to be a valid quantity to measure neuronal interactions (e.g. Nunez et al., 1997, 1999; Fries, 2005). However, there remains the problem of volume conduction. In contrast to the absolute value of the complex valued quantity coherency[1], Nolte et al. (2004) showed that the imaginary part of it is robust to volume conduction. The same holds true for the imaginary part of the cross-spectrum (ImCs) which is the non-normalized ImCoh.

The fundamental idea of this thesis is to base all computations on a quantity derived from the imaginary part of the coherency as a trustworthy source of information. This way, artifacts of volume conduction are diminished or even vanish. Figure 1.3 illustrates this approach. In conventional analysis approaches for functional connectivity from EEG/MEG data, sources are reconstructed first and then, a connectivity measure is applied to conclude on relationships between these sources (upper path in Figure 1.3). In this thesis, a connectivity metric robust to volume conduction is applied on sensor level first. Then, interacting sources are determined (lower path in Figure 1.3).

Please note that it is out of the scope of this thesis to provide a detailed comparison of the introduced methodology with other existing source localization techniques, connectivity measures or combinations among them. Some of the methods presented in the following denote conceptual improvements over existing methods. These improvements are tested and evaluated. In general, the behavior of the new methods is assessed in order to understand and to demonstrate their strengths and weaknesses.

[1] Sometimes in the literature also the complex quantity is called coherence. To avoid any confusion within this thesis, the complex quantity is termed "coherency" while the absolute value of it is termed "coherence".

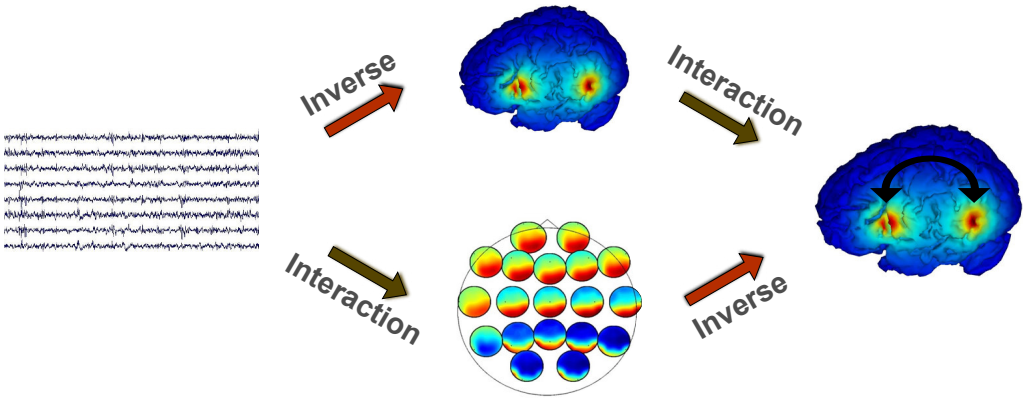

Figure 1.3.: Principle approaches to estimate functional connectivity between brain sources. Most commonly, neuronal sources are estimated from measured EEG or MEG data first. In a second step, relationships between these sources are determined (upper path). As this approach is error-prone due to volume conduction artifacts, an alternative is introduced within this thesis. Here, a sensor level interaction measure robust to volume conduction artifacts is calculated from the data. Then, interacting sources are estimated based on this trustworthy source of information (lower path).

This way, a potential user of these new data analysis techniques can judge in which application scenarios the methods can or cannot be used.

1.2. Outline

The present thesis is organized as follows: In Chapter 2 fundamental concepts of existing EEG and MEG data analysis techniques are reviewed. These are necessary to follow and judge the novel data analysis procedure as some of the new methods are improvements over existing methods. In Chapter 3, the novel methods are introduced theoretically. In Chapter 4 the behavior of the new methodology is evaluated in simulations. This is a fundamental step as usually the ground truth is not known for measured EEG and MEG data. Hence, it is difficult to judge the results of new analysis techniques. Furthermore, the applicability is demonstrated exemplarily on real data in Chapter 5. Finally, Chapter 6 provides a summary and a discussion of the results. Additionally, advantages as well as shortcomings are highlighted.

The novel methodology consists of four parts which can be seen as individual methods. All can be used one after the other to determine the location of interacting brain sources at a specific frequency. Figure 1.4 provides an overview. The first approach is to maximize the imaginary part of coherency. This can be seen as a theoretical framework from which practical applications and specific connectivity measures are derived. It is used for three purposes in this thesis: a) to automatically determine a frequency of interest, i.e. a frequency range where subject specific interactions take place; b) to derive additional connectivity measures called Multivariate Interaction Measure (MIM) and Maximized Imaginary Coherency (MIC) capable of investigating relationships between multiple given brain sources by optimizing the direction of dipoles. Due to specific properties of the measures derived within this

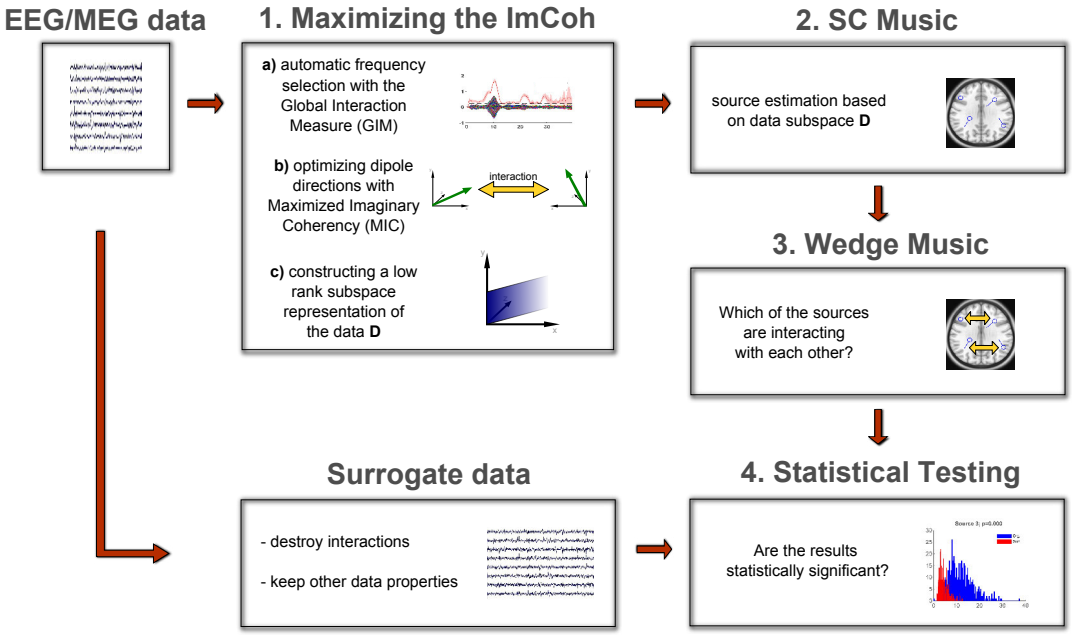

Figure 1.4.: Methodological overview. A description is provided in Section 1.2

framework, they are perfectly suited to compare the measurement modalities EEG and MEG. This will also be demonstrated; c) to define a data subspace representation **D** in which the imaginary part of coherency is maximized. Based on this data subspace at a specific frequency of interest, the second method called SC Music is used to estimate possibly interacting sources. Then, a third method, termed Wedge Music can be applied to specify which of the sources obtained from SC Music are synchronized, i.e. interacting[2]. Finally, a novel approach is presented in order to statistically test the obtained result based on surrogate data.

1.3. Publications

The following list provides an overview of my current publications in chronological order. Parts of these publications are included within this thesis.

Journal publications

[1] A. Ewald, L. Marzetti, F. Zappasodi, F. C. Meinecke, and G. Nolte. Estimating true brain connectivity from EEG/MEG data invariant to linear and static transformations in sensor space. NeuroImage, 60:476 – 488, 2012.

[2] Synchrony measured with coherence is understood to be a mechanism of interaction for large scale brain sources (Fries, 2005; Womelsdorf et al., 2007). Hence, the terms "interacting" and "synchronized" are used as synonyms throughout this thesis.

[2] A. Ewald, S. Aristei, G. Nolte, and R. A. Rahman. Brain oscillations and functional connectivity during overt language production. Frontiers in Psychology, 3:166, 2012.

[3] F. S. Avarvand, A. Ewald, and G. Nolte, Localizing true brain interactions from EEG and MEG data with subspace methods and modified beamformers. Computational and Mathematical Methods in Medicine, Vol. 2012, Article ID 402341, 11 pages, 2012.

[4] A. Ewald, F. S. Avarvand, and G. Nolte. Identifying causal networks of neuronal sources from EEG/MEG data with the phase slope index: a simulation study. Biomed. Tech. (Berl), 58(2):165–178, 2013.

[5] A. Sonnleitner, A., Treder, M.S., M. Simon, S. Willmann, A. Ewald, A. Buchner, and M. Schrauf. EEG alpha spindles and prolonged brake reaction times during auditory distraction in an on-road driving study. Accident; analysis and prevention, 62:110–118, 2014.

[6] F. Shahbazi, A. Ewald, and G. Nolte. Univariate normalization of bispectrum using Hölder's inequality. Journal of Neuroscience Methods. ISSN 0165-0270, 2014.

[7] A. Ewald, F. S. Avarvand, and G. Nolte. Wedge MUSIC: A novel approach to examine experimental differences of brain source connectivity patterns from EEG/MEG data. NeuroImage, 101:610–624, ISSN 1095-9572, 2014.

[8] F. S. Avarvand, A. Ewald, and G. Nolte., Self-Consistent MUSIC for localization of true brain interactions in EEG/MEG, in preparation for NeuroImage

Conference contributions

[9] A. Ewald, A. Ziehe, F. Shahbazi, and G. Nolte. Exploiting prior neurophysiological knowledge to improve brain computer interface performance. In S. Supek and A. Sušac, editors, 17th International Conference on Biomagnetism Advances in Biomagnetism – Biomag2010, number 28 in IFMBE Proceedings, pages 370–373. Springer Berlin Heidelberg, 2010.

[10] F. Shahbazi, A. Ewald, A. Ziehe, and G. Nolte. Constructing surrogate data to control for artifacts of volume conduction for functional connectivity measures. In S. Supek and A. Sušac, editors, 17th International Conference on Biomagnetism Advances in Biomagnetism – Biomag2010, number 28 in IFMBE Proceedings, pages 207–210. Springer Berlin Heidelberg, 2010.

[11] S. Haufe, M. Treder, M. Sagebaum, M. Gugler, A. Ewald, G. Curio, and B. Blankertz. Neural signatures enhance emergency braking intention detection during simulated driving, Poster presentation on Bernstein Conference on Computational Neuroscience. Abstract available under http://eprints.pascal-network.org/archive/00007841/, 2010.

[12] A. Ewald and G. Nolte. Estimating true brain connectivity from EEG/MEG data invariant to coordinate transformations. Book of abstracts SAN 2011 meeting, page 23., 2011

[13] G. Nolte, F. S. Avarvand, and A. Ewald. Localizing interacting brain activity from EEG and MEG data. International Journal of Psychophysiology, 85(3):347, 2012.

[14] A. Ewald, M.F. Gugler, S. Haufe, M. Sagebaum, A. Sonnleitner, M. Schrauf, G. Curio, B. Blankertz, and M.S. Treder, Monitoring attention in a simulated driving scenario using EEG-based connectivity measures, Poster presentation on 18th International Conference on Advances in Biomagnetism, 2012

[15] Y. Xu, A. Ewald, H. L. Graber, J. D. Nichols, M. E. Pflieger, A. Ossadtchi, C. H. Schmitz, and R. L. Barbour. A computing environment for multimodal integration of EEG and fNIRS. Poster presentation on fNIRS conference London, 2013.

[16] A. Ewald and G. Nolte. Evaluating non data-driven EEG/MEG source reconstruction methods with the Earth Mover's Distance. Poster presentation on the 20th Annual Meeting of the Organization for Human Brain Mapping (HBM), 2014.

2. Background

> If I were again beginning my studies, I would follow the advice of Plato and start with mathematics.
>
> *(Galileo Galilei)*

In this chapter, background information is reviewed to support the understanding of this thesis. Neurophysiological details are introduced such as the biological origin of EEG and MEG signals. Additionally, established data analysis techniques are described that are employed and partly revised within this thesis.

2.1. Neurophysiology

EEG and MEG can be subsumed as electrophysiological measurement techniques with identical neurophysiological basis as will be explained in the following. In principle, active groups of spatially aligned nerve cells produce currents. These currents themselves produce electric and magnetic fields spreading through the head. In the case of EEG, the electric fields are measured on the scalp surface as potential differences between two electrodes. In the case of MEG, magnetic fields are captured a few centimeters outside of the head.

2.1.1. Neuronal potentials and dipoles

There are two different types of potentials occurring in a neuronal cell inside the brain: Action Potentials (APs) and Excitatory Post Synaptic Potentials (EPSPs). APs are discrete voltage spikes that travel from the beginning of an axon at the cell body to the end of the axon where the synapses are. There, they cause neurotransmitters to be released (Hodgkin, 1951). EPSPs are generated by the binding of neurotransmitters at the receptors of the post synaptic cell, called apical dendrites. The membrane of the apical dendritic tree becomes electronegative with respect to the cell body and the basal dendrites. Figure 2.1.A illustrates this process. Here, the negative polarization at the apical dendrites is indicated by "-" signs and the positive polarization at the cell body and the basal dendrites with "+" signs. Consequently, a current flows from the non-excited cell body and the basal dendrites to the apical dendritic tree (Gloor, 1985). A portion of the ions will take the direct route inside the cell. This current is called the primary current. To complete the circuit for the conservation of electric charges, current also flows outside the cell in opposite direction. This extracellular

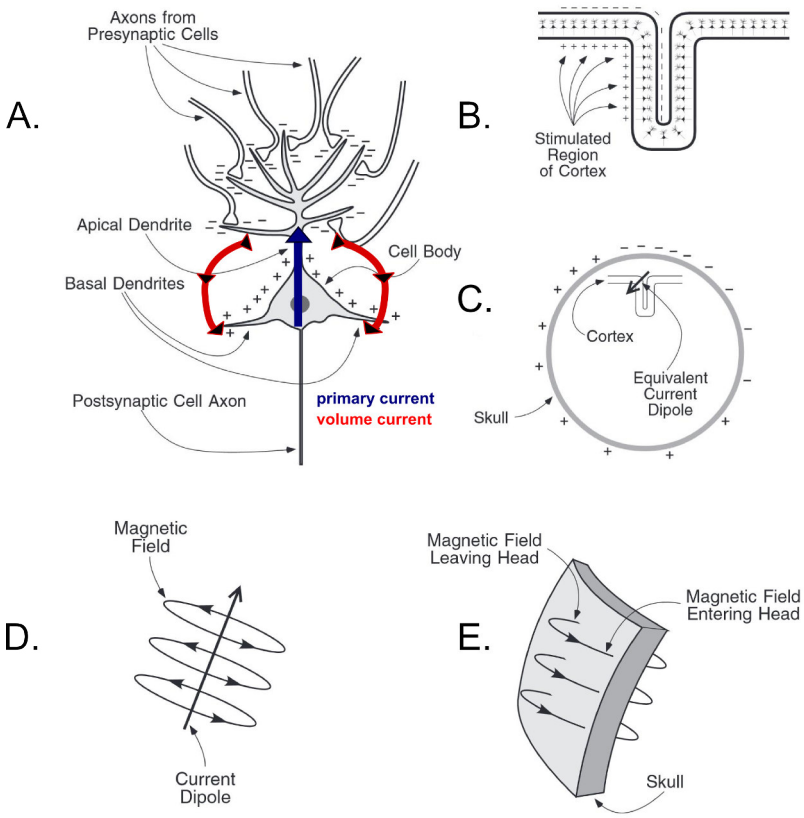

Figure 2.1.: Neurophysiological signal generation. From single cell currents to superimposed equivalent current dipoles and the resulting magnetic fields. Figure adopted from Luck (2005).

current is called volume or secondary current (Baillet et al., 2001). Detectable electric fields at the scalp and magnetic fields outside the head are, in general, caused by primary and volume currents (see Section 2.2.1 and Appendix A.1).

Currents generated in a single cell are too small to produce measurable electric or magnetic fields (Nunez and Srinivasan, 2006). Only the superposition of spatially structured arrangements of neuronal currents in a stimulated patch of cortex leads to currents large enough to be detected non-invasively (see Figure 2.1.B). Please note that depending on the individual cortex folding, certain arrangements also might lead to canceling effects. However, these so called macrocolumns of approximately tens of thousands pyramidical cortical neurons are believed to be the main EEG and MEG signal generators. These signal generators, as shown in Figure 2.1.C, are termed equivalent current dipoles or just dipoles and serve as a model of brain sources in the context of EEG and MEG data analysis. Please note that a dipole is uniquely determined by a location inside the brain and the so called dipole moment. The moment consists of the dipole orientation representing the direction of current flow and the current strength. Hence, measurements at EEG/MEG sensor level depend on the location and on the moment of a dipole (see Section 2.2.1).

2.1.2. Oscillatory brain activity

EEG and MEG signals can be characterized by distinct features. One of these data features are Event Related Potentials (ERPs) in case of EEG, or termed Event Related Fieldss (ERFs) in case of MEG. In general, an ERP or ERF is the direct response to an external stimulus that could be, for instance, visual, acoustic or tactile. Depending on the nature of the stimulus, characteristic properties of the ERP/ERF alter. Therefore, ERPs/ERFs can be interpreted in terms of how the brain processes different types of external information. But not only the characteristic time series alter due to the stimulus. Also does the location of the ERP/ERF and, hence, the distinct measurement sensor in which the ERP/ERF is observed most prominently reveals further relevant information. Usually, ERPs/ERFs are observed by averaging a few seconds of data around the stimulus over many repetitions of the stimulus presentation. This procedure increases the signal-to-noise ratio significantly which is necessary as EEG and MEG data are highly noisy. For an introduction to ERP data analysis see Luck (2005). For the single-trial analysis and the classification of ERP components, see e.g. Blankertz et al. (2011) and Lemm et al. (2011).

A different data feature of the EEG signal has been discovered by Hans Berger in the late 1920s as already mentioned in the introduction. He observed a strong rhythmic component in the data when subjects closed their eyes. Ongoing oscillations with a constant frequency of about 10 Hz became clearly detectable by visual inspection (Berger, 1929). These days, electrophysiological signals are commonly described in terms of rhythmic activity generated by rhythmically firing groups of neurons in different frequency bands. In healthy adults, amplitudes and frequencies change from one mental state to another, such as wakefulness and sleep. Furthermore, individual frequencies vary largely between subjects. The distinction between typical frequency bands is basically done by biological significance. There are five major brain waves. Table 2.1 gives a short overview over the different brain rhythms.

Besides the frequency of oscillatory activity, also the location of a signal inside the brain infers information about the brain's function. For example, large parts of the

Table 2.1.: EEG and MEG frequency bands

name	symb.	frequency range	coarse functional description
delta	δ	0 - 3 Hz	seen in adults in slow wave sleep
theta	θ	4 - 7 Hz	drowsiness or arousal in older children and adults
alpha	α	8 - 12 Hz	attention, visual involvement, motor activity
beta	β	12 - 30 Hz	motor activity, concentration
gamma	γ	34 - 130 Hz	higher cognitive functions

activity in the alpha range originates in the occipital cortex. Usually, this activity is associated with visual attention (e.g. Vanni et al., 1997). In contrast to that, alpha waves occurring in motor areas are most likely due to motor activity and belong to the so called μ-rhythm. The μ-rhythm is composed out of different frequency components in the alpha and beta range and is suppressed during movement or imagined movements (Pfurtscheller and Silva, 1999).

2.2. EEG and MEG neurophysics

The present section reviews how brain sources, modeled as equivalent current dipoles, are mapped into EEG and MEG sensors. From there, intrinsic problems for the reconstruction of brain sources from measured data and for investigating relationships among them are derived. These problems are fundamental for the present thesis. Novel data analysis methods are developed and evaluated in later chapters to approach these issues.

2.2.1. Introduction to forward calculation

Let's consider a distinct set of neuronal current sources in terms of dipoles, including locations and moments. Then, scalp potentials and external magnetic fields are uniquely computable. This procedure is called forward calculation and is briefly outlined in the present section. A more detailed description and a mathematical introduction can be found in Appendix A.1. In principle, the physics can be described by the quasi-static approximation of Maxwell's Equations because frequencies of interest for electrophysiological recordings are typically well below 1 kHz (see Table 2.1) (Plonsey and Heppner, 1967; Sarvas, 1987; Munck and Dijk, 1991).

In general, two different approaches are used to solve the forward problem. First, Boundary Element Methods (BEMs) assume that the head consists of a distinct set of shells where each has a constant and scalar conductivity, e.g. the brain, skull and scalp. Discontinuous field changes occur at the border of these different head compartments whereas the field propagation inside shells remains continuous (conductivities are assumed to be homogeneous and isotropic). The second approach are Finite Element Methods (FEMs) which are computationally exhaustive. Here, calculations are based on the distribution of electromagnetic fields over pre-defined elements inside the volume, i.e. the head. Each of these elements is assigned to a distinct compartment and possesses individual properties such as conductivity, permittivity and permeability.

A crucial point for the correctness of the forward calculation is the applied model of the head. As shown in the Appendix in Equation (Eq.) (A.6) and Eq.(A.5), surface integrals over boundary surfaces have to be evaluated for a BEM approach. Complete analytic solutions only exist when the head is assumed to consist of a set of nested concentric homogeneous spherical or spheroidal shells usually representing brain, (sometimes also the Cerebrospinal fluid (CSF)), skull and scalp (Munck, 1988). However, quasi-analytical solutions exist for volume conductors of realistic shape which

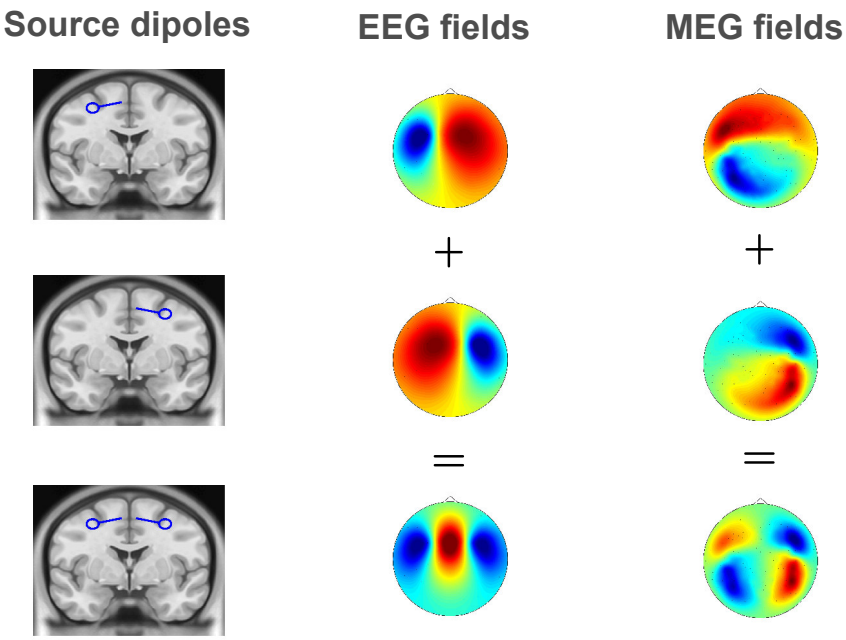

Figure 2.2.: Forward calculation and source mixing: In the first column modeled dipoles are shown. A circle indicates the location of each dipole whereas the corresponding line indicates the dipole moment. In the second column the resulting electric fields and in the third column the resulting magnetic fields are illustrated. For orientation purposes, a little triangle indicates the position of the nose. The individual fields due to two sources are superimposed as shown in the last row (see also Section 2.2.2).

e.g. account for the individual cortex folding. For example, there exist analytical approximations for realistic head models for EEG and for MEG (Nolte and Dassios, 2005; Nolte, 2003). These analytic expansions are used in this thesis to compute the so called leadfields for given sensor positions and head geometries. Leadfields are the solutions of the forward problem and link dipoles at a distinct position and orientation inside the brain to the corresponding electromagnetic fields at the measurement sensors (see also Section 2.2.2). As any kind of forward calculations is quite time consuming even with modern computer hardware, leadfields are usually pre-calculated as soon as sensor positions and the specific head geometry are known. Figure 2.2 provides an example of the forward calculation for a single dipole (upper two rows) and for two dipoles (lower row) both for EEG and MEG. The resulting sensor level fields are called spatial patterns or scalp topographies in the following.

In case of EEG measurements, caps are chosen that fit the individual head size. Therefore, and due to the standardized positioning of the EEG electrodes on the head, which follow the 10-20 system (Klem et al., 1999), the relative positions of the electrodes are constant and do not depend on individual head sizes. The scenario is quite different for MEG. Here, the MEG helmet is stiff and, hence, sensor positions vary with individual head sizes. Furthermore, they depend on the exact position of the head inside the MEG helmet. As a consequence, the specific head position has to be captured in each measurement session. In addition to that, the individual head

geometry obtained by a structural Magnetic Resonance Imaging (MRI) scan has to be aligned to the MEG sensor positions. To achieve this alignment, characteristic points at the subject's nasion and the earlobes, called fiducials, are marked as well in the MEG as in the MRI recording. This way, the MEG sensor positions can be exactly determined relative to the subject's head.

In order to compare modalities, subjects and to perform group statistics, a common standardized head model for both EEG and MEG is used in this thesis: the nonlinear symmetric ICBM 2009b (Fonov et al., 2011, 2009). It is based on the average of 152 subjects in the standard coordinate system of the Montreal Neurological Institute (MNI). This standard head is segmented into different tissue compartments having different electromagnetic properties such as conductivities. These compartments are white matter, gray matter, CSF, skull and scalp. Furthermore, the brain is parceled into non-overlapping and neighboring volume elements called voxels in the following. A set of voxels is also referred to as a source grid, denoting all possible locations where a brain source can occur. Different parcellation schemes are used within this thesis mainly because of computational complexity. Algorithms introduced in this thesis use the source grid as a search space. Computationally exhaustive procedures and some simulation are executed on a coarse grid with a rather large voxel size resulting in fewer number of voxels. In contrast to that, fast computations can be performed on a finer grid. In principle, finer grids increase accuracy and are, therefore, preferable.

2.2.2. Source mixing on sensor level

As described in Section 2.2.1, the mapping from brain sources, i.e. equivalent current dipoles inside the brain, to measurement sensors is uniquely defined by the leadfields. Source signals are instantaneously mixed into sensors due to the propagation of the electromagnetic fields. Mathematically, this mixing is expressed as follows: Let's consider a spatially discretized brain containing M voxels. For each point in time $t = 1 \dots T$, the source signal $\mathbf{s} = (s_1 \dots s_M)^\mathsf{T} \in \mathbb{R}^{M \times 1}$, with $(.)^\mathsf{T}$ denoting the matrix transpose, is linearly superimposed into N sensors $\mathbf{x} = (x_1 \dots x_N)^\mathsf{T} \in \mathbb{R}^{N \times 1}$ via the leadfield matrix[1] $\mathbf{A} \in \mathbb{R}^{N \times M}$. This leads to a system of linear equations which is expressed in matrix form as

$$\mathbf{x}(t) = \mathbf{A}\,\mathbf{s}(t) + \boldsymbol{\eta}(t) \tag{2.1}$$

with $\boldsymbol{\eta} \in \mathbb{R}^{N \times 1}$ being an additional noise term. Noise can be generated on sensor level, e.g. by electric measurement noise such as 50 Hz line noise, as well as on source level, e.g. by task irrelevant background activity. Furthermore, noise usually arises due to biological artifacts such as eye blinks or muscle activity. In principle, noise can be both correlated and uncorrelated.

Eq.(2.1) can be seen as a generative model for EEG and MEG data. Further

[1] Depending on the context, e.g. for Blind Source Separation approaches (see Section 2.3.1), the matrix $\mathbf{A}$ is often also called the source mixing matrix.

formal introductions to the linear mixing model can, for example, be found in Müller et al. (2003), Parra et al. (2005) and Haufe et al. (2014b). Unfortunately, Eq.(2.1) is not uniquely solvable for $\mathbf{s}$ as it is under-determined or ill-posed. Usually, there are many more brain voxels than measurement sensors. Common ranges are $2000 < M < 15000$ depending on the source grid and $30 < N < 250$. Following the dipolar brain source model, a source at a distinct location can have three different orientations leading to $3 \times M$ parameters for the source grid. Considering these numbers, i.e. $3M >> N$, the number of unknowns is several magnitudes greater than the number of equations. Hence, concluding on dipolar brain sources from EEG or MEG measurements is not uniquely possible without further assumptions. This problem is called the inverse problem and can be expressed by

$$\tilde{\mathbf{s}}(t) = \mathbf{W}^{\mathsf{T}} \mathbf{x}(t) \tag{2.2}$$

with $\tilde{\mathbf{s}}$ being a source estimate and where $\mathbf{W} \in \mathbb{R}^{N \times M}$, depending on the context called backward model or de-mixing matrix or spatial filter, links the sensor activity to the sources.

There exist various methods to solve the inverse problem as indicated in Table A.1 in Appendix A.4. In general, one can differentiate between two approaches. Blind Source Separation (BSS) techniques employ certain statistical assumptions on the sources $\mathbf{s}(t)$ to solve the source reconstruction problem. This can be seen as a purely data-driven fitting procedure. Other methods make use of the leadfield matrix $\mathbf{A}$ and aim to find solutions such that $\mathbf{W}^{\mathsf{T}} \mathbf{A} = \mathbf{I}_M$ with $\mathbf{I}_M$ being the $M \times M$ identity matrix. Some of these approaches are introduced in Section 2.3 and, furthermore, are refined throughout this thesis with a special focus on connectivity analysis.

2.2.3. The artifact of volume conduction

Brain sources are linearly superimposed into sensors due to volume conduction of electromagnetic fields. Therefore, time series of EEG/MEG measurement channels are correlated. Signals in neighboring channels are almost identical as generated by the same sources but mapped intro sensors with slightly different weights. In terms of connectivity analysis this problem is called the artifact of volume conduction or sometimes also field spread or spurious interactions. In fact, volume conduction is a misnomer as electromagnetic fields also would propagate in vacuum. Furthermore, volume conduction is not an artifact by itself but leads to misinterpretations in the context of connectivity analysis. Nevertheless, as the term is widely used in the literature and, hence, became convention, the nomenclature is also used in this thesis. Figure 2.3 illustrates the artifact of volume conduction due to source mixing. It becomes obvious that a statistical relationship between sensor signals does not necessarily provide information about relationships between the underlying brain sources (green arrows in Figure 2.3).

The artifact of volume conduction influences the estimation of interactions within the brain not only on sensor level. A common argument is that after solving the inverse problem, volume conduction can be neglected because sources are de-mixed.

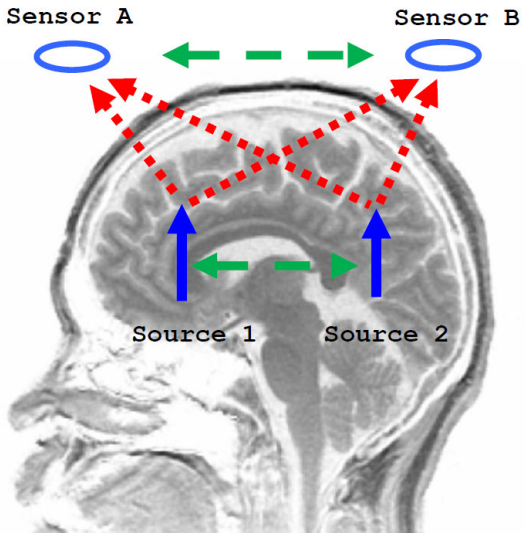

Figure 2.3.: Sensor level effects of volume conduction. A single source is mapped into many measurement sensors (red arrows). Hence, the measured signal is a mixture of the true brain sources. Statistical dependencies between the time series of different sensors reveals only little about the underlying source interactions (green arrows).

But this is not necessarily the case as previously outlined e.g. by Haufe et al. (2012), Sekihara and Nagarajan (2013) and demonstrated with two examples in the following simulation: A *single* dipole at an arbitrary location with arbitrary moment is modeled inside the brain. Source dynamics are modeled with an autoregressive (AR) model as described in Section 4.1 but are of no importance in this case. Source estimates for each voxel are obtained by a well-established method called eLoreta (see Appendix A.3 and Pascual-Marqui, 2007a). Figure 2.4 shows a reference voxel indicated by a black cross and coherence (introduced in Section 2.4.1) as a measure of connectivity to all other voxels color-coded. Two scenarios are shown demonstrating two types of artifacts of volume conduction on source level. Please keep in mind that no source interaction is underlying the data. Figure 2.4.A shows an effect called seed blur. The region around the reference voxel seems to show coherent activity with respect to the reference voxel. The inspection of Figure 2.4.B would lead to the interpretation of an interacting source pair. The reference voxel seems to be synchronized with a source in the frontal cortex. However, this ghost source is not present in the data and is solely an artifact of remaining volume conduction effects on source level.

2.2.4. General differences between EEG and MEG

Although sharing data analysis methods, the neurophysiological basis and the temporal resolution, there exist substantial differences between EEG and MEG. In fact, both are two completely different recording techniques. First of all, the recording procedure differs as indicated before: For EEG, electrodes are either glued directly to the scalp or, more commonly, fitted to pre-defined positions in an elastic cap scaled according to the subject's head size. For MEG, subjects are placed under a

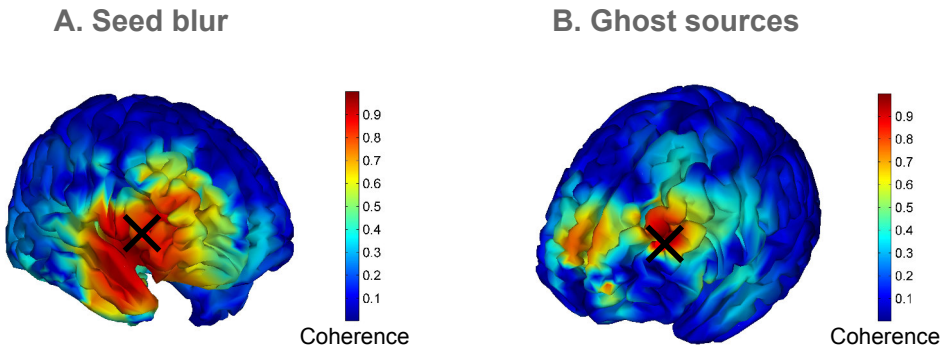

Figure 2.4.: Two artifacts of volume conduction for connectivity analysis on source level. In both cases a reference dipole is shown as a black cross. Coherence of this reference voxel to all other voxels is color-coded. No source interactions are modeled and all observed interactions are artifacts. A: Regions around the seed voxel seem to be highly coherent with respect to the reference voxel. B.: The reference voxel seems to be interacting with a source located a few centimeters next to it.

stiff helmet in which the measurement sensors are incorporated. Hence, the true position of the head inside the helmet is unknown and so are the positions of the measurement sensors relative to the head. Therefore, the position of the head is recorded at the beginning of an MEG measurement such that the sensor positions can be aligned to an individual MR image during post-processing. Alternatively, the MEG sensor positions can be scaled to fit to a standard head model. But either way, sensor positions have to be recorded.

Furthermore, the measurement sensors differ. In the case of EEG, electrodes pick up a potential difference with respect to a certain reference. The choice of reference is not trivial and can lead to additional problems (see e.g. Hagemann et al., 2001). In contrast to that, MEG is reference free. Superconducting Quantum Interference Devices (SQUIDs) are used to detect changes in the magnetic flux in a superconducting environment. SQUIDs are extremely sensitive amplifiers as neural currents produce particularly small magnetic fields in the order of tens of femto Teslas (Cohen, 1968).

An additional aspect in the comparison between the two electrophysiological measurement techniques is that MEG is insensitive for radial sources. Current dipoles pointing out of the scalp are barely captured by an MEG system due to cancellation effects of the magnetic fields. In contrast, tangential sources, i.e. sources oriented parallel to the scalp, produce a magnetic field well measurable with MEG. From this phenomena one can derive another weakness of MEG: a reduced sensitivity towards deeper sources. Let's consider the head shape approximated by a perfect sphere and a dipolar source at the center of the sphere. This source is necessarily pointing towards the sphere's surface and is, therefore, in radial direction. As stated before, the MEG would not be able to capture this source. Sources in deeper brain regions are more similar to this central source compared to superficial ones and, hence, less visible for MEG. The deeper a source, the more 'radial' and less visible it becomes. EEG is, in general, sensitive to both radial and tangential dipoles. However,

the performance of localizing neuronal activity is usually slightly better for MEG as for example much more measurement sensors can be used. Furthermore, the propagation of electric fields is much more suppressed by the skull compared to magnetic fields. Details about the different forward models of EEG and MEG and the corresponding impact on source localization can be found in Lopes da Silva et al. (1991). A comparison between EEG and MEG with novel data analysis methods focusing on the observation of source interactions is contained in thesis (see Sections 3.1.3 and 5.1.2).

2.3. Inverse calculation

An introduction to the inverse problem, i.e. the estimation of neuronal sources from EEG/MEG recordings, is given in Section 2.2.2. In the following, different particular solutions and methods are presented in more detail.

2.3.1. Blind Source Separation (BSS): PCA and ICA

Blind Source Separation (BSS) techniques are a family of methods that aim for the separation of linearly mixed signals without specific information about the source signals or the mixing process. However, they incorporate assumptions such as spatial orthogonality or temporal statistical independence to solve the decomposition[2] problem. Within this thesis, BSS approaches are used for certain pre-processing steps. The resulting estimates of the demixed time series or the corresponding scalp topographies, also called spatial patterns, will not be interpreted as true brain sources.

Principle Component Analysis (PCA)

One BSS technique is Principle Component Analysis (PCA) that linearly transforms a set of N variables $\mathbf{x}(t) = (x_1(t) \dots x_N(t))^\mathsf{T}$, i.e. time series in N EEG/MEG measurement channels, into N temporally uncorrelated variables $\mathbf{s}(t) = (s_1(t) \dots s_N(t))^\mathsf{T}$. The transformation is achieved by spatially orthogonal, so called principal components. These can be determined by an eigendecomposition of the covariance matrix $\mathbf{\Sigma} \in \mathbb{R}^{N \times N}$ estimated from the data. The factorization reads

$$\mathbf{\Sigma} = \mathbf{Q}\mathbf{\Lambda}\mathbf{Q}^\mathsf{T} \tag{2.3}$$

with $\mathbf{\Lambda} \in \mathbb{R}^{N \times N}$ being a diagonal matrix containing the eigenvalues $(\mathbf{\Lambda}_{jj} = \lambda_j) > (\mathbf{\Lambda}_{j+1,j+1} = \lambda_{j+1})$ on the diagonal in descending order. $\mathbf{Q}$ is an orthogonal quadratic matrix with the j-th column $\mathbf{q}_j$ being the j-th eigenvector of $\mathbf{\Sigma}$ belonging to the j-th

[2] The term inverse calculation is specifically used in the context of brain sources. BSS techniques are applied in many different fields of data science where the the problem often is referred to as a decomposition.

eigenvalue λ_j. One can interpret the first eigenvector $\mathbf{q}_1$ as the principle component explaining most of the variance of the data. Then, the component $\mathbf{q}_2$ is by construction orthogonal to $\mathbf{q}_1$ and explains second most variance. According to the PCA transformation, N uncorrelated source times series $\mathbf{s}(t)$ with spatial patterns $\mathbf{q}_j, j = 1 \dots N$ can be reconstructed via $\mathbf{s}(t) = \mathbf{Q}^\mathsf{T}\mathbf{x}(t)$. However, the orthogonality assumption of the resulting spatial patterns is not plausible for brain sources. Hence, PCA is rather rarely used for the estimation of spatial source patterns and source time series. Within this work, PCA is instead used in order to reduce the dimensionality of the data.

In addition to the described eigendecomposition, the related Singular Value Decomposition (SVD) can be used to perform a PCA. The SVD is defined by the decomposition of the either complex or real $N \times M$ matrix $\mathbf{S}$ with

$$\mathbf{S} = \mathbf{U}\mathbf{\Gamma}\mathbf{V}^\dagger \tag{2.4}$$

where $(.)^\dagger$ denotes the complex conjugate transpose. Then, $\mathbf{\Gamma} \in \mathbb{R}^{N \times M}$ is a rectangular matrix with non-negative real numbers $\mathbf{\Gamma}_{jj} = \gamma_j$ on the diagonal called singular values. These are the square roots of the eigenvalues of $\mathbf{S}^\dagger\mathbf{S}$ as well as $\mathbf{S}\mathbf{S}^\dagger$. $\mathbf{U}$ is a real or complex unitary $N \times N$ matrix containing the left singular vectors as columns. These are equal to the eigenvectors of $\mathbf{S}\mathbf{S}^\dagger$. The eigendecomposition and the SVD are formally equivalent if $\mathbf{S}$ is a normal and positive semi-definite matrix. This is, e.g. the case for the quadratic and symmetric covariance matrix. However, in contrast to the eigendecomposition, the SVD can generally be applied on complex and non-quadratic matrices which is exploited by methods introduced in Chapter 3.

To reduce the dimensionality of data, a lower dimensional subspace of a second order statistical moment such as the covariance matrix or the complex cross-spectrum (see Section 2.4.1) has to be found. Formally expressed, the quadratic $N \times N$ matrix $\mathbf{S}$ having rank N has to be approximated by a $P \times N$ matrix $\hat{\mathbf{S}}$ with lower rank $P < N$. This problem can be expressed as the constraint minimization

$$\arg\min_{\hat{\mathbf{S}}} \left\|\mathbf{S} - \hat{\mathbf{S}}\right\|_\mathrm{F} \text{ subject to } \mathrm{rank}(\hat{\mathbf{S}}) = P. \tag{2.5}$$

As shown by the Eckart–Young theorem (Eckart and Young, 1936; Stewart, 1993), the solution of Eq.(2.5) with $\|.\|_\mathrm{F}$ being the Frobenius norm is given by the SVD

$$\hat{\mathbf{S}} = \mathbf{U}\hat{\mathbf{\Gamma}}\mathbf{V}^\dagger \tag{2.6}$$

where $\hat{\mathbf{\Gamma}}$ is the same matrix as $\mathbf{\Gamma}$ in Eq.(2.4) except that $\hat{\mathbf{\Gamma}}$ only contains the P largest singular values. The other $N - P$ singular values are set to zero. This implicates that the first unitary left singular vectors (columns of $\mathbf{U}$) containing the P strongest components span a P-dimensional subspace of the matrix $\mathbf{S}$. In the literature, this procedure is also referred to as a truncated SVD.

Independent component analysis (ICA)

A further widely used blind source separation technique is Independent Component Analysis (ICA) (see e.g. Hyvärinen, 2013; Stone, 2004). ICA methods decompose measured data into statistically independent time series. Whereas PCA provides uncorrelated source signals, this assumption is not sufficient to achieve statistical independence. How the idea of statistical independence is approximated depends on the particular realizations of ICA-based methods. One family of methods minimizes the Gaussianity of the source signals as according to the central limit theorem the sum of two independent time series is closer to a Gaussian distribution than a single time series. Hence, these methods imply non-Gaussian distributed data. A famous method in this context is FastICA which maximizes kurtosis and uses projection pursuit directions in order to achieve non-Gaussianity (Hyvärinen, 1999). Further methods are Infomax which parallelizes the projection pursuit approach (Bell and Sejnowski, 1997) and Joint Approximate Diagonalization of Eigenmatrices (JADE) exploiting fourth-order cumulants (Cardoso and Souloumiac, 1993). A slightly different approach to achieve independence of the ICA filtered time series is implemented in Temporal Decorrelation Source Separation (TdSEP) (Ziehe and Müller, 1998) and Second-Order Blind Source Identification (SOBI) (Belouchrani et al., 1997) which are also applicable for Gaussian distributed data. Here, the additional assumption to uncorrelated signals is that also the delayed versions of signals are supposed to be uncorrelated. Algorithmically, this leads to joint diagonalization of multiple cross-correlation matrices obtained by using different time lags $t = 0 \dots \tau$.

Within this work, ICA-filtered data are not interpreted as source data originating from neural activity, since the aim is to study relationships between the resulting sources in a consecutive step. Assuming independence in order to reconstruct the sources contradicts the idea of studying connectivity among them. Nevertheless, this procedure has been successfully used and reported in several cases. An argument to do so is the inaccurate nature of the ICA algorithm leading to remaining statistical dependencies which can be studied (e.g. Astolfi et al., 2007; Makeig et al., 2004). In this thesis, ICA is used to identify and reject parts of the measured EEG/MEG data that do not emerge from the brain. As for example eye-blinks, 50 Hz line noise, muscle or cardiac artifacts are statistically independent from neuronal data, ICA has become a state-of-the-art tool to clean data in a pre-processing step (Ziehe et al., 2000; Jung et al., 2000; Escudero et al., 2007; James and Gibson, 2003; Joyce et al., 2004). Furthermore, ICA is used here to construct independent surrogate data in order to statistically validate the connectivity measures introduced in this thesis (see Section 3.4).

2.3.2. Beamforming

A famous source reconstruction method, widely used especially for MEG data analysis, is beamforming. In the literature, beamforming is often referred to as a spatial filtering technique. The basic concept of beamforming is to determine filter weights $\mathbf{W}$ such that a) a signal emerging in the brain at voxel m is passed

to the measurement sensors with unit gain and b) the overall power is minimized (Van Veen et al., 1997). The idea of minimizing the overall power as a boundary condition originates from the assumption that sources of interest and noise sources are independent. Hence, passing the signal of interest untouched and minimizing total power leads to a maximization of the Signal-to-Noise Ratio (SNR).

Mathematically, the idea is realized as follows. Considering the zero mean data matrix $\mathbf{X} \in \mathbb{R}^{N \times T}$ (N: number of measurement channels; T: number of samples over time), the covariance matrix $\mathbf{\Sigma} \in \mathbb{R}^{N \times N}$ can be estimated by $\mathbf{\Sigma} = \langle \mathbf{X}\mathbf{X}^{\mathsf{T}} \rangle$, where $\langle . \rangle$ denotes the expectation value which can be approximated by averaging over a large number of experimental repetitions or trials (Bendat and Piersol, 1971). As the signals have zero mean, the variance of each measurement channel, encoded on the diagonal of $\mathbf{\Sigma}$, is equal to the average power of that channel. Let's consider a specific source voxel m and the corresponding leadfield $\mathbf{A}_m \in \mathbb{R}^{N \times 3}$ for x-, y-, and z-direction. Then, the spatial filter $\mathbf{W}_m \in \mathbb{R}^{N \times 3}$ passing the signal at voxel m with unit gain and simultaneously minimizing over total source power can be expressed by

$$\mathbf{W}_m = \arg\min_{\mathbf{W}_m} \left(\mathbf{W}_m^{\mathsf{T}} \mathbf{\Sigma} \mathbf{W}_m \right) \text{ subject to } \mathbf{W}_m^{\mathsf{T}} \mathbf{A}_m = \mathbf{I}_3. \tag{2.7}$$

In analogy to the derivation in Appendix A.2, Eq.(2.7) can be resolved analytically to

$$\mathbf{W}_m = \mathbf{\Sigma}^{-1} \mathbf{A}_m \left(\mathbf{A}_m^{\mathsf{T}} \mathbf{\Sigma}^{-1} \mathbf{A}_m \right)^{-1} \tag{2.8}$$

and is termed a Linear Constraint Minimum Variance beamformer (LCMV) (Van Veen et al., 1997; Spencer et al., 1992). The LCMV beamformer as described in Eq.(2.8) belongs to the class of vector beamformers as a three-dimensional spatial filter is established per voxel denoting a filter in each unit direction. A dipole moment still has to be established in order to obtain a single source time series per voxel. This can be achieved in various ways. Usually, for each voxel a dipole orientation is chosen such that the signal is strongest, i.e. the direction that maximizes power. Using an SVD (see Section 2.3.1) of the three-dimensional subspace at each voxel, two procedures are common to estimate the power: a) taking the largest singular value corresponding to the dipole direction maximizing power or b) taking the trace of the matrix $\mathbf{\Gamma}$ in Eq.(2.4), which is the sum of the singular values. This way a source distribution $\tilde{\mathbf{s}} \in \mathbb{R}^{M \times 1}$ is constructed indicating source power per voxel. Instead of maximizing power, an alternative approach is introduced in this thesis in Section 3.2.4.

Instead of this two-step procedure of spatial filtering with a vector beamformer and then fixing the dipole moment, a scalar beamformer combines both steps. For example, another approach is Synthetic Aperture Magnetometry (SAM) introduced by Vrba and Robinson (2001). There, the dipole moment is chosen within the estimation of the spatial filter such that the ratio between the source power and a noise power estimate is maximized. This is in contrast to Anatomically Constraint Beamforming (ACB), where the moment is fixed such that the dipole is always orthogonal to the surface of the cortex (Hillebrand and Barnes, 2003).

As stated above, the idea of beamforming is to pass the signal at voxel m and minimize the power of all other sources. This approach implicitly requires independent, i.e. incoherent (see Section 2.4.1) sources. In case of correlated or coherent sources the LCMV beamformer apparently fails to suppress *and* pass identical signal parts at different locations in the brain which leads to partial cancellation at the signal of interest (Reddy et al., 1987). A remedy to this problem is the so called Nulling beamformer (Hui and Leahy, 2006; Dalal et al., 2006; Hui et al., 2010). There, additional constraints are introduced forcing zero gain at pre-defined interfering source locations $p = 1 \dots P$. In scalar form, i.e. considering a fixed dipole direction at voxel m with the leadfield $\mathbf{a}_m \in \mathbb{R}^{N\times 1}$ and the spatial filter $\mathbf{w}_m \in \mathbb{R}^{N\times 1}$, these can be written as

$$\mathbf{w}_m^\mathsf{T}\mathbf{a}_p = 0 \quad \text{for} \quad p \in \{1 \dots P; p \neq m\}\,. \tag{2.9}$$

To combine the unit gain constraint of the LCMV beamformer as in Eq.(2.7) and the nulling constraint in Eq.(2.9), a matrix $\mathbf{B} = [\mathbf{a}_1 \dots \mathbf{a}_P] \in \mathbb{R}^{N\times P}$ can be defined containing P leadfields for possibly correlated or coherent sources. Furthermore, a vector $\mathbf{f}_p = [0 \dots 0\ 1\ 0 \dots 0]^\mathsf{T} \in \mathbb{R}^{P\times 1}$ can be defined containing a one at the p-th element and zeros elsewhere. Now, the scalar variant of the Nulling beamformer is given by

$$\mathbf{w}_m = \arg\min_{\mathbf{w}_m} \left(\mathbf{w}_m^\mathsf{T}\boldsymbol{\Sigma}\mathbf{w}_m\right) \text{ subject to } \mathbf{w}_m^\mathsf{T}\mathbf{B} = \mathbf{f}_p^\mathsf{T}. \tag{2.10}$$

Following the derivation with Lagrange multipliers as demonstrated in Appendix A.2, the minimization can be solved to be

$$\mathbf{w}_m = \boldsymbol{\Sigma}^{-1}\mathbf{B}\left(\mathbf{B}^\mathsf{T}\boldsymbol{\Sigma}^{-1}\mathbf{B}\right)^{-1}\mathbf{f}_p. \tag{2.11}$$

Finally, Eq.(2.11) can be evaluated either over all voxels M assuming fixed dipole directions or $3M$ times with dipoles in each unit direction.

A variant of LCMV beamforming is Dynamic Imaging of Coherent Sources (DICS) where the beamforming procedure is performed in the frequency domain (Gross et al., 2001). Here, not the covariance matrix is used to establish the spatial filter but the real part of the complex cross-spectrum at a particular frequency (see Section 2.4.1). The real part is used because the mixing of sources into sensors can be assumed to be instantaneous which is reflected in the real part of the cross-spectrum as shown in Section 2.4.2. Mathematically, this can be derived by constraining the resulting filters to be real valued. It can be shown with the same line of arguments as in the Appendix A.2. In principle, the approach of LCMV beamforming as introduced above is identical to DICS. Assuming a narrow band filtered signal, both methods should theoretically lead to the same spatial filter.

2.3.3. Music and Rap Music

Another method capable of estimating brain sources from data measured at the scalp is Multiple Signal Classification (Music) introduced for EEG/MEG data by Mosher et al. (1999a). The fundamental idea behind Music is to separate data and noise

by defining a $P \ll N$ dimensional low-rank subspace projection of the data in N measurement channels and an orthogonal noise space. The so called signal subspace $\hat{\mathbf{\Sigma}} \in \mathbb{R}^{N \times P}$ is usually spanned by the first P orthonormal principle components (see Section 2.3.1) of the data's covariance matrix $\mathbf{\Sigma} \in \mathbb{R}^{N \times N}$, which itself has full rank for the noisy EEG/MEG data[3]. In practice, it is convenient that the subspace dimension P corresponds to the assumed number of sources. The noise subspace $\hat{\mathbf{\Sigma}}_{noise}$, orthogonal to $\hat{\mathbf{\Sigma}}$, is estimated by the span of the remaining $N - P$ eigenvectors of $\mathbf{\Sigma}$. Given the subspaces, a scan over all brain voxels is performed to determine whether a potential source at grid point m is consistent with the signal subspace $\hat{\mathbf{\Sigma}}$, i.e. whether it is included in the data subspace. This consistency can be expressed in terms of the canonical angle ϑ, determined between $\hat{\mathbf{\Sigma}}$ and the leadfield $\mathbf{a}_m \in \mathbb{R}^{N \times 1}$ at grid point m (Drmac, 2000). If ϑ is small or even zero, a source at grid point j is likely to be contained in the data subspace. For given dipole directions, the canonical or principle angle ϑ is defined as

$$\cos^2 \vartheta(\mathbf{a}_m, \hat{\mathbf{\Sigma}}) = \frac{\mathbf{a}_m^\top \hat{\mathbf{\Sigma}}^\top \hat{\mathbf{\Sigma}} \mathbf{a}_m}{\mathbf{a}_m^\top \mathbf{a}_m}. \tag{2.12}$$

For unknown dipole directions, the leadfield $\mathbf{a}_m$ can be expressed by

$$\mathbf{a}_m = \mathbf{A}_m \mathbf{d}_m \tag{2.13}$$

with $\mathbf{A}_m \in \mathbb{R}^{N \times 3}$ being the leadfield matrix for unit dipole directions in x-, y- and z- direction and $\mathbf{d}_m \in \mathbb{R}^{3 \times 1}$ being a vector defining the dipole direction at voxel m. Now, the angle ϑ can be determined by optimizing over $\mathbf{d}_m$, expressed by

$$\cos^2 \vartheta(\mathbf{A}_m, \hat{\mathbf{\Sigma}}) = \arg\max_{\mathbf{d}_m} \left(\frac{\mathbf{d}_m^\top \mathbf{A}_m^\top \hat{\mathbf{\Sigma}}^\top \hat{\mathbf{\Sigma}} \mathbf{A}_m \mathbf{d}_m}{\mathbf{d}_m^\top \mathbf{A}_m^\top \mathbf{A}_m \mathbf{d}_m} \right). \tag{2.14}$$

Considering the right hand side of Eq.(2.14) as the Rayleigh quotient $\frac{\mathbf{d}_m^\top \mathbf{E} \mathbf{d}_m}{\mathbf{d}_m^\top \mathbf{d}_m}$, the solution for the maximum of $\mathbf{d}_m$ is given by the eigenvector corresponding to the maximum eigenvalue of

$$\mathbf{E} := \left(\mathbf{A}_m^\top \mathbf{A}_m \right)^{-1} \mathbf{A}_m^\top \hat{\mathbf{\Sigma}}^\top \hat{\mathbf{\Sigma}} \mathbf{A}_m. \tag{2.15}$$

One drawback of the Music algorithm is its failure in the presence of increasing numbers of sources which leads to several local maxima for a single scan. Especially in the context of dependent, i.e. correlated or coherent source signals, Music based estimation does not lead to properly separated sources. In the field of acoustic signal processing, several improvements have been suggested based on estimating the sources sequentially (see Oh and Un, 1989; Stoica et al., 1995; Chen and Zhao,

[3] In general, a space is defined by the span of vectors. However, for the ease of reading, a matrix will be referred to as a space or subspace in the following if the column vectors contained in this matrix span the corresponding space.

2005). A popular method in the context of EEG/MEG data analysis is Recursively Applied Multiple Signal Classification (Rap Music) (Mosher and Leahy, 1999). Here, the strongest source (smallest angle ϑ) found by an initial Music scan is projected out and the Music scan is repeated. Hereafter, the first and the second strongest source are projected out and so on. This procedure is repeated for all $p = 1 \dots P$ sources as follows: Let's define a matrix $\mathbf{B} = \begin{bmatrix} \mathbf{a}_1 \dots \mathbf{a}_p \end{bmatrix} \in \mathbb{R}^{N \times p}$ containing all $p \leq P$ previously found dipole patterns as columns. Then, the projection matrix

$$\mathbf{Q} := \mathbf{I}_N - \mathbf{B} \left(\mathbf{B}^\mathsf{T} \mathbf{B} \right)^{-1} \mathbf{B}^\mathsf{T} \tag{2.16}$$

is applied to the leadfields $\mathbf{A}^p = \mathbf{Q}\mathbf{A}^{p-1}$ and $\hat{\mathbf{\Sigma}}^p = \mathbf{Q}\hat{\mathbf{\Sigma}}^{p-1}$, where the superscript denotes the p-th iteration of the algorithm. Finally, the data subspace $\hat{\mathbf{\Sigma}}^p$ has to be orthonormalized before a new Music scan with the updated quantities can be executed. Algorithm 2.1 provides an overview of the Rap Music procedure.

Algorithm 2.1 Rap Music algorithm (Mosher and Leahy, 1999)

construct signal subspace $\hat{\mathbf{\Sigma}}^0$
create empty set $\mathcal{L}$
for m=1 **to** M grid points **do**
  find ϑ_m with $\cos^2 \vartheta_m(\mathbf{a}_m, \hat{\mathbf{\Sigma}}^0) = \frac{\mathbf{a}_m^\mathsf{T} (\hat{\mathbf{\Sigma}}^0)^\mathsf{T} \hat{\mathbf{\Sigma}}^0 \mathbf{a}_m}{\mathbf{a}_m^\mathsf{T} \mathbf{a}_m}$
end for
for p=1 **to** P **do**
  find grid point $\tilde{m}$ with $\vartheta_{\tilde{m}} \leq \vartheta_j \; \forall \;\; j = 1 \dots M$
  add grid point $\tilde{m}$ to the set of grid points $\mathcal{L}$
  $\mathbf{B} := \begin{bmatrix} \mathbf{a}_1 \dots \mathbf{a}_p \end{bmatrix} \; \forall \; p \in \mathcal{L}$
  calculate projection matrix $\mathbf{Q} = \mathbf{I}_N - \mathbf{B} \left(\mathbf{B}^\mathsf{T} \mathbf{B} \right)^{-1} \mathbf{B}^\mathsf{T}$
  apply projection matrix to the leadfields $\mathbf{A}^p = \mathbf{Q}\mathbf{A}^{p-1}$
  apply projection matrix to the signal subspace $\hat{\mathbf{\Sigma}}^p = \mathbf{Q}\hat{\mathbf{\Sigma}}^{p-1}$
  orthonormalize the the signal subspace $\hat{\mathbf{\Sigma}}^p$
  for m=1 **to** M grid points **do**
    find ϑ_m with $\cos^2 \vartheta_m(\mathbf{a}_m, \hat{\mathbf{\Sigma}}^p) = \frac{\mathbf{a}_m^\mathsf{T} (\hat{\mathbf{\Sigma}}^p)^\mathsf{T} \hat{\mathbf{\Sigma}}^p \mathbf{a}_m}{\mathbf{a}_m^\mathsf{T} \mathbf{a}_m}$
  end for
end for

2.3.4. Additional source reconstruction approaches

Next to the different beamforming and Music approaches as introduced in the previous sections, there exist many more methods to perform EEG/MEG inverse source reconstruction. A widely-used family of methods are the minimum norm based estimates. These are not directly applied within this thesis but it is easily possible to combine them with the novel methodology introduced in Chapter 3. For example, methods like Exact Low Resolution Brain Electromagnetic Tomography

(eLoreta) (Pascual-Marqui, 2007a) also determine a spatial filter at each voxel in the three different unit directions such as a vector beamformer. Therefore, an introduction to minimum norm based inverse approaches can be found in the Appendix A.3. Furthermore, Appendix A.4 provides an overview of existing methods in tabular form. One can observe a large variety of methods, all implying different assumptions on the data or the noise.

2.4. Connectivity measures

In the following, methods are introduced that evaluate the strength of a linear relationship between two time series. Specific properties of EEG/MEG signals are explicitly considered. Measures introduced here form the basis for novel data analysis techniques introduced in later parts of this thesis.

2.4.1. Cross-spectra and coherency

As stated in Chapter 1, coherence has been identified to be a mechanism of large scale neuronal communication within the brain (Fries, 2005). Coherence can be seen as a form of a correlation measure applied in the frequency domain[4]. However, due to the oscillatory nature of EEG/MEG signals (see Section 2.1.2), coherence is an appropriate measure to quantify interactions between large populations of neurons. It is based on the complex valued cross-spectrum.

Let us consider a univariate time series $\dot{\mathbf{x}}_p \in \mathbb{R}^{1\times T}$ measured at $t = 1 \dots T$ sampling points with sampling frequency f_s in a measurement channel p. The Discrete Fourier Transform (DFT) (Jean Baptiste Joseph Fourier, 1822; Oppenheim et al., 1999) provides an estimate of the spectral or oscillatory content of this signal by decomposing the signal into a weighted sum of different sinusoidal functions at a distinct frequency. It is defined as the complex valued quantity

$$x_p(f) = \sum_{t=1}^{\mathsf{T}} \dot{\mathbf{x}}_p e^{\frac{-i2\pi ft}{(T+1)}} =: r_p(f)e^{i\phi_p(f)} \tag{2.17}$$

where r_p denotes the amplitude of an oscillation at a specific frequency f and where ϕ_p denoted the phase. The phase can be seen as the frequency representation of the time delay of the first zero crossing of a sinusoidal wave at f. Considering a segment (e.g. an event-related epoch) of measured EEG/MEG data in the pair of sensors p and q, the cross-spectrum is defined as

$$S_{pq}(f) = \left\langle x_p(f)x_q^*(f) \right\rangle = \left\langle r_p(f)r_q(f)e^{i(\phi_p(f)-\phi_q(f))} \right\rangle \tag{2.18}$$

where $(.)^*$ denotes complex conjugation. In the following, the matrix $\mathbf{S}(f) \in \mathbb{C}^{N\times N}$

[4] In fact, correlation and the real part of coherency are formally equivalent for narrow band filtered signals

will be referred to as the cross-spectrum between all $N \times N$ EEG or MEG channel pairs. It is complex, the real part is symmetric, the imaginary part antisymmetric and it contains the (real-valued) power for each individual channel on the diagonal. This can be seen by setting $p = q$ in Eq.(2.18). One can observe from Eq.(2.18) that the phase difference between signals in two channels at a distinct frequency is explicitly contained in the exponent and that it is weighted by the single trial signal amplitudes.
Coherency is now defined as the cross-spectrum normalized over the signal power in both channels p and q which leads to

$$C_{pq}(f) = \frac{S_{pq}(f)}{\sqrt{S_{pp}(f)S_{qq}(f)}} = \frac{\left\langle r_p(f) r_q(f) e^{i(\phi_p(f)-\phi_q(f))} \right\rangle}{\sqrt{\left\langle r_p^2(f) \right\rangle \left\langle r_q^2(f) \right\rangle}}. \tag{2.19}$$

The aim of the normalization is to focus on the phase difference between two signals and not on signal amplitudes. Coherency can be seen as a measure for phase difference consistency over trials which is illustrated in Fig.2.5. If the relative phase, i.e. phase difference between two signals, is randomly distributed over trials, the average is close to zero (see Fig.2.5.B). This is in contrast to a relative phase which is consistent over multiple trials. There, coherency has a value different from zero (see Fig.2.5.A). This constant phase relation indicates a synchronization between two signals at a particular frequency or within a band.

Please note that coherency is, analogous to the cross-spectrum, complex-valued. To prevent any misunderstanding, the complex value defined in Eq.(2.19) will be denoted as coherency and its absolute value as coherence (length of the black solid line in Fig.2.5.A). The imaginary part of a quantity, e.g. the cross-spectrum or coherency, will be denoted as $\Im(.)$ or alternatively, for the ease of notation, as $(.)^I$. In contrast to that, the real part is denoted as $\Re(.)$ or $(.)^R$. Although for most real-world applications it is appropriate to use coherence as a measure for synchronization between two time series, the imaginary part of coherency (length of the red dashed line in Fig.2.5.A) has a special meaning for the analysis of dynamics between brain regions. This thesis attempts to enhance existing and evolve new methods for connectivity analysis based upon the concept of the imaginary part of coherency. The special properties of this quantity will be derived in the following.

2.4.2. The imaginary part of coherency (ImCoh)

As introduced in Section 2.2.2, the signal in an EEG/MEG sensor p can be described as the linear superposition or mixture of M brain sources $\mathbf{s} = (s_1(f) \dots s_m(f))$. In the frequency domain and for a single channel, this mixture is expressed by

$$x_p(f) = \sum_{m=1}^{M} a_{pm} s_m(f). \tag{2.20}$$

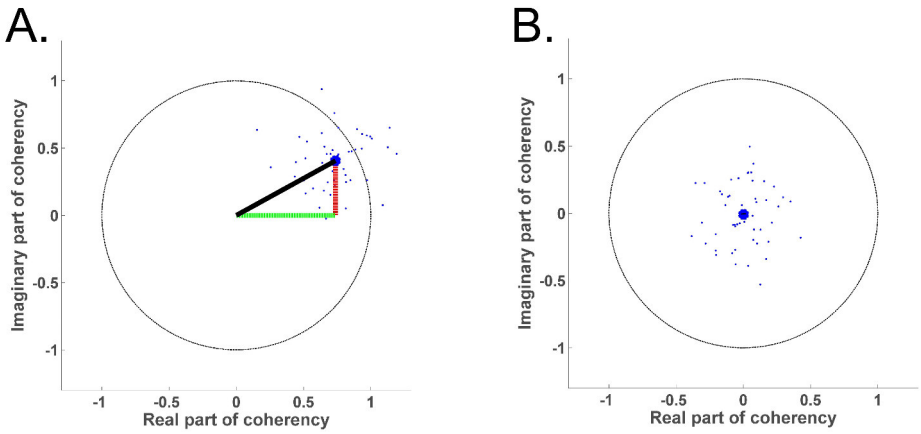

Figure 2.5.: Schematic illustration of coherency in the complex plane including the unit circle. Single trial phase differences are illustrated with small blue dots. The mean is indicated as a big blue dot. A.: The phase relation is not distributed around the origin and, hence, the mean is not equal to zero. A synchronization between the two time series is assumed. The mean of the distribution is a complex quantity and can be decomposed into real (length of green line) and imaginary part (length of red line). Furthermore, the absolute value of coherency, termed coherence, is displayed (length of black line). B.: Single trial normalized phase differences are distributed around zero. All real valued quantities (real part, imaginary part and absolute value of coherency) are equal or close to zero.

If one assumes an instantaneous mapping from sources to sensors, the mixing coefficients a_{pm} are real valued and the signal phases ϕ_p in sensor space are not distorted with respect to the phases in source space. This can be concluded from the validity of the quasi-static approximation of the Maxwell equations below 2 kHz, and is therefore valid in range of EEG/MEG frequencies of interest (see Section 2.1.2 and Plonsey and Heppner, 1967). Additionally, Stinstra and Peters (1998) looked at EEG and MEG data up to 100 Hz and did not find any phase shifts, i.e. time delays, in the mapping from sources to sensors. Further assuming only independent, i.e. non synchronized or interacting sources, and plugging Eq.(2.20) into Eq.(2.18), one can observe that the cross-spectrum between channels p and q can be written as

$$S_{pq}(f) = \sum_{m=1}^{M}\sum_{h=1}^{M} a_{pm}a_{qh}\left\langle s_m(f)s_h^*(f)\right\rangle = \sum_{m=1}^{M} a_{pm}a_{qm}\left\langle s_m(f)s_m^*(f)\right\rangle$$
$$= \sum_{m=1}^{M} a_{pm}a_{qm}\left\langle \left|s_m(f)^2\right|\right\rangle, \qquad (2.21)$$

and is purely real valued. This observation, which is originally presented in Nolte et al. (2004), implies that independent, i.e. non-synchronous brain sources are mapped only in the real part of the cross-spectrum. Hence, all significant deviation from zero of the Imaginary Part of the Cross-Spectrum (ImCs) can be interpreted as true brain interaction. Another point of view is that zero-phase difference, i.e. instantaneous synchronization is neglected or not interpreted as they are confounded by artifacts of volume conduction (see Section 2.2.3). This line of arguments is also valid for the Imaginary Part of Coherency (ImCoh) as the normalization in Eq.(2.19) is as

well real valued. One can also consider the exponent in the equation for coherency Eq.(2.19): If there is no consistent phase difference between the two signals, the exponent becomes zero, coherency is real valued and, hence, the imaginary part is equal to zero. In conclusion, ImCs and ImCoh can be considered to be robust to volume conduction artifacts. On sensor level, these measures are insensitive to mixing effect and on source level to seed blur and other remaining volume conduction artifacts originating from mapping data into estimated sources. In Section 3.1, the concept of the imaginary part of coherency is deepened and expanded.

2.4.3. Additional connectivity approaches

As for the different source reconstruction methods, there exist various methods to estimate a relationship between different time series. A non-exhaustive list of methods that have been successfully used in the context of functional connectivity for EEG and MEG data is provided in Appendix A.5. Additional overviews, comparisons and evaluations of measures can, for example, be found in Quian Quiroga et al. (2002), David et al. (2004), Wendling et al. (2009), Wu et al. (2011), Sakkalis (2011), Greenblatt et al. (2012), Haufe et al. (2012). Some of these existing methods are closely related to the imaginary part of coherency and the measures that are developed within this thesis. These relations will be elaborated in Section 3.1.8.

2.5. Statistics

EEG and MEG data are in general empirical and of finite sample size. They are subject to random fluctuations due to various kinds of noise, e.g. measurement noise and biological noise. Therefore, appropriate statistics are needed to make serious inferences about observed effects. This can be achieved by statistical null hypothesis testing (see e.g. Fisher, 1956; Casella and Berger, 2002): A null hypothesis H_0 is formulated stating that no systematic effect is present in the data. Furthermore, an alternative hypothesis H_1 is formulated stating the contrary. The idea is to assume the null hypothesis and see if the data provides evidence to reject it. Now, a test statistic is constructed as a scalar function of the data. Based on this test statistic, the hypothesis test determines what result of an analysis would lead to a rejection of the null hypothesis. An example for a test statistic would be the empirical mean as used in the example below. Furthermore, a pre-defined level of significance or likelihood α is chosen. A common value is $\alpha = 0.05$ indicating that the probability that an observed effect only occurred by chance equals 5% (Stigler, 2008). Finally, the pre-defined alpha level is compared to a p-value derived from the test statistic. The p-value is the probability of obtaining a test statistic that is at least as extreme as the one observed given that the null hypothesis is true. If the p-value is below the given α-level, i.e. the probability of observing the effect at random is lower than α, the null hypothesis is rejected and the result is considered as statistically significant. Otherwise the null hypothesis will be retained. Two types of errors can be made. The "Type I Error" refers to a rejection of H_0 although it is true and "Type II Error"

refers to an acceptance of H_0 although being false.

2.5.1. Parametric testing

To calculate the p-value, certain probability distributions of the test statistic can be assumed depending on the test statistic and the distribution of the data. Considering K Gaussian distributed data points $x \sim \mathcal{N}(\mu, \sigma^2)$, a common application of hypothesis testing is to ask whether the data's mean μ is different from a given mean μ_0. Given the null hypothesis $\mu = \mu_0$, the test statistic

$$t = \frac{\bar{\mu} - \mu_0}{(\bar{\sigma}/\sqrt{K})} = \frac{\bar{\mu} - \mu_0}{\bar{\sigma}_{\text{mean}}} \tag{2.22}$$

with $\bar{\mu}$ being the sample mean, $\bar{\sigma}$ the sample standard deviation and $\bar{\sigma}_{\text{mean}}$ the standard deviation of the mean, follows a Student's t-distribution. The t-distribution is a bell shaped curve similar to the Gaussian distribution but with heavier tails. It includes a single parameter, the degree of freedom which is for this example defined by $\nu = K - 1$. Now, the integral of Student's probability density function, known as cumulative distribution function of the t-distribution $f(t, \nu)$, can be used to calculate the corresponding p-value. The area under the Student's probability density function determines the probability that any value of t is smaller than the one calculated from the data has occurred by chance. This procedure is known as the one-sided T-test as well as one-sample or one-tailed T-test. For identifying the probability that any t being at least as extreme as the one calculated to occur by chance, one can evaluate $f(2\,|t|\,, \nu)$. This is termed the two-sided T-test.

Additionally, different hypothesis tests for different distributions of the test statistic exist. These are for example the Z-test for a Gaussian distribution, the F-Test for a f-distribution or the Chi-squared-test for a chi-squared distribution. Please note that according to the central limit theorem, the cumulative distribution function $f(t, \infty)$ with $\nu \to \infty$ approaches the one of a Gaussian distribution and, hence, Z-test and T-test provide the same p-value. In both cases an α-level of 0.05 corresponds to a critical value under the distribution curve of $t_c = 1.96$ for a two-sided test. This implies that every value of the test statistic fulfilling $|t| \geq t_c$ leads to a significant result.

2.5.2. Bootstrap

The methods for statistical hypothesis testing introduced in the previous section belong to the family of parametric tests. They assume a certain distribution of the test statistic and make inferences about the parameters of the distribution. Non-parametric tests do not make these assumptions. Instead, they aim to estimate the distribution of the test statistic. One famous method is the bootstrap resampling procedure (Efron and Tibshirani, 1994), which works as follows: Let's consider K data points $\mathbf{x} = (x_1, \ldots, x_K)$ from which any test statistic, e.g. the mean or a connectivity metric, is computed. Now, B so called bootstrap samples $\mathbf{x}_{(j)} = (x_1, \ldots, x_K),\ j =$

$1 \dots B$ can be generated by drawing K data points from $\mathbf{x}$ with replacement. Hence, each bootstrap sample $\mathbf{x}_{(j)}$ is likely to contain some values of $\mathbf{x}$ multiple times whereas some values of $\mathbf{x}$ will not be contained. For each resampling step $j = 1 \dots B$ the test statistic can be re-calculated providing a distribution for the test statistic with B bootstrap samples. Denoting the evaluation of the test statistic $t(\mathbf{x})$ of the j-th bootstrap repetition as $t(\mathbf{x}_{(j)})$, the standard deviation is then given by

$$\hat{\sigma}_{\text{bootstrap}} = \left(\frac{1}{B-1} \sum_{j=1}^{B} \left[\bar{t}(\mathbf{x}_{(j)}) - t(\mathbf{x}_{(j)}) \right]^2 \right)^{1/2} \tag{2.23}$$

with $\bar{t}(\mathbf{x}_{(j)})$ being the mean of the test statistic over all B bootstrap samples defined as

$$\bar{t}(\mathbf{x}_{(j)}) = \frac{1}{B} \sum_{l=1}^{B} t(\mathbf{x}_{(l)}). \tag{2.24}$$

A one-sided empirical p-value can be obtained as follows: Let's denote the number of values of the test statistic of all bootstrap samples that are greater or equal to the one observed from the original data as

$$r := \#\left(t(\mathbf{x}_{(j)}) \geq t(\mathbf{x}) \right) \quad \forall \;\; j = 1 \dots B \tag{2.25}$$

with # denoting the number or count. Then, the p-value is given by

$$p = \frac{r+1}{B} \tag{2.26}$$

with B being the number of bootstrap runs.

2.5.3. Jackknife

A different resampling technique is jackknife (Quenouille, 1949, 1956; Tukey, 1958). It represents a linear approximation of bootstrap with usually lower computational cost (Cameron and Trivedi, 2005). The idea is to leave out each of the K data points $\mathbf{x} = (x_1, \dots, x_K)$ once and re-calculate the test statistic $t(\mathbf{x}_{(j)})$ on K jackknife samples $\mathbf{x}_{(j)} = (x_1, \dots, x_{j-1}, x_{j+1}, \dots, x_{K-1})$ (for a review see Miller, 1974). With $\bar{x}$ being the original sample mean, the jackknife sample mean of the j-th repetition can be written as

$$\bar{x}_{(j)} = \frac{1}{K-1} \sum_{\substack{l=1 \\ l \neq j}}^{K-1} x_l = \frac{K\bar{x} - x_j}{K-1}. \tag{2.27}$$

This can be seen from the derivation

$$\bar{x} = \frac{1}{K}\sum_{l=1}^{K} x_l \;\Leftrightarrow\; K\bar{x} \;=\; \sum_{l=1}^{K} x_l \;\Leftrightarrow\; K\bar{x} - x_j = \sum_{\substack{l=1 \\ l\neq j}}^{K-1} x_l$$

$$\Leftrightarrow\; \frac{K\bar{x} - x_j}{K-1} \;=\; \frac{1}{K-1}\sum_{\substack{l=1 \\ l\neq j}}^{K-1} x_l \;=\; \bar{x}_{(j)}. \tag{2.28}$$

The jackknife estimate of the standard deviation of the test statistic is defined by

$$\hat{\sigma}_{\text{jackknife}} = \left(\frac{K-1}{K}\sum_{j=1}^{K}\left[\bar{t}(\mathbf{x}_{(j)}) - t(\mathbf{x}_{(j)})\right]^2\right)^{1/2} \tag{2.29}$$

with $\bar{t}(\mathbf{x}_{(j)})$ being the mean of test statistic over all K jackknife samples. If the test statistic is the mean itself, i.e. $\bar{t}(\mathbf{x}_{(j)}) = \bar{x}$ and $t(\mathbf{x}_{(j)}) = \bar{x}_{(j)}$, and using Eq.2.28, the standard deviation of the mean is given by

$$\hat{\sigma}_{\text{jackknife, mean}} = \left(\sum_{j=1}^{K}\frac{\left(x_j - \bar{x}\right)^2}{(K-1)K}\right)^{1/2} = \frac{\bar{\sigma}}{\sqrt{K}} \tag{2.30}$$

with $\bar{\sigma}$ being the standard deviation of the original sample. Hence, it can be observed from Eq.(2.30) that the standard deviation estimated by jackknife is underestimated and has to be corrected by the factor $\sqrt{K}$ in order to conclude on the true underlying standard deviation of the mean. This can also be seen by comparing the bootstrap estimate in Eq.(2.23) and the jackknife estimate in Eq.(2.29) of the standard deviation. The jackknife factor is much larger and is used to compensate for the small jackknife deviation compared to bootstrap. Intuitively, the jackknife samples are more similar to the original data. The jackknife (or bootstrap) estimate of the standard deviation can also be employed to conduct any parametric test such as a T-test or Z-test. Then, p-values and confidence intervals are obtained with a non-parametric estimate of the standard deviation.

2.5.4. Permutation testing

Considering a two class problem, a suited resampling technique is a permutation test (Fisher, 1951; Pitman, 1937). In the context of neuroscientific research, a permutation test is particularly useful if data are recorded in two experimental conditions A and B, where differences between them are under investigation. The idea is to randomly re-assign the class labels of data points and to re-calculate the test statistic over a large number of runs. This way, a distribution of the test statistic is generated given that the null-hypothesis is true, i.e. class labels are exchangeable because no effect differentiating the two classes is present in the data. Now, a p-value can be derived to determine how likely the effect measured with the true class labels has occurred

by chance. If the original observation value lies in the main body of the distribution, the observation is likely to have occurred by chance. If the value lies in the tail or even outside the distribution, it has rarely occurred by chance and a significant result can be assumed. In analogy to the bootstrap procedure (see Section 2.5.2), a p-value can be determined by counting how many results of the test statistic $t(\mathbf{x}_{(j)})$ over all permutation runs $j = 1 \dots K$ are bigger or equal to the originally observed value $t(\mathbf{x})$. Denoting this number as ζ the p-value in a permutation test is given by

$$p = \frac{\zeta + 1}{K}. \tag{2.31}$$

In this thesis mostly connectivity metrics in the frequency domain will be subject to statistical analysis. As described in Section 2.4.1, the basis for these measures is the Discrete Fourier Transform that is calculated from epochs of continuous time series data. Therefore, these data epochs are treated as single samples which are resampled according to the non-parametric testing procedures described in the present and previous sections.

In addition to that, surrogate data testing can be considered as a variant of permutation testing. It originates from detecting non-linearity in a time series and was initially introduced by Theiler et al. (1992). Here, surrogate data is not constructed by shuffling class labels, but by randomly assigning Fourier phases. However, in Section 3.4 a novel approach will be presented to construct surrogate data in order to statistically test relations between sensor or source time series. Note that this approach is not limited to a two class problem. Several surrogate data sets are constructed under the null hypothesis stating that no interaction is present in the data. Then, a connectivity measure (e.g. ImCoh being the test statistic) between two given voxels from the original data can be compared to the connectivity measure for the same voxel pair from the surrogate data sets. If these are significantly different, the null hypothesis is rejected and true interaction between this specific voxel pair is assumed. The p-value can be calculated according to Eq.(2.31).

2.5.5. Correction for multiple comparisons

When testing for a set of statistical inferences simultaneously, the problem of multiple comparisons arises. By performing many statistical test at once, it becomes much more likely that a significant result just occurs by chance. In the context of neural data analysis this is the case as brain activity in many voxels is determined. A striking example to motivate the use of correction for multiple hypothesis testing is presented in Bennett et al. (2010). In their "study", the authors found statistically significant fMRI brain activity in a dead salmon due to non-corrected statistics. In the context of EEG/MEG connectivity analysis on source level, the problem would be even more striking if relationships between all pairs of voxels are investigated. For M brain voxels, the number of tests would be given by

$$\eta = \frac{M(M-1)}{2}. \tag{2.32}$$

A straight forward solution gives the Bonferroni correction (Bonferroni, 1935; Dunn, 1961). There, it is suggested to adapt the alpha level by dividing it by the number of tested hypothesis. For source localization this would be the number of brain voxels, for source connectivity analysis it would be η as defined in Eq.(2.32). This procedure corresponds to testing a single hypothesis. Although the Bonferroni correction is a quite conservative technique, it is widely used among neuroimaging studies. A different famous approach to correct for multiple comparison is the False Discovery Rate (FDR) (Benjamini and Hochberg, 1995; Benjamini, 2010). Instead of reducing the probability of a single false positive discovery as done for the Bonferroni correction, the FDR aims to control the rate of false discoveries at a given level.

However, due to the statistical testing procedure applied in this thesis a correction for multiple comparison is implicitly contained in the maximum test statistic. In principle, only the voxel pair with the maximum test statistic values are compared with the surrogate data. This will be explained in more details in Section 4.6.2, when the analysis pipeline and results are demonstrated in a simulation.

2.6. Distance measures

An important point in the context of source localization is how to judge and rate the results. As indicated in Section 2.3, most methods result in a source distribution. This means that a value, e.g. representing source power or interaction strength, is assigned to each brain voxel. In the ideal case, this spatial distribution is sparse and exhibits a clear maximum. Around this maximum, values decay with distance. Especially as the underlying source model is dipolar, i.e. point-wise and not distributed (see Section 2.2.1), the sparser the solution the better. But due to the limited spatial resolution of EEG and MEG and due to the ill-defined inverse problem, practical solutions are rather blurred.

One approach to judge the quality of a particular inverse solution with respect to a modeled dipolar source, is to only consider the maximum of the source distribution. Defining the location of this maximum as $\boldsymbol{\theta} = (\theta_x\, \theta_y\, \theta_z)^\mathsf{T}$ in a three dimensional Cartesian coordinate system and the location of the modeled dipole as $\boldsymbol{\phi} = (\phi_x\, \phi_y\, \phi_z)^\mathsf{T}$, a reasonable error measure would be the Euclidean distance between $\boldsymbol{\theta}$ and $\boldsymbol{\phi}$ given by

$$d_{\mathrm{EUC}} = \sqrt{\sum_{j=1}^{3} (\theta_j - \phi_j)^2}. \tag{2.33}$$

However, the Euclidean distance does not account for the spatial extent of the sources. A measure that does is the Earth Mover's Distance (EMD), which is in the field of mathematics also termed Wasserstein metric (Monge, 1781; Rubner et al., 2000). It has also previously been used in the context of EEG and MEG source localization by Haufe et al. (2012). Intuitively, two spatial distributions can be seen as two piles of dirt. Then, the EMD denotes the minimum cost of transforming one pile into the other. This is algorithmically not trivial to assess especially if the two distributions

are not equal in size. One approach that has been successfully implemented is the Hungarian algorithm introduced in Kuhn (1955). In our case, however, not the similarity of two distributions has to be considered. Here, a source distribution as a result of a reconstruction technique should be compared to a given location of a modeled dipole. Let's denote the distribution as $\mathbf{c} = (c_1 \dots c_M)^\mathsf{T} \in \mathbb{R}^{M\times 1}$ with c_j being the value of the distribution at the j-th out of M voxels. Furthermore, let $\boldsymbol{\gamma}_j = (\gamma_{jx}\, \gamma_{jy}\, \gamma_{jz})^\mathsf{T}$ be the location of the j-th voxel. Now, the EMD between the distribution and the modeled dipole at the location $\boldsymbol{\phi} = (\phi_x\, \phi_y\, \phi_z)^\mathsf{T}$ can be expressed as

$$d_{\mathrm{EMD}} = \sum_{k=1}^{M} \frac{c_k}{\|c\|_1} \sqrt{\sum_{l=1}^{3} (\gamma_{kl} - \phi_l)^2} \tag{2.34}$$

with $\|.\|_1$ being the ℓ^1-norm, i.e. the sum over all elements in $\mathbf{c}$ in this case. Eq. (2.34) can be seen as a weighted sum of Euclidean distances over all voxels. For a perfect match, the distance is zero as all coefficients in $\mathbf{C}$ would be zero except for the one voxel where the dipole is modeled. There, the Euclidean distance would be zero, resulting in $d_{\mathrm{EMD}} = 0$ for this scenario. On the contrary, high values of the source distribution at distant locations result in a high error. Hence, the EMD is a valuable error measure for source distributions and modeled dipoles.

3. Theory

> It is the theory which decides what can be observed.
>
> *(Albert Einstein)*

In the current chapter data analysis methods that aim at detecting interactions between brain regions are theoretically introduced. Mainly, four different techniques are derived that can be used sequentially to finally provide an interaction profile on source level for given EEG or MEG data (for an overview see Figure 1.4). Furthermore, additional possible applications of the methods are highlighted.

3.1. Connectivity measures invariant to linear and static transformations

The imaginary part of coherency (ImCoh) as introduced in Nolte et al. (2004) and revisited in Section 2.4.2, is a measure that detects phase synchronization between two time series and is robust to volume conduction artifacts. This robustness indicates that the ImCoh vanishes for independent sources, even if mixed into sensors or estimated sources. If the ImCoh or other measures robust to volume conduction show a significant deviation from zero, this represents a signature of true interaction which cannot be explained by a mixing artifact. Despite the method's property of being robust to artifacts of volume conduction, the interpretation in terms of brain connectivity is far from trivial. Although a quantity vanishes for independent sources, the actual value, if non-vanishing, still depends on the mapping of sources into sensors, i.e. on volume conduction (see Section 2.2.3). For example, if there are strong mixing artifacts present this will suppress the value of imaginary coherency on the sensor level leading to a detection of interactions rather between remote sensors.

If there are not more sources than sensors, the mixing of sources into sensors corresponds mathematically to a linear transformation which could be inverted if the exact forward matrix was known (see Section 2.2.2). However, since this assumption barely ever holds, it seems promising to construct measures which are strictly invariant under linear spatial, i.e. static, transformations of the data. This invariance then implies independence of the actual forward model, i.e. the mapping of sources into sensors. In this section, a general framework for connectivity measures invariant to linear and static transformation is acquainted. It was initially introduced in Ewald et al. (2012) and large parts of this section are adopted from the theory presented

there. In general, there are several ways to achieve such an invariance. The most simple but not generic form of invariance is achieved by construction. For example, an algorithm which transforms data to a common average reference, is invariant to the original reference by construction. In the context of brain interaction, one can construct a measure invariant to linear transformations by finding spatial weights for virtual channels in between which the ImCoh is maximized. Any prior linear transformation would then indeed lead to different weights, but to identical virtual channels and to an identical ImCoh between them.

Note that this approach has a close formal correspondence to the well-established Canonical Correlation Analysis (CCA) (Hotelling, 1936) which maximizes the correlation between two multivariate data sets. Like CCA, which yields a canonical correlation that is independent of the basis in each data space, also the methods derived in the following are invariant to any linear transformation. However, in contrast to CCA, the new methods will also allow to measure synchronization *within* a single multivariate time series, i.e. the ImCoh of a multivariate time series with itself. In such a setting, CCA would find only trivial solutions since the correlation of any signal with itself is always one. However, the imaginary part of the coherency vanishes for identical univariate signals preventing the new method from converging to such trivial solutions.

3.1.1. Maximized Imaginary Coherency (MIC)

To see how the imaginary part of coherency can be maximized, let's consider two data spaces A and B. These are of dimension N_A and N_B, respectively, and can be but do not have to be equal. In the frequency domain, the data can be formulated as the complex vectors $\mathbf{x}_A(f) = [x_1(f) \dots x_{N_A}(f)]^\mathsf{T} \in \mathbb{C}^{N_A \times 1}$ and $\mathbf{x}_B(f) = [x_{N_A+1}(f) \dots x_{N_A+N_B}(f)]^\mathsf{T} \in \mathbb{C}^{N_B \times 1}$. The data spaces can have different meanings. For example, they could denote three dimensional dipole moments at two given brain voxels A and B. This would result in $N_A = N_B = 3$ and each value corresponds to a distinct dipole direction for each frequency. As a further example, the two data spaces could denote two different groups of EEG/MEG sensors embraced in A and B. Then, each entry $x_j(f)$ is the complex Fourier transform of the measured time signal in the j-th out of the N_A or N_B sensors.

Combining the data in A and B to $\mathbf{x}(f) = \begin{bmatrix} \mathbf{x}_A^\mathsf{T}(f) & \mathbf{x}_B^\mathsf{T}(f) \end{bmatrix}^\mathsf{T}$, the complex cross-spectrum defined in Eq.(2.18) exhibits the block form

$$\mathbf{S}(f) = \left\langle \mathbf{x}(f)\mathbf{x}^\dagger(f) \right\rangle = \begin{pmatrix} \mathbf{S}_{AA}^R(f) + i\mathbf{S}_{AA}^I(f) & \mathbf{S}_{AB}^R(f) + i\mathbf{S}_{AB}^I(f) \\ \\ \mathbf{S}_{BA}^R(f) + i\mathbf{S}_{BA}^I(f) & \mathbf{S}_{BB}^R(f) + i\mathbf{S}_{BB}^I(f) \end{pmatrix}, \qquad (3.1)$$

where $(.)^\dagger$ denotes the complex conjugate transpose of a matrix or vector and where $\mathbf{S}^R$ denotes the real and $\mathbf{S}^I$ the imaginary part, respectively. Furthermore, the subscript indicates which components of the two spaces make up the individual cross-spectra. For example, $\mathbf{S}_{AA}$ denotes the cross-spectrum within data space A, i.e.

for all components $\mathbf{x}_A(f)$. In contrast to that, the matrix $\mathbf{S}_{AB} \in \mathbb{C}^{N_A \times N_B}$ denotes the cross-spectrum between all components in the data spaces A and B. For the ease of reading, the dependence on the frequency is omitted in the following. Please keep in mind that further considerations are valid for a distinct frequency (or averages over a range of frequencies).

Let us consider a coordinate transformation of the data $\mathbf{x}$ with the symmetric transformation matrix

$$\mathbf{T} = \begin{pmatrix} \left(\mathbf{S}_{AA}^R\right)^{-\frac{1}{2}} & \mathbf{0}_{N_A N_B} \\ \mathbf{0}_{N_A N_B} & \left(\mathbf{S}_{BB}^R\right)^{-\frac{1}{2}} \end{pmatrix} \tag{3.2}$$

where $\mathbf{0}_{N_A N_B} \in 0^{N_A \times N_B}$ is a matrix containing solely zero elements. This leads to the transformed data $\mathbf{y} = \mathbf{T}\mathbf{x}$. Now, the cross-spectrum calculated on the transformed data is given by

$$\mathbf{D} = \left\langle \mathbf{y}\mathbf{y}^\dagger \right\rangle = \mathbf{T}\mathbf{S}\mathbf{T}^\mathsf{T} = \begin{pmatrix} \mathbf{I}_{N_A} + i\mathbf{D}_{AA}^I & \mathbf{D}_{AB}^R + i\mathbf{D}_{AB}^I \\ \\ \mathbf{D}_{BA}^R + i\mathbf{D}_{BA}^I & \mathbf{I}_{N_B} + i\mathbf{D}_{BB}^I \end{pmatrix}, \tag{3.3}$$

where

$$\mathbf{D}_{AB}^I = \left(\mathbf{S}_{AA}^R\right)^{-\frac{1}{2}} \left(\mathbf{S}_{AB}^I\right) \left(\mathbf{S}_{BB}^R\right)^{-\frac{1}{2}} = \Im\left(\left\langle \mathbf{y}_A \mathbf{y}_B^\dagger \right\rangle\right) \tag{3.4}$$

can be seen as the imaginary part of the cross-spectrum between the two data spaces A and B under the linear basis transformation $\mathbf{T}$. The basis transformation itself can be interpreted as a spatial whitening based on the real part of the cross-spectrum. It removes the real part of the cross-spectrum between all channels within each of the data spaces. Hence, all non-diagonal elements of $\mathbf{S}_{AA}^R$ and $\mathbf{S}_{BB}^R$ become zero. Furthermore, the transformation normalizes the real valued auto-spectra S_{jj} on the diagonal to one which leads to $\mathbf{S}_{AA}^R = \mathbf{I}_{N_A}$ and $\mathbf{S}_{BB}^R = \mathbf{I}_{N_B}$.

Furthermore, let's consider two virtual channels $z_A = \mathbf{a}^\mathsf{T}\mathbf{y}_A$ and $z_B = \mathbf{b}^\mathsf{T}\mathbf{y}_B$ in which the whitened data $\mathbf{y}$ is linearly combined. The column vectors $\mathbf{a} \in \mathbb{R}^{N_A \times 1}$ and $\mathbf{b} \in \mathbb{R}^{N_B \times 1}$ can be interpreted as weights, e.g. for the corresponding EEG/MEG channels or dipole directions. The aim is now to find weight vectors $\mathbf{a}$ and $\mathbf{b}$ such that the ImCoh between the virtual channels is maximized.

The complex coherency between the two virtual channels is, according to Eq.(2.19), given by

$$C_z = \frac{\left\langle z_A z_B^\dagger \right\rangle}{\sqrt{\left\langle z_A z_A^\dagger \right\rangle \left\langle z_B z_B^\dagger \right\rangle}} = \frac{\mathbf{a}^\mathsf{T} \left\langle \mathbf{y}_A \mathbf{y}_B^\dagger \right\rangle \mathbf{b}}{\sqrt{\left(\mathbf{a}^\mathsf{T} \left\langle \mathbf{y}_A \mathbf{y}_A^\dagger \right\rangle \mathbf{a}\right) \left(\mathbf{b}^\mathsf{T} \left\langle \mathbf{y}_B \mathbf{y}_B^\dagger \right\rangle \mathbf{b}\right)}}. \tag{3.5}$$

As the aim is to maximize the *imaginary* part of coherency as a connectivity measure robust to volume conduction, let's take a closer look at the imaginary part of the complex quantity derived in Equation (3.5), i.e. $\Im(C_z)$. In the nominator one can

substitute $\Im\left(\left\langle \mathbf{y}_A \mathbf{y}_B^\dagger \right\rangle\right) = \mathbf{D}_{AB}^I$ according to Eq.(3.4). For the denominator, it follows

$$\begin{aligned} \mathbf{a}^\mathsf{T} \left\langle \mathbf{y}_A \mathbf{y}_A^\dagger \right\rangle \mathbf{a} &= \left(\mathbf{a}^\mathsf{T} \left(\mathbf{I}_A + i\mathbf{D}_{AA}^I\right) \mathbf{a}\right) \\ &= \mathbf{a}^\mathsf{T}\mathbf{I}_A\mathbf{a} + i\left(\mathbf{a}^\mathsf{T}\mathbf{D}_{AA}^I\mathbf{a}\right) \\ &= \mathbf{a}^\mathsf{T}\mathbf{a} = \|\mathbf{a}\|^2 \end{aligned} \tag{3.6}$$

as $\mathbf{a}^\mathsf{T}\mathbf{D}_{AA}^I\mathbf{a} = 0$. This can be concluded from the antisymmetry of $\mathbf{D}_{AA}^I$, i.e. $\mathbf{D}_{AA}^I = -(\mathbf{D}_{AA}^I)^\mathsf{T}$. As $\mathbf{a}^\mathsf{T}\mathbf{D}_{AA}^I\mathbf{a}$ is a scalar quantity, it must be equal to its transpose:

$$\begin{aligned} \mathbf{a}^\mathsf{T}\mathbf{D}_{AA}^I\mathbf{a} &\overset{!}{=} (\mathbf{a}^\mathsf{T}\mathbf{D}_{AA}^I\mathbf{a})^\mathsf{T} \\ &= \mathbf{a}^\mathsf{T}(\mathbf{a}^\mathsf{T}\mathbf{D}_{AA}^I)^\mathsf{T} \\ &= \mathbf{a}^\mathsf{T}(\mathbf{D}_{AA}^I)^\mathsf{T}\mathbf{a} \\ &= -\mathbf{a}^\mathsf{T}\mathbf{D}_{AA}^I\mathbf{a}. \end{aligned} \tag{3.7}$$

However, the relation in Eq.(3.7) only holds for $\mathbf{a}^\mathsf{T}\mathbf{D}_{AA}^I\mathbf{a} = 0$. As the derivation in Eq.(3.6) is true for $\mathbf{b}$, respectively, the imaginary part of coherency between the two virtual channels can be written as

$$\Im(C_z) = \frac{\mathbf{a}^\mathsf{T}\mathbf{D}_{AB}^I\mathbf{b}}{\sqrt{\|\mathbf{a}\|^2\|\mathbf{b}\|^2}} = \frac{\mathbf{a}^\mathsf{T}\mathbf{D}_{AB}^I\mathbf{b}}{\|\mathbf{a}\|\|\mathbf{b}\|}. \tag{3.8}$$

The maximization of this term can be achieved either by using Lagrange multipliers or by setting the partial derivatives with respect to $\mathbf{a}$ and $\mathbf{b}$ to zero. As shown in the Appendix A.6, this leads to

$$\mathbf{D}_{AB}^I\mathbf{b} = \lambda_A\mathbf{a}, \tag{3.9}$$

$$(\mathbf{D}_{AB}^I)^\mathsf{T}\mathbf{a} = \lambda_B\mathbf{b}. \tag{3.10}$$

with

$$\lambda := \lambda_A = \lambda_B = \mathbf{a}^\mathsf{T}\mathbf{D}_{AB}^I\mathbf{b} = \frac{\mathbf{a}^\mathsf{T}\mathbf{D}_{AB}^I\mathbf{b}}{\|\mathbf{a}\|\|\mathbf{b}\|}. \tag{3.11}$$

Finally, one can combine Equations (3.9) and (3.10), e.g. by solving Eq.(3.9) for $\mathbf{a}$ and plugging it into Eq.(3.10). This leads to the eigenvalue equations

$$(\mathbf{D}_{AB}^I)^\mathsf{T}\mathbf{D}_{AB}^I\mathbf{b} = \lambda^2\mathbf{b} \tag{3.12}$$

$$\mathbf{D}_{AB}^I(\mathbf{D}_{AB}^I)^\mathsf{T}\mathbf{a} = \lambda^2\mathbf{a}. \tag{3.13}$$

Hence, the eigenvectors belonging to the largest eigenvalues of $(\mathbf{D}_{AB}^I)^\mathsf{T}\mathbf{D}_{AB}^I$ and $\mathbf{D}_{AB}^I(\mathbf{D}_{AB}^I)^\mathsf{T}$ determine the weights $\mathbf{a}$ and $\mathbf{b}$ that maximize the imaginary part of coherency between the two virtual channels z_A and z_B of the initially given data $\mathbf{x}$. The maximized imaginary part of coherency itself is determined by the largest eigenvalue and can be used to study the synchronization between multivariate series.

This quantity, defined as

$$\text{MIC} := \max\left(\Im(C_z)\right) = |\lambda_1|\,, \tag{3.14}$$

will be termed Maximized Imaginary Coherency (MIC).

Please keep in mind, that all quantities are frequency dependent and weights have to be determined for each frequency or frequency band separately. As an additional remark, the sign of MIC is, without prior assumptions, a matter of convention: the transformation $\mathbf{a} \to -\mathbf{a}$ or $\mathbf{b} \to -\mathbf{b}$ leads to $\lambda \to -\lambda$.

3.1.2. Multivariate Interaction Measure (MIM)

In principle, not only the largest but all eigenvalues can be studied as meaningful measures of brain interaction invariant to linear transformations as will be shown formally in Section 3.1.5. The question is how to choose or combine them. In the following, an interaction measure is proposed based on the sum of all eigenvalues. This sum is a measure of total interaction between two subspaces. It does not require the actual calculation of the eigenvalues and some statistical properties can be calculated analytically as will be shown below.

From Eq.(3.12) and (3.13) one can observe that the calculated eigenvectors diagonalize the matrix $\mathbf{D}^I_{AB}$. Let $\mathbf{U}_A = (\mathbf{u}_{1_A} \ \dots \ \mathbf{u}_{N_A})$ be the orthogonal matrix containing the eigenvectors of $\mathbf{D}^I_{AB}(\mathbf{D}^I_{AB})^\mathsf{T}$, denoted as $\mathbf{u}_{1_A}, \dots, \mathbf{u}_{N_A}$, as columns. Furthermore, let $\mathbf{U}_B = (\mathbf{u}_{1_B} \ \dots \ \mathbf{u}_{N_B})$ be the matrix containing the eigenvectors of $(\mathbf{D}^I_{AB})^\mathsf{T}\mathbf{D}^I_{AB}$ accordingly. From Eq.(3.9) it follows that

$$\begin{aligned} \mathbf{D}^I_{AB}\mathbf{U}_B &= \mathbf{U}_A\mathbf{\Lambda} \\ \mathbf{U}_A^\mathsf{T}\mathbf{D}^I_{AB}\mathbf{U}_B &= \mathbf{\Lambda} \end{aligned} \tag{3.15}$$

where $\mathbf{\Lambda}$ is a diagonal matrix containing all eigenvalues. As stated above, the idea is to combine all eigenvalues to define a synchronization measure between the two spaces. Here, it is proposed to sum the squares of all eigenvalues. This measure, denoted as the Multivariate Interaction Measure (MIM), can also be expressed in terms of the trace of $(\mathbf{D}^I_{AB})(\mathbf{D}^I_{AB})^\mathsf{T}$. Recalling the initial variables from Eq.(3.4), using the symmetry of $\mathbf{S}^R$ and using $\text{tr}(\mathbf{EF}) = \text{tr}(\mathbf{FE})$ for two arbitrary matrices $\mathbf{E}$

and **F**, the MIM between subspaces A and B is defined as

$$\begin{aligned}
\mathrm{MIM}_{AB} &= \mathrm{tr}\left[(\mathbf{D}^I_{AB})(\mathbf{D}^I_{AB})^\mathsf{T}\right] \\
&= \mathrm{tr}\left[\left(\mathbf{S}^R_{AA}\right)^{-\frac{1}{2}}\left(\mathbf{S}^I_{AB}\right)\left(\mathbf{S}^R_{BB}\right)^{-\frac{1}{2}}\left(\left(\mathbf{S}^R_{AA}\right)^{-\frac{1}{2}}\left(\mathbf{S}^I_{AB}\right)\left(\mathbf{S}^R_{BB}\right)^{-\frac{1}{2}}\right)^\mathsf{T}\right] \\
&= \mathrm{tr}\left[\left(\mathbf{S}^R_{AA}\right)^{-\frac{1}{2}}\left(\mathbf{S}^I_{AB}\right)\left(\mathbf{S}^R_{BB}\right)^{-\frac{1}{2}}\left(\left(\mathbf{S}^R_{BB}\right)^{-\frac{1}{2}}\right)^\mathsf{T}\left(\mathbf{S}^I_{AB}\right)^\mathsf{T}\left(\left(\mathbf{S}^R_{AA}\right)^{-\frac{1}{2}}\right)^\mathsf{T}\right] \\
&= \mathrm{tr}\left[\left(\mathbf{S}^R_{AA}\right)^{-\frac{1}{2}}\left(\mathbf{S}^I_{AB}\right)\left(\mathbf{S}^R_{BB}\right)^{-1}\left(\mathbf{S}^I_{AB}\right)^\mathsf{T}\left(\left(\mathbf{S}^R_{AA}\right)^{-\frac{1}{2}}\right)^\mathsf{T}\right] \\
&= \mathrm{tr}\left[\left(\mathbf{S}^R_{AA}\right)^{-1}\mathbf{S}^I_{AB}\left(\mathbf{S}^R_{BB}\right)^{-1}\left(\mathbf{S}^I_{AB}\right)^\mathsf{T}\right] \qquad (3.16)
\end{aligned}$$

with $\mathrm{tr}(.)$ being the trace of a square matrix. Please note that with Eq.(3.16), the whole information of connectivity between two subspaces is reduced to a single value per frequency. This leads to an enormous reduction of information. Furthermore, it is not necessary to actually compute the eigenvectors or any linear transformation. The appropriate real and imaginary parts of the cross-spectra can be inserted directly.

One must emphasize that MIM_{AB} is invariant to transformations within each subspace but not to mixtures between the subspaces. If it had such a property a non-vanishing MIM could not be interpreted as an interaction between the subspaces but could also be caused from interactions entirely within one of the subspaces. Invariance with respect to any linear (and static) transformation of the data can be considered as a special case by setting $A = B$ and will be dealt with in the next section.

3.1.3. Global Interaction Measure (GIM)

As an alternative of studying connectivity between two subspaces, one might also want to investigate connectivity within a single data space, e.g. a complete sensor data set. This leads to the case of identical subspaces, i.e. $A = B$, and has to be treated slightly differently compared to MIM. First, the eigenvalue equations (3.12) and (3.13) are degenerate which implies that every eigenvalue has two eigenvectors. Hence, **a** and **b** are equal and can be determined by evaluating only one of the two equations.

For the interaction measure described in Eq.(3.16), each interaction would be considered twice. Therefore, the factor $1/2$ is included within the new measure in the following. As only a single cross-spectrum **S** is given, the resulting connectivity measure for a single data space, termed Global Interaction Measure (GIM), is defined by

$$\mathrm{GIM} = \frac{1}{2} tr\left(\left(\mathbf{S}^R\right)^{-1}\mathbf{S}^I\left(\mathbf{S}^R\right)^{-1}\left(\mathbf{S}^I\right)^\mathsf{T}\right). \qquad (3.17)$$

In principle, the GIM could be normalized to be in the range $[0, 1]$ by dividing it

by $N/2$, with N being the number of channels, since all eigenvalues of $\left(\mathbf{S}^R\right)^{-1}\mathbf{S}^I\mathbf{S}^R$ are bounded between 0 and 1. A similar normalization could be done for MIM. However, both measures are not normalized because in the present form the results do not explicitly depend on the number of measurement channels. Sometimes, for example, channels containing noise are excluded from the analysis. Roughly speaking, MIM and GIM represent 'total interaction' rather than 'total interaction per channel'. This allows a more objective comparison of systems with slightly different channel numbers. However, as will be demonstrated in Section 4.2.1, the magnitude of the measures do depend on the subspace sizes if the differences in channels numbers are large.

For two channels p and q the GIM can be calculated explicitly. In the bivariate case, the cross-spectrum is given by

$$\mathbf{S}_{pq} = \begin{pmatrix} S_{pp} & S^R_{pq} + iS^I_{pq} \\ S^R_{pq} - iS^I_{pq} & S_{qq} \end{pmatrix} \tag{3.18}$$

and, hence, the inverse of the real part of the cross-spectrum case can be written as

$$\left(\mathbf{S}^R_{pq}\right)^{-1} = \frac{1}{\det(\mathbf{S}^R_{pq})} \begin{pmatrix} S_{qq} & -S^R_{pq} \\ -S^R_{pq} & S_{pp} \end{pmatrix} \tag{3.19}$$

with $\det(.)$ denoting the determinant. If imaginary and real part of the bivariate cross-spectrum from Eq.(3.18) are inserted into Eq.(3.17), the matrix multiplication and the evaluation of the trace and the determinant leads to

$$\begin{aligned} \mathrm{GIM}_{pq} &= \frac{1}{2}\frac{2S_{qq}\left(S^I_{pq}\right)^2 S_{pp} - 2(S^R_{pq})^2(S^I_{pq})^2}{det(\mathbf{S}^R_{pq})^2} \\ &= \frac{(S^I_{pq})^2}{S_{pp}S_{qq} - (S^R_{pq})^2} = \frac{(S^I_{pq})^2}{S_{pp}S_{qq}(1 - \frac{(S^R_{pq})^2}{S_{pp}S_{qq}})} \\ &= \frac{\left(C^I_{pq}\right)^2}{1 - \left(C^R_{pq}\right)^2} \end{aligned} \tag{3.20}$$

where C^I_{pq} denotes the imaginary part of coherency and C^R_{pq} the real part respectively. This bivariate measure is identical to the one proposed by Pascual-Marqui (2007b). In Section 3.1.8, relations to this and other measures are elaborated in more detail. To compare GIM_{pq} with the imaginary part of coherency it is convenient to take the square root of Eq.(3.20) and to define the Corrected Imaginary Part of Coherency (cImCoh) as

$$\mathrm{cImCoh} = \frac{C^I_{pq}}{\sqrt{\left(1 - \left(C^R_{pq}\right)^2\right)}}. \tag{3.21}$$

Then, cImCoh^2 = GIM and cImCoh is invariant to linear transformations apart from the sign.

3.1.4. Invariance to linear transformations

The connectivity measures derived in the previous sections exhibit the property to be invariant to arbitrary linear transformations. As the mapping from sources to sensors in EEG and MEG recordings is a linear transformation (see Sections 2.2.2 and 2.3), the measures do not depend on how the sources superimpose on the sensor level provided that this transformation is invertible. Therefore, they can be used to compare the two measurement modalities EEG and MEG. Theoretically, both measure the same neurophysiological phenomena but differ in the forward mapping.

To show the invariance property of the MIM, let's consider the Fourier transforms of two multivariate time series $\mathbf{x}_A(f)$ and $\mathbf{x}_B(f)$. Again, for the ease of reading the dependence on frequency is omitted in the following. An arbitrary linear transformation of the data in each subspace yields new data $\hat{\mathbf{x}}_A = \mathbf{T}_A\mathbf{x}$ and $\hat{\mathbf{x}}_B = \mathbf{T}_B\mathbf{x}$. The cross-spectrum in the subspace A for the transformed data now reads

$$\left\langle \hat{\mathbf{x}}_A \hat{\mathbf{x}}_A^\dagger \right\rangle = \mathbf{T}_A \left\langle \mathbf{x}_A \mathbf{x}_A^\dagger \right\rangle \mathbf{T}_A^\mathsf{T} = \mathbf{T}_A \mathbf{S}_{AA} \mathbf{T}_A^\mathsf{T} \tag{3.22}$$

and $\mathbf{T}_B\mathbf{S}_{BB}\mathbf{T}_B^\mathsf{T}$ for the $\mathbf{x}_B$ in subspace B respectively. Furthermore, the cross-spectrum between the two subspaces including the transformation can be written as

$$\left\langle \hat{\mathbf{x}}_A \hat{\mathbf{x}}_B^\dagger \right\rangle = \mathbf{T}_A \left\langle \mathbf{x}_A \mathbf{x}_B^\dagger \right\rangle \mathbf{T}_B^\mathsf{T} = \mathbf{T}_A \mathbf{S}_{AB} \mathbf{T}_B^\mathsf{T}. \tag{3.23}$$

Now, the transformed cross-spectra from Eq.(3.22) can be inserted into the formula for MIM in Eq.(3.16). Assuming that $\mathbf{T}$ is invertible this leads to

$$\begin{aligned} \text{MIM} &= \text{tr}\left[\left(\mathbf{T}_A \mathbf{S}_{AA}^R \mathbf{T}_A^\mathsf{T} \right)^{-1} \left(\mathbf{T}_A \mathbf{S}_{AB}^I \mathbf{T}_B^\mathsf{T} \right) \left(\mathbf{T}_B \mathbf{S}_{BB}^R \mathbf{T}_B^\mathsf{T} \right)^{-1} \left(\mathbf{T}_A \mathbf{S}_{AB}^I \mathbf{T}_B^\mathsf{T} \right)^\mathsf{T} \right] \\ &= \text{tr}\left[\left(\mathbf{S}_{AA}^R \right)^{-1} \mathbf{S}_{AB}^I \left(\mathbf{S}_{BB}^R \right)^{-1} \left(\mathbf{S}_{AB}^I \right)^\mathsf{T} \right], \end{aligned} \tag{3.24}$$

which is exactly the same as the measure for the original data in Eq.(3.16).

MIC is as well as MIM, by construction, invariant to arbitrary (invertible) transformations within each subspace. To explicitly show that the invariance property holds for all of the eigenvalues of Eq.(3.12) and Eq.(3.13), let's rewrite Eq.(3.12) into its original form

$$\left(\mathbf{S}_{BB}^R \right)^{-\frac{1}{2}} \left(\mathbf{S}_{AB}^I \right)^\mathsf{T} \left(\mathbf{S}_{AA}^R \right)^{-1} \mathbf{S}_{AB}^I \left(\mathbf{S}_{BB}^R \right)^{-\frac{1}{2}} \mathbf{a} = \lambda \mathbf{a}. \tag{3.25}$$

Now, one can observe that with $\mathbf{a}$ being an eigenvector of $(\mathbf{D}_{AB}^I)^\mathsf{T}\mathbf{D}_{AB}^I$ with the

corresponding eigenvalue λ, the vector

$$\tilde{\mathbf{a}} = \left(\mathbf{S}^R_{BB}\right)^{-\frac{1}{2}} \mathbf{a} \tag{3.26}$$

fulfills the eigenvalue equation

$$\left(\mathbf{S}^I_{AB}\right)^{\mathsf{T}} \left(\mathbf{S}^R_{AA}\right)^{-1} \mathbf{S}^I_{AB} \left(\mathbf{S}^R_{BB}\right)^{-1} \tilde{\mathbf{a}} = \lambda \tilde{\mathbf{a}} \tag{3.27}$$

with the same eigenvalue λ. According to the definition

$$\mathbf{F} := \left(\mathbf{S}^I_{AB}\right)^{\mathsf{T}} \left(\mathbf{S}^R_{AA}\right)^{-1} \mathbf{S}^I_{AB} \left(\mathbf{S}^R_{BB}\right)^{-1}, \tag{3.28}$$

and by exploiting the antisymmetry of $\mathbf{S}^I_{AB}$, any linear transformation of the initial data $\hat{\mathbf{x}}_A = \mathbf{T}_A \mathbf{x}_A$ and $\hat{\mathbf{x}}_B = \mathbf{T}_B \mathbf{x}_B$ (see also Section 3.1.4) leads to a transformation of the matrix $\mathbf{F}$ with

$$\begin{aligned}
\hat{\mathbf{F}} &= \left(\mathbf{T}_A \mathbf{S}^I_{AB} \mathbf{T}_B\right)^{\mathsf{T}} \left(\mathbf{T}_A \mathbf{S}^R_{AA} \mathbf{T}_A\right)^{-1} \left(\mathbf{T}_A \mathbf{S}^I_{AB} \mathbf{T}_B\right) \left(\mathbf{T}_B \mathbf{S}^R_{BB} \mathbf{T}_B\right)^{-1} \\
&= \mathbf{T}_B (\mathbf{S}^I_{AB})^{\mathsf{T}} \mathbf{T}_A \mathbf{T}_A^{-1} (\mathbf{S}^R_{AA})^{-1} \mathbf{T}_A^{-1} \mathbf{T}_A \mathbf{S}^I_{AB} \mathbf{T}_B \mathbf{T}_B^{-1} (\mathbf{S}^R_{BB})^{-1} \mathbf{T}_B^{-1} \\
&= \mathbf{T}_B (\mathbf{S}^I_{AB})^{\mathsf{T}} (\mathbf{S}^R_{AA})^{-1} \mathbf{S}^I_{AB} (\mathbf{S}^R_{BB})^{-1} \mathbf{T}_B^{-1} \\
&= \mathbf{T}_B \mathbf{F} \mathbf{T}_B^{-1}.
\end{aligned} \tag{3.29}$$

This transformation is a similarity transform under which all eigenvalues are invariant. Therefore, the eigenvalues of $\hat{\mathbf{F}}$ and $\mathbf{F}$ are identical and a linear transformation does not change the eigenvalues in Eq.(3.12). The analogous argument applies to the eigenvalues of $\mathbf{D}^I_{AB}(\mathbf{D}^I_{AB})^{\mathsf{T}}$.

3.1.5. A general perspective

In order to demonstrate that the eigenvalues in Eq.(3.12) and in Eq.(3.13) are the *complete* set of invariants, the problem can be viewed from a slightly different angle. If one is seeking measures of brain connectivity which vanish for non interacting sources and are invariant to linear transformations, it follows that all information must then be contained in the imaginary part of the transformed cross-spectrum. Without loss of generality, the real part of the transformed cross-spectrum has to be the identity matrix. First, let's consider the case in which the subspaces A and B are identical. A linear transformation to a system where the real part of the cross-spectrum is the identity matrix is unique up to an arbitrary orthogonal matrix $\mathbf{O}$ which leaves the identity matrix unchanged. Specifically, if $\mathbf{S}$ is the original cross-spectrum (defined in Eq.(3.1) with $A = B$), then, with $\mathbf{T} = \mathbf{O}(\mathbf{S}^R)^{-1/2}$ and

$\mathbf{O}^T = \mathbf{O}^{-1}$ the transformed cross-spectrum

$$\hat{\mathbf{S}} \quad = \quad \mathbf{O}(\mathbf{S}^R)^{-\frac{1}{2}}\mathbf{S}(\mathbf{S}^R)^{-\frac{1}{2}}\mathbf{O}^{-1} \tag{3.30}$$

has unit real part for any orthogonal $\mathbf{O}$. Furthermore, for the imaginary part of the transformed cross-spectrum

$$\hat{\mathbf{S}}^I = (\mathbf{S}^R)^{-\frac{1}{2}}\mathbf{S}^I(\mathbf{S}^R)^{-\frac{1}{2}}, \tag{3.31}$$

any measure of connectivity $g(\hat{\mathbf{S}}^I)$ invariant to linear transformations must have the property

$$g(\hat{\mathbf{S}}^I) = g(\mathbf{O}\hat{\mathbf{S}}^I\mathbf{O}^{-1}) \tag{3.32}$$

which is fulfilled if g measures an invariant of $\hat{\mathbf{S}}^I$ under similarity transforms. A complete set of invariants under similarity transforms is given by the set of all eigenvalues of a matrix. The (orthogonal) eigenvectors, however, can be set arbitrarily with an appropriate $\mathbf{O}$. Since a matrix is uniquely determined with the set of all eigenvalues and eigenvectors, it follows that any measure of connectivity invariant to linear transformations must be a function of the eigenvalues of $g(\hat{\mathbf{S}}^I)$.

The discussion for different subspaces A and B is similar. Any measure invariant to linear transformations can, without loss of generality, be written in a coordinate system such that the real parts of the cross-spectra in both subspaces are identical to the unit matrices. This coordinate system is unique up to orthogonal transformations $\mathbf{O}_A$ and $\mathbf{O}_B$ for the subspaces A and B, respectively. Thus, the most general expression for the between-subspace imaginary part of the cross-spectrum in such a coordinate system reads

$$\hat{\mathbf{S}}^I_{AB} = \mathbf{O}_A\mathbf{S}^I_{AB}\mathbf{O}_B^{\mathsf{T}} = \mathbf{O}_A\mathbf{S}^I_{AB}\mathbf{O}_B^{-1}. \tag{3.33}$$

Writing $\mathbf{S}^I_{AB}$ as the singular value decomposition

$$\mathbf{S}^I_{AB} = \mathbf{U}\mathbf{\Gamma}\mathbf{V}^\dagger \tag{3.34}$$

with $\mathbf{U}$ and $\mathbf{V}$ having orthogonal and normalized columns and $\mathbf{\Gamma}$ being diagonal with real and positive entries one can observe that

$$\hat{\mathbf{S}}^I_{AB} = \hat{\mathbf{U}}\mathbf{\Gamma}\hat{\mathbf{V}}^\dagger \tag{3.35}$$

with

$$\hat{\mathbf{U}} = \mathbf{O}_A\mathbf{U} \quad \text{and} \quad \hat{\mathbf{V}} = \mathbf{O}_B\mathbf{V} \tag{3.36}$$

provides the same singular values as in Eq.(3.34). Again, while the (orthogonal) basis of the SVD decomposition can be set arbitrarily by choosing $\mathbf{O}_A$ and $\mathbf{O}_B$, all the singular values are invariant to linear transformations. These singular values are identical to solutions for λ in (3.12) and (3.13).

3.1.6. Overfitting

An issue that has to be taken into account within the application of MIC, MIM and GIM is the problem of overfitting (Everitt, 2006). Simulations demonstrating the effects of overfitting will be presented in Section 4.2.1. The filters **a** and **b**, described in Section 3.1.1 are calculated such that the imaginary part of coherency between the two subspaces A and B or within a single space is maximized. However, it occurs that the spatial filters are not generalizable to new data due to overfitting. To overcome the problem of overfitting, a reduction of dimensionality before calculating the spatial filters for each frequency is proposed. Due to the spectral theorem (e.g. Hawkins, 1975), the frequency-dependent antisymmetric imaginary part of the cross-spectrum $\mathbf{S}^I \in \mathbb{R}^{N\times N}$ times its transpose can be decomposed by a singular value decomposition (see Section 2.3.1) into

$$\mathbf{S}^I(\mathbf{S}^I)^\mathsf{T} = \mathbf{U}\mathbf{\Gamma}\mathbf{V}^\mathsf{T} \tag{3.37}$$

with real singular values on the diagonal of $\mathbf{\Gamma}$. Now, the cross-spectrum is reduced by choosing column wise the first P components of the matrix $\mathbf{U} \in \mathbb{R}^{N\times N}$ in Eq.(3.37), such that $\bar{\mathbf{U}} \in \mathbb{R}^{N\times P}$. Finally the complex cross-spectrum is projected onto a lower dimensional space and separated into real and imaginary part by

$$\begin{aligned} \bar{\mathbf{S}} &= \bar{\mathbf{U}}^\mathsf{T}\mathbf{S}\bar{\mathbf{U}} \\ &= \bar{\mathbf{S}}^R\bar{\mathbf{S}}^I \end{aligned} \tag{3.38}$$

resulting in $\bar{\mathbf{S}}^R \in \mathbb{R}^{P\times P}$.

An alternative approach for the reduction of dimensionality would be to use spatial filters that extract oscillatory signals as proposed by Nikulin et al. (2011) and further elaborated by Haufe et al. (2014a).

3.1.7. Bias

The MIM and GIM introduced in Section 3.1.2 and 3.1.3 are positive definite and will therefore contain a bias towards a positive value for a finite number of averages even if there is no true interaction. This bias can be calculated approximately under certain conditions. Let's assume that the entire signal is a superposition of independent sources and the cross-spectral matrices are estimated from K independent trials. Since K is finite, GIM is a stochastic variable, and one can derive an approximation for the expectation value of GIM, i.e. for $\langle \mathrm{GIM} \rangle$. Here, the expectation value $\langle\cdot\rangle$ denotes averaging over an infinite number of hypothetical repetitions of the entire experiment. Without loss of generality one can assume that the true cross-spectral matrix $\mathbf{S}$ is proportional to the identity matrix. For independent sources, the off-diagonal elements become zero and the signal power is contained on the diagonal. Because the GIM is invariant to linear transformations, one can always transform any real valued $\mathbf{S}$ to the identity matrix without changing the GIM. Hence, with increasing K, the estimate $\hat{\mathbf{S}}$ converges to $\mathbf{S} = \mathbf{I}_N$ and $(\hat{\mathbf{S}}^R)^{-1} \sim \mathbf{I}_N$. Now, one can

approximate the bias in leading order of K with

$$\langle GIM \rangle = \frac{1}{2} \left\langle \mathrm{tr} \left[\left(\hat{\mathbf{S}}^R \right)^{-1} \hat{\mathbf{S}}^I \left(\hat{\mathbf{S}}^R \right)^{-1} \left(\hat{\mathbf{S}}^I \right)^{\mathsf{T}} \right] \right\rangle \approx \frac{1}{2} \left\langle \mathrm{tr} \left[\hat{\mathbf{S}}^I \left(\hat{\mathbf{S}}^I \right)^{\mathsf{T}} \right] \right\rangle. \tag{3.39}$$

Lets denote by x_{mk} the complex signal in channel m at trial k at a distinct frequency. Writing the imaginary part of the cross-spectrum between channel m and n as

$$\hat{S}^I_{mn} = \frac{1}{2iK} \sum_k (x_{mk} x^*_{nk} - x^*_{mk} x_{nk}), \tag{3.40}$$

the contribution for each pair of channels with indices $m \neq n$ is given by

$$\begin{aligned} \left\langle \left(\hat{S}^I_{mn} \right)^2 \right\rangle &= -\frac{1}{4K^2} \sum_{kl} \langle (x_{mk} x^*_{nk} - x^*_{mk} x_{nk})(x_{ml} x^*_{nl} - x^*_{ml} x_{nl}) \rangle \\ &= -\frac{1}{2K^2} \sum_k \left\langle (x^2_{mk} \, (x^*_{nk})^2 - |x_{mk}|^2 |x_{nk}|^2 \right\rangle \\ &= \frac{1}{2K^2} \sum_k \left\langle |x_{mk}|^2 \right\rangle \left\langle |x_{nk}|^2 \right\rangle = \frac{1}{2K}. \end{aligned} \tag{3.41}$$

with $|.|$ denoting the absolute value. As Eq.(3.41) describes the bias for a single channel pair, one has to take all pairs into account. This leads to a complete approximation of the bias for the GIM obtained from N measurement channels

$$\langle \mathrm{GIM} \rangle \approx \frac{1}{2} N(N-1) \frac{1}{2K} = \frac{N(N-1)}{4K} =: \mathrm{bias}_{GIM}. \tag{3.42}$$

The measure between different spaces A and B with N_A and N_B channels, respectively, is only invariant with respect to linear transformations within each subspace. However, the result also depends on correlations across subspaces, which are for independent sources induced by mixing artifacts. If such mixing artifacts only exist within but not across subspaces, which depends on the application, the previous analysis equally applies for the MIM defined in Eq.(3.16). This leads to

$$\langle \mathrm{MIM} \rangle \approx \frac{N_A N_B}{2K} =: \mathrm{bias}_{MIM} \tag{3.43}$$

It must be emphasized that the results presented above only hold if the trials are independent of each other. To verify the quality of approximation derived analytically in this section, a simulation is conducted in Section 4.2.2.

3.1.8. Relation to other work

For a bivariate scenario, the GIM is equivalent to the measure proposed by Pascual-Marqui (Pascual-Marqui, 2007a), called Lagged Phase Coherence (LPC). In the

general case, the measure is defined for each frequency by

$$\mathrm{LPC}_{AB} = 1 - \frac{\left[\det\begin{pmatrix}\mathbf{S}_{AA} & \mathbf{S}_{AB}\\ \mathbf{S}_{BA} & \mathbf{S}_{BB}\end{pmatrix}/\det\begin{pmatrix}\mathbf{S}_{AA} & \mathbf{0}_{N_AN_B}\\ \mathbf{0}_{N_BN_A} & \mathbf{S}_{BB}\end{pmatrix}\right]}{\left[\det\begin{pmatrix}\mathbf{S}^R_{AA} & \mathbf{S}^R_{AB}\\ \mathbf{S}^R_{BA} & \mathbf{S}^R_{BB}\end{pmatrix}/\det\begin{pmatrix}\mathbf{S}^R_{AA} & \mathbf{0}_{N_AN_B}\\ \mathbf{0}_{N_BN_A} & \mathbf{S}^R_{BB}\end{pmatrix}\right]} \tag{3.44}$$

as the connectivity between the two multivariate time series in the subspaces A and B with $\det(.)$ being the determinant. With the definition in Eq.(3.18) and notation applied above, the LPC can be written in the bivariate case for the two time series p and q as

$$LPC_{pq} = 1 - \frac{\left[\det\left(\mathbf{S}_{pq}\right)/\det\begin{pmatrix}S_{pp} & 0\\ 0 & S_{qq}\end{pmatrix}\right]}{\left[\det(\mathbf{S}^R_{pq})/\det\begin{pmatrix}S^R_{pp} & 0\\ 0 & S^R_{qq}\end{pmatrix}\right]} = \frac{(C^I_{pq})^2}{1-(C^R_{pq})^2} \tag{3.45}$$

which, as shown in the Appendix A.7, is the same result as for GIM_{pq} in Eq.(3.20). This equivalence, however, holds only for the bivariate case. It is, for example, not possible to measure an interaction of a space with itself using the LPC because for $A = B$ some matrices are rank deficient and the measure is ill-defined. It should also be noted, that this measure is in general invariant to linear transformations within but not across the subspaces. The fact, that it is still invariant to transformations across subspaces if the subspaces are one-dimensional is a special property of the restricted space. Mathematically, it can be traced back to the fact that in this case $\mathbf{S}_{AA}$ and $\mathbf{S}_{BB}$ are real valued. In comparison, the MIM proposed in Eq.(3.16) is *not* invariant with respect to transformations *across* subspaces also if these spaces are one-dimensional. Then the MIM is just the square of standard imaginary coherency. Rather, invariance is achieved from setting $A = B$ as two-dimensional subspaces and using the GIM introduced in Eq.(3.17). Although properties of MIM and the LPC are similar, the measures are not equivalent. It is, for example, not clear how the bias for the LPC can be calculated analytically.

A second measure is related to the connectivity measures presented in the previous sections. Vinck et al. (2011) have proposed a nonlinear measure, termed Weighted Phase Lag Index (WPLI), to solve the problem of mixing distortions. With frequency dependence still omitted, the authors define the WPLI between two signals at channels p and q as

$$\mathrm{WPLI}_{pq} = \frac{|\langle\Im(x_p x_q^*)\rangle|}{\langle|\Im(x_p x_q^*)|\rangle}. \tag{3.46}$$

Please note the difference of order between the expectation value $\langle.\rangle$ and the absolute value $|.|$ in the numerator and the denominator in Eq.(3.46). If one transforms to a

new coordinate system

$$\begin{pmatrix} y_p \\ y_q \end{pmatrix} = \underbrace{\begin{pmatrix} t_{11} & t_{12} \\ t_{21} & t_{22} \end{pmatrix}}_{:=\mathbf{T}} \begin{pmatrix} x_p \\ x_q \end{pmatrix}, \tag{3.47}$$

it is with the definition of coherency in Eq.(2.19) straight-forward to check that

$$\begin{aligned} \Im(y_p y_q^*) &= \Im((t_{11}x_p + t_{12}x_q)(t_{21}x_p + t_{22}x_q)^*) \\ &= (t_{11}t_{22} - t_{12}t_{21})\Im(x_p x_q^*) \\ &= \det(\mathbf{T})\Im(x_p x_q^*) \end{aligned} \tag{3.48}$$

such that $|\det(\mathbf{T})|$ cancels in the numerator and denominator of Eq.(3.46) and therefore, the WPLI is invariant with respect to linear transformations.

Since Eq.(3.46) describes a nonlinear measure, there is no generally valid relationship between WPLI as a bivariate measure and the GIM_{pq} in Eq.(3.20) and, equivalently, LPC_{ab} in Eq.(3.45). However, considering (zero mean) Gaussian distributed data the statistical properties are determined completely by the cross-spectral matrix $\mathbf{S}$. Furthermore, due to the invariance property one can, without loss of generality, transform the cross-spectrum to the form

$$\mathbf{S} = \begin{pmatrix} 1 & i\theta \\ -i\theta & 1 \end{pmatrix} \tag{3.49}$$

with θ being real valued and being the only parameter. Any measure of connectivity invariant to linear transformations can only depend on θ and relations between different measures can be expressed as functions of θ. While

$$|\theta| = \sqrt{\mathrm{GIM}_{pq}} = |cImCoh| \tag{3.50}$$

from Eq.(3.20), it is shown in the Appendix A.8 that

$$WPLI = \frac{2|\theta|}{1+\theta^2} \tag{3.51}$$

for Gaussian distributed data. As a consequence, for small to moderate connection strengths, the value of WPLI is about doubled compared to GIM and the measures are about equal for large connection strengths.

The functional relationship seems to imply that the measures are equally useful when applied to bivariate data. However, the measures have different statistical properties which might become very relevant when data are not Gaussian distributed. The most important difference is that in the denominator of WPLI the signal at channel p occurs linearly (as a product with the signal at channel q with $p \neq q$). In contrast, GIM contains the power in the normalization which consists of the squares of the signals. Thus, strong but rare outliers occurring independently in the channels

will affect GIM more than WPLI making the latter particularly robust to outliers while probably compromising mildly for Gaussian distributed data.

3.2. Self-consistent Music (SC Music)

A common method to estimate sources of brain activity is Rap Music as introduced in Section 2.3.3. It is based on the Music algorithm and aims to diminish the methodological issues of Music in the presence of correlated sources. Nevertheless, Rap Music still exhibits problems in separating non-independent sources as shown in simulations in Section 4.4. In the following, a novel method is introduced that can be seen as an improvement over Rap Music with a special focus on interacting brain sources.

3.2.1. Constructing subspaces

Subspace methods such as Music and Rap Music are based on a low rank approximation of the data space. Most common, the covariance matrix of the data is decomposed into a noise subspace $\hat{\mathbf{\Sigma}}_N$ and a signal subspace $\hat{\mathbf{\Sigma}}_S$ as described in Section 2.3.3. In this thesis, however, the focus lies on the investigation of interacting sources. Therefore, the imaginary part of the cross-spectrum (ImCs) denoted as $\mathbf{S}^I$ is used instead of the covariance matrix. The ImCs serves as a basis for interacting sources robust to the artifact of volume conduction and, hence, provides trustworthy and complete information for second order statistics. The idea of using the cross-spectrum as a frequency domain data representation for EEG/MEG source localization has previously been exploited by DICS beamforming (Gross et al., 2001). The idea of employing the imaginary part due to its special properties in combination with Rap Music has previously been published in collaborative work in Avarvand et al. (2012). A straightforward approach to construct a signal subspace from the ImCs is to perform a singular value decomposition

$$\mathbf{S}^I = \mathbf{U}\mathbf{\Lambda}\mathbf{V}^\mathsf{T} \tag{3.52}$$

with the diagonal matrix $\mathbf{\Lambda}$ containing the singular values in descending order and $\mathbf{U}$ containing the corresponding singular vectors as columns. Now, the P singular vectors belonging to the P largest singular values denoted as $\hat{\mathbf{U}} = (\mathbf{u}_1 \dots \mathbf{u}_P) \in \mathbb{R}^{N \times P}$ (N: number of measurement channels) span the signal subspace $\hat{\mathbf{S}}_S^I$.

An alternative approach is to use the subspace obtained from the maximization of the imaginary part of coherency which was introduced in Section 3.1.1. Depending on the particular noise level of the data and the number of measurement channels N, it is suggested to regularize the ImCs. This can be achieved via

$$\tilde{\mathbf{S}} = \mathbf{S} + \rho \left(\frac{1}{N} \mathrm{tr}(\mathbf{S}) \, \mathbf{I}_N \right) \tag{3.53}$$

with $\frac{1}{N}\mathrm{tr}(\mathbf{S})$ being the average signal power which is encoded on the diagonal

elements of the cross-spectrum and ρ being a regularization parameter. A reasonable choice of ρ would be for example in the range of $0.05 \leq \rho \leq 0.2$. According to the theory in Section 3.1.1, the regularized ImCs now can be pre-whitened with

$$\mathbf{D}^I = (\tilde{\mathbf{S}}^R)^{-\frac{1}{2}} \tilde{\mathbf{S}}^I (\tilde{\mathbf{S}}^R)^{-\frac{1}{2}} \tag{3.54}$$

and decomposed by a singular value decomposition with

$$\mathbf{D}^I = \mathbf{U}\mathbf{\Lambda}\mathbf{V}^\mathsf{T}. \tag{3.55}$$

Again, the P largest left-singular vectors, i.e. the first P columns of $\mathbf{U}$ denoted as $\mathbf{u}_1 \dots \mathbf{u}_P$ can be used to define the signal subspace. These left-singular vectors, however, have to be projected back to the original data space in correspondence to the leadfields. This leads to the final vectors

$$\tilde{\mathbf{u}}_j = (\tilde{\mathbf{S}}^R)^{\frac{1}{2}} \mathbf{u}_j \quad \forall\, j = 1 \dots P \tag{3.56}$$

defining the signal subspace in which the imaginary part of coherency is maximized. In the following the subspace is denoted as

$$\hat{\mathbf{D}}^I = [\tilde{\mathbf{u}}_1 \dots \tilde{\mathbf{u}}_P] \quad \in \mathbb{R}^{N \times P} \tag{3.57}$$

The backprojection in Eq.(3.56) can also be seen as transforming spatial filters into interpretable patterns as described in Haufe et al. (2014b) and Nikulin et al. (2011). Using the signal subspace constructed from the orthogonal vectors in Eq.(3.56) has the practical purpose of detecting interactions which are eventually too weak to be observed directly due to a low signal-to-noise ratio. A comparison between the two ways of constructing a subspace based on the ImCs that are described in this section is given in Section 4.3.

3.2.2. The number of sources

A common problem of subspace methods is how to determine the dimension of the subspace size P. In the case of Music and Rap Music this number most commonly coincides with the assumed number of sources and has to be estimated. The general scenario yields the separation of meaningful information encoded in early axes obtained from a PCA and remaining trivial axes summarizing all kinds of noise and inaccuracies. This issue has been largely discussed in the signal processing and machine learning literature. For example Peres-Neto et al. (2005) provide a good overview and compare different methods how to determine the number of non-trivial axes. Furthermore, the problem has also been addressed in the neuroscientific field of research, e.g. by Hansen et al. (1999) for fMRI data and by Maris (2003), Knösche et al. (1998) and Sekihara et al. (1999) for EEG and MEG data. All studies concerning EEG/MEG data suggest a pre-whitening such that the spatial covariance matrix of the transformed noise matrix is the identity matrix. In the case of the ImCs one can consider the real part of the cross-spectrum as the spatial noise matrix that is

transformed to the identity matrix due to Eq.(3.4). Hence, the idea of pre-whitening is already incorporated when the subspace is constructed by the vectors given by Eq.(3.56).

One way to visualize the significance of the axes obtained by the SVD, as described above, is to plot the singular values against their rank order. This is called a scree plot. In an optimal scenario one should observe a huge drop between the meaningful and the trivial singular values. Actually, in a noise-free setting all trivial axes would belong to a singular value equal to zero and meaningful axes would have a singular value greater than zero. In practice, however, the singular values are decreasing. An observed drop in the scree plot would serve as a valid cut-off or stopping rule to conclude on the number of meaningful axes. However, a significant drop is not always visible for real data even including prewhitening. As proposed by e.g. Maris (2003) and Peres-Neto et al. (2005), a resampling approach can be used to estimate the largest trivial singular value. Within this work such a resampling approach is used in combination with surrogate data. The surrogate data is constructed in a way such that all data properties are maintained and only interactions, i.e. phase synchronizations are destroyed. The procedure of constructing this kind of surrogate data will be described in details in Section 3.4. From these surrogate data bootstrap estimates of the singular values are generated. To account for outliers, 95% of the largest singular values out of all bootstrap repetitions is chosen as the cut-off singular value for the last still meaningful axes. Hence, the number of singular values of the true data, that is larger than the cut-off value, is interpreted as the number of interacting sources present in the data. This number then also serves as the subspace dimension P. Please note that the number of estimated sources and the subspace dimension do in principle not have to be equivalent. However, due to simplicity and practical experience this assumption seems to be a good choice. These considerations will be demonstrated and validated in Sections 4.5 and 5.2.1.

3.2.3. Algorithmic improvements to Rap Music

The subspace methods Music and Rap Music described in Section 2.3.3 are designed to find source locations for which the forward model coincides well with the signal subspace. The subspace is constructed from P orthogonal vectors and its dimension is assumed to be equal to the number of sources. However, the signal subspace is rank-deficient when sources are perfectly correlated. Then, the subspace is likely estimated to be too small in order to capture all source activity. This problem can also arise for a subspace constructed from the ImCs. Remarkably, a subspace constructed from the ImCs is always rank deficient when the number of sources is odd. Due to the antisymmetric nature of the ImCs reflecting pair-wise synchronization, singular values also occur in pairs. Hence, the application of Rap Music based on a subspace constructed from the ImCs fails for an odd number of sources. This will be demonstrated in Section 4.4. As an additional point, the estimation of sources itself with Music is substantially biased by correlated or coherent sources (Mosher and Leahy, 1999).

In the following a novel algorithm is introduced based on the idea that the absence

of *all* other sources improves localization and, additionally, circumvents the effect of subspace rank deficiency. The algorithm is termed Self-Consistent Music (SC Music) and works as follows: Let's consider P given sources obtained from an initial Rap Music scan based on a subspace constructed from the ImCs. Now, considering the strongest source j, the remaining $P-1$ sources are projected out leading to a non rank-deficient subspace. The projection works analogous to the projection executed for Rap Music as described by Eq.(2.16) in Section 2.3.3. Then, a new Music scan for source j is executed. This way the location of source j is estimated without the influence of all other sources. For the following iteration, which considers the second strongest source $j+1$, the updated source location of j leads to a better estimate of the new subspace by projecting out source j more precise. This procedure is first repeated for all P sources. Second, the whole scheme is repeated with constantly updated source locations and subspaces until the estimated locations of all sources converge. For the implementation used in this thesis, binary convergence c_l in the l-th run is defined as

$$c_l := \begin{cases} 1 & \text{if } \frac{\|\mathbf{s}_{l-1}-\mathbf{s}_l\|_{\mathrm{F}}}{\|\mathbf{s}_{l-1}+\epsilon\|_{\mathrm{F}}} < 10^{-9} \\ \\ 0 & \text{otherwise,} \end{cases} \tag{3.58}$$

with $\mathbf{s}_l \in \mathbb{R}^{M\times P}$ being the estimated source distributions of the P sources and ϵ being the distance from the number 1.0 to the next largest double-precision number Matlab can represent, that is $\epsilon = 2^{-52}$. The reason for the presence of ϵ in the denominator in Eq.(3.58) is numeric stability. Algorithm 3.1 provides an overview of the SC Music procedure.

Algorithm 3.1 Self-Consistent Music (SC Music)

1: construct signal subspace $\hat{\mathbf{D}}^I_{0,0}$ (see Section 3.2.1)
2: perform Rap Music scan for P sources on $\hat{\mathbf{D}}^I_{0,0}$ (see Algorithm 2.1)
3: l=0
4: **repeat**
5: l=l+1
6: **for** $j = 1$ **to** P **do**
7: project out all sources $k = 1 \dots P; k \neq j$ from $\hat{\mathbf{D}}^I_{l,j-1}$ (see Eq.(2.16))
8: Music scan for j on subspace $\hat{\mathbf{D}}^I_{l,j}$
9: Update source location of j
10: **end for**
11: **if** (source locations in step l-1) $\approx$ (source locations in step l) **then**
12: c_l=true
13: **else**
14: c_l=false
15: **end if**
16: **until** c_l

3.2.4. SC Music, modified beamforming and MIC

Having determined sources based on the ImCs with SC Music, the question remains which source is actually interacting with which. For example, a system of four sources can be composed of two synchronized pairs independent of the respective other pair. Hence, it is desired to make inferences about the dynamics at source level. A method well capable of projecting data measured at EEG/MEG sensor level into source space is beamforming as introduced in Section 2.3.2. However, beamforming lacks accuracy when sources are dependent. To overcome this limitation, one can exploit the information gained from SC Music in combination with the MIC (see Section 3.1.1) in order to estimate optimal dipole directions. This procedure initially published for Rap Music in collaborative work in Avarvand et al. (2012) is revised in the following.

Let's consider $\mathbf{B} = (\mathbf{b}_1 \dots \mathbf{b}_P) \in \mathbb{R}^{N \times P}$ as the matrix containing the source topographies, i.e. the forward projections, of the P dipoles found by SC Music. Following the approach of a Nulling beamformer as introduced in Section 2.3.2, the spatial filter $\mathbf{w}_p \in \mathbb{R}^{N \times 1}$ projecting the sensor level frequency domain[1] data of N sensors to the source locations $p = 1 \dots P$ is given by

$$\mathbf{w}_p = (\mathbf{S}^R)^{-1}\mathbf{B}\left(\mathbf{B}^\mathsf{T}(\mathbf{S}^R)^{-1}\mathbf{B}\right)^{-1}\mathbf{f}_p. \tag{3.59}$$

with $\mathbf{f}_p = [0 \dots 0\ 1\ 0 \dots 0]^\mathsf{T}$ being a vector that contains a one at the p-th element and zeros elsewhere (see also Eq.(2.11)). Furthermore, $\mathbf{S}^R \in \mathbb{R}^{N \times N}$ denotes the real part of the cross-spectrum which is convenient to use for a frequency domain beamformer. Hence, the Fourier transformed data $\mathbf{X} \in \mathbb{C}^{N \times 1}$ projected to a source location p is given by

$$z_p = \mathbf{w}_p^\mathsf{T}\mathbf{X} \quad \forall \quad p = 1 \dots P. \tag{3.60}$$

Please note that it is crucial to use the Nulling beamformer for the sources obtained with SC Music. As the source activity z_p is already known to be coherent to the other $P - 1$ sources, the construction of the spatial filter will substantially improve.

For all other $M - P$ source locations on the grid, a LCMV (or DICS) beamformer solution can be used. Due to prior knowledge these sources are independent of other sources. In contrast to the P sources found by SC Music, the dipole direction is not known. Denoting $\mathbf{d}_m \in \mathbb{R}^{3 \times 1}$ as the dipole direction at grid point m, the frequency domain data at voxel m is given by

$$z_m = \mathbf{d}_m^\mathsf{T}\mathbf{W}_m^\mathsf{T}\mathbf{X} \quad \forall \quad m = 1 \dots M, m \neq p \tag{3.61}$$

with

$$\mathbf{W}_m = (\mathbf{S}^R)^{-1}\mathbf{A}_m\left(\mathbf{A}_m^\mathsf{T}(\mathbf{S}^R)^{-1}\mathbf{A}_m\right)^{-1} \tag{3.62}$$

being of size $N \times 3$ and $\mathbf{A}_m \in \mathbb{R}^{N \times 3}$ being the leadfields for dipoles in x-, y- and

[1] Frequency dependence is again omitted for notation simplicity.

z-direction at grid point m.

With the definitions above, the cross-spectrum on source level between a source p (prior determined by SC Music) and any other source at grid point m is given by

$$\left\langle z_p z_m^\dagger \right\rangle = \left\langle (\mathbf{w}_p^\mathsf{T}\mathbf{X})(\mathbf{d}_m^\mathsf{T}\mathbf{W}_m^\mathsf{T}\mathbf{X})^\dagger \right\rangle = \mathbf{w}_p^\mathsf{T} \left\langle \mathbf{X}\mathbf{X}^\dagger \right\rangle \mathbf{W}_m\mathbf{d}_m = \mathbf{w}_p^\mathsf{T}\mathbf{S}\mathbf{W}_m\mathbf{d}_m =: \mathbf{E}_{pm} \quad (3.63)$$

with $\mathbf{S} = \left\langle \mathbf{X}\mathbf{X}^\dagger \right\rangle$ being the complex cross-spectrum on sensor level. Similarly, one can write

$$\left\langle z_p z_p^\dagger \right\rangle = \mathbf{w}_p^\mathsf{T} \left\langle \mathbf{X}\mathbf{X}^\dagger \right\rangle \mathbf{w}_p = \mathbf{w}_p^\mathsf{T}\mathbf{S}\mathbf{w}_p =: \mathbf{E}_{pp} \quad (3.64)$$

and

$$\left\langle z_m z_m^\dagger \right\rangle = \mathbf{d}_m^\mathsf{T}\mathbf{W}_m^\mathsf{T} \left\langle \mathbf{X}\mathbf{X}^\dagger \right\rangle \mathbf{W}_m\mathbf{d}_m = \mathbf{d}_m^\mathsf{T}\mathbf{W}_m^\mathsf{T}\mathbf{S}\mathbf{W}_m\mathbf{d}_m =: \mathbf{E}_{mm}. \quad (3.65)$$

Now, the imaginary part of coherency depending on the dipole direction at grid point m is given by

$$\mathbf{C}_{pm}^I(\mathbf{d}_m) = \frac{\mathbf{w}_p^\mathsf{T}\mathbf{S}^I\mathbf{W}_m\mathbf{d}_m}{\left(\mathbf{w}_p^\mathsf{T}\mathbf{S}^R\mathbf{w}_p\right)^{\frac{1}{2}} \left(\mathbf{d}_m^\mathsf{T}\mathbf{W}_m^\mathsf{T}\mathbf{S}^R\mathbf{W}_m\mathbf{d}_m\right)^{\frac{1}{2}}} = \frac{\mathbf{E}_{pm}^I}{(\mathbf{E}_{pp}^R)^{\frac{1}{2}}(\mathbf{E}_{mm}^R)^{\frac{1}{2}}} \quad (3.66)$$

In order to choose the dipole direction at voxel m that maximizes the imaginary part of coherency, one can evaluate the derivative of Eq.(3.66) and set it to zero. As shown in the Appendix A.9 this leads to

$$\frac{\partial \mathbf{C}_{pm}^I}{\partial \mathbf{d}_m} = \frac{\frac{\partial \mathbf{E}_{pm}^I}{\partial \mathbf{d}_m}}{(\mathbf{E}_{pp}^R)^{\frac{1}{2}}(\mathbf{E}_{mm}^R)^{\frac{1}{2}}} - \frac{1}{2}\frac{\mathbf{E}_{pp}^R}{(\mathbf{E}_{pm}^I)^{\frac{1}{2}}(\mathbf{E}_{mm}^R)^{\frac{3}{2}}}\frac{\partial \mathbf{E}_{mm}^R}{\partial \mathbf{d}_m} \stackrel{!}{=} 0. \quad (3.67)$$

Finally, resolving for $\mathbf{d}_m$ results in

$$\mathbf{d}_m = \left(\mathbf{W}_m^\mathsf{T}\mathbf{S}^R\mathbf{W}_m\right)^{-1}\mathbf{W}_m^\mathsf{T}\mathbf{S}^I\mathbf{w}_p \quad (3.68)$$

which is the dipole direction at grid point m that maximizes the ImCoh between a source found by SC Music at grid point p and the respective source at grid point m. Iterating over the whole grid with M voxels provides a picture of which sources are interacting with the source at grid point p. Pleas note that Eq.(3.68) can be seen as a special case of the MIC on source level incorporating Nulling and DICS beamformer solutions.

3.3. Wedge Music (WM)

In the previous section a method was presented to investigate the relationship between a given source and all other potential sources in the brain. The dipole direction is optimized for the whole brain such that the ImCoh between the given source and all other sources is maximized. This procedure, however, is not well applicable if

a difference in experimental conditions shall be examined. A standard approach in neuroscientific research is to contrast data recorded in two or more different conditions or classes. This way, a certain effect of interest can be exposed without taking common background activity into account. In the case of exploring differences in interactions of two classes, the ImCoh is not a suitable technique. Considering the definition of coherency in Eq.(2.19), power is given in the denominator as a normalization of the cross-spectrum. Hence, ImCoh itself also depends on non-interacting sources and, therefore, the interpretation, of differences of ImCoh between different conditions may be misleading. In general, it is possible that such a difference is caused by effects which are not related to the interaction. To solve this issue, a novel approach called Wedge Music (WM), which has recently been published in Ewald et al. (2014), is presented in the following. The main idea behind Wedge Music is to estimate the contribution of two sources at distinct locations inside the brain to the imaginary part of the cross-spectrum (ImCs) only and to quantify this contribution properly. In contrast to ImCoh, independent sources have no systematic effect on ImCs and any difference between two ImCs must be due to a difference of the interacting system.

3.3.1. Contribution of two sources to the ImCs

As Wedge Music quantifies how much an interaction between two sources at specific voxels k and j inside the brain contributes to the ImCs, it is first derived how a synchronization of two single sources is reflected in the ImCs. Let's consider two brain source time series transformed in the frequency domain $\mathbf{y} = (y_1\ y_2)^\mathsf{T} \in \mathbb{C}^{2\times 1}$. These are mapped into sensor space according to the linear source mixing model by their respective topographies via $\mathbf{x} = \mathbf{T}\mathbf{y}$ with $\mathbf{T} = (\mathbf{t_1}, \mathbf{t_2}) \in \mathbb{R}^{N\times 2}$. The source topographies $\mathbf{t_1} \in \mathbb{R}^{N\times 1}$ and $\mathbf{t_2} \in \mathbb{R}^{N\times 1}$ depend on the leadfields of the particular brain voxels k and j and the dipole moments, i.e. orientations, as will be described in more detail in the following. Now, the cross-spectrum, introduced in Eq.(2.18), reads

$$\mathbf{S_x} = \left\langle \mathbf{x}\mathbf{x}^\dagger \right\rangle = \left\langle\ (\mathbf{T}\mathbf{y})(\mathbf{T}\mathbf{y})^\dagger \right\rangle = \mathbf{T} \left\langle\ \mathbf{y}\mathbf{y}^\dagger \right\rangle \mathbf{T}^\dagger = \mathbf{T}\mathbf{S_y}\mathbf{T}^\mathsf{T}. \tag{3.69}$$

As the topographies included in $\mathbf{T}$ are real-valued quantities, one can use the matrix transpose $(.)^\mathsf{T}$ here. In this bivariate scenario, the *imaginary part* of the cross-spectrum on source level $\Im(\mathbf{S_y})$ only depends on a single number a due to its antisymmetric nature and can be written as

$$\mathbf{S}_\mathbf{y}^I = \begin{pmatrix} 0 & a \\ -a & 0 \end{pmatrix}. \tag{3.70}$$

Hence, the imaginary part of the cross-spectrum for two sources on sensor level can be reformulated as

$$\mathbf{S}_{\mathbf{x}}^{I} = \mathbf{T}\begin{pmatrix} 0 & a \\ -a & 0 \end{pmatrix}\mathbf{T}^{\mathsf{T}} = \begin{pmatrix} (0-t_{21})a & t_{11}a \\ (0-t_{22})a & t_{11}a \\ \vdots & \vdots \\ (0-t_{2N})a & t_{1N}a \end{pmatrix}(\mathbf{t_1},\mathbf{t_2})^{\mathsf{T}} = a\,(-\mathbf{t_2},\mathbf{t_1})\,(\mathbf{t_1},\mathbf{t_2})^{\mathsf{T}}$$

$$= a\left(-\mathbf{t_2}\mathbf{t}_1^{\mathsf{T}} + \mathbf{t}_1\mathbf{t}_2^{\mathsf{T}}\right) = a\left(\mathbf{t}_1\mathbf{t}_2^{\mathsf{T}} - \mathbf{t}_2\mathbf{t}_1^{\mathsf{T}}\right) = a(\mathbf{t}_1 \wedge \mathbf{t}_2) \tag{3.71}$$

with $\wedge$ denoting the wedge product or exterior product of the brain source topographies $\mathbf{t}_1$ and $\mathbf{t}_2$ (Grassmann, 1844; Clifford, 1878). To quantify the effect of a bivariate source synchronization on the ImCs, it is reasonable to eliminate noise and to define a signal subspace in analogy to the Music procedure already described in Section 2.3.3. Again, a low-rank approximation of the ImCs with P dimensions is used as introduced in Eq.(3.57) in Section 3.2.1. According to Eq.(3.57) it is denoted by $\hat{\mathbf{D}}_P^I$. To evaluate if the synchronization of a pair of brain sources is contained in the ImCs, one now can subtract the wedge product of the two source topographies from $\hat{\mathbf{D}}_P^I$ and evaluate if the matrix $\hat{\mathbf{D}}_P^I$ loses rank. If a synchronization between sources at voxels k and j with their respective topographies $\mathbf{t}_k$ and $\mathbf{t}_j$ is contained in $\hat{\mathbf{D}}_P^I$, subtracting $(\mathbf{t}_k \wedge \mathbf{t}_j)$ from $\hat{\mathbf{D}}_P^I$, with the scale of a in Eq.(3.71) absorbed into these topographies, would lead to a rank decline in the resulting matrix. If no phase synchronization between sources at voxels k and j would be present in the measured data, the rank of

$$\hat{\mathbf{E}}_P = \hat{\mathbf{D}}_P^I - (\mathbf{t}_k\mathbf{t}_j^{\mathsf{T}} - \mathbf{t}_j\mathbf{t}_k^{\mathsf{T}}) \tag{3.72}$$

would be unchanged and equal to the rank of $\hat{\mathbf{D}}_P^I$. To quantify the change of rank, one can investigate the product of all singular values of $\hat{\mathbf{E}}_P$. If a synchronization between sources with given topographies is perfectly contained in $\hat{\mathbf{E}}_P$, one singular value will be equal to zero and therefore the whole product. Mathematically, this approach leads to a function

$$g_{k,j} = \prod_{l=1}^{p} SV_l(\hat{\mathbf{E}}_P) = \prod_{l=1}^{P} SV_l(\mathbf{E}_P - (\mathbf{t}_k\mathbf{t}_j^{\mathsf{T}} - \mathbf{t}_j\mathbf{t}_k^{\mathsf{T}})), \tag{3.73}$$

where $SV_l(\hat{\mathbf{E}}_P)$ denotes the l-th singular value of the matrix $\hat{\mathbf{E}}_P$. Concluding, Eq. (3.73) describes a function to estimate how much a particular synchronization between two sources at voxels k and j is contained in measured data or rather the imaginary part of the cross-spectrum.

As stated before, an individual source topography, e.g. $\mathbf{t}_j$ depends on the particular pre-calculated leadfield at the corresponding location $\mathbf{L}_j \in \mathbb{R}^{N\times 3}$ (N: number of measurement channels) and the dipole orientation $\boldsymbol{\alpha}_j \in \mathbb{R}^{3\times 1}$ and can be expressed as

$$\mathbf{t}_j = \mathbf{L}_j\boldsymbol{\alpha}_j. \tag{3.74}$$

The dipole moment $\boldsymbol{\alpha}_j$ is usually not known which leads to the three different applications of the proposed methodology as introduced in the following.

3.3.2. Wedge Music Scan

The first approach based on the observation in the previous sections is to optimize over the dipole moment $\boldsymbol{\alpha}_j = (\alpha_{jx}\ \alpha_{jy}\ \alpha_{jz})^\mathsf{T}$ describing the dipole strength in each direction in the three-dimensional Cartesian coordinate space. Assuming a given topography $\mathbf{t}_k$ originated from a prior source reconstruction technique at voxel k, e.g. from SC Music (see Section 3.2), the measure of interaction between two sources at voxels k and j is defined as

$$h_{k,j} = \frac{g_{k,j}(\mathbf{0})}{min_{\boldsymbol{\alpha}}\ g_{k,j}(\boldsymbol{\alpha}_j)}. \tag{3.75}$$

Please note that the function g introduced in Eq.(3.73) now depends on the three dimensional dipole moments that is determined by minimizing g with respect to $\boldsymbol{\alpha}_j$. The interaction measure h described in Eq.(3.75) quantifies the decrease of rank of the matrix $\hat{\mathbf{E}}_p$. The term $g_{k,j}(\mathbf{0})$ in the numerator implies no assumed synchronization between sources at voxels k and j. In contrast to that, the denominator denotes a synchronization for the best possible dipole moment at j. Hence, the ratio measures the strenght of the synchronization between sources a k and j. If it is perfectly contained in the ImCs, the denominator in Eq.(3.75) will be close to zero, leading to a large value of h, in fact tending towards infinity.

The measure h defined in Eq.(3.75) can be evaluated over all voxels $j = 1 \dots M$ which leads to a scan over the entire brain space in order to investigate with which source another source with topography $\mathbf{t}_k$ is interacting by means of phase synchronization robust to volume conduction effects. A source at k is termed a seed voxel or reference voxel in the following as a scan is executed to determine an interaction with respect to this reference voxel. Due to the analogy of a brain scan and the application of subspaces, this method is subjoined to the family of Music algorithms. Including the wedge product as derived in Eq.(3.71), it is termed Wedge Music (WM). In particular, this variant with a given reference voxel and the optimization over the dipole moment is termed a Wedge Music scan.

3.3.3. Scalar Wedge Music

The second possible variant of applying Wedge Music is to determine the interaction between two given source topographies or two sources with known dipole directions and locations. These could again be identified by a prior source localization technique. Consider a given set of brain sources at a certain frequency or frequency band, the question arises 'Which source is interacting with which?' in a bivariate sense. A conceivable scenario would, for example, be a system consisting of two interacting source pairs. Here, only the relative strength between the two topographies $\mathbf{t}_k$ and $\mathbf{t}_j$ matters, i.e. if a source with given dipole direction is stronger with respect to the other. This can be expressed by single number $\hat{\alpha}$ which leads to a slightly different

product of singular values

$$\hat{g}_{k,j}(\hat{\alpha}) = \prod_{l=1}^{p} SV_l(\mathbf{E}_p - \hat{\alpha}(\mathbf{t}_k\mathbf{t}_j^\mathsf{T} - \mathbf{t}_j\mathbf{t}_k^\mathsf{T})), \tag{3.76}$$

and, finally, to the interaction measure termed scalar Wedge Music (scWM) that can be expressed by

$$\hat{h}_{k,j} = \frac{\hat{g}_{k,j}(0)}{min_{\hat{\alpha}}\ \hat{g}_{k,j}(\hat{\alpha})}. \tag{3.77}$$

3.3.4. Complete Wedge Music

The third variant of Wedge Music works without any prior knowledge or prior source localization algorithm to obtain reference voxels. On the contrary, a scan over all *pairs* of voxels k and j is executed. In this case the dipole orientations $\boldsymbol{\alpha}_k \in \mathbb{R}^{3\times1}$ and $\boldsymbol{\beta}_j \in \mathbb{R}^{3\times1}$ for both topographies $\mathbf{t}_k = \mathbf{L}_k\boldsymbol{\alpha}_k$ and $\mathbf{t}_j = \mathbf{L}_j\boldsymbol{\beta}_j$ are unknown. This can again be solved with the optimization introduced before. Although intuitively 6 parameters would have to be optimized, namely the dipole strength in x-, y- and z-direction, the absolute strength of the individual topographies is irrelevant for the present calculations. Therefore, the optimization can be expressed by only 5 variables, e.g. in polar coordinates. This variation is termed complete Wedge Music in the following.

3.4. Surrogate data

A suitable approach to statistically test the connectivity measures proposed in this thesis are resampling methods as introduced in Section 2.5.2. However, as most measures are positively biased they cannot be tested according to the null hypothesis stating that a measure is zero in the absence of any interaction. Therefore, a novel approach is proposed here to test the connectivity measures against the values obtained from surrogate data. The surrogate data is constructed such that source interactions present in the data are destroyed but other data properties are maintained. This will give an estimate of the positive bias of the individual methods. If a value of a connectivity measure obtained for the real data is significantly larger than the value obtained from the surrogate data, one can conclude that a significant interaction is present. The idea of surrogate data has been used before. For example Theiler et al. (1992) suggested surrogate data to test for non-linearity. One approach to construct the surrogate data is the random generation of the phases of the Fourier coefficients of the data. Furthermore, Breakspear et al. (2003) discussed an alternative based on resampling the wavelet coefficients of the data. Because randomly generating Fourier phases or wavelet coefficients would destroy all synchronization in terms of coherency it does not maintain the data properties with respect to volume conduction. Due to volume conduction, recorded data on sensor level would still be coherent although no true interaction between sources

is present. Therefore, a different approach is introduced in the following, initially published as joint work in Shahbazi et al. (2010).

In order to construct surrogate data from real measured EEG or MEG data where all phase synchronization between brain sources is destroyed as far as possible, a three-step procedure is employed that is described in the following.

3.4.1. Statistical independence between neuronal components

As a first step, an ICA (see Section 2.3.1) is used to construct time series that are minimally dependent. Considering the linear source mixing model introduced in Section 2.2.2, the time-dependent EEG/MEG data $\mathbf{x}(t) = (x_1(t), \ldots, x_N(t))^\mathsf{T} \in \mathbb{R}^{N\times 1}$ in N channels can be decomposed into N time series

$$\mathbf{s}(t) = \mathbf{W}\,\mathbf{x}(t) \tag{3.78}$$

where $\mathbf{W} \in \mathbb{R}^{N\times N}$ is an estimate of the demixing matrix obtained from the ICA algorithm. As a particular ICA implementation, TdSEP (see Section 2.3.1) will be used in the following (Ziehe and Müller, 1998), although in principle all ICA implementations are conceivable. Some words on practical considerations: To assure that dependency between components of neuronal activity is minimized it seems to be reasonable to, again, reduce the dimensionality of the data. Especially, in the case of many measurement sensors (e.g. $N \approx 250$ for MEG) the ICA is more likely to fail in finding true statistically independent components due to many different noise components with low power. Here, it is not the aim to identify and separate noise components but to minimize dependency between brain sources. Therefore, a dimensionality reduction prior to the ICA helps to focus on dominant brain sources and, hence, to diminish dependency among them. Reducing the dimensionality can be achieved by a PCA decomposition of the covariance matrix of the data estimated by $\Sigma = \mathbf{X}\mathbf{X}^\mathsf{T} \in \mathbb{R}^{N\times N}$ where $\mathbf{X} \in \mathbb{R}^{N\times T}$ is the data over all samples T. This gives

$$\mathbf{\Sigma} = \mathbf{U}\mathbf{\Lambda}\mathbf{U}^\mathsf{T}, \tag{3.79}$$

where the first Q columns of $\mathbf{U}$ are the Q eigenvectors belonging to the Q largest eigenvalues. Summarizing these eigenvectors or principle components in the matrix $\hat{\mathbf{U}}_Q = (\mathbf{u}_0 \ldots \mathbf{u}_Q) \in \mathbb{R}^{N\times Q}$, the ICA decomposition now reads

$$\hat{\mathbf{s}}(t) = \hat{\mathbf{W}}\,\hat{\mathbf{U}}_Q^\mathsf{T}\mathbf{x}(t), \tag{3.80}$$

with the ICA demixing matrix $\hat{\mathbf{W}}$ being of size $Q \times Q$ and $\hat{\mathbf{s}}(t) = (\hat{s}_1(t), \ldots, \hat{s}_Q(t))^\mathsf{T} \in \mathbb{R}^{Q\times 1}$ being the surrogate data in ICA space. Please note that the choice of Q is not crucial in the present setting in contrast to the reduction of dimensionality for SC Music or Wedge Music, where the subspace dimension corresponds to the number of sources that are assumed to be present in the data. As a side effect, a prior PCA massively reduces the computation time for large data sets in space and time.

As a second useful preprocessing step before the actual ICA decomposition, the data should be filtered. According to the $1/f$ nature of the spectrum of EEG/MEG

data in a logarithmic scale (see e.g. Pritchard, 1992), low frequency components (e.g. below 1 Hz) contain much signal power. Therefore, the ICA is heavily confound by these dominating low frequency components which are not reflecting brain sources at frequencies of interest. For example, to investigate source activity in the alpha band (8-13 Hz) a broad range band-pass filter between 4 and 45 Hz seems reasonable. Using a broad band filter is also a necessary requirement for the TdSEP algorithm in this scenario. Because TdSEP is based on covariance matrices constructed by introducing multiple time lags, very narrow filter frequencies would hamper the identification of statistically independent components with TdSEP.

3.4.2. Shifting data segments

The components $\hat{\mathbf{s}}(t) = (\hat{s}_1(t), \ldots, \hat{s}_Q(t))^\mathsf{T} \in \mathbb{R}^{Q\times 1}$ have been constructed by an ICA to be statistically independent from each other. However, in practice, independence is only maximized and the resulting components still exhibit small but non neglectable relationships. Details depend on the distinct ICA algorithm applied. Therefore, an additional step is performed to eliminate remaining dependencies. The individual ICA components are shifted in time with different delays for each component. Please note that coherency and other connectivity measures are evaluated over many epochs, i.e. experimental trials. Assuming that these trials are statistically independent, any dependency between the shifted time series will be removed. In fact, the dependency is not destroyed but put out of reach for the connectivity measure.

Shifting the k-th out of Q components can be formulated as

$$\tilde{s}_j(t) = \hat{s}_j\,(t + (j-1)\tau) \tag{3.81}$$

with τ being a time delay that is constant for all components. One can observe that each component j is shifted with a different delay than component $k = 1 \ldots Q; k \neq j$. An example: If $\tau = 1$ second, which, let's say, corresponds to the length of one epoch, the first ICA component will not be shifted, the second by one epoch, the third by two epochs and so on. As a requirement, the number of epochs η has to be larger than the number of principle components Q (for τ having the length of a single epoch). Otherwise the shifting described in Eq.(3.81) would lead to the same shifting for $\tilde{s}_1$ and for $\tilde{s}_{\eta+1}$.

3.4.3. Backprojection to sensor space

Having established maximally independent time series $\tilde{\mathbf{s}} = (\tilde{s}_1(t), \ldots, \tilde{s}_Q(t))^\mathsf{T}$ in the ICA space, these data has to be projected back to sensor space in order to obtain a surrogate data representation that can be compared to measured data $\mathbf{x}$. This is achieved by applying the mixing matrix estimated with the ICA algorithm $\hat{\mathbf{W}}^{-1} \in \mathbb{R}^{Q\times Q}$ (see Section 3.4.1), which leads to

$$\tilde{\mathbf{x}}(t) = \hat{\mathbf{U}}_Q \;\; \hat{\mathbf{W}}^{-1}\, \tilde{\mathbf{s}}(t). \tag{3.82}$$

Now, $\tilde{\mathbf{x}}(t)$ in Eq.(3.82) denotes sensor data assured that all source interaction present in the real data $\mathbf{x}(t)$ has been destroyed or at least minimized.

Comparing the statistical properties of the real data $\mathbf{x}(t)$ and the surrogate data $\tilde{\mathbf{x}}(t)$, one can observe that mean and variance are preserved. Neither ICA nor shifting the data epochs influence mean or variance. It might be argued that the variance of surrogate data is reduced due to rejected $N - Q$ components with the PCA decomposition. However, as will be shown by investigating singular values of MEG resting state data in Section 5.2.1, principle components with small singular values barely contain any signal power. Hence, the power spectrum in each channel is also retained.

4. Simulations

> All theories are legitimate, no matter. What matters is what you do with them.
>
> *(Jorge Luis Borges)*

A fundamental problem for the development of new methods in the context neuroscientific research is the lack of a ground truth. Compared to other signal processing or machine learning fields such as e.g. acoustics or image analysis, it is difficult to judge the validity of results. Source reconstruction on EEG or MEG data always leads to a result. But even with appropriate statistics applied, it is hard to make serious inferences, especially by employing a novel methodology. Therefore, it is crucial to evaluate the behavior of new methods in simulations. Here, the ground truth is known. In the current chapter, different aspects of the methods introduced before are investigated in various simulations. Furthermore, the results are compared to existing methods.

4.1. Modeling EEG data with underlying interacting sources

Many of the simulations carried out in the following share constant properties such as sensor set, head model and leadfields but also the underlying source dynamics. Therefore, the modeling procedure is described in the following exemplary for four brain sources consisting of two interacting pairs. Only individual differences in the modeling procedure will be pointed out in the respective section.

Simulations are treated as EEG recordings with an electrode set of 56 channels according to the standardized 10-20 system. The standardized MNI head consisting of 152 averaged brains is used as a head model (Fonov et al., 2011). This MNI brain is parceled into a continuous grid consisting out of 2113 voxels. Leadfields are generated as described in Nolte and Dassios (2005). Four different dipolar sources are modeled inside the brain as depicted in Figure 4.1.A. These are located in a common plane for illustrative purposes. This way, only a single MRI slice has to be displayed. The four sources are divided into two pairs. The two sources of each pair are modeled to be synchronized. The dynamics of a bivariate underlying neuronal system is constructed according to an autoregressive (AR) model. An AR model at time point $t = 1 \dots T$ for the data vector $\mathbf{x} = (x_1 \dots x_O)^\mathsf{T}$ with O (here $O = 2$) time series is defined as

$$\mathbf{x}(t) = \mathbf{A}^{(0)} + \sum_{j=1}^{\rho-1} \mathbf{A}^{(j)} \mathbf{x}(t-j) + \boldsymbol{\eta}(t) \tag{4.1}$$

where the ρ matrices $A^{(j)} \in \mathbb{R}^{O\times O}, j = 0 \dots \rho - 1$ contain the so called AR coefficients which primarily determine the behavior of the system. One can observe from Eq.(4.1) that the values of $\mathbf{x}(t)$ depend on past values of $\mathbf{x}(t)$, namely $\mathbf{x}(t-1)$ up to the model order $\mathbf{x}(t-\rho+1)$. Furthermore, the off-diagonal elements of the AR matrices determine the dependencies between the O different time series included in $\mathbf{x}$. Additionally, a so called innovation term $\boldsymbol{\eta}(t) \in \mathbb{R}^{O\times 1}$ is included in the model which drives the system. In this particular simulation, white Gaussian noise with zero mean and unit variance is used. Furthermore, for each pair of sources an AR-model with the following non-zero coefficients is defined: $a_{11}^{(1)} = 0.45, a_{22}^{(1)} = 0.45, a_{22}^{(2)} = -0.9, a_{21}^{(2)} = 1, a_{11}^{(4)} = -0.65$. From the coefficients one can observe that a single non-diagonal element is non-zero which indicates a connection between the two sources. Coefficients have been chosen to achieve a system behavior close to EEG/MEG signals, i.e. an oscillatory signal with a peak in the alpha range. Additional noise is modeled on source level as Gaussian white noise for each brain voxel and projected to the scalp resulting in realistically correlated noise on sensor level. Please note that the frequency characteristic of the noise does not have an important impact on the later analysis procedure as the analysis is carried out at a distinct single frequency or a narrow band. Data and noise were normalized by their respective power (maximum channel power at peak frequency) and summed with a fixed signal-to-noise ratio of $SNR = \sqrt{10}$. As well as the AR coefficients, the SNR is selected such that the modeled data reflect known data properties of EEG data. Figure 4.1.B shows the imaginary part of coherency between all pairs of sensors over frequency in a so called butterfly plot. The average noise level of approximately 0.1 and the value of the ImCoh at the peak frequency at 11 Hz of approximately 0.3 are in line with what often can be observed in real EEG or MEG data. Therefore, a reasonable noise level is modeled by applying the parameters described. The prominent signal peak at 11 Hz is picked as a frequency of interest for further calculations by an automated selection process based on the GIM (see Section 3.1.3). The GIM is optimized for its signal-to-noise ratio over frequency as follows: For each frequency bin f a noise level $G_n(f) = \frac{1}{2}\left(\mathrm{GIM}(f+\delta f) + \mathrm{GIM}(f-\delta f)\right)$ and a pseudo-signal $G_s(f) = \mathrm{GIM}(f) - G_n(f)$ are estimated. Finally, the ratio

$$\frac{G_s(f)}{G_n(f)} = \frac{\mathrm{GIM}(f) - \frac{1}{2}\left(\mathrm{GIM}(f+\delta f) + \mathrm{GIM}(f-\delta f)\right)}{\frac{1}{2}\left(\mathrm{GIM}(f+\delta f) + \mathrm{GIM}(f-\delta f)\right)} := G(f) \tag{4.2}$$

is computed to identify frequencies with strongly synchronized signals. This measure $G(f)$ is also displayed in Subfigure 4.1.B pointing to a strong peak at 11 Hz. δf is chosen to be 3 Hz and the frequency with the largest $G(f)$ in the alpha band ($8-15$ Hz) is selected for further processing.

Figure 4.1.C depicts the connection topography of the underlying neuronal system at 11 Hz in a so called head-in-head plot. The head-in-head plot shows the ImCoh for each sensor with respect to all other sensors. The big circle represents the scalp with the nose on top indicated by a little triangle. Each small circle depicts one measurement sensor at its respective position on the scalp. Within the little circles

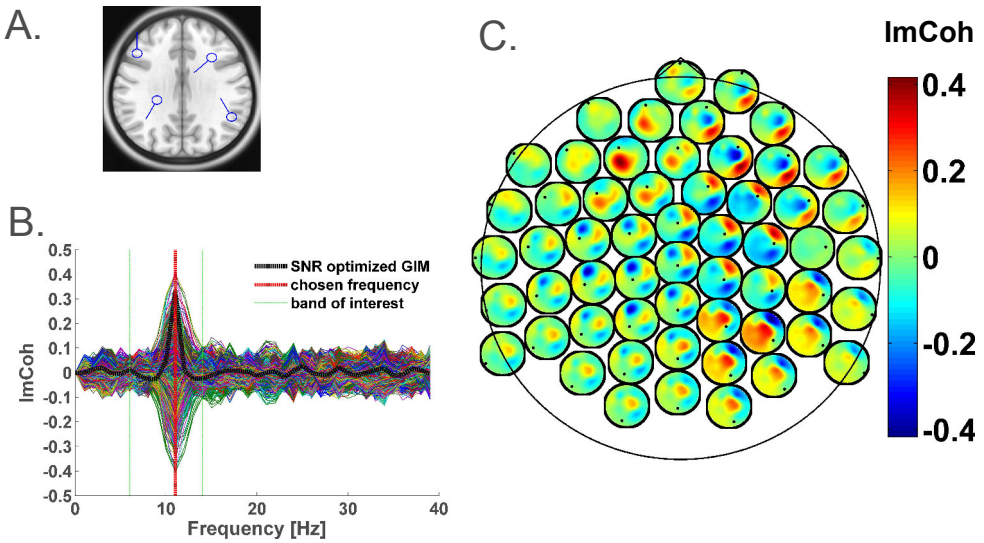

Figure 4.1.: Simulated data. A.: Modeled dipoles and their interaction profile. Two synchronized, i.e. interacting sources in each hemisphere. There exist a connection between sources within but not across hemispheres. B.: The imaginary part of coherency for all 56×56 sensor pairs and the SNR optimized GIM. C.: The imaginary part of coherency on sensor level at 11 Hz. Each small circle represents the connection (ImCoh) of a particular measurement channel to all other measurement channels.

the connections to all other sensors are color-coded. For the sake of orientation, a dot inside a small circle again represents the position of the reference sensor on the scalp. However, the modeled neuronal sources and their respective dynamics cannot be clearly recovered by visualizing the ImCoh on sensor level. This example illustrates even more the need for methods making the transition to source space for investigating neuronal interactions.

4.2. Properties of MIC, GIM, MIM and cImCoh

In the following, properties of the connectivity measures presented in Section 3.1 such as the Maximized Imaginary Coherency (MIC), the Global Interaction Measure (GIM), and the Corrected Imaginary Part Of Coherency (cImCoh) are analyzed in details. Some of the simulations correspond to results presented in Ewald et al. (2012).

4.2.1. Overfitting and bias

First of all, the effect of overfitting of the GIM, as theoretically described in Section 3.1.6, is demonstrated on simulated white noise. Complex independent and identically distributed (i.i.d.) Gaussian data were generated for $N = 100$ channels. These data then have been projected onto a $P-$dimensional subspace and cross-spectra were calculated for a different number of trials, i.e. $K = 50, 100, 150, 200$. For each K and P, 100 different data sets were simulated and the Maximized Imaginary

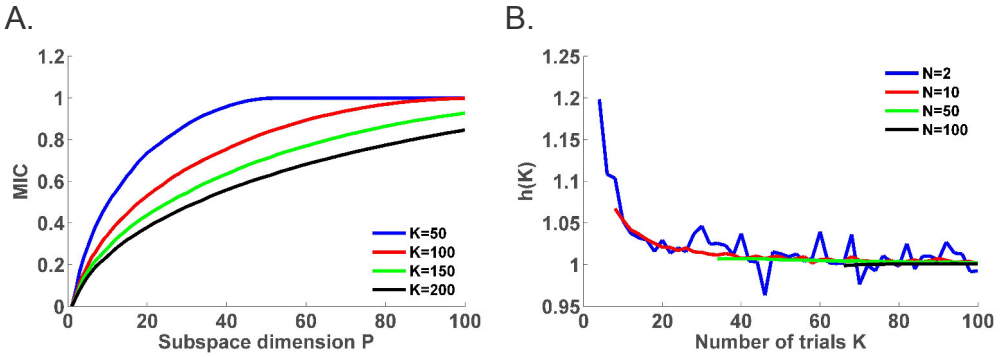

Figure 4.2.: Overfitting of MIC and Bias of GIM. A. The MIC for white noise data for different number of channels N and trials K. B. The validity of the analytical approximation of the bias for the GIM.

Coherency (MIC) according to Eq.(3.8) was averaged over these data sets. The results are shown in Figure 4.2.A. One can observe substantial positive values, especially for few trials and large subspace dimensions, although no source synchronization is present in the data.

Related to this is the bias occurring in GIM for finite data sets. An analytic approximation of the bias has been presented in Section 3.1.7. To test the accuracy of this approximation, again i.i.d. complex Gaussian noise for K trials for various number of channels N has been generated. For each K and N, the GIM of 100,000 data sets was averaged. Denoting this average as $\overline{GIM}$, the ratio of this average and the bias approximation $bias_{GIM}$ (defined in Eq.(3.42))

$$h(K,N) = \frac{\overline{GIM}}{bias_{GIM}}. \tag{4.3}$$

is presented Figure 4.2.B. Please note that in order to calculate the GIM, the real part of the cross-spectrum has to be inverted, which becomes singular if the number of trials is less than half the number of the channels[1]. Therefore, only results $K \geq N/2$ are shown. One can observe that for a reasonable number of trials the approximation is excellent and approaches the value '1'. Only for a very few number of trials the bias is slightly underestimated. One can also observe that for only two channels the variance of the bias estimate is noticeable even after 100,000 averages.

4.2.2. Comparison of GIM and ImCoh

A further simulation addresses the question how the measures depend on the forward mapping when there are more sources than sensors. In this case the forward mapping cannot be inverted by a linear transformation in sensor space and also the invariant measures presented in Chapter 3.1 will show dependence on

[1] For each trial the rank increases by two because the data are complex and both the real and the imaginary parts of the Fourier transformed data contribute to the real part of the cross-spectrum.

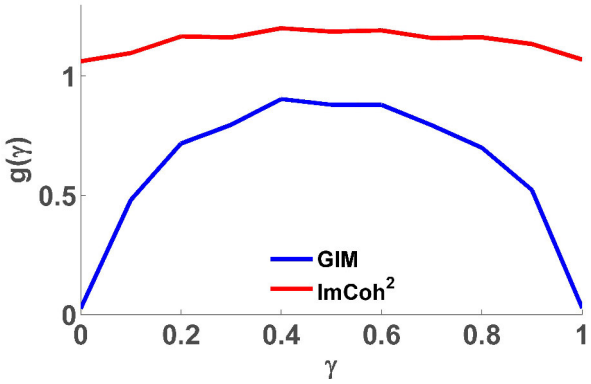

Figure 4.3.: Dependence on forward mapping of GIM and ImCoh^2

forward mapping. The goal of the simulation outlined below, is to analyze how the connectivity measures vary with varying forward mapping for fixed, but randomly chosen source configurations. A single data set in source space was constructed as two pairs of interacting sources, for each pair using a bivariate 4^{th} order AR model with random parameters. The two bivariate data sets in source space are denoted as $\mathbf{X}$ and $\mathbf{Y}$, respectively, with $\mathbf{X}$ and $\mathbf{Y}$ being $2 \times N$ matrices for $N = 1000$ data points. The data in two-dimensional channel space was constructed according to

$$\mathbf{Z} = \gamma \frac{\mathbf{AX}}{\|\mathbf{AX}\|_{\mathrm{F}}} + (1-\gamma)\frac{\mathbf{BY}}{\|\mathbf{BY}\|_{\mathrm{F}}} \tag{4.4}$$

with $\mathbf{A}$ and $\mathbf{B}$ being random 2×2 matrices, $\|.\|_{\mathrm{F}}$ being the Frobenius norm, and γ being the parameter which controls the relative strength of the two pairs. For each $\mathbf{X}$ and $\mathbf{Y}$, $\mathbf{Z}$ was calculated for 50 different random matrices $\mathbf{A}$ and $\mathbf{B}$. To calculate the cross-spectra, the data were divided into 100 trials of 10 data points each, Hanning windowed, and Fourier transformed. Cross-spectra were calculated at the third (out of five) frequency bins. For each $\mathbf{Z}$, ImCoh^2 and GIM were calculated and for all 50 random forward matrices, the mean and standard deviation of each measure. Finally, the ratio of standard deviation and mean for each measure was obtained. For each γ, the ratio was averaged across the 200 different source configurations. The average is denoted as $g(\gamma)$.

Results are shown in Figure 4.3. In the case of $\gamma = 0$ or $\gamma = 1$ only one source pair is mapped into the sensors and hence, the number of sources is equal to the number of sensors. In this case GIM, in contrast to ImCoh, shows no variation as expected. Quite generally, GIM is more robust to varying forward mappings than ImCoh. However, the advantage is minor if approximately equally strong sources are mixed, i.e. $\gamma \approx 0.5$.

4.2.3. Spatial bias of the ImCoh

To compare the ImCoh and the *corrected* imaginary part of coherency (cImCoh) as defined in Eq.(3.21), two sources have been modeled according to an AR-model with additive brain noise as described in Section 4.1. The two sources that are depicted in Figure 4.4.A were projected to EEG sensor space for $N = 56$ sensors and ImCoh and cImCoh were evaluated for each pair of sensors. Figure 4.4.B shows the ImCoh for each sensor pair over frequency. At the peak at 11 Hz, ImCoh and cImCoh are visualized as a head-in-head plot in Figure 4.4.C, and Figure 4.4.D respectively. For illustrative purposes the sensor Cz is magnified.

Comparing the plots for ImCoh and cImCoh, one can observe a spatial bias towards remote interactions for the ImCoh. In the vicinity of the reference sensor no interactions are indicated although the modeled sources are quite close to each other. This spatial bias is diminished in the cImCoh. One can quantify this effect by summing the distances from the sensor Cz to the two sensors with maximum and minimum score for cImCoh and ImCoh respectively. For ImCoh this summed distance is 0.63 cm and for cImCoh it is 0.36 cm. Hence, the cImCoh has a smaller spatial bias. The mean of the summed distances over all sensors is 0.97 cm for cImcoh and 1.26 cm for ImCoh.

A second point that can be emphasized with this simulations is the need for source space connectivity analysis. Even for two single sources, the sensor level representation does not provide a clear picture about the underlying source connectivity.

4.3. Subspace construction for SC and Wedge Music

In Sections 3.2 and 3.3 methods have been introduced which are based on a subspace of the imaginary part of the cross-spectrum. Furthermore, two ways of constructing a suitable subspace have been described in Section 3.2.1. One is based on a singular value decomposition of the ImCs. The other is based on the maximization of the imaginary part of coherency (see Section 3.1.1) and includes a prewhitening of the ImCs. In the following, both are compared.

Two interacting sources, one located in each hemisphere, were modeled as described in Section 4.1. The simulation was repeated for a signal-to-noise ratio ranging from 0.15 to 2 in steps of 0.005 and for both ways of subspace construction. Then, an SC Music scan for the two sources was executed. The sources were sorted according to the minimum Euclidean distance between the maximum voxel and the original modeled dipoles. Finally, the Earth Mover's Distance (EMD, see Section 2.6) between each SC Music result and the original dipole was calculated to obtain a localization error. This error was averaged over the two sources. The same simulation was performed for Wedge Music.

The results are shown in Figure 4.5. Subfigure A. shows a scatter plot in order to compare the two approaches of subspace generation for SC Music. One can observe that especially for larger errors (> 5cm), which occur due to a low SNR, the error is in most simulation runs smaller for the subspace based on the maximization

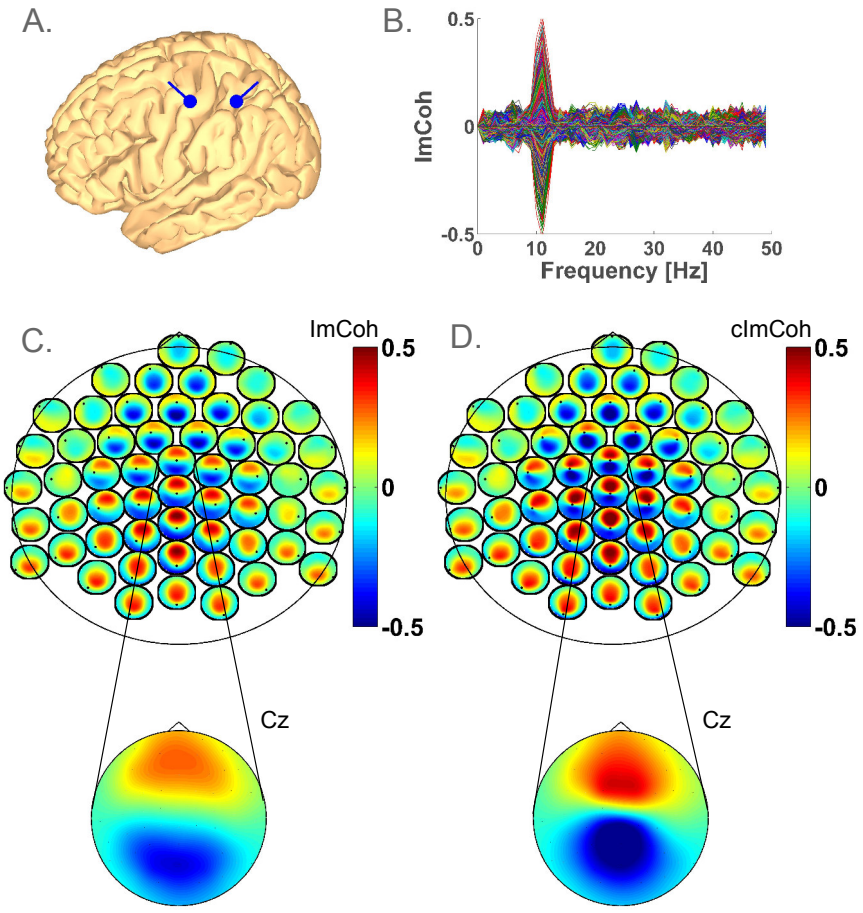

Figure 4.4.: Comparison of ImCoh and cImCoh. A.: Two modeled dipoles. B.: ImCoh for all pairs of sensors over frequency. C.: ImCoh as a head-in-head plot at 11 Hz. For each EEG measurement sensor, the ImCoh to each other sensor is displayed. The ImCoh for electrode Cz with respect to all other measurement sensors is magnified. D. Same representation for cImCoh at 11 Hz.

of the ImCoh (MaxImCoh) than for the subspace constructed by a singular value decomposition of the ImCs (SVD(ImCS)). This is also indicated by the red cross in Figure 4.5.A, which denotes the average and lies slightly below the diagonal line. The mean EMD error for all runs was 4.62 cm for SVD(ImCS) and 4.54 cm for MaxImCoh. Figure 4.5.B shows the smoothed EMD localization error with respect to the SNR for both ways of subspace generation. Here, one can again see that the error is smaller for MaxImCoh.

Whereas for SC Music the subspace construction based on MaxImCoh seems to improve the localization performance, it does not make a difference for Wedge Music as shown in Figure 4.5.C. The mean EMD error for both ways of subspace construction was 5.78 cm. A potential reason that the subspace construction rather matters for SC Music than for Wedge Music, is the optimization included in Wedge

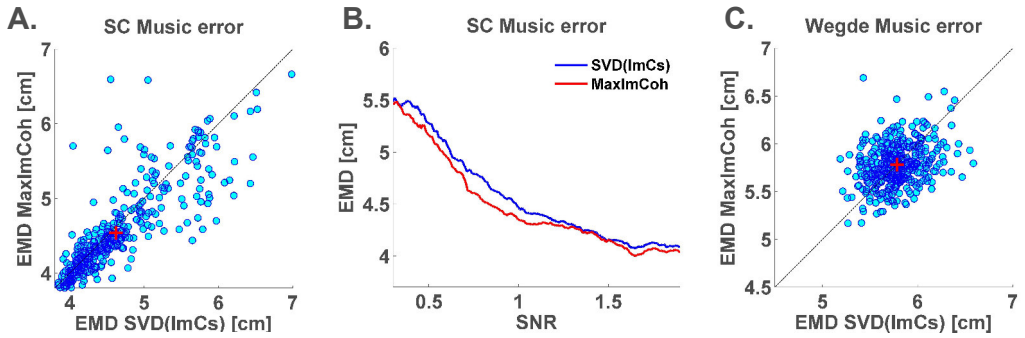

Figure 4.5.: Subspace construction for SC and Wedge Music. Two possibilities of constructing subspaces for SC and Wedge Music are compared for two interacting sources with different levels of brain noise. One way of subspace construction is based on the maximization of the ImCoh (MaxImCoh) and the other one on a singular value decomposition of the ImCs (SVD(ImCs)). Both are described in details in Section 3.2.1. A: Source localization errors in terms of the Earth Mover's Distance (EMD) for SC Music are displayed as a scatter plot. B: The smoothed EMD errors over the SNR C: EMD errors as a scatter plot for Wedge Music.

Music (see Section 3.3.3). As the dipole direction at each voxel is adopted to be most consistent to the data subspace, the final result seems to be less dependent on the individual data representation as long as the interacting source pair is still included in the data space.

Please note that the overall EMD localization error within this simulation is rather large (around 4 to 6 cm). This, however, is a consequence of using the EMD as an error measure and of simulating brain noise in a realistic fashion. Since the spatial source distribution is taken into account by the EMD and EEG/MEG inverse solution are rather blurry in general, high EMD error terms are likely to occur.

As a consequence arising from the simulation presented above, the subspace construction based on the maximization of the imaginary part of coherency as described in Section 3.2.1 will be used for all computations in the following.

4.4. Comparision of Rap and SC Music

SC Music, as introduced in Section 3.2, can be seen as an algorithmic improvement over Rap Music. The advantages, especially in the context of statistically dependent sources, have already been pointed out. In following, the drawbacks of Rap Music are demonstrated in different simulation scenarios. Furthermore, Rap Music and SC Music are directly compared for identically simulated data.

4.4.1. Visualization of Music source scans

As described in Sections 2.3.3 and 3.2.3, the family of Music source reconstruction methods including Music, Rap Music and SC Music, determine the principle angle ϑ between a potential source at a particular voxel and a data subspace. A small angle ϑ for a grid point can then be interpreted as a source. However, to visualize source scans, it is more convenient that a high number instead of a low one represents

a high probability of a source being present at a particular voxel given the data. Therefore, not the angle itself, but the value

$$\Theta(\vartheta) = \frac{1}{1 - \cos^2(\vartheta)} \tag{4.5}$$

is shown for each voxel. Hence, small angles will result in a large number $\Theta(\vartheta)$. These can then be overlaid in a transparent fashion over MRI slices to obtain a picture of source activity inside the brain.

4.4.2. Multiple synchronized source

In the following simulation four dipoles have been modeled. The dynamics of source interactions are as described in Section 4.1. Figure 4.6 shows the localization results for Rap Music (Figure 4.6.A) and SC Music (Figure 4.6.B). Although Rap Music is able to locate the activity of the four sources in the four scans, sources are not being separated well. In each scan except the fourth scan in the lower right corner, the modeled EEG activity is located at two spots simultaneously. The picture differs for SC Music. Here, all four sources are clearly separated in each scan. This is exactly what is theoretically expected and can also be seen by comparing the EMD for this example which is 5.33 cm for SC Music and 6.27 cm for Rap Music. As the localization procedure is influenced by statistically dependent sources at other locations inside the brain, the improvement of SC Music over Rap Music leads to clearly distinguishable sources. This can also be seen by evaluating the localization error in terms of the the Earth Mover's distance. Figure 4.7.A shows the error for four randomly chosen dipoles over 500 runs. The error in terms of the EMD is larger for Rap Music (5.9 cm on average) than for SC Music (5.7 cm on average).

4.4.3. Odd number of sources

The algorithmic advantage of SC Music over Rap Music becomes even more prominent when the number of sources underlying the data is odd. In the present simulation, three dipolar sources are modeled at locations as shown in Figure 4.7.B. The two sources in the left hemisphere are modeled according to the AR model described in Section 4.1. The third source, located in the right hemisphere, corresponds to the time series of the first source but delayed by two samples and with additive noise (SNR=0.9). Figure 4.7.B shows the localization of all three sources with Rap and SC Music. It is obvious that, in contrast to SC Music, Rap Music is not able to separate the three sources properly. This is due to the subspace rank deficiency resulting from an odd number of sources as explained in Section 3.2.3.

4.5. The number of sources

In the present simulation the estimation of the number of sources which is described in Section 3.2.2 is demonstrated. Two interacting source pairs are modeled as

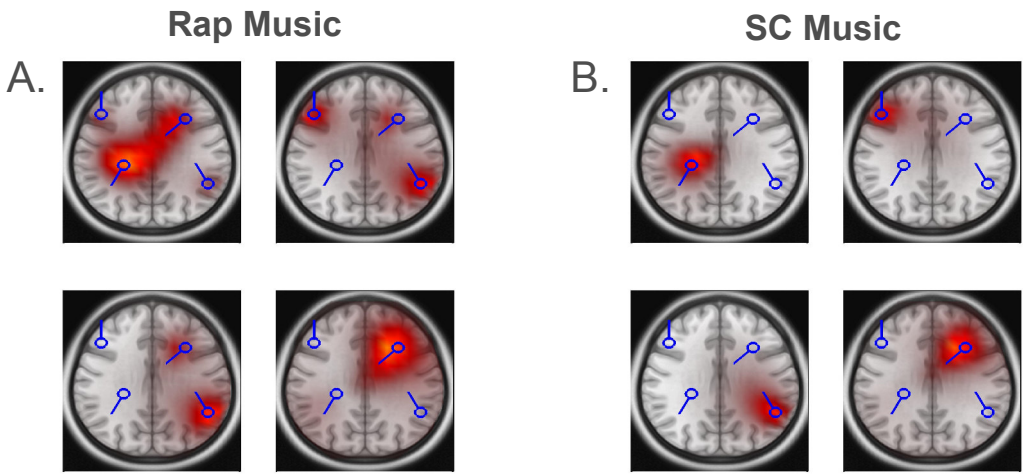

Figure 4.6.: Comparison of Rap and SC Music for 4 modeled sources and 4 resulting scans. The modeled dipoles are shown in blue. The Rap and SC Music scans are color-coded. As the individual color intensities do not play a role for the present simulation, color bars are omitted. In contrast to SC Music, Rap Music is not able to separate the synchronized sources in each scan.

described in Section 4.1. Figure 4.8 shows scree plots for the simulated data. The singular values of the ImCs are represented as a black solid line in the left panel. One can observe that the singular values occur in pairs due to the antisymmetric nature of the ImCs. Furthermore, it becomes clear that they rapidly converge towards zero as only four data sources are present. However, it is not clearly possible to distinguish between components with a meaningful signal and noise components from the resulting scree plot. No clear gap between two pairs of singular values is visible. It is hard to judge from the scree plot if the underlying number of sources is two or four or even six. The picture is different in the right panel. There, the singular values of the ImCs prewhitened according to Eq. (3.54) are shown. One can observe a clear drop after four singular values which well indicates the number of underlying sources. However, for real data this drop might not always be visible. Therefore, a second criteria based on surrogate data is employed to conclude on the number of sources. In Section 3.4, a method is described how to destroy interactions present in data but to preserve all other data properties. This is used here to estimate a noise level for the singular values. The magenta colored curves in Figure 4.8 show the singular values for the surrogate data, repeatedly calculated in a bootstrap procedure (see Section 2.5.2). As an ICA algorithm to construct the surrogate data, Tdsep (time lag values of $1 \ldots 100$) was used. The time shifting parameter (see Eq. 3.81) was set to $\tau = 100 * 5$ which corresponds to a time shift of 5 epochs as the length of one epoch corresponds to 100 data samples. As stated in Section 3.2.1, 95% of the largest singular value pair in all bootstrap runs is chosen as cut-off rule. This cut-off is indicated by the horizontal line leading to the correct estimate for the number of sources on both cases.

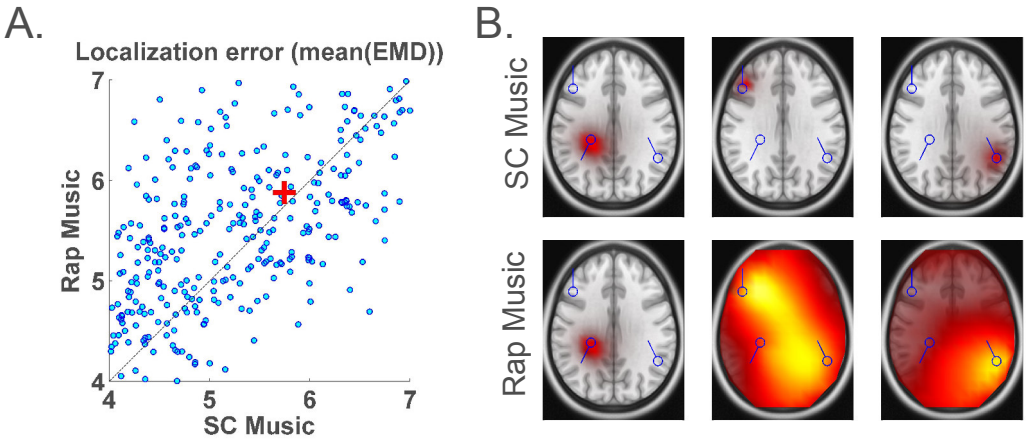

Figure 4.7.: Comparison of Rap and SC Music. A. The mean of the Earth Mover's Distance over the localization error of randomly chosen dipole locations and moments. B. A localization example for three synchronized sources.

4.6. Combining SC and Wedge Music

In the following, the successive application of SC Music and Wedge Music, based on a subspace constructed by prewhitening the ImCs is demonstrated. Although Wedge Music can in principle be applied without any prior source localization, practical considerations suggest the use of an inverse technique to obtain sources first. In a second step, Wedge Music then determines which of the sources are interacting in a pair-wise sense. The application of Wedge Music without using a prior source localization is demonstrated in Section 4.9. The following, examples are based on data simulated for a single experimental condition. For the investigation of class differences, please refer to Section 4.8. Furthermore, it is shown in the current section how statistical inferences concerning the results of the data analysis are made by employing surrogate data.

4.6.1. SC Music and scalar Wedge Music

In the present simulation the use of scalar Wedge Music in combination with SC Music is outlined. Again, four dipolar sources were modeled consisting of two interacting pairs, each in one hemisphere. Figure 4.9.A shows the localization result obtained from SC Music including the originally modeled dipoles. One can see that SC Music is able to recover the sources for the simulated data. To investigate which of the four sources are interacting, scalar Wedge Music is applied for each combination of the four sources. As an input to Wedge Music, the scalp topographies, i.e. the forward model of each source is used. Table 4.1 illustrates the results according to Eq.(3.77) for all source pairs. The actual value and the standard deviations estimated with a bootstrap estimator are shown. First of all, one can observe that all diagonal elements are equal to one (and have zero standard deviation). This is in line with the theory as the optimization over the factor α in Eq.(3.77) cannot not lead to a rank decline of the subspace of the prewhitened ImCs for identical sources. In the

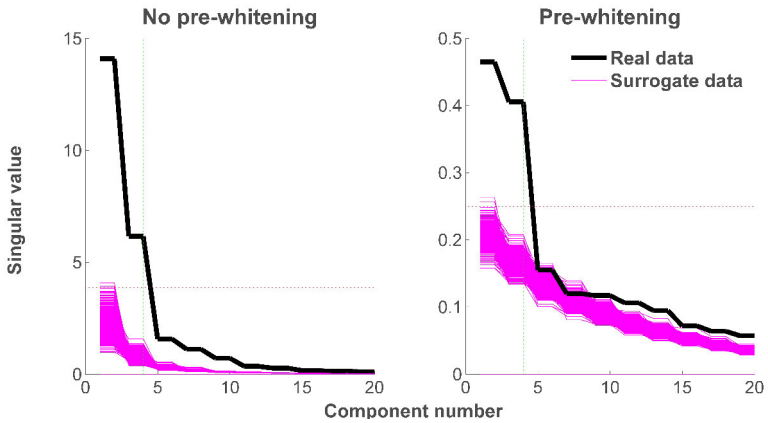

Figure 4.8.: Estimation of the number of sources. In the left panel the singular values of the ImCs are shown as black line. Same representation in the right panel for the ImCs prewhitened according to Eq.(3.54) are shown. Magenta colored lines denote the singular value obtained by a bootrap resampling procedure on surrogate data. 95% of the largest singular value of the surrogate data serves as a noise estimate and, hence, as a cut-off to differentiate noise from data components. This is indicated by a horizontal line in each plot. Finally, the vertical line represents the automatically determined number of sources. In both cases it is correctly estimated.

ideal case, the scalar Wedge Music value for non-interacting sources is expected to be equal to one, too. However, due to limited data and its stochastic and noisy nature, the ideal case is only approximated. Nevertheless, values for the source pairs which are modeled to be synchronized highly differ from the value one, even accounting for the standard deviation. For example, source 4 and source 1 are found to be synchronized and source 2 and source 3, which is exactly how dynamics are modeled.

In an additional simulation the behavior of scalar Wedge Music is tested for random dipoles. This can also be seen as a test for the positive bias of scalar Wedge Music. The results are presented as a histogram in Figure 4.9.B. Most of 10,000 runs revealed a result equal or close to the value one as expected (see left panel of Figure 4.9.B). In the right panel the factor α is shown which is distributed around zero with values ranging up to approximately 50.

Table 4.1.: Results of scalar Wedge Music (scalar Wedge Music score $\hat{h}_{ij}$, see Eq.(3.77)) for all source pairs $i, j = 1 \ldots 4$ and the corresponding standard deviation. The sources and their corresponding labels are shown in Figure 4.9.A

	Source 1	**Source 2**	**Source 3**	**Source 4**
Source 1	1.00	2.10 ± 0.73	1.38 ± 0.55	40.85 ± 8.93
Source 2	2.10 ± 0.73	1.00	25.23 ± 10.68	1.28 ± 0.48
Source 3	1.38 ± 0.55	25.23 ± 10.68	1.00	1.05 ± 0.17
Source 4	40.85 ± 8.93	1.28 ± 0.48	1.05 ± 0.17	1.00

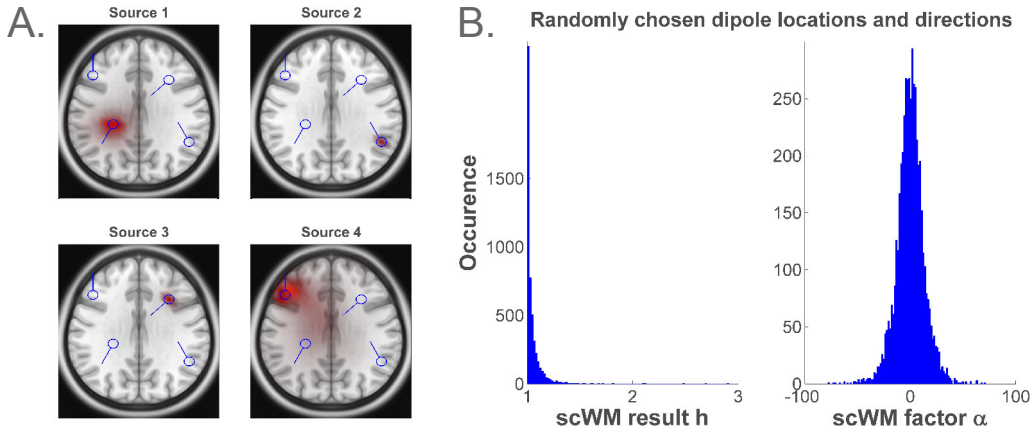

Figure 4.9.: SC Music and scalar Wedge Music. A.: The color coded source distributions obtained by SC Music and the original modeled dipoles. The results for scalar Wedge Music for these sources can be found in Table 4.1; B.: Distribution of scalar Wedge Music result h (see Eq.(3.77)) and factor α (see Eq.(3.75)) for randomly chosen dipoles.

4.6.2. SC Music and a Wedge Music scan

Instead of using scalar Wedge Music, one can also apply a Wedge Music scan to determine which sources from a prior localization are interacting. One advantage is a plausibility check. Given e.g. four SC Music sources and using one of them as a reference, one of the other three sources is supposed to be found by a Wedge Music scan over all grid points. This effect is also demonstrated in the results presented in Figure 4.10. Source dynamics and the four dipoles have been modeled as described in Section 4.1. In the left column of Figure 4.10.A the four sources obtained by SC Music are shown. Each one of the SC Music sources is then used as a reference for a Wedge Music scan. One can see that the four color-coded SC Music sources match the modeled dipoles. Furthermore, the results from each Wedge Music scan again corresponds to one of the modeled dipoles. It is also observable that the dynamics of the simulation are correctly revealed: one interacting source pair in each hemisphere. As indicated before, each source pair shows up twice as each source serves as a reference for the respective other. Here, source pair #3 and source pair #4 are identical as well as source pair #1 and source pair #2. In comparison to the simulation presented in Section 4.6.1 with identical source locations and dynamical properties, one can also observe the arbitrary order of sources (compare SC Music sources in Figure 4.10 and Figure 4.9).

Figure 4.10.B and Figure 4.10.C show the statistics for each Wedge Music and SC Music source. A bootstrap procedure with $r = 500$ runs was employed to estimate the distribution of SC Music and Wedge Music sources. As the resulting order of sources from SC Music is arbitrary, all sources are sorted according to decaying magnitude of the voxel with the maximum SC Music value in each scan. In order to make inferences about the statistical significance of an interacting source pair at two voxels, the result of SC and Wedge Music obtained for the real data at that particular 'maximum' voxel pair is compared against surrogate data. The surrogate data is

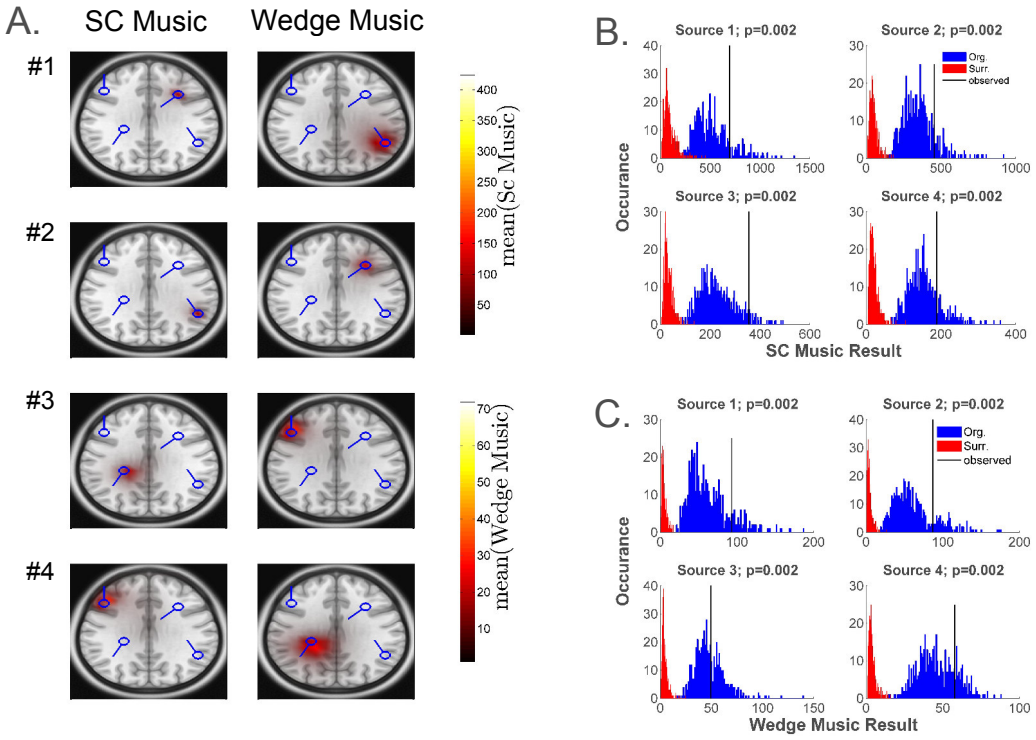

Figure 4.10.: SC Music and Wedge Music scan. A.: SC Music sources in the left column serve as a reference for a Wedge Music scan. The Wedge Music result can be found in the right column. B.: Permutation statistics for all four SC Music sources. Results for the surrogate data subjected to a bootstrap procedure are colored in red. The vertical line indicates the SC Music score (see Eq.(4.5)) of the maximum of each source distribution for the original modeled data which is compared against the surrogate data. The bootstrap results for the original modeled data are shown in blue C.: Same representation as in B. but for the Wedge Music scan. For each source the maximum score of the Wedge Music scan (see Eq.(3.75)) is displayed for the bootstrapped original (blue) and surrogate data (red).

constructed from the modeled data as described in Section 3.4 and preserves all data properties except underlying interactions. Then, a p-value is constructed by counting the number of resampling runs from the bootstrapped surrogate data where the result is larger than the one for the original data (see also Section 2.5). As neither for SC Music nor for Wedge Music a single value from the surrogate data bootstrap runs is larger than the original value, each p-value equals 0.002. Please note that a correction for multiple comparison is implicitly included by employing a maximum statistic (Holmes et al., 1996; Nichols and Holmes, 2002). This can be seen from the fact, that not a distribution of a statistic at a particular voxel is obtained. Instead, a distribution of the maximal voxel statistic over the whole brain volume is calculated.

4.6.3. The influence of a wrong reference source on Wedge Music

An additional simulation is used to evaluate the influence of a mislocated reference source as an input for a Wedge Music scan. The question is how sensitive Wedge Music is to a localization error of a prior source reconstruction. Therefore, the

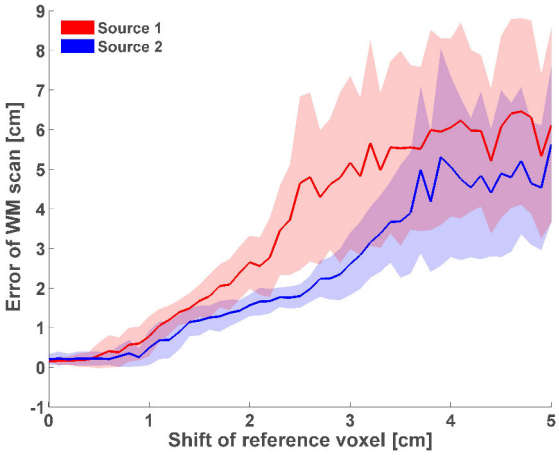

Figure 4.11.: Sensitivity of Wedge Music scan with respect to a misclocated reference source. The localization error (Euclidean distance) of a Wedge Music scan for two sources is shown as a solid line. The transparent areas indicate the standard deviation over 50 runs.

original modeled dipole was used as the reference source and shifted in steps of 0.1 cm in random x-, y- or z-direction. For each shifting step, the whole simulation was repeated 50 times. Figure 4.11 shows the localization error determined by the average Euclidean distance between the true source location and the result obtained by a Wedge Music scan.

The results of the simulation indicate that a mislocated reference source has almost no impact under approximately 1 centimeter. Exceeding this distance, the Wedge Music localization error rises linearly. From around 2.5 cm the standard deviation obtained by the 50 repetitions largely increases. It is clear that no reliable synchronous source can be found when the reference source is wrong. However, due to the poor spatial resolution of EEG/MEG measurements, some source signal is contained not only at a single voxel but also at neighboring ones. Therefore, a slight mislocation of the reference source does not have a huge impact. Furthermore, one can observe from the present simulation that the error does not explode even for a large reference voxel mislocation.

4.7. Combining SC Music, modified beamforming and MIC

The simulation executed for the combination of SC Music and a Wedge Music scan was repeated in the same fashion for the combination of SC Music a modified nulling beamformer and MIC. As theoretically introduced in Section 3.2.4, one can use the sources found by SC Music, first, for a beamformer inverse solution that nulls out activity at all other source locations. This way, scalp activity can be mapped to source space bypassing the inaccuracy of a beamformer in the case of dependent source activity. Second, MIC can be applied in order to scan the brain for coherent activity with each SC Music source as reference. Similar to Wedge Music, this procedure

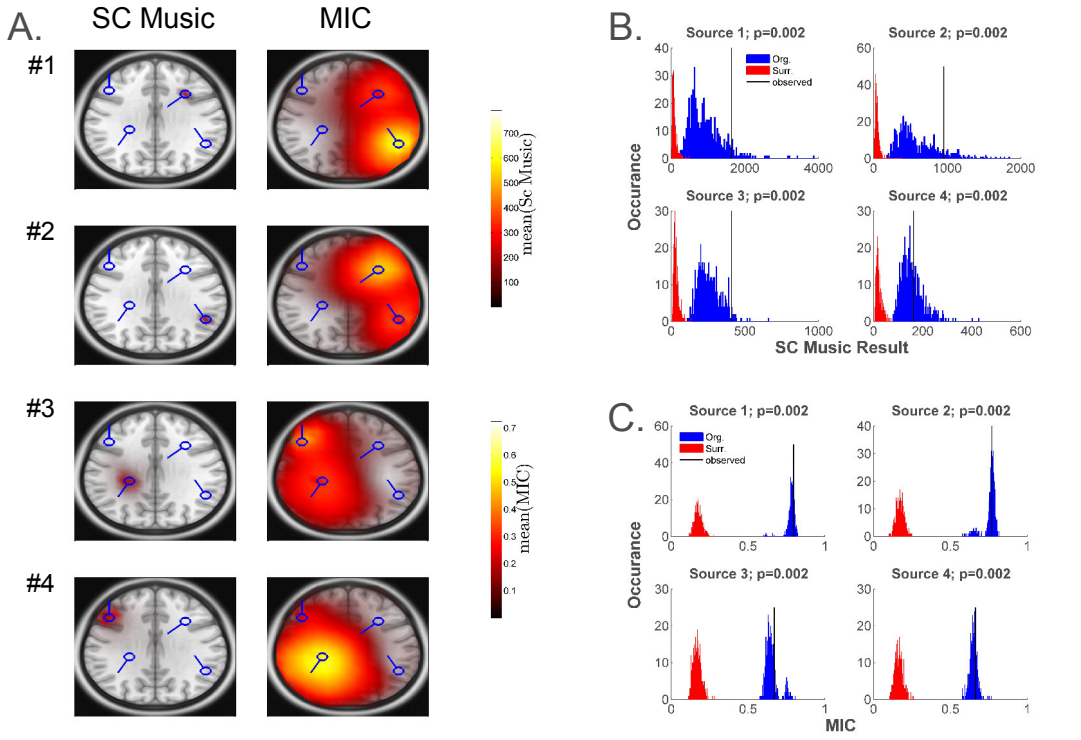

Figure 4.12.: SC Music combined with a modified DICS nulling beamformer and MIC. A.: SC Music sources in the left column are used for nulling beamforming. Furthermore they serve as a reference source for MIC on source level. The interaction profile of each reference source obtained by MIC can be found in the right column. B.: Permutation statistics for all four SC Music sources. The maxima of each source scan for the surrogate data subjected to a bootstrap procedure are colored in red. The vertical line indicates the maximum SC Music score for each source for the original modeled data which is compared against the surrogate data distribution. The bootstrap results for the original modeled data are shown in blue C.: Same representation as in B. but for MIC (see Eq.(3.14)).

investigates the question with which other source a particular SC Music source is interacting.

4.7.1. MIC on source level

Four source dipoles are modeled at the same locations as described before and also the dynamics are modeled in an identical fashion (see Section 4.1). Figure 4.12.A shows the result of the source localization of SC Music in the left column. First of all, one can see that SC Music correctly finds the sources as they are modeled. In the right column of Figure 4.12.A, the result of the MIC in combination with a DICS and a nulling beamformer is shown with each corresponding SC Music source as a reference. Hence, each row in Figure 4.12.A forms an interacting source pair. Clearly, the modeled interactions are revealed by this approach and the correct source locations are discovered. Although the distribution is more widely spread in comparison to the results of Wedge Music, source maxima are at the correct spot. Figures 4.12.B and 4.12.C show statistics for this scenario. Again, the original values

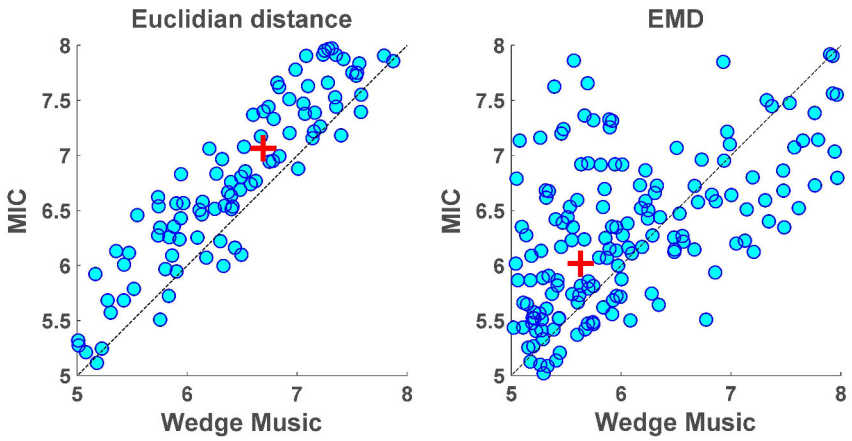

Figure 4.13.: Comparison of Wedge Music and MIC on source level for a single data class. In the left panel the localization error in terms of the Euclidean distance and in the right panel in terms of the the Earth Mover's distance is shown (see Section 2.6).

for SC Music and MIC are tested against surrogate data containing no source level data dependencies in a resampling test. Obviously, the results for SC Music are similar to the ones presented in Section 4.6.2 as the data are modeled in the same fashion (compare Figure 4.10). In addition to that, the result for the MIC on source level is also highly significant for this simulated data set.

4.7.2. Comparison to Wedge Music

As shown in Sections 4.6.2 and 4.7.1, both Wedge Music and MIC combined with a nulling beamformer are capable of uncovering source dynamics from given reference sources. The question remains if one of the methods outperforms the other. Therefore, a simulation is conducted with random source locations repeated over 500 runs. Source dynamics are modeled with an AR model as described in Section 4.1. In each run data is newly generated and both methods are evaluated. Figure 4.13 shows the mean localization error over the four sources in a scatter plot. In the left panel, the mean Euclidean distance between each estimated source maximum and the true source location is shown. One can observe that MIC has a larger error for all four sources (Wedge Music: 6.69 cm; MIC: 7.06 cm). The same picture is provided by evaluating the Earth Mover's Distance (EMD) as the localization error which is shown in the right panel (Wedge Music: 5.63 cm; MIC: 6.02 cm). By comparing the examples shown in the previous sections (Figures 4.10.A and 4.12.A), one can observe that for both methods the source maximum well coincides with the true modeled sources. However, the spatial distribution obtained by MIC is much larger than the one for a Wedge Music scan. This is also due to the fact that Wedge Music values approach infinity for perfectly correlated sources and the MIC is bounded. As the EMD takes the broadness of the spatial distribution into account it becomes clear why Wedge Music outperforms MIC in terms of the EMD.

4.8. Interacting sources differing between experimental conditions

In the previous sections, the application of Wedge Music and MIC on source level is demonstrated in order to estimate which of the sources determined by SC Music are synchronized. Continuous data have been simulated under the assumption of stemming from a single controlled experimental condition or consisting out of many repetitions of such an experimental condition. However, in psychological or neuroscientfic research it is common to acquire data from two experimental conditions in order to investigate the specific difference. Otherwise, data are confounded by background activity which might hamper the investigation of the activity of interest in an experiment. Here, the assumption comes into play that common activity cancels out and only the effect that differs between conditions remains. In the following, the investigation of class differences by combining SC Music with Wedge Music or the MIC approach is demonstrated and compared.

4.8.1. Comparing MIC and WM for class differences

In general, it is not trivial to access class differences of interacting sources based on the imaginary part of coherency (ImCoh). Recalling the definition of coherency in Eq.(2.19), the cross-spectrum is normalized by power. As the focus of interest lies on interaction differences between classes and not on power differences, this normalization might bear difficulties. One can imagine that the coupling between sources might be consistent, whereas the strength of sources changes. In this case, the imaginary part of coherency would be significantly different, although the interaction remains unchanged. In an extreme scenario, only the noise level between two conditions may change but power and interaction strength stay constant. This case might also lead to a change of the ImCoh. Hence, measures based on the ImCoh are not perfectly suited to invest class differences. Taking a theoretical point of view, coherence calculated from the difference of cross-spectra is meaningless because it is not bounded and the diagonal elements can even become negative

These issues are avoided by applying Wedge Music. Here, calculations are solely based on the non-normalized imaginary part of the cross-spectrum. Hence, one can easily construct $\Delta\text{ImCs} = \text{ImCs}_1 - \text{ImCs}_2$ and perform all calculations in the same fashion as for a single data class on ΔImCs. Furthermore, the same is true for SC Music.

Figure 4.14 shows the result of a simulation that illustrates the effect of different noise levels for different conditions. Two data classes were modeled with an identical interaction profile: two synchronous sources, each one approximately in the motor cortex in each hemisphere. The source locations are shown by the blue dipoles in Figure 4.15.A. For the present simulation only the outer two dipoles were present, i.e. the most left and most right one. Dynamics were simulated using an AR model as before and as described in Section 4.1. The only difference between the two data classes was the noise level which differed by a factor of 20. Cross-spectra were calculated with the same parameters as before for each single class. Then, the

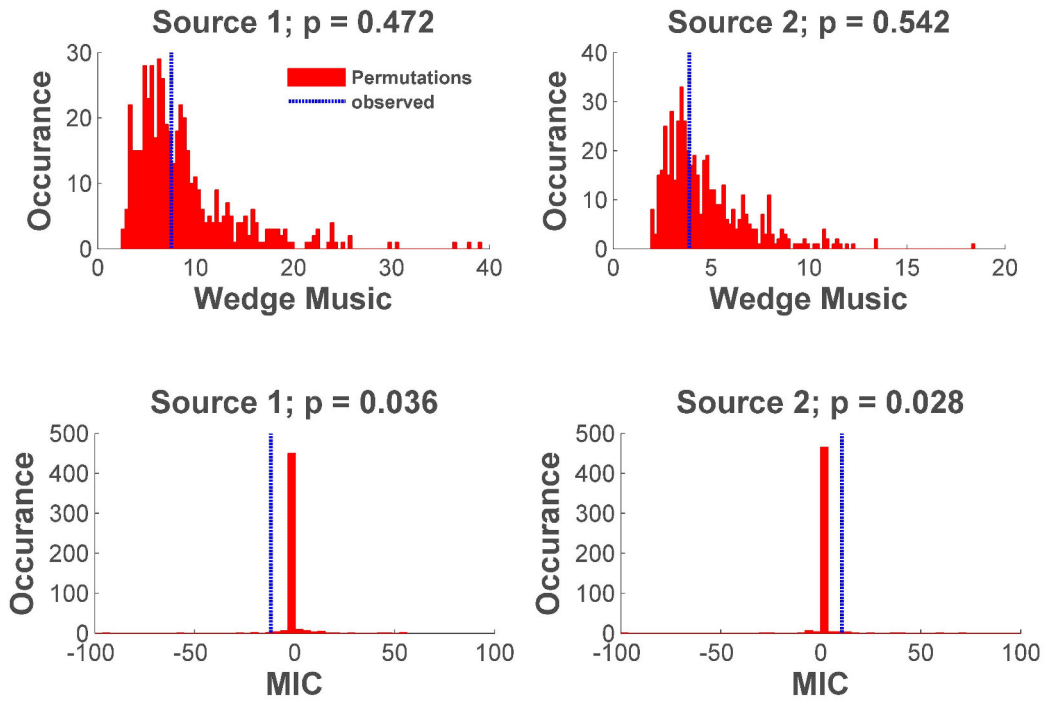

Figure 4.14.: Wedge Music (upper row) and MIC on source level (lower row) for class differences for two modeled sources. Source 1 is displayed in the left column and source 2 in the right column. The blue horizontal line indicates the score of the Wedge Music scan (or MIC respectively) for the maximum of each source scan for the original data. The maximum scores of Wedge Music and MIC for 500 permutation runs are shown as histograms colored in red. Interaction strength is modeled to be identical for both classes. Only the noise level is different. Wedge Music does not find a significant ($p<0.05$) difference in interaction between the two classes according to a permutation test. On the contrary, applying MIC and a permutation test suggests that there exists a difference in interaction between the two classes.

automated frequency selection procedure based on the GIM as described in Section 4.1 and SC Music were applied on the difference of the individual cross-spectra $\Delta\text{ImCs} = \text{ImCs}_1 - \text{ImCs}_2$. Finally, both Wedge Music and MIC combined with DICS and the nulling beamformer have been evaluated using the sources obtained by SC Music as reference sources. To assess statistical significance, a permutation test (randomly shuffling class labels of epochs of both classes, see Section 2.5.4) with 500 runs was used embracing the whole procedure starting with the automatic frequency selection. The results of this permutation test are displayed in Figure 4.14. The upper row shows the results for Wedge Music applied on the class difference. The value of Wedge Music for the original class difference lies in the middle of the distribution of the Wedge Music values for the 500 permutation runs yielding a non-significant ($p>0.05$) result. This is correct as the interaction is identical for both simulated data classes. The situation is different for MIC as shown in the lower row of Figure 4.14. Although most of the resulting MIC values within the 500 permutation runs are zero or close to zero, the observed value for the original class difference is larger leading to a significant result ($p<0.05$).

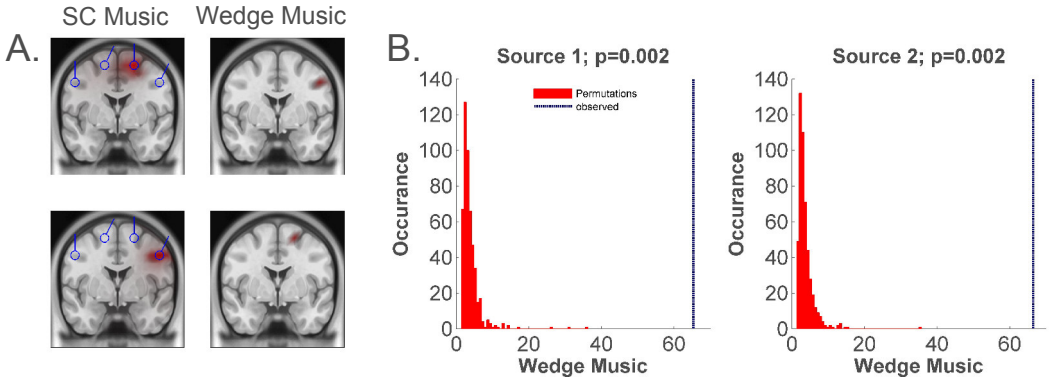

Figure 4.15.: SC Music and Wedge Music applied on ΔImCs. A.: Source locations revealed by SC Music applied on the class difference $\Delta\text{ImCs} = \text{ImCs}_1 - \text{ImCs}_2$ in the left column. The first class contains two pairs of synchronized sources, one in each hemisphere. The second class contains only the pair in the left hemisphere. SC Music correctly uncovers the sources remaining for the class difference, i.e. the ones in the right hemisphere. Each of the two sources serve as a reference for a Wedge Music scan (right column). Wedge Music correctly finds the corresponding interacting sources. The original modeled dipoles are shown in blue. B.: Results of a permutation test (random shuffling of class labels) for each Wedge Music source. The blue line indicates the maximum score of the Wedge Music scan for the true class labels. The scores for the permuted class labels over 500 runs are shown as a histogram colored in red.

4.8.2. Wedge Music for class differences

In the previous section it has been shown that Wedge Music is conceptually better suited to investigate interaction differences between two data classes compared to the MIC. In the following the application of SC Music and Wedge Music on class differences is demonstrated.

For the first class, four sources were simulated as shown in Figure 4.15.A by the blue dipoles. Each pair in one hemisphere was modeled to be interacting according to an AR model as described in Section 4.1. For the second class, only the source pair in the left hemisphere was present. The source locations were exactly the same as for the first data class. SC Music and Wedge Music were performed for two sources on the difference of the imaginary part of coherency $\Delta\text{ImCs} = \text{ImCs}_1 - \text{ImCs}_2$. The left column of Figure 4.15.A shows the result of SC Music. The source maxima revealed by SC Music served as a reference for a Wedge Music scan. The results for the Wedge Music scan are shown in the right column of Figure 4.15.A. One can see that SC Music correctly finds the remaining source pair. Furthermore, Wedge Music finds the respective other remaining source that is interacting with the SC Music reference.

Statistics are obtained by a permutation test (see Section 2.5.2). The class labels of all epoch are randomly assigned for 500 runs and for each run the whole calculation is repeated. Figure 4.15.B illustrates the results for Wedge Music. For both sources, none of the permutation runs revealed a larger Wedge Music result than the observed result for the true class labels. This leads to a highly significant p-value of p=0.002 for both sources.

Please note, that the data classes do not necessarily have to arise from different experimental conditions. It is also conceivable to test against a pre-stimulus baseline

in order to cancel out common background activity. One could also take the cross-spectrum frequency bins next to the frequency peak of interest in increase the signal-to-noise-ratio.

4.9. Wedge Music without prior source reconstruction

As introduced in Section 3.3.4, Wedge Music does not necessarily have to be applied using reference sources. It is also conceivable to iterate Wedge Music over the whole grid, i.e. all possible pairs of sources. To limit computation time, a coarser grid was used for this simulation in contrast to the previous ones. Here, the rather coarse grid consisted out of 624 voxels. As pointed out in Section 3.3.4, the optimization for complete Wedge Music is executed within a larger search space, which increases computation time compared to a Wedge Music scan with a given reference voxel. A single iteration, using an arbitrary voxel as a reference and scanning through the whole brain, needs about 6.2 minutes using an Intel i7 2.0 GHz processor with four cores. This leads to a computation time of about 64.7 hours for a complete scan on a very coarse grid. Using a finer grid would quadratically increase computation time. Considering multiple subjects and resampling statistics would lead to infeasible computation times. For example employing the same grid with 624 voxels, having 10 subjects and using a permutation test with 500 runs would result in a computation time of 36.9 years. Hence, practical considerations suggest to apply a prior source localization technique in combination with Wedge Music.

A further issue with complete Wedge Music is how to treat the results. The outcome is an approximately symmetric connectivity matrix of size voxels times voxels. A straightforward approach to visualize the results is to take the row-wise maximum, use the respective voxel as a reference and to show the interaction of this reference to all other voxels. Figure 4.16 illustrates this for the six row-wise maxima. It becomes clear that the intra-hemisperic interaction (modeled source locations are as shown in Figure 4.15.A) is revealed by complete Wedge Music. However, one can observe that the way of visualizing the results does not uncover the strongest source interactions. Instead, patterns are repetitive. This is a consequence of the blurred inverse solutions leading to the phenomenon that neighboring voxels may also show large interactions. A possible solution to this would be a clustering approach. Nevertheless and despite the limitations described, the present simulation indicates that complete Wedge Music is capable of providing a meaningful picture of true interactions on source level.

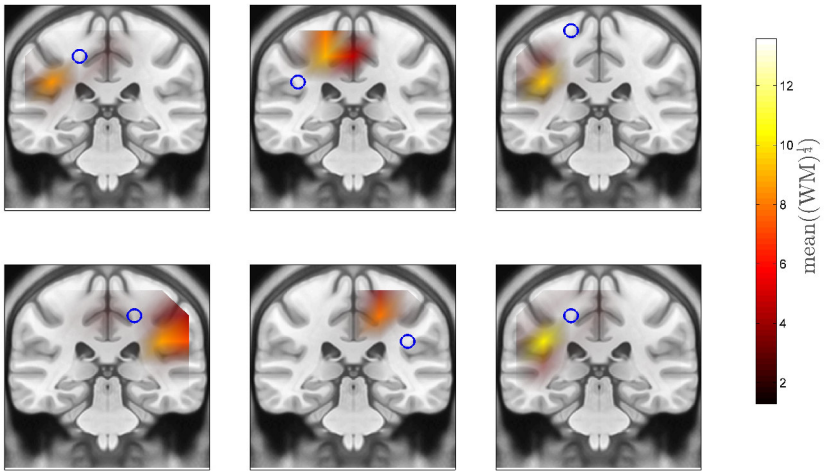

Figure 4.16.: Complete Wedge Music (see Section 3.3.4). From the connectivity matrix linking each voxel to all other voxels, the maxima in each row are selected and the six strongest components are shown as blue circles. For each of this references the connection strength to all other voxels is color-coded.

5. Application

How empty is theory in the presence of fact!

(Mark Twain)

The behavior of the methods introduced in this thesis has been evaluated in various simulations in the previous chapter. In addition to that, possible application scenarios and additional statistical tests have been demonstrated. However, simulations are a necessary but not sufficient way to judge the applicability of new methodology. Certain intrinsic data properties could have been missed or erroneously modeled. Therefore, it is important to additionally quantify the behavior of new data analysis techniques in real-world examples. In the following, different types of data sets are investigated, highlighting certain properties of the methods. Both EEG and MEG data are considered, which conceptually proofs the suitability of the methods for each modality. In principle, data acquired according to any experimental paradigm can be investigated with the methods introduced in this thesis. The only requirement is sufficient data recorded with an adequate sampling frequency in order to capture the frequency of interest according to the Nyquist theorem (Nyquist, 1928; Shannon, 1998). Enough epochs have to be recorded in order to reliably estimate the cross-spectrum. In general, it is not feasible to come up with a rule of thumb to estimate the number of data epochs needed. The necessary amount of data largely depends on the true underlying interaction strength, which itself is the subject of investigation. Furthermore, it can vary according to other factors, such as the individual cortex folding which is difficult to account for. Obviously, the rule 'the more data the better' applies. Due to many averages, any random effects like biological and measurement noise are reduced.

In this chapter, data from two different types of experimental paradigms are investigated. One is the so called resting state data, where the subject does not have a particular task. For the other, the subject was instructed to move either fingers or the whole hand for a distinct period of time. The reason for that is that both paradigms evoke strong oscillatory brain activity and are well investigated also with complementary measurement modalities such as fMRI (see e.g. Lotze et al., 1999; Bernard et al., 2002; Lacourse et al., 2005; Milton et al., 2008) and NIRS (see e.g. Koch et al., 2010; Habermehl et al., 2012). Therefore, the expected source activity is known and can be compared to the results obtained by the new methodology. Within this chapter the application of the novel methodology is demonstrated for single subject data. The purpose of group analysis and grand averages is covered in the discussion in Chapter 6.

5.1. GIM on sensor level

In the current section, application examples for the Global Interaction Measure (GIM) on sensor level, as introduced in Section 3.1, are given. First, the application of the GIM and the validity of the theoretical considerations are demonstrated. Second, the measurement modalities EEG and MEG are compared with respect to their capability of observing interactions.

5.1.1. GIM for eyes closed resting state EEG data

The GIM as defined in Eq.(3.17) is applied on resting state EEG data which are available online[1]. From the ten data sets online, Subject 2 and Subject 10 are chosen for illustrative purposes as they show interesting structures in various frequencies. Please note that oscillatory frequencies vary substantially over subjects. In some subjects even a distinct frequency peak may not be observable.

Data were recorded with 19 scalp electrodes for approximately 12 minutes. The subjects were instructed to close their eyes which is known to enhance oscillatory brain activity in the alpha band range (~8-13 Hz, see Table 2.1) (Jensen et al., 2002; Palva and Palva, 2007). To calculate the cross-spectrum, data were split into epochs of two seconds length. Within each epoch the Fourier transform of the the Hanning windowed data was calculated and evaluated according to Eq.(2.18) for each channel pair. Coherency was obtained by normalizing the cross-spectrum according to Eq.(2.19). Finally, the GIM was calculated without treatment for overfitting (see Section 3.1.6) and the bias was estimated as described in Eq.(3.41).

The upper row in Figure 5.1 visualizes the ImCoh for all channel pairs as a butterfly plot over frequency for both subjects. One can observe a prominent peak in the alpha range at approximately 10 Hz as expected. The GIM, which is shown in the same figure colored in red, also indicates an ongoing synchronization at this frequency. However, the GIM identifies additional frequency bands of ongoing synchronization such as beta (a distinct peak at 22 Hz for Subject 2 and a rather broadband interaction within 16–19 Hz for Subject 10) and gamma (for Subject 10 at approximately 29 Hz). The peaks in higher frequency bands become much more prominent compared to the ImCoh due to the maximization procedure described in Section 3.1.1. Also compared to channel power, the GIM facilitates the identification of frequencies of ongoing oscillations. The second row in Figure 5.1 shows the channel power for each channel. Although having a different meaning, it is common to study channel power in order to identify frequency peaks of interest. Especially for investigating interaction, the GIM seems to be a more suitable choice. A further advantage is the reduction of dimensionality achieved by the GIM. Information of $19 \times 19 = 361$ channel pairs is reduced to a single value. Hence, automated frequency selection procedures can be constructed based on the GIM. A straightforward approach, based on optimizing the SNR over frequency, has been introduced in Section 4.1 and has

[1] see http://clopinet.com/causality/data/nolte/

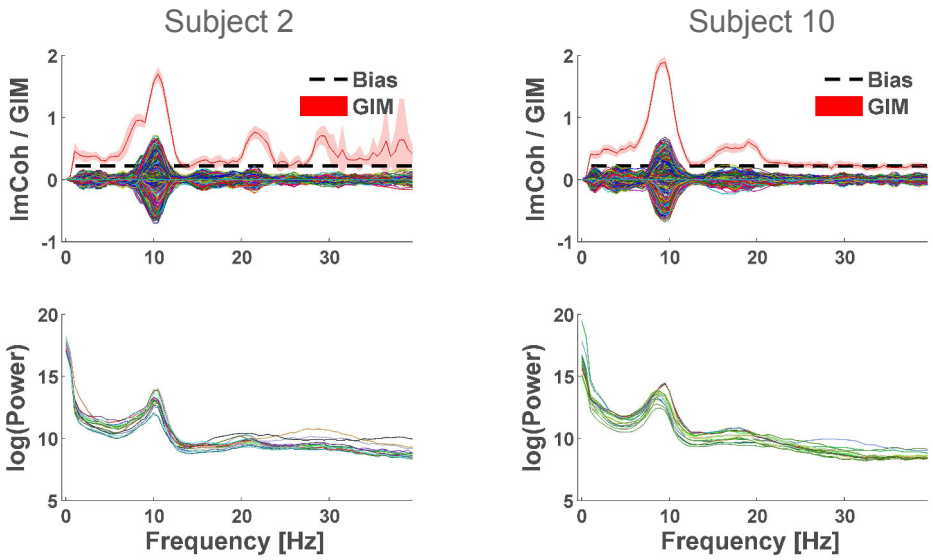

Figure 5.1.: ImCoh, GIM and power over frequency for EEG data. In the left column, resting state data is shown whereas in the right column data from the imagined movement condition is shown. The upper row illustrated the ImCoh for all channel pairs as a butterfly plot. Furthermore, the GIM is represented as a red solid line. The standard deviation of the GIM estimated with Jackknife is displayed as a red transparent underlay. Finally, the analytical approximation of the bias is shown as a dashed black line. The lower row shows the power spectrum in a logarithmic scale.

been used for the simulations in Chapter 4. It will also be used in the following for the investigation of real EEG/MEG data.

Figure 5.1 additionally shows the standard deviation of the GIM, estimated with a Jackknife procedure, illustrated as an underlay. One can observe that for most of the frequencies it is narrowly distributed and, hence, the GIM is robust. Using the jackknife estimate of the standard deviation in a parametric test (see Section 2.5), one can observe that

$$\frac{\mathrm{GIM}(f) - \mathrm{bias}}{std(\mathrm{GIM}(f))} > 1.96 \tag{5.1}$$

and, therefore, the results are significant below 30 Hz. Only for higher frequencies (>30 Hz) in Subject 2 one can see a larger standard deviation. This is most likely due to muscle artifacts since the data has not been cleaned in a previous analysis step and these kinds of artifacts typically occur in this frequency range. Finally, Figure 5.1 shows the estimated bias indicated by a black dashed line. It becomes clear that the theoretical considerations presented in Section 3.1.7 well match the real data as the bias defines a lower bound of the GIM.

5.1.2. Comparison of EEG and MEG with the GIM

As stated in Section 3.1, both GIM and MIM are invariant to linear and static transformations which implies that these measures are independent of the respective forward mapping and source mixing on sensor level. This is exact if there are not

more sources than sensors and approximate if the number of sensors is large enough to capture the most relevant activity. Hence, GIM and MIM are well suited to compare capabilities of the measurement modalities EEG and MEG in terms of observing source interactions. In Section 2.2.4 it is described that the neurophysiological basis is identical for EEG and MEG. Despite technical aspects, both theoretically only differ in the in the mapping from sources to sensors. If one modality picks up interacting sources and the other does not, it can be quantified by applying the GIM on simultaneously measured data. This is done in the following.

MEG data were acquired with a 165-channel MEG system in a magnetically shielded room. The system comprised 153 DC SQUID integrated magnometers arranged on a helmet covering the whole head and 12 additional reference channels (for a detailed system description see Della Penna et al. (2000)). From the total channel set, 21 magnometers were switched off as they previously showed malfunctioning behavior. For the whole duration of the experiment, the subject had to perform a finger tapping task for 20 seconds which alternated with a resting state period (eyes open, subjects had to focus a fixation cross in order to reduce eye movements) for again 20 seconds. Data have been cleaned with an ICA artefact rejection procedure. By visual inspection of ICA components of the EEG data, two components have been rejected leading to 14 remaining data space dimensions. Hence, the cross-spectrum of the cleaned EEG data has been reduced to p=14 components as described in Section 3.1.6. To fairly compare the EEG and MEG measurements, the MEG data has also been reduced to the same amount. Even more, a sparse subset of 16 MEG channels has been selected and then reduced to p=14 components to enhance comparability. This reduction, furthermore, is necessary as for GIM and MIM the real part of the cross-spectrum has to be inverted and becomes singular for rank deficient data spaces.

Figure 5.2.A and 5.2.B show the GIM for the simultaneously measured data, where subfigure A. shows the rest conditions and subfigure B. the fingertapping condition. The most dominant interaction at 10 Hz is detected both by EEG and MEG. Strikingly, a large low frequency interaction at 4 Hz is observable for MEG but not for EEG. Furthermore, two rather small high frequency peaks at 36 Hz and 48 Hz are observable in the MEG data but not in the EEG data for both conditions. Additionally, in the rest condition some beta band interaction at about 16 Hz can only be detected from the MEG data. In contrast to that, a different beta band interaction at about 21 Hz is observable for both data sets. Summarizing, there seems to be evidence, that MEG is capable of observing oscillatory phase locked synchronization between different brain regions that cannot be seen in simultaneously measured EEG data.

5.2. Source interactions for resting state MEG data

In the present section the application of SC Music and Wedge Music based on a pre-whitened subspace of the imaginary part of the cross-spectrum is demonstrated. MEG data were recorded continuously in a magnetically shielded room with a

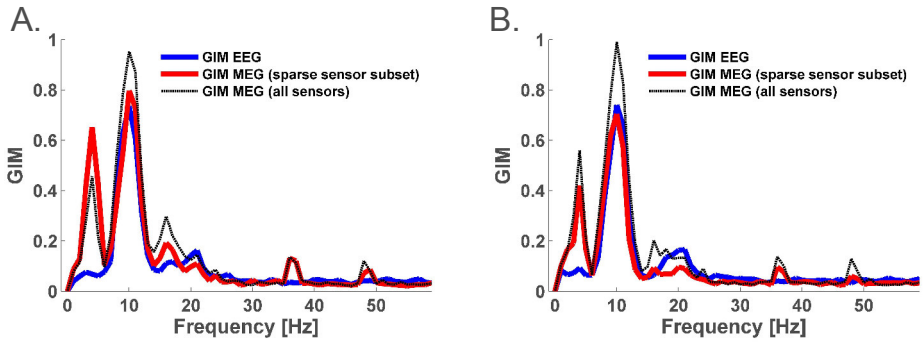

Figure 5.2.: GIM for simultaneously measured EEG and MEG data. A.: resting state condition, B.: finger tapping condition

275-channel system covering the whole head (Omega 2000, CTF-Systems). Two squids were malfunctioning such that the analysis comprised 273 MEG channels. The recording session lasted for approximately 10 minutes, where the subject had to focus a fixation cross that was displayed on a screen. No further task was required. The head position relative to the MEG sensors was measured with a set of head coils (nasion, left and right ears) and mapped to an individual anatomical MRI. The head model obtained from the individual MRI was then mapped to a standard MNI template head for visualization and to prepare for potential group analysis and assure comparability between subjects (Fonov et al., 2009, 2011). The brain was parceled into 5003 grid points or voxels. With respect to these voxels, leadfields were generated as described in Nolte (2003). MEG signals were recorded with a sampling frequency of 1200 Hz and sampled down to 200 Hz with the FieldTrip toolbox (Oostenveld et al., 2010). An online low-pass filter with a cutoff frequency of 300 Hz was applied during recording and, furthermore, data was detrended offline, i.e. the mean of each channel times series was subtracted. Cardiac, muscle related and eye artifacts were removed by visual inspection of 30 ICA components obtained from a prior PCA decomposition of the sensor data (see Section 2.3.1).

To compute the cross-spectrum, data were divided in segments with length of 1 second and a 50% overlap between segments, leading to a frequency resolution of 1 Hz. Figure 5.3.A shows the imaginary part of coherency for all channel pairs. The frequency, $f = 13$ Hz was chosen according to the maximum value for the SNR optimized GIM (see Eq.4.2) within the alpha band, defined here as 8 Hz $\leq f_\alpha \leq$ 13 Hz.

5.2.1. Estimating the number of sources

Having determined a frequency of interest, the number of interacting sources in that specific frequency range has to be estimated for further processing. Please note that this number corresponds to the subspace dimension of the ImCs. As theoretically described in Section 3.2.2 and, furthermore, demonstrated in a simulation in Section 4.5, the corresponding scree plot is shown in Figure 5.3.B. One can observe a clear

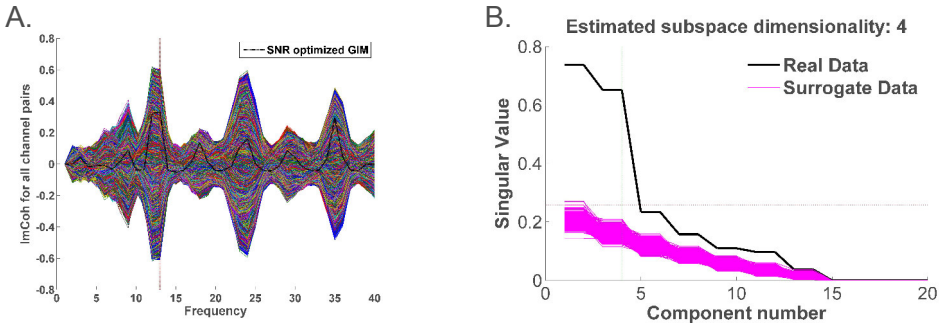

Figure 5.3.: Frequency selection and estimation of the number of sources for MEG resting state data. A.: ImCoh for all channel pairs as a butterfly plot and the SNR optimized GIM. The frequency with maximum SNR optimized GIM within the alpha band is chosen for further processing and illustrated as a vertical line. B.: Singular values of the prewhitened ImCs in descending order are illustrated as a black solid line (scree plot). The same representation for 500 bootstrap runs on surrogate data colored in magenta. 95% of the largest value of the surrogate data runs is chose as a cut-off to estimate the number of sources (horizontal line). This procedure results in an estimated number of sources equal to four.

drop of the magnitude of the transformed singular values after four components. To obtain an objective noise threshold, surrogate data is generated as described in Section 3.4 and subjected to a bootstrap procedure. Now, 95% of the largest singular value is chosen as a cut-off indicated by the horizontal line in Figure 5.3.B. This procedure also leads to an estimated number of four sources, as does visual inspection of the scree plot. Concluding, four sources are estimated with SC and Wedge Music in the following.

5.2.2. SC and Wedge Music

Figure 5.4 shows the four source pairs obtained by SC Music and a corresponding Wedge Music scan that has been performed for each one of the SC Music sources as references. The upper row in each source pair plot shows the SC Music source, i.e. the reference voxel for the Wedge Music scan. Each source is shown in three different views: sagittal, coronal and axial. Red lines indicate the slice cutting in each view that is conducted at the maximum of each source.

One can observe that two interacting source pairs arise, one in each hemisphere. All sources are located in motor related areas. Apparently, the rhythmic activity used for localization at 12 Hz is the sensorymotor idle rhythm. This rhythm is strongly present in the alpha range if no movement is executed or imagined by the subject (Pfurtscheller and Neuper, 1997). This is the case for the present data where the subject was at rest. The sources also correspond to source locations from the somatosensorymotor default mode network revealed by fMRI (see e.g. Raichle et al., 2001; Engel et al., 2013). Hence, the methodological procedure presented here provides reasonable source locations in this case. As a sanity check, source locations found by SC Music are consistent with results obtained by the Wedge Music scan. In other words, Wedge Music exactly finds those sources within a scan over the entire brain that have been unraveled before by SC Music. This can be seen by the fact that

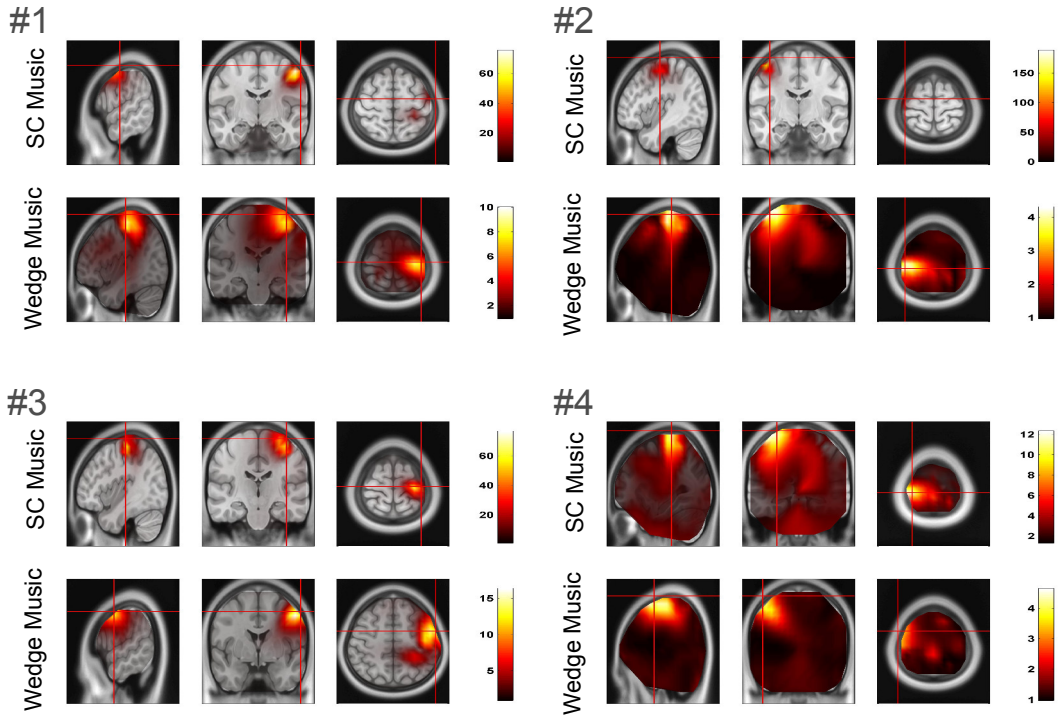

Figure 5.4.: Interacting sources in MEG resting state data. In the upper row of each source pair plot the SC Music source is displayed. This source, i.e. the voxel with the maximum value, then served a reference for a Wedge Music scan. The result of this Wedge Music scan in displayed in the lower row of each source pair. Each source is displayed in three different views: sagittal, coronal and axial. The MRI slices were cut at the maximum of each source (red lines).

the source pairs #1 and #3 and the pairs #2 and #4 are identical. For example, the SC Music source in pair #1 is the same as the Wedge Music source in pair #3 and vice versa. The same picture as obtained by the Wedge Music scan, is provided by scalar Wedge Music (see Section 3.3.3). Table 5.1 shows the results for scalar Wedge Music for all combinations of SC Music sources as shown in the top row in Figure 5.4. It is apparent that out of all four sources, only two source pairs show a large scalar Wedge Music result. These are the source pairs consisting of source 1 and source 3 and, additionally, of source 2 and source 4. Considering the source locations of each individual source as shown in Figure 5.4, this is exactly the same picture as provided by the Wedge Music scan.

To test for random effects, surrogate data were constructed, where all dependencies within the data have been destroyed. These surrogate data then were resampled according to a bootstrap approach and compared to the observed values of SC and Wedge Music of the original data. Figure 5.5 shows the results for all four SC and Wedge Music sources. One can observe a narrow distribution for the surrogate results over 500 bootstrap runs. The results for the real data significantly differ from the results for the surrogate data yielding a p-value of $p = 0.002$ for all four sources for SC Music as well as for Wedge Music.

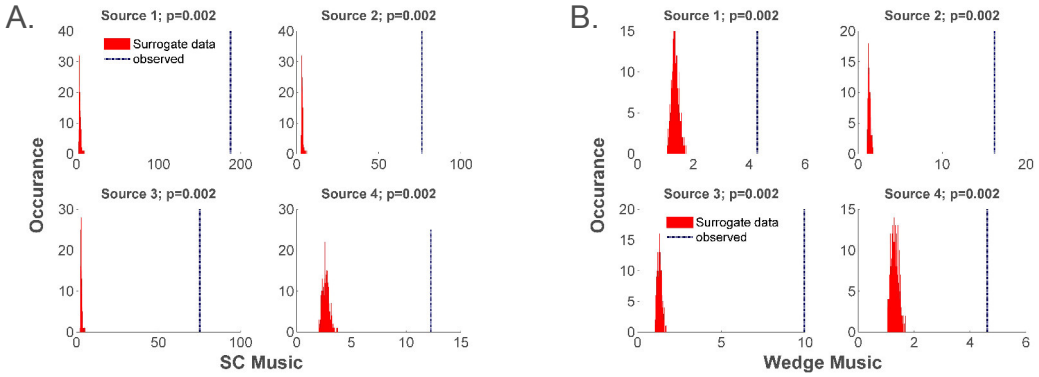

Figure 5.5.: Statistics for A.: Maximum scores of SC Music source distributions and B.: Maximum scores of source distributions obtained by a Wedge Music scan with the SC Music sources as references. The observed values (vertical lines) of SC and Wedge Music are compared to a distribution (red histograms) obtained by performing the same calculations on bootstrapped surrogate data (see Sections 2.5 and 3.4)

5.3. Class differences

As demonstrated in Section 4.8, a tremendous advantage of Wedge Music is its direct applicability on a difference of two cross-spectra arising from two experimental conditions. A real-data example is given in the following, where class differences in interaction for motor imagery data are investigated. In a training session for later Brain Computer Interface (BCI) application, the subject was instructed to imagine the movement of either the right hand, the left hand or the foot but not to execute it (Blankertz et al., 2006). Previous research has shown that brain activity for real executed movements and imagined movements are located in the same areas in the cortex (Pfurtscheller and Neuper, 1997). As the only difference, the activity is usually stronger for executed movements. Hence, interacting sources in the hand and foot movement related brain areas such as the primary sensorymotor areas are expected. A good review concerning synchronization within the motor system can be found in van Wijk et al. (2012).

Table 5.1.: Scalar Wedge Music score $\hat{h}_{ij}$ (see Eq.(3.77)) for all possible pairs of SC Music sources $i, j = 1 \ldots 4$ (i.e. voxel with maximum SC Music score for each source according to Eq.(4.5)). The SC Music source distributions and the corresponding source labels are shown in Figure 5.4. One can see from the individual scalar Wedge Music scores that the SC Music sources 1 and 3 and the sources 2 and 4 form interacting source pairs.

	Source 1	**Source 2**	**Source 3**	**Source 4**
Source 1	1.00	1.01	9.41	1.03
Source 2	1.01	1.00	1.00	4.36
Source 3	9.41	1.00	1.00	1.16
Source 4	1.03	4.36	1.16	1.00

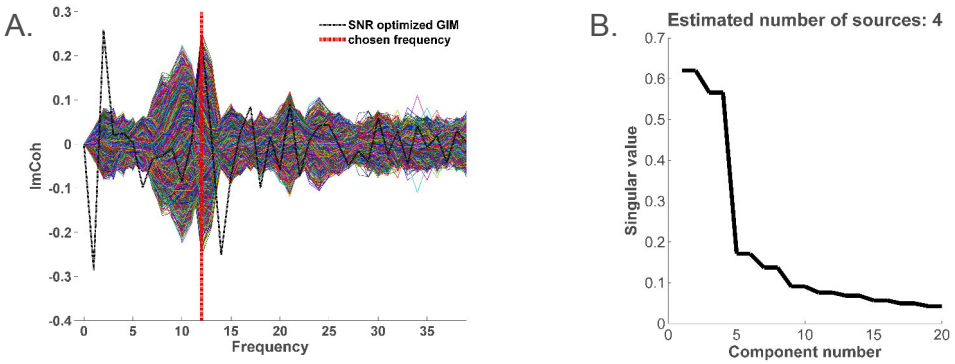

Figure 5.6.: Frequency selection and estimation of the number of sources for the difference in interaction between imagined hand and foot movement. A.:The imaginary part of coherency for the difference of hand vs. foot movement. The frequency $f = 12$ Hz has been selected for further analysis due to the largest SNR optimized GIM in the alpha range. B.: Scree plot. The singular values of the prewhitened ImCs. A clear drop can be observed after 4 components.

EEG data were recorded with a multichannel EEG BrainAmp amplifier using 118 Ag/AgCl electrodes in an extended 10–20 system. Data were cut into trials lasting for 3.5 seconds, beginning with the movement instruction onset. This procedure leads to 70 trials for each individual class (left hand, right hand, foot). Data were sampled down to 100 Hz and each trial was segmented into 25% overlapping windows with the duration of 1 second. These segments were then Hanning windowed and Fourier transformed to compute the cross-spectrum. To investigate the difference in interaction between hand and foot movement and to avoid any biasing effect due to a larger amount of data in one condition, left and right hand movement were combined by randomly choosing 70 epochs in total out of these two classes. The imaginary part of the cross-spectrum obtained by the imagined foot movement data then was subtracted from the imaginary part of the cross-spectrum of the newly generated hand movement data class. Figure 5.6 shows the imaginary part of coherency for the class differences for all channels over frequency. As before, the frequency with maximum SNR optimized GIM in the alpha range was automatically chosen, i.e. 12 Hz. At the selected frequency of interest, the number of interacting sources to be determined by SC and Wedge Music has to be estimated. Figure 5.6 shows a scree plot for the prewhitened ImCs. One can observe a clear drop after four components making an additional test with e.g. permuted data unnecessary. Finally, SC and Wedge Music were applied on the difference of the imaginary part of the cross-spectra at 12 Hz.

Figure 5.7 shows the results of both SC and Wedge Music in the same style as for the MEG resting state data (see Section 5.2.2). For each source pair, the SC Music source is shown in the upper row, the corresponding Wedge Music source in the lower row. Each source space scan is presented in three different views cut at the maximum for each scan. The results shown in Figure 5.7 indicate that two source pairs differ between imaginary hand and foot movement. One on them (shown as source pair #1 and source pair #2) is a local interaction within foot movement

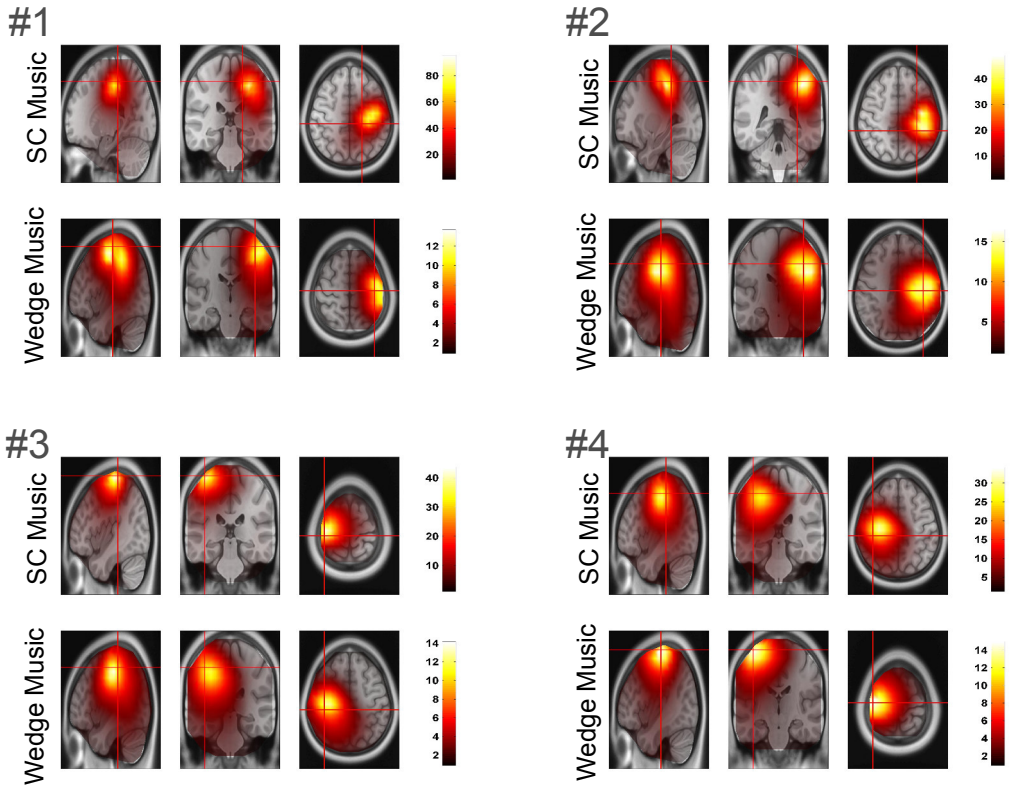

Figure 5.7.: The results for SC and Wedge Music scans applied on the difference of the ImCs belonging to imagined hand and foot movement. For each source pair, the upper row shows the SC Music scan and the lower row the Wedge Music scan.

related brain regions in the right hemisphere. The other one (shown as source pair #3 and source pair #4) represents a functional synchronization between a brain region associated with right hand movement (SC Music source in source pair #3) and the foot movement region in the same hemisphere. Due to the nature of a Wedge Music scan one can judge the plausibility of the result. It is shown in Figure 5.7 that the sources obtained with SC Music are found again with Wedge Music.

Figure 5.8 presents statistics obtained by permutation testing. Epochs from both data classes (hand and foot) were randomly assigned to two new classes and the whole computational procedure was repeated for 500 runs. In Figure 5.8.A the statistical results for the Wedge Music scan are shown. For all source pairs a significant result $p < 0.05$ is obtained. Table 5.2 shows the results for scalar Wedge Music. The same picture is provided as for the Wedge Music scan: The SC Music sources (depicted in Figure 5.7) 1 and 2 are interacting as well as sources 3 and 4.

A well-established and famous data analysis technique in the context of class differences in BCI research is Common Spatial Patterns (CSP, see e.g. Blankertz et al., 2008b; Fukunaga, 1990; Koles, 1991; Blankertz et al., 2002; Tomioka et al., 2006; Krauledat et al., 2007; Blankertz et al., 2008a; Sannelli et al., 2010; Samek et al.,

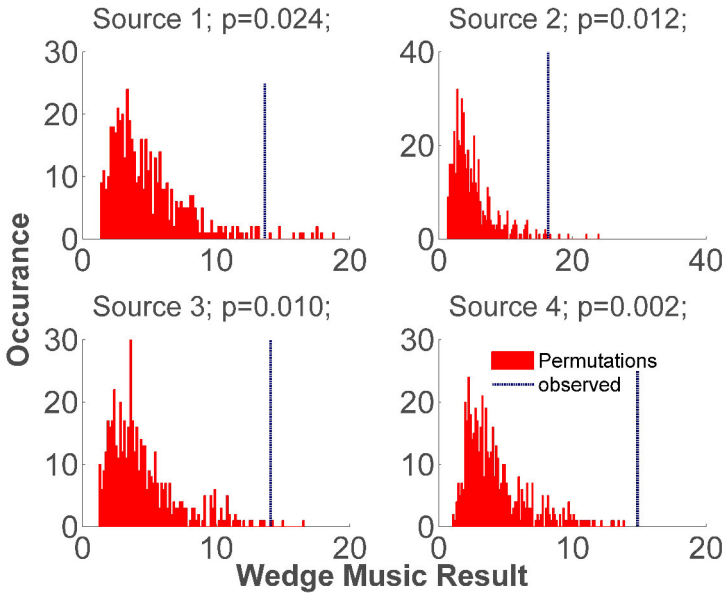

Figure 5.8.: Permutation statistics for the difference of imagined hand vs. imagined foot movement for Wedge Music. The score of the Wedge Music scan (see Eq.(3.75)) for all permutation runs is shown as a histogram colored in red. In contrast to that, the blue solid line indicates the Wedge Music score for the true class labels.

2012; Kawanabe et al., 2013). The idea behind this supervised data decomposition technique is to construct spatial filters such that two classes can be best discriminated, e.g. for the subsequently application of a linear classifier on the CSP-filtered data. This optimal discrimination is achieved by spatial filters which maximize the variance of the filtered data for one data class and simultaneously minimize the variance for the other class. As variance is equal to signal power for narrow-band filtered signals, the CSP algorithm reveals spatial patterns of brain sources whose signal power differs between the two classes. Hence, it is appealing to compare strong neuronal signal generators as obtained by CSP with the interacting sources obtained by SC and Wedge Music.

In order to apply CSP, data were pre-processed as for the SC and Wedge Music

Table 5.2.: Scalar Wedge Music score $\hat{h}$ (see Eq.(3.77)) for all possible pairs of SC Music sources. The sources are depicted and labeled in Figure 5.7.

	Source 1	**Source 2**	**Source 3**	**Source 4**
Source 1	1.00	4.73	1.03	1.00
Source 2	4.73	1.00	1.03	1.00
Source 3	1.03	1.03	1.00	7.53
Source 4	1.00	1.00	7.53	1.00

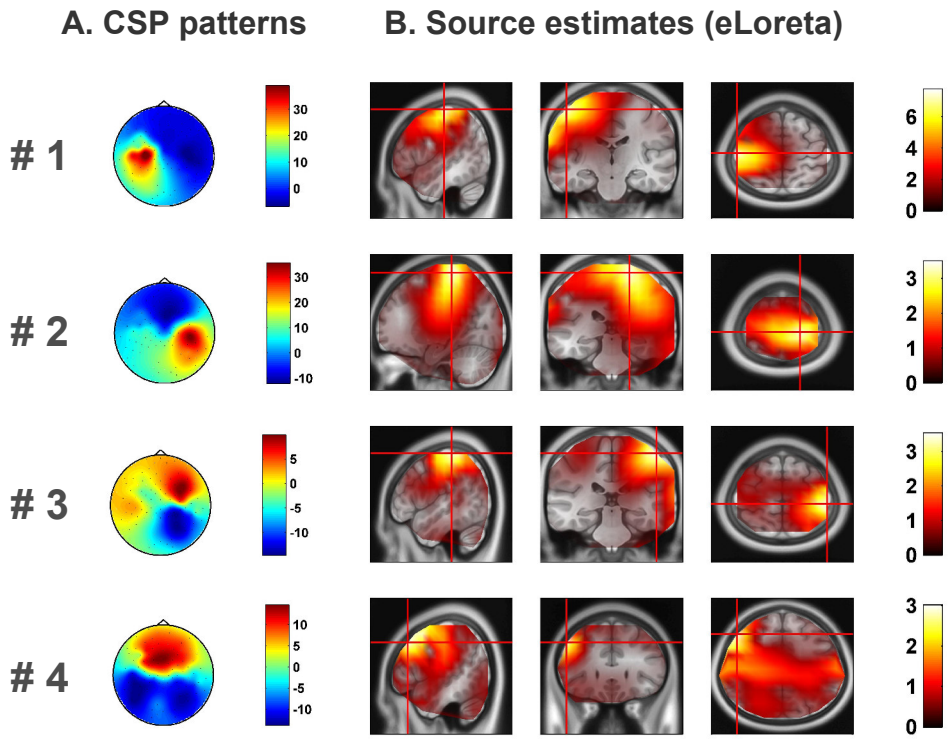

Figure 5.9.: Common spatial pattern analysis to investigate class differences in power in the alpha band between imagined hand and imagined foot movement. A. Spatial patterns of sources whose power differs between the two data classes. B. Source projection of each corresponding pattern with eLoreta (Pascual-Marqui et al., 2011). Please note that the units of the patterns source distributions are arbitrary.

analysis and additionally band-pass filtered in the alpha range (9 - 13 Hz). According to the determined number of sources, the four strongest CSP components are considered in the following. The spatial filters were transformed into interpretable patterns as described in Haufe et al. (2014b). These are shown in Figure 5.9.A on the left. One can observe that the CSP patterns depict neurophysiologically plausible brain sources considering the experimental paradigm of motor imagery. Finally, these patterns were projected into source space by applying eLoreta (see Appendix A.3). The resulting source distributions are shown in Figure 5.9.B next to each pattern in the same fashion as the sources in Figure 5.7. As for SC and Wedge Music (see Figure 5.7), one can observe two sources in each hemisphere in the motor cortex which are a little more blurred but, in general, well coincide with the SC and Wedge Music sources. The average Euclidean distance between the maximum of the SC Music source distributions and the CSP source distributions is 3 cm. Considering the two completely complementary data analysis approaches, the default inaccuracy of the inverse solution, the non-individual EEG head model and, hence, additional inaccuracies inferred by the forward model, one can consider both results as identical. However, the interaction profile of the sources can in contrast to SC and Wedge Music not be uncovered by using CSP and eLoreta.

Please bear in mind that strongly phase synchronized sources as revealed by SC and Wedge Music and sources with strong signal power can but do not necessarily have to coincide. In principle, both analysis approaches investigate different features inherited in the data. For example, it has been hypothesized in Engel et al. (2013) that source power co-fluctuation is an additional mechanism of functional brain interaction. One way to examine source power correlations is to compute the Hilbert transform of a band-pass filtered signal and to correlate the signal envelopes of different sources (Hipp et al., 2012). A different approach has recently been proposed by Dähne et al. (2014b) where spatial filters are generated to extract sources showing strong power correlations or, alternatively, where the power of one source correlates with an external, e.g. behaviorally relevant, target variable (Dähne et al., 2014a). A spatial filtering approach to extract source pairs with ImCoh different between data classes can be derived from the framework presented in Section 3.1 where the maximization of the ImCoh is described. This leads to a method termed Common Spatial Interacting Patterns (CSIP) and is described in details in the PhD thesis of Frank C. Meinecke (Meinecke, 2012).

6. Summary and discussion

> One good thing about music, is when it hits, you feel no pain.
>
> *(Bob Marley)*

Within this thesis, several multivariate data analysis techniques have been introduced, which can be used subsequently in order to determine synchronized, i.e. interacting brain sources from EEG or MEG measurements. Special attention is paid on artifacts of volume conduction, which occur due to the mixing of neuronal sources into measurement sensors. As a basis to circumvent this issue, the concept of the Imaginary Part of Coherency (ImCoh), which ignores instantaneous synchronization effects, underlies all methods presented within this work. Please note that a detailed discussion about statistical properties of the ImCoh itself and its drawbacks, such as the insensitivity to phase delays of π and 2π, can be found in Nolte et al. (2004).

In Section 3.1 it has been shown how the ImCoh can be maximized, which constitutes a theoretical framework with different application purposes. Based on this theory, various measures of functional connectivity have been derived: Maximized Imaginary Coherency (MIC), the Global Interaction Measure (GIM), the Multivariate Interaction Measure (MIM) and the Corrected Imaginary Part Of Coherency (cImCoh). All four exhibit two main properties. First, for an infinite number of data points, the measures vanish exactly if all sources are dynamically independent, regardless of the number of sources and of how the sources are mapped into sensors, provided that the mapping is instantaneous. In practice and for finite data sets, these measures will fluctuate around zero for independent sources. Then, the question arises whether a deviation from zero is statistically significant or not. This can be assessed for example with a Jackknife estimate of the standard deviation. Second, the measures are strictly invariant to linear and instantaneous transformations of the multivariate signals. Assuming that source activities can be expressed as a linear combination of sensor signals, it is therefore not necessary to actually find the respective inverse mapping because the result is independent of that mapping. At first sight, these findings might suggest that all effects of volume conduction on sensor level are now removed. In general, this is not the case because a hypothetical perfect demixing of sensors into sources is only possible when the mixing matrix is invertible. However, this is only true when there are fewer sources than sensors. The unavoidable presence of sensor noise and, even more critical, brain noise is a clear violation of that assumption. In practice, this means that one can only reduce the dependence of volume conduction but one cannot remove it completely. It remains open if other, for example nonlinear measures, can be constructed which are

invariant under mixing of sources into sensors even for more sources than sensors. Furthermore, the independence with respect to the forward mapping comes with the cost of losing spatial information. For example, GIM compresses multivariate data to a single number such that all spatial information is removed. One way to preserve the spatial information within this framework is to consider a subspace of the source topographies, spanned by the eigenvectors of the maximization approach described by Eq.(3.12) and Eq.(3.13). To conclude on the source topographies based on this subspace, additional assumptions are required. Appropriate approaches would be e.g. to minimize the spatial source overlap (see Marzetti et al., 2008) or to maximize effective connectivity (e.g. defined by the Phase Slope Index, see Nolte et al., 2008). Alternatives to exploit a data subspace derived from the maximization of the ImCoh, in order to conclude on the source locations, are presented in this thesis by introducing SC Music and Wedge Music.

Despite these limitations, the maximization approach has practical benefits as were presented in this work. In Section 4.2.3, it has been shown that the bivariate measures have a smaller bias towards remote interactions than classical ImCoh. Furthermore, GIM forms the basis of an automated frequency selection procedure, which is used throughout the whole thesis. Due to the invariance property and the data compression, GIM allows the comparison of subjects or measurement modalities, even with different sensor configurations. This has been shown by comparing simultaneously recorded EEG and MEG in Section 5.1.2, where more interactions seem to be observable with MEG. The special advantage of GIM, that the highly subject dependent source topographies are irrelevant, also makes grand averages and thereby group comparisons less complicated. In general, the maximization of the ImCoh within or across multivariate data sets increases the signal-to-noise ratio by construction, potentially leading to observations of interactions which are otherwise hidden in the noise. This is in particular exploited in order to construct data subspaces for subsequent source analysis and for the estimation of the number of interacting sources underlying the data. It has been shown in Sections 4.3 and 4.5 that applying an additional prewhitening outperforms standard approaches. Finally, especially the multivariate measures like MIC and MIM are well suited to be used in source space. For inverse solutions like beamforming or minimum norm based estimates, dipole orientations are not assumed to be known and a reconstructed dipole field contains activities in all three dipole directions for each voxel. Using the proposed measures, one can either fix the dipole orientation according to maximum ImCoh with MIC or estimate a total interaction between the 3-dimensional subspaces with MIM. This has been demonstrated in Section 4.7.

As stated above, connectivity measures derived from maximizing the ImCoh omit spatial information. Furthermore, it has been shown, e.g. in Section 4.1, that sensor level connectivity measures provide only little information about the underlying source locations. But as locations of brain sources play an important role concerning brain function due to functional segregation, inverse methods are needed. In this thesis, the novel method SC Music has been introduced expanding the existing approach Rap Music. To focus on synchronized sources in the frequency domain, a subspace based on the cross-spectrum is used instead of the covariance matrix.

To account for volume conduction artifacts, the respective imaginary part is used. A known issue of the Music algorithm is its failure when sources are correlated or coherent. In an extreme scenario, i.e. for fully correlated sources, the data subspace even becomes rank deficient. Therefore, SC Music projects out previously found sources except one and re-localizes the remaining source. This way, a localization bias due to other (correlated) sources can be avoided. It has been shown in simulations in Section 4.4 that SC Music outperforms Rap Music by correctly determining source locations of coherent sources. Furthermore, SC Music is in contrast to Rap Music able to deal with an odd number of sources. Please bear in mind that due to the antisymmetric nature of the ImCs, singular values occur in pairs. Hence, due to the proposed procedure to estimate the number of interacting sources based on the ImCs and surrogate data, it will always be even. However, other application scenarios of SC Music are conceivable where the capability of dealing with an odd number might be of advantage.

Next to SC Music, a further source localization technique termed Wedge Music has been introduced in this thesis. It can be used in combination with SC Music to determine which out of a given set of sources are synchronized in a bivariate sense. This is possible with either a scalar variant or with a scan over all brain voxels which incorporates a plausibility check. In principle, Wedge Music can also be used without prior source localization. However, to assess the practical applicability of this variant termed complete Wedge Music, the significant computational and accompanying time effort has to be accounted for. Recalling the considerations presented in Section 4.9, the data analysis of multiple subjects, including proper statistics, is with current computer hardware only feasible by using a prior source localization technique. However, if dipole orientations would have been fixed by additional, e.g. anatomical, constraints, one could perform scalar Wedge Music for all pairs of voxels. This would lead to a much lower computation time as the optimization over dipole orientations is avoided. Another possibility would be to define brain regions of interest based on prior knowledge, e.g. from other measurement modalities.

A main property of SC Music and Wedge Music is that both techniques are based entirely on the imaginary part of the cross-spectrum. Specifically, the methods do not depend on signal power as it is the case for the imaginary part of coherency because of its normalization. Such a dependency may induce conceptual problems when studying differences between two conditions: a difference between two ImCohs may be caused by the presence or absence of non-interacting sources which modify power but not the imaginary part of the cross-spectrum. In contrast, the imaginary part of the cross-spectrum itself is not affected systematically by non-interacting sources. Of course, random effects still exist which are suppressed by $\sqrt{K}$ for K independent averages but cannot be removed completely.

The feasibility of using SC and Wedge Music has been demonstrated for simulated data in Chapter 4 as well as for real data examples in Chapter 5. However, some questions remain open, such as how to perform group analysis. Although the results of Music scans cannot necessarily be interpreted as distributed source activity, it might be practically meaningful to average them over all measured subjects for a certain experiment. However, this approach might not lead to satisfying results

as EEG and MEG data usually contain large subject dependent variability and the resulting picture might get too blurry on average. The most convenient way to obtain a reasonable picture of interacting brain sources within a population of measured subjects would be to apply an appropriate clustering approach. A promising novel clustering approach worthwhile to consider for this purpose has recently been published by Rodriguez and Laio (2014).

An effect that can be observed in the results presented in this work is the sensitivity of SC and Wedge Music with respect to local interactions. Especially for the resting state data, relatively local interactions have been found. In principle, one could even think of applying Wedge Music on a single voxel. Because of the blurry source localization, a single voxel could include source activity from two interacting sources such that two dipoles with different orientation can be found to be interacting within a single voxel. In contrast to other methods, which are using fixed dipole orientations, Wedge Music does not have any bias towards remote or long distance interactions.

The last novel approach presented within this work is a method to statistically test the obtained results for a one-class problem, e.g. for resting state data. Whereas for two-class problems, e.g. differences between experimental conditions or a stimulus condition versus baseline, a permutation test is a reasonable approach, it is not applicable if only a single data class is available. Therefore, a resampling strategy has been introduced in Section 3.4 based on surrogate data. These data are constructed such that dependencies between source signals are destroyed whereas other data properties are maintained as good as possible. Based on these surrogate data, a bootstrap approach is used in order to estimate a sampling distribution which can be tested against the originally observed results. It might be of interest to quantify performance effects with respect to the particular ICA implementation used or with respect to prior filtering in the frequency domain. Nevertheless, it has been shown for simulated and real data that the introduced approach is well capable to assess statistical significance of results from brain connectivity analysis.

Please keep in mind that this thesis deals with *linear* functional connectivity measures applied on (quasi-)*stationary* signals. In general, EEG and MEG signals are highly non-stationary. Over time, one usually can observe large drifts for example due to drying gel for EEG measurements. However, relatively short epochs of data can be considered stationary, i.e. statistical moments stay constant within single epochs. Nevertheless, the assumption of stationarity might still be violated. One idea to circumvent this issue would be to construct measures that do not assume stationary data. This might even lead to yet unobserved phenomena underlying EEG or MEG data. A different approach would be to separate data into a stationary subspace and a non-stationary subspace (see von Bünau et al., 2009, for details). Concerning non-linearity, Chella et al. (2014) recently published a measure to investigate non-linear interactions robust to volume conduction artifacts by using the antisymmetric part of the bispectrum which can also be applied to investigate cross-frequency coupling. In general, cross-frequency coupling (see e.g. Jensen and Colgin, 2007), power envelope correlations (see e.g. Hipp et al., 2012; Dähne et al., 2014b) and phase-amplitude coupling (see e.g. Tort et al., 2010) seem to be additional mechanisms of functional communication between neural populations (see also Engel et al., 2013).

To conclude, the different data analysis techniques presented in this work are capable of having a practical impact to the field of experimental neuroscience. The robustness towards volume conduction artifacts, incorporated into inverse source reconstruction, is a unique feature and provides trustworthy results. Furthermore, the potential investigation of class differences in terms of connectivity is a huge benefit. Hence, these methods can be applied not only to investigate the resting brain. In addition to that, they can be used, for example, to contrast patients with healthy control subjects in order to understand and, finally, to alleviate neuronal diseases. Furthermore, these features allow to focus on a controlled experimental difference in order to cancel out common task irrelevant background activity. As most neuroscientific research is planned and conducted by targeting particular differences between subjects or tasks, the methods presented in this work are well suited to find broad application in the field of experimental neuroscientific research. In the end, they can serve to further understand the brain and everything coming along with that.

A. Appendix

In the appendix additional information is provided that is not necessary for the understanding of this thesis. However, the the reader might be interested to gain deeper knowledge concerning distinct aspects. Therefore, methods that are only touched peripherally within this thesis but are fundamental for the field of EEG/MEG source connectivity analysis are briefly introduced in the following. Furthermore, detailed proofs for data analysis methods presented in this work as well as coarse tabular overviews over existing methods are given in this appendix.

A.1. Forward calculation

In the present section the forward problem, introduced in Section 2.2.1, is described in more details following the notation and argumentation in Baillet et al. (2001). A complete overview of relevant physical laws used for the subsequent derivation is given in (Sarvas, 1987). Please note that the notation in this particular section slightly differs from the rest of this thesis. Capital bold letters denote higher dimensional functions instead of matrices.

As indicated in Table 2.1, frequencies of interest for electrophysiological recordings are typically well below 1 kHz. Thus, physics can be described by the quasi-static approximation of Maxwell's Equations (Plonsey and Heppner, 1967). The current flow $\mathbf{J}(\tilde{\mathbf{r}})$ at the location $\tilde{\mathbf{r}} = (\tilde{r}_x, \tilde{r}_y, \tilde{r}_z)^\mathsf{T}$ inside the brain can be connected to the magnetic field $\mathbf{B}(\mathbf{r})$ at a different location $\mathbf{r}$, i.e. the observation point or SQUID, by the Biot Savart law

$$\mathbf{B}(\mathbf{r}) = \frac{\mu_0}{4\pi} \int \mathbf{J}(\tilde{\mathbf{r}}) \times \frac{\mathbf{r} - \tilde{\mathbf{r}}}{\|\mathbf{r} - \tilde{\mathbf{r}}\|^3} \, \mathrm{d}\tilde{v} \tag{A.1}$$

with μ_0 being the vacuum permittivity, $\times$ denoting the vector cross product, and $\int \mathrm{d}\tilde{v}$ the integration over the volume $\tilde{v}$. The total current density in the head $\mathbf{J}(\tilde{\mathbf{r}})$ can be divided into two different current flows with distinct physiological meanings as described in Section 2.1.1. The primary current due to the original neural activity is denoted by $\mathbf{J}^P(\tilde{\mathbf{r}})$ and the volume current by $\mathbf{J}^V(\tilde{\mathbf{r}})$. These two currents form the total current density $\mathbf{J}(\tilde{\mathbf{r}})$ by

$$\begin{aligned} \mathbf{J}(\tilde{\mathbf{r}}) &= \mathbf{J}^P(\tilde{\mathbf{r}}) + \mathbf{J}^V(\tilde{\mathbf{r}}) && \text{(A.2)} \\ &= \mathbf{J}^P(\tilde{\mathbf{r}}) + \sigma(\tilde{\mathbf{r}}) E(\tilde{\mathbf{r}}) && \text{(A.3)} \\ &= \mathbf{J}^P(\tilde{\mathbf{r}}) - \sigma(\tilde{\mathbf{r}}) \nabla V(\tilde{\mathbf{r}}) && \text{(A.4)} \end{aligned}$$

with $\sigma(\tilde{\mathbf{r}})$ being the isotropic conductivity profile of the head tissues and ∇ being

the Nabla operator. Due to the quasi-static approximation, the electric field $E(\tilde{\mathbf{r}})$ is equal to the negative gradient of the electric potential $V(\tilde{\mathbf{r}})$ as indicated in Eq.(A.4).

Assuming that the head consists of a distinct set of regions where each has a constant and scalar conductivity σ_i, $i = 1 \dots 3$, representing the brain, skull and scalp, Equation A.4 can now be rewritten as

$$\mathbf{B}(\mathbf{r}) = \mathbf{B}_0(\mathbf{r}) + \frac{\mu_0}{4\pi} \sum_{ij} (\sigma_i - \sigma_j) \int_{S_{ij}} V(\tilde{\mathbf{r}}) \frac{\mathbf{r} - \tilde{\mathbf{r}}}{\|\mathbf{r} - \tilde{\mathbf{r}}\|^3} \times \mathbf{d}\tilde{\mathbf{S}}_{ij} \tag{A.5}$$

with $j = i + 1$, which indicates the sum over the borders of the shells, and $\tilde{\mathbf{S}}_{ij}$ is the surface between the shell compartments i and j. $\mathbf{B}_0(\mathbf{r})$ represents the magnetic field with respect to only the primary current $\mathbf{J}^{\mathbf{P}}(\tilde{\mathbf{r}})$. The second term is the contribution of the volume current to the magnetic field, that is formed as a sum of surface integrals over the boundaries of the different head tissues scalp, skull and brain.

Using Equation A.5 and given the primary current distribution, which is in fact the moment and location of the equivalent current dipole, the magnetic field $\mathbf{B}(\mathbf{r})$ at the location r can be determined. A similar equation can be derived for the electric potential $V(\mathbf{r})$ (Hamalainen, 1992; Geselowitz, 1970), which leads to

$$(\sigma_i + \sigma_j) V(\mathbf{r}) = 2\sigma_0 V_0(\tilde{\mathbf{r}}) - \frac{1}{2\pi} \sum_{ij} (\sigma_i - \sigma_j) \int_{S_{ij}} V(\tilde{\mathbf{r}}) \frac{\mathbf{r} - \tilde{\mathbf{r}}}{\|\mathbf{r} - \tilde{\mathbf{r}}\|^3} \cdot \mathbf{d}\tilde{\mathbf{S}}_{ij} \tag{A.6}$$

again with $j = i + 1$ and $\cdot$ denoting the scalar product. Equations A.5 and A.6 are the general eqations for the forward problem. When a primary current distribution $\mathbf{J}^P(\tilde{\mathbf{r}})$ is specified, the primary potential $V_0(\mathbf{r})$ and the primary magnetic field $\mathbf{B_0}(\mathbf{r})$ can be calculated by

$$V_0(\mathbf{r}) = \frac{1}{4\pi\sigma_0} \int \mathbf{J}^P(\tilde{\mathbf{r}}) \cdot \frac{\mathbf{r} - \tilde{\mathbf{r}}}{\|\mathbf{r} - \tilde{\mathbf{r}}\|^3} \, d\tilde{\mathbf{r}} \tag{A.7}$$

and

$$\mathbf{B_0}(\mathbf{r}) = \frac{\mu_0}{4\pi} \int \mathbf{J}^P(\tilde{\mathbf{r}}) \times \frac{\mathbf{r} - \tilde{\mathbf{r}}}{\|\mathbf{r} - \tilde{\mathbf{r}}\|^3} \, d\tilde{\mathbf{r}}. \tag{A.8}$$

Finally, the primary potential from A.7 can be used to compute the potentials on all surfaces as described in Equation A.6 in order to solve the EEG forward problem. The same way, Equations A.8 and A.5 can be used to compute the magnetic fields outside the head and, hence, solve the MEG forward problem. Please note that by applying a realistically shaped head model, the corresponding equations are not analytically solvable anymore (see Section 2.2.1).

A.2. Derivation of the spatial filter for beamforming

In this section it is shown how to derive the spatial filter that is used for LCMV beamforming. In contrast to Section 2.3.2, not the vector beamformer is used that

simultaneously originates a filter for all the unit directions. Here, a scalar one is described. Therefore, the basic quantities are slightly refined. However, the derivation of the vector beamformer can be done analogously.

Let's consider the zero mean data matrix $\mathbf{X} \in \mathbb{R}^{N \times T}$ (N: number of measurement channels; T: number of samples over time), and the covariance matrix $\mathbf{\Sigma} \in \mathbb{R}^{N \times N}$ estimated by $\mathbf{\Sigma} = \langle \mathbf{X}\mathbf{X}^\mathsf{T} \rangle$. Furthermore, let's consider a specific source voxel m with the leadfield $\mathbf{a} \in \mathbb{R}^{N \times 1}$ for a single direction. Then, the spatial filter $\mathbf{w} \in \mathbb{R}^{N \times 1}$ passing the signal at voxel m with unit gain and simultaneously minimizing over total source power can be expressed by

$$\mathbf{w} = \arg\min_{\mathbf{w}} \left(\mathbf{w}^T \mathbf{\Sigma} \mathbf{w}\right) \text{ subject to } \mathbf{w}^T \mathbf{a} = 1. \tag{A.9}$$

The minimization problem can now be reformulated using the methods of Lagrange multipliers (Lasdon, 1970). The cost function $\mathbf{L}(\mathbf{w}, \zeta)$, including the constant ζ, results in

$$\mathbf{L}(\mathbf{w}, \zeta) = \mathbf{w}^T \mathbf{\Sigma} \mathbf{w} + 2\zeta(\mathbf{w}^T \mathbf{a} - 1). \tag{A.10}$$

Setting the partial derivatives to zero yields for symmetric $\mathbf{\Sigma}$ to

$$\frac{\partial \mathbf{L}}{\partial \mathbf{w}} = 2\mathbf{\Sigma}\mathbf{w} + 2\zeta\mathbf{a} = 0 \tag{A.11}$$

and

$$\mathbf{w} = -\zeta \mathbf{\Sigma}^{-1} \mathbf{a} \tag{A.12}$$

Transposing Eq.(A.12) and exploiting the symmetry of $\mathbf{\Sigma}$ results in

$$\begin{aligned} \mathbf{w}^\mathsf{T} &= -\zeta^\mathsf{T} (\mathbf{\Sigma}^{-1} \mathbf{a})^\mathsf{T} \\ &= -\zeta \mathbf{a}^\mathsf{T} (\mathbf{\Sigma}^{-1})^\mathsf{T} \\ &= -\zeta \mathbf{a}^\mathsf{T} \mathbf{\Sigma}^{-1}. \end{aligned} \tag{A.13}$$

Setting the partial derivative with respect to ζ to zero gives

$$\frac{\partial \mathbf{L}}{\partial \zeta} = \mathbf{w}^\mathsf{T} \mathbf{a} - 1 = 0 \Leftrightarrow \mathbf{w}^\mathsf{T} \mathbf{a} = 1. \tag{A.14}$$

Plugging Eq.(A.13) in Eq.(A.14) gives

$$(-\zeta \mathbf{a}^\mathsf{T} \mathbf{\Sigma}^{-1}) \mathbf{a} = 1 \tag{A.15}$$

and

$$\zeta = -(\mathbf{a}^\mathsf{T} \mathbf{\Sigma}^{-1} \mathbf{a})^{-1}. \tag{A.16}$$

Finally, inserting ζ from Eq.(A.16) in Eq.(A.12) leads to the solution for a scalar beamformer

$$\mathbf{w} = \mathbf{\Sigma}^{-1} \mathbf{a} (\mathbf{a}^\mathsf{T} \mathbf{\Sigma}^{-1} \mathbf{a})^{-1} \tag{A.17}$$

which is formally equivalent to the vector one presented in Eq.(2.8) assuming matrix

quantities. Please remember that Eq.(A.17) denotes the spatial filter for a specific voxel and a specific direction and has to be evaluated iteratively over voxels and directions to obtain the full spatial filter.

A.3. Minimum norm based inverse estimates

Let's refine the source mixing model of EEG and MEG described in Eq. (2.1) slightly to account for the unknown dipole orientation. At a single time instance one can observe a signal at N measurement channels $\mathbf{x} \in \mathbb{R}^{N\times 1}$. The source signal $\mathbf{s} \in \mathbb{R}^{3M\times 1}$ within the brain consists of M pre-defined volume elements (voxels) at which each dipolar source has a three-dimensional orientation. The leadfield, i.e. the mapping from sources to sensors according to the forward model (see Section 2.2.1), is expressed by the matrix $\mathbf{A} \in \mathbb{R}^{N\times 3M}$. This, again, leads to the linear mixing model

$$\mathbf{x} = \mathbf{A}\mathbf{s}. \tag{A.18}$$

Please note that the distinction between noise and sources is neglected here in contrast to the notation in Section 2.2.2 as it is kind of arbitrary. Obviously, brain noise is also comprised out of sources inside the brain. However, it is assumed that the data has been cleaned from external artifacts such as eye blinks, 50Hz line noise, muscle activity and movement artifacts.

The estimation of the spatial filter $\mathbf{W} \in \mathbb{R}^{N\times 3M}$ (see Section 2.2.2) and, hence, the sources $\tilde{\mathbf{s}} = \mathbf{W}^{\mathsf{T}}\mathbf{x}$ can be approximated by minimizing source (and implicitly noise) power while explaining the measured data $\mathbf{x}$. This additional assumption necessary to solve the undetermined system of equations (A.18) leads to

$$\tilde{\mathbf{s}}_{MN} = \arg\min_{s} \|\mathbf{s}\|_2^2 \;\text{ subject to }\; \mathbf{x} = \mathbf{A}\mathbf{s}. \tag{A.19}$$

with $\|.\|_2$ being the ℓ^2-norm. Eq.(A.19) can be solved by calculating the Moore–Penrose pseudoinverse of the matrix $\mathbf{A}$, denoted as $(.)^+$ (Penrose, 1955) and given by

$$\mathbf{A}^+ = (\mathbf{A}^{\mathsf{T}}\mathbf{A})^{-1}\mathbf{A}^{\mathsf{T}}. \tag{A.20}$$

Finally, the source estimates are obtained by

$$\tilde{\mathbf{s}} = \mathbf{A}^+\mathbf{x} \tag{A.21}$$

which is referred to as a Minimum Norm Estimate (MNE). If one assumes Gaussian noise with zero mean and variance σ^2, i.e. $\boldsymbol{\eta}(t) \sim \mathcal{N}(\mathbf{0}, \sigma^2\mathbf{I}_N)$, the minimum norm solution can also be expressed as a maximum-likelihood estimation (Aldrich, 1997).

It is argued in Hauk (2004) that a rather simple minimum norm estimate is a valuable choice for EEG/MEG source estimation if no prior knowledge about the sources is present. However, minimum norm based source estimation can be significantly improved by a proper regularization. One way to achieve regularization is to add additional constraints to the minimization in Eq.(A.19) which leads to a

reduction of problem complexity (Tikhonov and Arsenin, 1977). It can be interpreted in different ways: First of all, it assures numerical stability for inverting matrices that are potentially close to singular. This is especially the case as the forward mapping for close by dipoles with similar orientations might be very similar. Second, it can be seen as a tool to avoid fitting noise components of the data, i.e. to prevent overfitting and, hence, assures generalizability of the solution. Third, prior knowledge or assumptions about the source behavior can be incorporated due to regularization. A famous way of regularizing is the Weighted Minimum Norm Estimate (WMNE) defined by

$$\tilde{\mathbf{s}}_{WMN} = \arg\min_{s} \|\mathbf{x} - \mathbf{A}\mathbf{s}\|_2^2 + \kappa \|\mathbf{\Omega}\mathbf{s}\|_2^2 . \tag{A.22}$$

where $\kappa \geq 0$ controls the impact of the regularization term relative to the minimization of the error (Jeffs et al., 1987; Ioannides et al., 1990). It often depends on an estimate of the noise covariance or is determined by cross-validation. Hence, WMNE is in contrast to the MNE usually a data-driven or adaptive method, although it can also be applied choosing a fixed κ and a pre-defined non data driven $\mathbf{\Omega}$. For example, $\mathbf{\Omega} \in \mathbb{R}^{3M \times 3M}$ can be chosen to be a depth weighting matrix that used to compensate a bias towards superficial sources (Hämäläinen and Ilmoniemi, 1994; Lin et al., 2006). The electric or magnetic field decays quadratically with distance from source to sensor. Therefore, a deep source has to be way stronger in order to produce the same measurement at the scalp than a superficial one. $\mathbf{\Omega}$ is often chosen to diminish this effect by assigning stronger weights to deeper sources. An assumption underlying the WMNE is smoothness of the source distribution which is implicitly incorporated by the ℓ^2 norm in the regularization term. The idea is that neighboring voxels show similar activation and no abrupt changes occur in close by grid points. This reasonable assumption is explicitly modeled in Low Resolution Brain Electromagnetic Tomography (Loreta) where the regularization term consists of a discrete Laplace operator that implements spatial smoothing. Improvements of Loreta are Standardized Low Resolution Brain Electromagnetic Tomography (sLoreta) introduced in Pascual-Marqui (2002) and eLoreta introduced in Pascual-Marqui (2007a). It has been demonstrated that the maximum of an sLoreta source distribution matches a single dipolar source in a noise-free environment with zero error in terms of the Euclidian distance. sLoreta is based on the WMNE solution (Eq.(A.22)) with $\mathbf{\Omega} = \mathbf{I}_{3M}$ as smoothness constraint which is in the second step 'standardized' to obtain an estimation of the power $\tilde{\mathbf{s}}_p$ at each voxel. The power estimate at voxel $m = 1 \ldots M$ is given by

$$\tilde{p}_m = (\tilde{\mathbf{s}}_{WMN,m})^{\mathsf{T}} \mathbf{\Sigma}_m^{-1} (\tilde{\mathbf{s}}_{WMN,m}) \tag{A.23}$$

with $\mathbf{\Sigma}_m \in \mathbb{R}^{3\times 3}$ being the covariance matrix at voxel m occurring in block form on the diagonal of the matrix

$$\mathbf{\Sigma} = \mathbf{A}^{\mathsf{T}} (\mathbf{A}\mathbf{A}^{\mathsf{T}} + \kappa \mathbf{H}_N)^{+} \mathbf{A} \tag{A.24}$$

as derived in (Pascual-Marqui, 2002). Please note that for all Loreta derivates and

EEG measurements, common average referencing is required such that zero-error and other properties are met. Re-referencing can be realized by linearly transforming the measured data and the leadfields with the operator

$$\mathbf{H}_N := \mathbf{I}_N - \frac{\mathbf{1}_N \mathbf{1}_N^\mathsf{T}}{\mathbf{1}_N^\mathsf{T} \mathbf{1}_N} \tag{A.25}$$

with $\mathbf{1}_N \in \mathbb{R}^{N \times 1}$ being a row vector of length N containing ones. The reference operator $\mathbf{H}$ is also used in Eq.(A.26). Please note that for MEG this is not necessary as MEG is free of reference.

The concept of eLoreta is different. Weights are determined from the analytical solution of the WMNE given by

$$\mathbf{W}_{eloreta} = \mathbf{\Omega}^{-1}\mathbf{A}(\mathbf{A}\mathbf{\Omega}^{-1}\mathbf{A}^\mathsf{T} + \kappa\mathbf{H})^{+}. \tag{A.26}$$

It is derived in Pascual-Marqui (2007a) that weights producing an inverse solution with zero localization error (meaning that the maximum of the source distribution has zero Euclidean distance to the true dipole in case of a single dipole only) have to satisfy the following set of equations for $m = 1 \dots M$:

$$\mathbf{\Omega}_m^2 = \mathbf{A}_m^\mathsf{T}(\mathbf{A}\mathbf{\Omega}^{-1}\mathbf{A}^\mathsf{T} + \kappa\mathbf{H})^{+}\mathbf{A}_m. \tag{A.27}$$

Here, $\mathbf{\Omega}_m \in \mathbb{R}^{3\times 3}$ denotes a block matrix around the M diagonal elements of $\mathbf{\Omega}$. An iterative and quickly converging algorithm described in Pascual-Marqui (2007a) solves for the weights $\mathbf{\Omega}$ which are plugged into Eq.(A.26) to form the eLoreta spatial filter.

As already mentioned, using the ℓ^2-norm in the regularization term in Eq.(A.22) leads to smooth and, therefore, blurry source power distributions. An alternative assumption is to generate sparse source distributions as they are closer to the equivalent current dipole model. This can be achieved by using the ℓ^1-norm (i.e. "taxi-driver norm") leading to

$$\tilde{\mathbf{s}}_{MCE} = \arg\min_{s} \|\mathbf{x} - \mathbf{A}\mathbf{s}\|_2^2 + \kappa \|\mathbf{\Omega}\mathbf{s}\|_1 . \tag{A.28}$$

This approach is known as the lasso regularization (Tibshirani, 1994). The lasso estimate incorporates the assumption of spatially Laplacian distributed sources which are way more peaky than Gaussian distributions and have longer tails. In the context of EEG/MEG source reconstruction the idea is initially employed in a method called weighted Minimim Current Estimate (MCE) (Matsuura and Okabe, 1995). Additionally, Focal Underdetermined System Solution (FOCUSS) uses the assumption of sparseness in a recursive re-weighting approach (Gorodnitsky et al., 1995). Finally, there exist methods trying to find a trade-off between sparsity and smoothness. One of them is S-Flex, introduced in Haufe et al. (2011).

A.4. Overview of source reconstruction techniques

The following table gives a non-exhaustive overview of existing source localization approaches and provides a sketch of the large variety of methods in the field.

Name	Abbreviation	Publication
Minimum norm based methods		
Minimum Norm Estimate	MNE	e.g. Aldrich (1997); Hauk (2004)
Weighted Minimum Norm Estimate	WMNE	Jeffs et al. (1987); Ioannides et al. (1990)
Low resolution brain electromagnetic tomography	LORETA	Pascual-Marqui et al. (2002)
Standardized low resolution brain electromagnetic tomography	sLORETA	Pascual-Marqui (2002)
Exact low resolution brain electromagnetic tomography	eLORETA	Pascual-Marqui et al. (2011)
Local Autoregressive Averages	LAURA	Grave de Peralta Menendez et al. (2004)
Focal Vector Field Reconstruction	FVR	Haufe et al. (2008)
Electric Activity Imaging	ELECTRA	Grave de Peralta Menendez et al. (2000)
Minimum Current Estimate	MCE	Matsuura and Okabe (1995)
Focal Underdetermined System Solution	FOCUSS	Gorodnitsky et al. (1995)
Source reconstruction with Spatial Flexibity	S-Flex	Haufe et al. (2011)
Beamformer solutions		
Linear Contraint Minimum Variance beamformer	LVMV	Van Veen et al. (1997); Spencer et al. (1992)
Synthetic Aperture Magnetometry	SAM	Vrba and Robinson (2001)
Anatomically Constraint Beamforming	ACB	Hillebrand and Barnes (2003)
Nulling Beamformer	Nulling	Hui and Leahy (2006)
Dynamic Imaging of Coherent Sources	DICS	Gross et al. (2001)
Music based methods		
Multiple Signal Classification	MUSIC	Mosher et al. (1999b)
Recursively Applied and Projected Music	RAP-MUSIC	Mosher and Leahy (1999)
Bayesian methods		
Champagne	Champagne	Owen et al. (2012)
Bayesian Inference	BI	Schmidt et al. (1999)
Parametrized fitting procedures		
Dipole Fitting	DF	Scherg and Berg (1991)
Multipole Fitting	MF	Jerbi et al. (2004)

A.5. Overview of connectivity measures

The following table gives an overview of existing measures used in the context of EEG/MEG connectivity analysis. Again, this list is not exhaustive. Please note that the focus within this thesis lies on linear methods for functional connectivity.

Name	Abbreviation	Publication
Functional connectivity		
Linear		
Coherence	Coherence	Nunez et al. (1997)
Phase Locking Value	PLV	Lachaux et al. (1999)
Imaginary Part of Coherency	ImCoh	Nolte et al. (2004)
Lagged Phase Coherence	LPC	Pascual-Marqui (2007b)
Phase Lag Index	PLI	Stam et al. (2007)
Weighted Phase Lag Index	WPLI	Vinck et al. (2011)
Sparsely Connected Sources Analysis	SCSA	Haufe et al. (2010)
Non Linear		
Transfer entropy	TE	Vicente et al. (2011)
Orthogonalized Power Envelope Correlations	OPEC	Hipp et al. (2012)
Generalized Synchronization	GS	Pereda et al. (2005)
Continuity Measure	CM	Netoff et al. (2006)
Synchronization Likelihood	SL	Stam and van Dijk (2002)
Mutual Information	MI	Li (1990)
Effective Connectivity		
Phase Slope Index	PSI	Nolte et al. (2008)
Granger Causality	GC	Granger (1969, 1980); Hesse et al. (2003)
Partial Directed Coherence	PDC	Baccala and Sameshima (2001)
Direct Transfer Function	DTF	Kaminski and Blinowska (1991)
Transfer Entropy	GS	Schreiber (2000)
Dynamic Causal Modeling[1]	DCM	Friston et al. (2003)

[1] In fact, DCM combines source reconstruction and connectivity.

A.6. Maximizing the ImCoh

In the following it is demonstrated how to find the maxima of the function

$$f(\mathbf{a},\mathbf{b}) = \frac{\mathbf{a}^\top \mathbf{E}\mathbf{b}}{\|\mathbf{a}\|\|\mathbf{b}\|}. \tag{A.29}$$

In contrast to Section 3.1.1, $\mathbf{E} := \mathbf{D}^I_{AB}$ is defined for notation simplicity. Maxima of Eq.(A.29) can be obtained by setting the partial derivatives with respect to $\mathbf{a}$ and $\mathbf{b}$ to zero. Here, maximization is shown by using Lagrange multipliers. The nominator of Eq.(A.29) is maximized with the boundary condition that the weight vectors $\mathbf{a}$ and $\mathbf{b}$ are normalized, i.e. $\|\mathbf{a}\| = \|\mathbf{b}\| = 1$. Hence, the cost function in vector and index notation is defined as

$$\begin{aligned}
\mathbf{L}(\mathbf{a},\mathbf{b}) &= \mathbf{a}^\top \mathbf{E}\mathbf{b} + \lambda_A(\|\mathbf{a}\| - 1) + \lambda_B(\|\mathbf{b}\| - 1) \\
&= \sum_{i,j} a_i E_{ij} b_j - \lambda_A \left(\sqrt{\sum_i a_i^2} - 1 \right) - \lambda_B \left(\sqrt{\sum_i b_i^2} - 1 \right) \\
&= \sum_{i,j} a_i E_{ij} b_j - \lambda_A \left(\sum_i a_i^2 - 1 \right) - \lambda_B \left(\sum_i b_i^2 - 1 \right)
\end{aligned} \tag{A.30}$$

Please note that the square root can be neglected as $\|\mathbf{a}\| = \|\mathbf{a}\|^2 = 1$. Taking the derivative of $\mathbf{L}(\mathbf{a},\mathbf{b})$ with respect to the k-th element of $\mathbf{a}$ denoted as a_k leads to

$$\begin{aligned}
\frac{\partial \mathbf{L}}{\partial a_k} &= \sum_{i,j} \delta_{ik} E_{ij} b_j - \lambda_A \sum_i \delta_{ik} a_i \qquad \forall\, k = 1 \ldots N_A \\
&= \sum_j E_{kj} b_j - \lambda_A a_k \qquad \forall\, k = 1 \ldots N_A \\
&= \mathbf{E}\mathbf{b} - \lambda_A \mathbf{a}
\end{aligned} \tag{A.31}$$

with δ_{ij} being the Kronecker delta, defined as

$$\delta_{ij} := \begin{cases} 1 & : i = j \\ 0 & : i \neq j. \end{cases} \tag{A.32}$$

Furthermore, setting Eq.(A.31) to zero gives

$$\mathbf{E}\mathbf{b} = \lambda_A \mathbf{a}. \tag{A.33}$$

Performing the same calculation for b_k leads to

$$\mathbf{E}^\top \mathbf{a} = \lambda_A \mathbf{b}. \tag{A.34}$$

Now, one can solve for λ by left-multiplying Eq.(A.33) with $\mathbf{a}^\mathsf{T}$, which gives with the normalization constraint $\|\mathbf{a}\| = \|\mathbf{b}\| = 1$

$$\lambda_A = \mathbf{a}^\mathsf{T}\mathbf{E}\mathbf{b}. \tag{A.35}$$

Respectively, left-multiplying Eq.(A.34) with $\mathbf{b}^\mathsf{T}$ results in

$$\lambda_B = (\mathbf{b}^\mathsf{T}(\mathbf{E}^\mathsf{T}\mathbf{a}))^\mathsf{T} = (\mathbf{E}^\mathsf{T}\mathbf{a})^\mathsf{T}\mathbf{b} = \mathbf{a}^\mathsf{T}\mathbf{E}\mathbf{b}. \tag{A.36}$$

From Eq.(A.35) and Eq. (A.36) one can observe that

$$\lambda_A = \lambda_B = \mathbf{a}^\mathsf{T}\mathbf{E}\mathbf{b} = \frac{\mathbf{a}^\mathsf{T}\mathbf{E}\mathbf{b}}{\|\mathbf{a}\|\|\mathbf{b}\|} =: \lambda \tag{A.37}$$

and see that λ is equal to the imaginary part of the coherency.

A.7. Equivalence of LPC and GIM in the bivariate case

As introduced in Section 3.1.8, the connectivity measure called Lagged Phase Coherence proposed by Pascual-Marqui (2007b) can be written in the bivariate case for the two time series p and q as

$$LPC_{pq} = 1 - \frac{\left[\det\left(\mathbf{S}_{pq}\right) / \det\begin{pmatrix} S_{pp} & 0 \\ 0 & S_{qq} \end{pmatrix}\right]}{\left[\det(\mathbf{S}^R_{pq}) / \det\begin{pmatrix} S^R_{pp} & 0 \\ 0 & S^R_{qq} \end{pmatrix}\right]} \tag{A.38}$$

With the definition of the bivariate cross-spectrum

$$\mathbf{S}_{pq} = \begin{pmatrix} S_{pp} & S^R_{pq} + iS^I_{pq} \\ S^R_{pq} - iS^I_{pq} & S_{qq} \end{pmatrix} = \begin{pmatrix} S_{pp} & S^R_{pq} \\ S^R_{pq} & S_{qq} \end{pmatrix} + i\begin{pmatrix} 0 & S^I_{pq} \\ -S^I_{pq} & 0 \end{pmatrix} \tag{A.39}$$

the LPC reads

$$\begin{aligned} LPC_{pq} &= 1 - \frac{S_{pp}S_{qq} - \left(S^R_{pq} - iS^I_{pq}\right)\left(S^R_{pq} + iS^I_{pq}\right)}{S_{pp}S_{qq} - S^R_{pq}S^R_{pq}} \\ &= 1 - \frac{S_{pp}S_{qq} - \left((S^R_{pq})^2 + (S^I_{pq})^2\right)}{S_{pp}S_{qq} - S^R_{pq}S^R_{pq}} \\ &= \frac{\left(S_{pp}S_{qq} - S^R_{pq}S^R_{pq}\right) - \left(S_{pp}S_{qq} - \left((S^R_{pq})^2 + (S^I_{pq})^2\right)\right)}{S_{pp}S_{qq} - (S^R_{pq})^2} \\ &= \frac{(S^I_{pq})^2}{S_{pp}S_{qq} - (1 - \frac{(S^R_{pq})^2}{S_{pp}S_{qq}})} \\ &= \frac{(C^I_{pq})^2}{1 - (C^R_{pq})^2} \end{aligned} \tag{A.40}$$

where C^I_{pq} and C^R_{pq} denote the imaginary and real part of coherency as defined in Eq.(2.19).

A.8. Relationship of WPLI and GIM

In the following it is shown that for Gaussian distributed data and two channels p and q with the cross-spectrum $\mathbf{S}_{pq}$ (see e.g. Eq.(A.39)) and for an infinite number of data points, WPLI assumes the value

$$\text{WPLI} = \frac{2|\theta|}{1 + \theta^2} \tag{A.41}$$

with

$$\theta = \frac{S^I_{pq}}{\sqrt{S_{pp}S_{qq} - (S^R_{pq})^2}}. \tag{A.42}$$

Since the WPLI is invariant to real valued linear transformations as shown in Section 3.1.8, one can, without loss of generality, transform to a coordinate system such that the cross-spectrum in this coordinate system has the form

$$\tilde{\mathbf{S}} = \begin{pmatrix} 1 & i\theta \\ -i\theta & 1 \end{pmatrix} \tag{A.43}$$

with θ given in Eq.(A.42). With

$$\mathrm{WPLI}_{pq} = \frac{\left|\left\langle \Im(x_p x_q^*)\right\rangle\right|}{\left\langle\left|\Im(x_p x_q^*)\right|\right\rangle} \tag{A.44}$$

the numerator is the absolute value of imaginary part of the cross spectrum:

$$\left|\left\langle \Im(x_p x_q^*)\right\rangle\right| = |\theta|\,. \tag{A.45}$$

The denominator reads in its explicit form

$$\left\langle\left|\Im(x_p x_q^*)\right|\right\rangle = \frac{1}{\left|det(\tilde{\mathbf{S}})\right|\pi^2}\int\left|\Im(z_p z_q^*)\right| e^{\left(-\mathbf{z}^\dagger\tilde{\mathbf{S}}^{-1}\mathbf{z}\right)} Dz_p Dz_q \tag{A.46}$$

where $Dz_p = dz_p^R dz_p^I$ indicates integration over the complex plane spanned by real and imaginary parts of z_p, and $\mathbf{z} = \left[z_p\ z_q\right]^\mathsf{T}$. The coordinates are now transformed with a (complex valued) unitary transformation matrix $\mathbf{U}$ which diagonalizes $\tilde{\mathbf{S}}$:

$$\mathbf{y} = \mathbf{U}^\dagger\mathbf{z} \tag{A.47}$$

with

$$\mathbf{U} = \frac{1}{\sqrt{2}}\begin{pmatrix} 1 & 1 \\ i & -i \end{pmatrix} \tag{A.48}$$

With these coordinates and using $\left|\det(\tilde{\mathbf{S}})\right| = 1-\theta^2$ the integral in Eq.(A.46) becomes

$$\begin{aligned}\left\langle\Im\left|(x_p x_q^*)\right|\right\rangle \quad &= \quad \frac{1}{2(1-\theta^2)\pi^2}\quad \cdots \\ &\cdots \quad \int\left|\left|y_p\right|^q - \left|y_q\right|^2\right| e^{\left(-\frac{|y_p|^2}{1-\theta}-\frac{|y_q|^2}{1+\theta}\right)} Dy_p Dy_q\end{aligned} \tag{A.49}$$

The function to be integrated has no dependence on phases which can be integrated out giving a factor of $4\pi^2$. Using spherical coordinates, $y_j = r_j e^{i\Phi_j}$ for $j = p, q$ the integral reduces to

$$\left\langle\Im\left|(x_p x_q^*)\right|\right\rangle = \frac{2}{(1-\theta^2)}\int_0^\infty\int_0^\infty\left|r_p^2 - r_q^2\right| e^{\left(-\frac{r_p^2}{1-\theta}-\frac{r_q^2}{1+\theta}\right)} r_q dr_q r_p dr_p. \tag{A.50}$$

The term $\left|r_p^2 - r_q^2\right|$ leads to a splitting of the integral depending on whether r_p is bigger or smaller than r_q. A convenient way to write this is

$$\left\langle \Im \left| (x_p x_q^*) \right| \right\rangle = \frac{2}{(1-\theta^2)} \int_0^\infty r_p e^{\left(-\frac{r_p^2}{1-\theta}\right)} * \quad \ldots$$

$$\ldots \quad \left[\int_0^\infty r_q \left(r_q^2 - r_p^2\right) e^{\left(-\frac{r_q^2}{1+\theta}\right)} dr_q + 2 \int_0^{r_p} r_q \left(r_p^2 - r_q^2\right) e^{\left(-\frac{r_q^2}{1+\theta}\right)} dr_q \right] dr_p \quad \text{(A.51)}$$

The remaining integrals can be evaluated using the following relationships

$$\begin{aligned} \int_0^y x e^{(-x^2\gamma)} dx &= \frac{1}{2\gamma}(1 - e^{(-y^2\gamma)}) \\ \int_0^y x^3 e^{(-x^2\gamma)} dx &= \frac{1}{2\gamma^2}(1 - e^{(-y^2\gamma)}) - \frac{y^2}{2\gamma^2} e^{(-y^2\gamma)} \end{aligned} \quad \text{(A.52)}$$

with $\gamma := \frac{1}{1+\theta}$. Applying the integration rules in Eq.(A.52) several times for the evaluation of Eq.(A.51) results in

$$\langle \Im | (x_1 x_2^*) | \rangle = \frac{1+\theta^2}{2}. \quad \text{(A.53)}$$

Together with the numerator in Eq.(A.45), this leads to the final result

$$WPLI = \frac{2|\theta|}{1+\theta^2} \quad \text{(A.54)}$$

also provided in Equation(3.51) in Section 3.1.8.

A.9. Optimizing the dipole direction

In this Section it shown in more details how the dipole direction at source voxel m can be chosen such that the ImCoh between a source at voxel p (determined e.g. by SC Music in a prior step) and a source at voxel m is maximized. Recalling the definitions of the cross-spectra

$$\left\langle z_p z_m^\dagger \right\rangle = \mathbf{w}_p^\mathsf{T} \mathbf{S} \mathbf{W}_m \mathbf{d}_m =: \mathbf{E}_{pm} \quad \text{(A.55)}$$

and

$$\left\langle z_p z_p^\dagger \right\rangle = \mathbf{w}_p^\mathsf{T} \mathbf{S} \mathbf{w}_p =: \mathbf{E}_{pp} \quad \text{(A.56)}$$

and

$$\left\langle z_m z_m^\dagger \right\rangle = \mathbf{d}_m^\mathsf{T} \mathbf{W}_m^\mathsf{T} \mathbf{S} \mathbf{W}_m \mathbf{d}_m =: \mathbf{E}_{mm}, \tag{A.57}$$

the imaginary part of coherency depending on the dipole direction $\mathbf{d}_m$ at grid point m is given by

$$\mathbf{C}_{pm}^I(\mathbf{d}_m) = \frac{\mathbf{w}_p^\mathsf{T} \mathbf{S}^I \mathbf{W}_m \mathbf{d}_m}{\left(\mathbf{w}_p^\mathsf{T} \mathbf{S}^R \mathbf{w}_p\right)^{\frac{1}{2}} \left(\mathbf{d}_m^\mathsf{T} \mathbf{W}_m^\mathsf{T} \mathbf{S}^R \mathbf{W}_m \mathbf{d}_m\right)^{\frac{1}{2}}} = \frac{\mathbf{E}_{pm}^I}{(\mathbf{E}_{pp}^R)^{\frac{1}{2}} (\mathbf{E}_{mm}^R)^{\frac{1}{2}}}. \tag{A.58}$$

with superscripts I and R denoting imaginary and real part of a complex valued matrix. Using the quotient rule, the derivative results in

$$\frac{\partial \mathbf{C}_{pm}^I}{\partial \mathbf{d}_m} = \frac{\left(\frac{\partial \mathbf{E}_{pm}^I}{\partial \mathbf{d}_m}\right) \left((\mathbf{E}_{pp}^R)^{\frac{1}{2}} (\mathbf{E}_{mm}^R)^{\frac{1}{2}}\right) - \mathbf{E}_{pm}^I \left(\frac{\partial}{\partial \mathbf{d}_m} (\mathbf{E}_{pp}^R)^{\frac{1}{2}} (\mathbf{E}_{mm}^R)^{\frac{1}{2}}\right)}{(\mathbf{E}_{pp}^R)(\mathbf{E}_{mm}^R)} \tag{A.59}$$

with

$$\frac{\partial \left((\mathbf{E}_{pp}^R)^{\frac{1}{2}} (\mathbf{E}_{mm}^R)^{\frac{1}{2}}\right)}{\partial \mathbf{d}_m} = (\mathbf{E}_{pp}^R)^{\frac{1}{2}} \frac{\partial (\mathbf{E}_{mm}^R)^{\frac{1}{2}}}{\partial \mathbf{d}_m} = \frac{(\mathbf{E}_{pp}^R)^{\frac{1}{2}}}{2(\mathbf{E}_{mm}^R)^{\frac{1}{2}}} \frac{\partial \mathbf{E}_{mm}^R}{\partial \mathbf{d}_m} \tag{A.60}$$

because $\mathbf{E}_{pp}^R$ is not dependent on $\mathbf{d}_m$ and

$$\frac{\partial (\mathbf{E}_{mm}^R)^{\frac{1}{2}}}{\partial \mathbf{d}_m} = \frac{1}{2(\mathbf{E}_{mm}^R)^{\frac{1}{2}}} \frac{\partial \mathbf{E}_{mm}^R}{\partial \mathbf{d}_m}. \tag{A.61}$$

Plugging Eq.(A.60) and Eq.(A.61) into Eq.(A.59) leads to

$$\begin{aligned} \frac{\partial \mathbf{C}_{pm}^I}{\partial \mathbf{d}_m} &= \frac{\frac{\partial \mathbf{E}_{pm}^I}{\partial \mathbf{d}_m}}{(\mathbf{E}_{pp}^R)^{\frac{1}{2}} (\mathbf{E}_{mm}^R)^{\frac{1}{2}}} - \frac{\mathbf{E}_{pm}^I}{(\mathbf{E}_{pp}^R)(\mathbf{E}_{mm}^R)} \frac{1}{2} \frac{(\mathbf{E}_{pp}^R)^{\frac{1}{2}}}{(\mathbf{E}_{mm}^R)^{\frac{1}{2}}} \frac{\partial \mathbf{E}_{mm}^R}{\partial \mathbf{d}_m} \\ &= \frac{\frac{\partial \mathbf{E}_{pm}^I}{\partial \mathbf{d}_m}}{(\mathbf{E}_{pp}^R)^{\frac{1}{2}} (\mathbf{E}_{mm}^R)^{\frac{1}{2}}} - \frac{1}{2} \frac{\mathbf{E}_{pm}^I}{(\mathbf{E}_{pm}^R)^{\frac{1}{2}} (\mathbf{E}_{mm}^R)^{\frac{3}{2}}} \frac{\partial \mathbf{E}_{mm}^R}{\partial \mathbf{d}_m} \end{aligned} \tag{A.62}$$

and setting the derivative to zero gives

$$\frac{\partial \mathbf{E}_{pm}^I}{\partial \mathbf{d}_m} = \frac{1}{2} \frac{\mathbf{E}_{pm}^I}{\mathbf{E}_{mm}^R} \frac{\partial \mathbf{E}_{mm}^R}{\partial \mathbf{d}_m}. \tag{A.63}$$

Now, one can calculate the individual derivatives

$$\frac{\partial \mathbf{E}_{pm}^I}{\partial \mathbf{d}_m} = \left(\mathbf{w}_p^\mathsf{T} \mathbf{S}^I \mathbf{W}_m\right)^\mathsf{T} = \mathbf{W}_m^\mathsf{T} \mathbf{S}^I \mathbf{w}_p \tag{A.64}$$

and

$$\frac{\partial \mathbf{E}^R_{mm}}{\partial \mathbf{d}_m} = 2\mathbf{W}_m^\mathsf{T}\mathbf{S}^R\mathbf{W}_m\mathbf{d}_m \tag{A.65}$$

which can be seen from the derivation of a symmetric matrix $\mathbf{A}$ in its quadratic form with a vector $\mathbf{x}$

$$\begin{aligned}\frac{\partial}{\partial \mathbf{x}}\left(\mathbf{x}^\mathsf{T}\mathbf{A}\mathbf{x}\right) &= \frac{\partial}{\partial \mathbf{x}}\left(\sum_i\sum_j x_i a_{ij} x_j\right) = \frac{\partial}{\partial \mathbf{x}}\left(\sum_i x_i^2 a_{ii} + \sum_i\sum_{j>i} x_i a_{ij} x_j\right)\\ &= (\mathbf{A}\mathbf{A}^\mathsf{T})\mathbf{x} = 2\mathbf{A}\mathbf{x} = 2\mathbf{A}^\mathsf{T}\mathbf{x}.\end{aligned} \tag{A.66}$$

Applying the derivatives given in Eq.(A.64) and Eq.(A.65) to Eq.(A.63) leads to

$$\mathbf{W}_m^\mathsf{T}\mathbf{S}^I\mathbf{w}_p = \frac{1}{2}\frac{\mathbf{w}_p^\mathsf{T}\mathbf{S}^I\mathbf{w}_p\mathbf{d}_m}{\underbrace{\mathbf{d}_m^\mathsf{T}\mathbf{W}_m^\mathsf{T}\mathbf{S}^R\mathbf{W}_m\mathbf{d}_m}_{=:\gamma}}\, 2\mathbf{W}_m^\mathsf{T}\mathbf{S}^R\mathbf{W}_m\mathbf{d}_m. \tag{A.67}$$

Please note that the cost function to be maximized given by Eq.(A.58) has infinitely many solutions. It is independent of the scale of $\mathbf{d}_m$. In other words any $\alpha\mathbf{d}_m$ is also a solution that maximizes the cost function. This can be seen by inserting $\alpha\mathbf{d}_m$ into Eq.(A.67). The factor α cancels as Eq.(A.67) is linear in $\mathbf{d}_m$. Hence, one can pick a particular solution $\gamma = 1$ leading to

$$\mathbf{d}_m = \left(\mathbf{W}_m^\mathsf{T}\mathbf{S}^R\mathbf{W}_m\right)^{-1}\mathbf{W}_m^\mathsf{T}\mathbf{S}^I\mathbf{w}_p. \tag{A.68}$$

Abbreviations

AP	Action Potential
AR	autoregressive
BEM	Boundary Element Method
BSS	Blind Source Separation
CCA	Canonical Correlation Analysis
cImCoh	Corrected Imaginary Part of Coherency
CSF	Cerebrospinal fluid
DFT	Discrete Fourier Transform
DICS	Dynamic Imaging of Coherent Sources
EEG	Electroencephalography
eLoreta	Exact Low Resolution Brain Electromagnetic Tomography
EPSP	Excitatory Post Synaptic Potential
Eq.	Equation
ERF	Event Related Fields
ERP	Event Related Potential
FDR	False Discovery Rate
FEM	Finite Element Method
FOCUSS	Focal Underdetermined System Solution
GIM	Global Interaction Measure
i.i.d.	independent and identically distributed
ICA	Independent Component Analysis
ImCoh	Imaginary Part of Coherency
ImCs	Imaginary Part of the Cross-Spectrum

JADE	Joint Approximate Diagonalization of Eigenmatrices
LCMV	Linear Constraint Minimum Variance beamformer
Loreta	Low Resolution Brain Electromagnetic Tomography
LPC	Lagged Phase Coherence
MCE	Minimim Current Estimate
MEG	Magnetoencephalography
MIC	Maximized Imaginary Coherency
MIM	Multivariate Interaction Measure
MNE	Minimum Norm Estimate
MNI	Montreal Neurological Institute
MRI	Magnetic Resonance Imaging
Music	Multiple Signal Classification
PCA	Principle Component Analysis
Rap Music	Recursively Applied Multiple Signal Classification
SAM	Synthetic Aperture Magnetometry
SC Music	Self-Consistent Music
sLoreta	Standardized Low Resolution Brain Electromagnetic Tomography
SNR	Signal-to-Noise Ratio
SOBI	Second-Order Blind Source Identification
SQUID	Superconducting Quantum Interference Device
SVD	Singular Value Decomposition
TdSEP	Temporal Decorrelation Source Separation
WM	Wedge Music
WMNE	Weighted Minimum Norm Estimate
WPLI	Weighted Phase Lag Index

List of Figures

Bibliography

J. Aldrich. Fisher and the making of maximum likelihood 1912-1922. *Statistical Science*, 12(3):162–176, Sept. 1997. ISSN 0883-4237, 2168-8745. doi: 10.1214/ss/1030037906. URL http://projecteuclid.org/euclid.ss/1030037906. Mathematical Reviews number (MathSciNet) MR1617519, Zentralblatt MATH identifier 0955.62525. 108, 111

L. Astolfi, H. Bakardjian, F. Cincotti, D. Mattia, M. G. Marciani, F. De Vico Fallani, A. Colosimo, S. Salinari, F. Miwakeichi, Y. Yamaguchi, P. Martinez, A. Cichocki, A. Tocci, and F. Babiloni. Estimate of causality between independent cortical spatial patterns during movement volition in spinal cord injured patients. *Brain topography*, 19(3):107–123, 2007. ISSN 0896-0267. doi: 10.1007/s10548-007-0018-1. 20

F. S. Avarvand, A. Ewald, and G. Nolte. Localizing true brain interactions from EEG and MEG data with subspace methods and modified beamformers. *Comp. Math. Methods in Medicine*, 2012, 2012. 4, 49, 53

L. A. Baccala and K. Sameshima. Partial directed coherence: a new concept in neural structure determination. *Biol. Cybern.*, 84:463–474, 2001. 112

S. Baillet, J. Mosher, and R. Leahy. Electromagnetic brain mapping. *Signal Processing Magazine, IEEE*, 18(6):14 –30, Nov. 2001. ISSN 1053-5888. doi: 10.1109/79.962275. 3, 10, 105

A. Bell and T. J. Sejnowski. The "independent components" of natural scenes are edge filters. *Vision research*, 37(23):3327–3338, Dec. 1997. ISSN 0042-6989. URL http://www.ncbi.nlm.nih.gov/pmc/articles/PMC2882863/. 20

A. Belouchrani, K. Abed-Meraim, J.-F. Cardoso, and E. Moulines. A blind source separation technique using second-order statistics. *IEEE Transactions on Signal Processing*, 45(2):434–444, 1997. ISSN 1053-587X. doi: 10.1109/78.554307. 20

J. S. Bendat and A. G. Piersol. *Random data; analysis and measurement procedures*. Wiley-Interscience New York, 1971. ISBN 047106470. 21

Y. Benjamini. Discovering the false discovery rate. *Journal of the Royal Statistical Society: Series B (Statistical Methodology)*, 72(4):405–416, 2010. ISSN 1467-9868. doi: 10.1111/j.1467-9868.2010.00746.x. URL http://onlinelibrary.wiley.com/doi/10.1111/j.1467-9868.2010.00746.x/abstract. 33

Y. Benjamini and Y. Hochberg. Controlling the false discovery rate: A practical and powerful approach to multiple testing. *Journal of the Royal Statistical Society. Series B (Methodological)*, 57(1):289–300, 1995. ISSN 00359246. doi: 10.2307/2346101. URL http://dx.doi.org/10.2307/2346101. 33

C. M. Bennett, A. A. Baird, M. B. Miller, and G. L. Wolford. Neural correlates of interspecies perspective taking in the post-mortem atlantic salmon: An argument for proper multiple comparisons correction. *JSUR, 2010. 1(1):1-5 | Journal of Serendipitous and Unexpected Results*, 1(1):1–5, 2010. URL http://www.jsur.org/v1n1p1. 32

P. D. H. Berger. Über das elektrenkephalogramm des menschen. *Archiv für Psychiatrie und Nervenkrankheiten*, 87(1):527–570, Dec. 1929. ISSN 0003-9373, 1433-8491. doi: 10.1007/BF01797193. URL http://link.springer.com/article/10.1007/BF01797193. 2, 11

M. G. Berman, J. Jonides, and D. E. Nee. Studying mind and brain with fMRI. *Social Cognitive and Affective Neuroscience*, 1(2):158–161, Jan. 2006. ISSN 1749-5016, 1749-5024. doi: 10.1093/scan/nslo19. URL http://scan.oxfordjournals.org/content/1/2/158. 2

R. A. Bernard, D. A. Goran, S. T. Sakai, T. H. Carr, D. McFarlane, B. Nordell, T. G. Cooper, and E. J. Potchen. Cortical activation during rhythmic hand movements performed under three types of control: An fMRI study. *Cognitive, Affective, & Behavioral Neuroscience*, 2(3):271–281, Sept. 2002. ISSN 1530-7026, 1531-135X. doi: 10.3758/CABN.2.3.271. URL http://link.springer.com/article/10.3758/CABN.2.3.271. 85

B. Blankertz, G. Curio, and K.-R. Müller. Classifying single trial EEG: Towards brain computer interfacing. In T. G. Diettrich, S. Becker, and Z. Ghahramani, editors, *Advances in Neural Inf. Proc. Systems (NIPS 01)*, volume 14, pages 157–164, 2002. 94

B. Blankertz, G. Dornhege, M. Krauledat, K. R. Müller, V. Kunzmann, F. Losch, and G. Curio. The berlin brain-computer interface: EEG-based communication without subject training. *IEEE Transactions on Neural Systems and Rehabilitation Engineering*, 14(2):147–152, June 2006. ISSN 1534-4320. doi: 10.1109/TNSRE.2006.875557. 92

B. Blankertz, M. Kawanabe, R. Tomioka, F. Hohlefeld, V. Nikulin, and K.-R. Müller. Invariant common spatial patterns: Alleviating nonstationarities in brain-computer interfacing. In J. Platt, D. Koller, Y. Singer, and S. Roweis, editors, *Advances in Neural Information Processing Systems 20*, pages 113–120. MIT Press, Cambridge, MA, 2008a. 94

B. Blankertz, R. Tomioka, S. Lemm, M. Kawanabe, and K. R. Müller. Optimizing spatial filters for robust EEG single-trial analysis. *IEEE Signal Processing Magazine*, 25(1):41–56, 2008b. ISSN 1053-5888. doi: 10.1109/MSP.2008.4408441. 94

B. Blankertz, S. Lemm, M. Treder, S. Haufe, and K.-R. Müller. Single-trial analysis and classification of ERP components–a tutorial. *NeuroImage*, 56(2):814–825, May 2011. ISSN 1095-9572. doi: 10.1016/j.neuroimage.2010.06.048. 11

C. Bonferroni. Il calcolo delle assicurazioni su gruppi di teste. In *Studi in Onore del Professore Salvatore Ortu Carboni*, pages 13–60. Rome: Italy, 1935. 33

M. Breakspear, M. Brammer, and P. A. Robinson. Construction of multivariate surrogate sets from nonlinear data using the wavelet transform. *Physica D: Nonlinear Phenomena*, 182(1–2):1–22, Aug. 2003. ISSN 0167-2789. doi: 10.1016/S0167-2789(03)00136-2. URL `http://www.sciencedirect.com/science/article/pii/S0167278903001362`. 58

K. Brodmann. *Vergleichende Lokalisationslehre der Grosshirnrinde in ihren Prinzipien dargestellt auf Grund des Zellenbaues*. Johann Ambrosius Barth Verlag, 1909. 2

A. C. Cameron and P. K. Trivedi. *Microeconometrics: methods and applications*. Cambridge University Press, Cambridge; New York, 2005. ISBN 9780521848053 0521848059. 30

J.-F. Cardoso and A. Souloumiac. Blind beamforming for non-gaussian signals. *Radar and Signal Processing, IEE Proceedings F*, 140(6):362–370, 1993. ISSN 0956-375X. 3, 20

G. Casella and R. L. Berger. *Statistical inference*. Thomson Learning, Australia; Pacific Grove, CA, 2002. ISBN 0534243126 9780534243128. 28

F. Chella, L. Marzetti, V. Pizzella, F. Zappasodi, and G. Nolte. Third order spectral analysis robust to mixing artifacts for mapping cross-frequency interactions in EEG/MEG. *NeuroImage*, 91:146–161, May 2014. ISSN 1095-9572. doi: 10.1016/j.neuroimage.2013.12.064. 102

H. Chen and J. Zhao. Coherent signal-subspace processing of acoustic vector sensor array for DOA estimation of wideband sources. *Signal Processing*, 85(4):837–847, Apr. 2005. ISSN 0165-1684. doi: 10.1016/j.sigpro.2004.07.030. URL `http://www.sciencedirect.com/science/article/pii/S0165168404003305`. 23

P. Clifford. Applications of grassmann's extensive algebra. *American Journal of Mathematics*, 1(4):350–358, Jan. 1878. ISSN 0002-9327. doi: 10.2307/2369379. URL `http://www.jstor.org/stable/2369379`. ArticleType: research-article / Full publication date: 1878 /. 56

D. Cohen. Magnetoencephalography: Evidence of magnetic fields produced by alpha-rhythm currents. *Science*, 161(3843):784–786, 1968. ISSN 0036-8075(Print). doi: 10.1126/science.161.3843.784. 2, 17

S. S. Dalal, K. Sekihara, and S. S. Nagarajan. Modified beamformers for coherent source region suppression. *IEEE transactions on bio-medical engineering*, 53(7):1357–1363, July 2006. ISSN 0018-9294. doi: 10.1109/TBME.2006.873752. URL `http://www.ncbi.nlm.nih.gov/pmc/articles/PMC3066091/`. 22

O. David, D. Cosmelli, and K. J. Friston. Evaluation of different measures of functional connectivity using a neural mass model. *NeuroImage*, 21(2):659–673, Feb. 2004. ISSN 1053-8119. doi: 10.1016/j.neuroimage.2003.10.006. URL http://www.sciencedirect.com/science/article/pii/S1053811903006566. 28

S. Della Penna, C. Del Gratta, C. Granata, A. Pasquarelli, V. Pizzella, R. Rossi, M. Russo, K. Torquati, and S. Erne. Biomagnetic systems for clinical use. *Philosophical Magazine B: Physics of Condensed Matter, Statistical Mechanics, Electronic, Optical, and Magnetic Properties*, 80(5):937–948, May 2000. ISSN 0141-8637. International Workshop on Semiconducting and Superconducting Materials, Turin, Italy, Feb, 1999. 88

S. Dähne, F. C. Meinecke, S. Haufe, J. Höhne, M. Tangermann, K.-R. Müller, and V. V. Nikulin. SPoC: a novel framework for relating the amplitude of neuronal oscillations to behaviorally relevant parameters. *NeuroImage*, 86:111–122, Feb. 2014a. ISSN 1095-9572. doi: 10.1016/j.neuroimage.2013.07.079. 97

S. Dähne, V. V. Nikulin, D. Ramírez, P. J. Schreier, K.-R. Müller, and S. Haufe. Finding brain oscillations with power dependencies in neuroimaging data. *NeuroImage*, 96:334–348, Aug. 2014b. ISSN 1053-8119. doi: 10.1016/j.neuroimage.2014.03.075. URL http://www.sciencedirect.com/science/article/pii/S1053811914002365. 97, 102

N. U. Dosenbach, D. A. Fair, F. M. Miezin, A. L. Cohen, K. K. Wenger, R. A. Dosenbach, M. D. Fox, A. Z. Snyder, J. L. Vincent, M. E. Raichle, B. L. Schlaggar, and S. E. Petersen. Distinct brain networks for adaptive and stable task control in humans. *Proc. Natl. Acad. Sci. U.S.A.*, 104(26):11073–11078, June 2007. 2

Z. Drmac. On principal angles between subspaces of euclidean space. *SIAM J. Matrix Anal. Appl.*, 22(1):173–194, Apr. 2000. ISSN 0895-4798. doi: 10.1137/S0895479897320824. URL http://dx.doi.org/10.1137/S0895479897320824. 23

O. J. Dunn. Multiple comparisons among means. *Journal of the American Statistical Association*, 56(293):52–64, 1961. ISSN 0162-1459. doi: 10.1080/01621459.1961.10482090. URL http://www.tandfonline.com/doi/abs/10.1080/01621459.1961.10482090. 33

C. Eckart and G. Young. The approximation of one matrix by another of lower rank. *Psychometrika*, 1(3):211–218, Sept. 1936. ISSN 0033-3123, 1860-0980. doi: 10.1007/BF02288367. URL http://link.springer.com/article/10.1007/BF02288367. 19

B. Efron and R. J. Tibshirani. *An Introduction to the Bootstrap*. Chapman and Hall/CRC, 1 edition, May 1994. ISBN 0412042312. URL http://www.worldcat.org/isbn/0412042312. Published: Hardcover. 29

A. K. Engel, P. Fries, and W. Singer. Dynamic predictions: Oscillations and synchrony in top-down processing. *Nature Reviews Neuroscience*, 2(10):704–716, Oct. 2001. 3

A. K. Engel, C. Gerloff, C. C. Hilgetag, and G. Nolte. Intrinsic coupling modes: Multiscale interactions in ongoing brain activity. *Neuron*, 80(4):867–886, Nov. 2013. ISSN 0896-6273. doi: 10.1016/j.neuron.2013.09.038. URL `http://www.cell.com/neuron/abstract/S0896-6273(13)00869-6`. 3, 90, 97, 102

J. Escudero, R. Hornero, D. Abásolo, A. Fernández, and M. López-Coronado. Artifact removal in magnetoencephalogram background activity with independent component analysis. *IEEE transactions on bio-medical engineering*, 54(11):1965–1973, Nov. 2007. ISSN 0018-9294. doi: 10.1109/TBME.2007.894968. 20

B. S. Everitt. *The Cambridge Dictionary of Statistics*. Cambridge University Press, Cambridge, 2006. 45

A. Ewald, L. Marzetti, F. Zappasodi, F. C. Meinecke, and G. Nolte. Estimating true brain connectivity from EEG/MEG data invariant to linear and static transformations in sensor space. *NeuroImage*, 60:476 – 488, 2012. ISSN 1053-8119. doi: 10.1016/j.neuroimage.2011.11.084. URL `http://www.sciencedirect.com/science/article/pii/S1053811911013668`. 4, 35, 65

A. Ewald, F. S. Avarvand, and G. Nolte. Identifying causal networks of neuronal sources from EEG/MEG data with the phase slope index: a simulation study. *Biomed Tech (Berl)*, 58(2):165–178, Apr. 2013. 4

A. Ewald, F. S. Avarvand, and G. Nolte. Wedge MUSIC: A novel approach to examine experimental differences of brain source connectivity patterns from EEG/MEG data. *NeuroImage*, 101:610–624, Nov. 2014. ISSN 1095-9572. doi: 10.1016/j.neuroimage.2014.07.011. 55

R. A. Fisher. *Statistical methods and scientific inference*, volume viii. Hafner Publishing Co., Oxford, England, 1956. 28

S. R. A. Fisher. *The Design of Experiments*. Hafner Publishing Company, 1951. 31

V. Fonov, A. C. Evans, K. Botteron, C. R. Almli, R. C. McKinstry, and D. L. Collins. Unbiased average age-appropriate atlases for pediatric studies. *NeuroImage*, 54(1): 313 – 327, 2011. ISSN 1053-8119. doi: 10.1016/j.neuroimage.2010.07.033. URL `http://www.sciencedirect.com/science/article/pii/S1053811910010062`. 14, 63, 89

V. S. Fonov, A. C. Evans, R. C. McKinstry, C. R. Almli, and D. L. Collins. Unbiased nonlinear average age-appropriate brain templates from birth to adulthood. *NeuroImage*, 47, 2009. ISSN 1053-8119. doi: 10.1016/S1053-8119(09)70884-5. URL `http://www.sciencedirect.com/science/article/pii/S1053811909708845`. 14, 89

P. Fries. A mechanism for cognitive dynamics: neuronal communication through neuronal coherence. *TRENDS in Cognitive Sciences*, 9(10):474–480, Oct. 2005. 3, 4, 6, 25

K. J. Friston. Modalities, modes, and models in functional neuroimaging. *Science*, 326 (5951):399–403, Oct. 2009. ISSN 0036-8075, 1095-9203. doi: 10.1126/science.1174521. URL `http://www.sciencemag.org/content/326/5951/399`. 2

K. J. Friston. Functional and effective connectivity: a review. *Brain connectivity*, 1(1): 13–36, 2011. ISSN 2158-0022. doi: 10.1089/brain.2011.0008. 3

K. J. Friston, L. Harrison, and W. Penny. Dynamic causal modelling. *Neuroimage*, 19 (4):1273–1302, Aug. 2003. 112

K. Fukunaga. *Introduction to Statistical Pattern Recognition, Second Edition*. Academic Press, Boston, 2 edition edition, Oct. 1990. ISBN 9780122698514. 94

F. J. F. J. Gall and W. Lewis. *On the functions of the brain and of each of its parts: with observations on the possibility of determining the instincts, propensities, and talents, or the moral and intellectual dispositions of men and animals, by the configuration of the brain and head*. Boston, Marsh, Capen & Lyon, 1835. URL `http://archive.org/details/onfunctionsofbra0506gall`. 1

D. B. Geselowitz. On the magnetic field generated outside an inhomogeneous volume conductor by internal current sources. *IEEE Transactions on Magnetics*, 6(2):346–347, 1970. ISSN 0018-9464. doi: 10.1109/TMAG.1970.1066765. 106

P. Gloor. Neuronal generators and the problem of localization in electroencephalography: application of volume conductor theory to electroencephalography. *Journal of clinical neurophysiology: official publication of the American Electroencephalographic Society*, 2(4):327–354, Oct. 1985. ISSN 0736-0258. 9

J. J. Gonzalez, S. Manas, L. D. Vera, L. D. Mendez, S. Lopez, J. M. garrido, and E. Pereda. Assessment of electroencephalographic functional connectivity in term and preterm neonates. *Clinical Neurophysiology*, 122(4):696–702, 2011. 4

I. F. Gorodnitsky, J. S. George, and B. D. Rao. Neuromagnetic source imaging with FOCUSS: a recursive weighted minimum norm algorithm. *Electroencephalography and clinical neurophysiology*, 95(4):231–251, Oct. 1995. ISSN 0013-4694. 110, 111

C. W. J. Granger. Investigating causal relations by economic models and cross-sprectal methods. *Econometrica*, 37:424–438, 1969. 112

C. W. J. Granger. Testing for causality: a personal viewpoint. *Journal of Econ. Dynamics Control*, 2:329–352, 1980. 112

H. Grassmann. *Die lineale Ausdehnungslehre ein neuer Zweig der Mathematik: dargestellt und durch Anwendungen auf die übrigen Zweige der Mathematik, wie auch auf die Statik, Mechanik, die Lehre vom Magnetismus und die Krystallonomie erläutert*. O. Wigand, 1844. 56

R. Grave de Peralta Menendez, S. L. Gonzalez Andino, S. Morand, C. M. Michel, and T. Landis. Imaging the electrical activity of the brain: ELECTRA. *Human brain mapping*, 9(1):1–12, 2000. ISSN 1065-9471. 111

R. Grave de Peralta Menendez, M. M. Murray, C. M. Michel, R. Martuzzi, and S. L. Gonzalez Andino. Electrical neuroimaging based on biophysical constraints. *NeuroImage*, 21(2):527–539, Feb. 2004. ISSN 1053-8119. doi: 10.1016/j.neuroimage.2003.09.051. 111

R. E. Greenblatt, M. E. Pflieger, and A. E. Ossadtchi. Connectivity measures applied to human brain electrophysiological data. *Journal of Neuroscience Methods*, 207(1):1–16, May 2012. ISSN 0165-0270. doi: 10.1016/j.jneumeth.2012.02.025. URL `http://www.sciencedirect.com/science/article/pii/S0165027012000817`. 28

J. Gross, J. Kujala, M. Hamalainen, L. Timmermann, A. Schnitzler, and R. Salmelin. Dynamic imaging of coherent sources: Studying neural interactions in the human brain. *Proceedings of the National Academy of Sciences of the United States of America*, 98(2):694–699, Jan. 2001. 3, 22, 49, 111

C. Habermehl, S. Holtze, J. Steinbrink, S. P. Koch, H. Obrig, J. Mehnert, and C. H. Schmitz. Somatosensory activation of two fingers can be discriminated with ultrahigh-density diffuse optical tomography. *NeuroImage*, 59(4):3201–3211, Feb. 2012. ISSN 1095-9572. doi: 10.1016/j.neuroimage.2011.11.062. 85

D. Hagemann, E. Naumann, and J. F. Thayer. The quest for the EEG reference revisited: a glance from brain asymmetry research. *Psychophysiology*, 38(5):847–857, Sept. 2001. ISSN 0048-5772. 17

M. S. Hamalainen. Magnetoencephalography: a tool for functional brain imaging. *Brain Topogr.*, 5:95–102, 1992. 106

L. K. Hansen, J. Larsen, F. A. Nielsen, S. C. Strother, E. Rostrup, R. Savoy, N. Lange, J. Sidtis, C. Svarer, and O. B. Paulson. Generalizable patterns in neuroimaging: how many principal components? *NeuroImage*, 9(5):534–544, May 1999. ISSN 1053-8119. doi: 10.1006/nimg.1998.0425. 50

J. Harlow. Recovery from the passage of an iron bar through the head. *Publ Mass Med Soc.*, pages 327–347, 1868. 1, 2

S. Haufe, V. V. Nikulin, A. Ziehe, K.-R. Müller, and G. Nolte. Combining sparsity and rotational invariance in EEG/MEG source reconstruction. *NeuroImage*, 42(2):726 – 738, 2008. ISSN 1053-8119. doi: 10.1016/j.neuroimage.2008.04.246. URL `http://www.sciencedirect.com/science/article/pii/S1053811908005144`. 111

S. Haufe, R. Tomioka, G. Nolte, K.-R. Müller, and M. Kawanabe. Modeling sparse connectivity between underlying brain sources for EEG/MEG. *IEEE transactions on bio-medical engineering*, 57(8):1954–1963, Aug. 2010. ISSN 1558-2531. doi: 10.1109/TBME.2010.2046325. 112

S. Haufe, R. Tomioka, T. Dickhaus, C. Sannelli, B. Blankertz, G. Nolte, and K.-R. Müller. Large-scale EEG/MEG source localization with spatial flexibility. *NeuroImage*, 54(2):851–859, Jan. 2011. ISSN 1095-9572. doi: 10.1016/j.neuroimage.2010.09.003. 3, 110, 111

S. Haufe, V. Nikulin, K. Müller, and G. Nolte. A critical assessment of connectivity measures for EEG data: A simulation study. *NeuroImage*, 2012. 4, 16, 28, 33

S. Haufe, S. Dähne, and V. V. Nikulin. Dimensionality reduction for the analysis of brain oscillations. *NeuroImage*, 101:583–597, Nov. 2014a. ISSN 1095-9572. doi: 10.1016/j.neuroimage.2014.06.073. 45

S. Haufe, F. Meinecke, K. Görgen, S. Dähne, J.-D. Haynes, B. Blankertz, and F. Bießmann. On the interpretation of weight vectors of linear models in multivariate neuroimaging. *NeuroImage*, 87:96–110, Feb. 2014b. ISSN 1053-8119. doi: 10.1016/j.neuroimage.2013.10.067. URL http://www.sciencedirect.com/science/article/pii/S1053811913010914. 15, 50, 96

O. Hauk. Keep it simple: a case for using classical minimum norm estimation in the analysis of EEG and MEG data. *NeuroImage*, 21(4):1612–1621, Apr. 2004. ISSN 1053-8119. doi: 10.1016/j.neuroimage.2003.12.018. URL http://www.sciencedirect.com/science/article/pii/S1053811903007845. 108, 111

T. Hawkins. Cauchy and the spectral theory of matrices. *Historia Mathematica*, 2 (1):1–29, Feb. 1975. ISSN 0315-0860. doi: 10.1016/0315-0860(75)90032-4. URL http://www.sciencedirect.com/science/article/pii/0315086075900324. 45

W. Hesse, E. Moller, M. Arnold, and B. Schack. The use of time-variant EEG granger causality for inspecting directed interdependencies of neural assemblies. *Journal of Neuroscience Methods*, 124(1):27–44, 2003. 112

A. Hillebrand and G. R. Barnes. The use of anatomical constraints with MEG beamformers. *NeuroImage*, 20(4):2302–2313, Dec. 2003. ISSN 1053-8119. doi: 10.1016/j.neuroimage.2003.07.031. URL http://www.sciencedirect.com/science/article/pii/S1053811903004610. 21, 111

J. F. Hipp, D. J. Hawellek, M. Corbetta, M. Siegel, and A. K. Engel. Large-scale cortical correlation structure of spontaneous oscillatory activity. *Nat. Neurosci.*, 15 (6):884–890, June 2012. 3, 97, 102, 112

M. Hämäläinen and R. Ilmoniemi. Interpreting magnetic fields of the brain: minimum norm estimates. *Medical and Biological Engineering and Computing*, 32(1): 35–42, 1994. ISSN 0140-0118. URL http://dx.doi.org/10.1007/BF02512476. 10.1007/BF02512476. 3, 109

M. Hämäläinen, R. Hari, R. J. Ilmoniemi, J. Knuutila, and O. V. Lounasmaa. Magnetoencephalography—theory, instrumentation, and applications to noninvasive studies of the working human brain. *Reviews of Modern Physics*, 65(2):413–497, Apr. 1993. doi: 10.1103/RevModPhys.65.413. URL http://link.aps.org/doi/10.1103/RevModPhys.65.413. 3

A. L. Hodgkin. The ionic basis of electrical activity in nerve and muscle. *Biological Reviews*, 26(4):339–409, 1951. ISSN 1469-185X. doi: 10.1111/j.1469-185X.1951.

tb01204.x. URL http://onlinelibrary.wiley.com/doi/10.1111/j.1469-185X.1951.tb01204.x/abstract. 9

A. P. Holmes, R. C. Blair, G. Watson, and I. Ford. Nonparametric analysis of statistic images from functional mapping experiments. *Journal of Cerebral Blood Flow & Metabolism*, 16(1):7–22, Jan. 1996. ISSN 0271-678X. doi: 10.1097/00004647-199601000-00002. URL http://www.nature.com/jcbfm/journal/v16/n1/full/9590002a.html. 76

B. Horwitz. The elusive concept of brain connectivity. *NeuroImage*, 19(2 Pt 1):466–470, June 2003. ISSN 1053-8119. 2

H. Hotelling. Relations between two sets of variates. *Biometrika*, 28(3):321–377, 1936. 36

B. Hui, D. Pantazis, S. L. Bressler, and R. M. Leahy. Identifying true cortical interactions in MEG using the nulling beamformer. *Neuroimage*, 49(4):3161–74, 2010. 22

H. B. Hui and R. Leahy. Linearly constrained MEG beamformers for MVAR modeling of cortical interactions. In *3rd IEEE International Symposium on Biomedical Imaging: Nano to Macro, 2006*, pages 237–240, 2006. doi: 10.1109/ISBI.2006.1624896. 22, 111

A. Hyvärinen. Fast and robust fixed-point algorithms for independent component analysis. *IEEE transactions on neural networks / a publication of the IEEE Neural Networks Council*, 10(3):626–634, 1999. ISSN 1045-9227. doi: 10.1109/72.761722. 20

A. Hyvärinen. Independent component analysis: recent advances. *Philosophical Transactions of the Royal Society A: Mathematical, Physical and Engineering Sciences*, 371 (1984):20110534, Feb. 2013. ISSN 1364-503X, 1471-2962. doi: 10.1098/rsta.2011.0534. URL http://rsta.royalsocietypublishing.org/content/371/1984/20110534. 20

A. A. Ioannides, J. P. R. Bolton, and C. J. S. Clarke. Continuous probabilistic solutions to the biomagnetic inverse problem. *Inverse Problems*, 6(4):523, 1990. URL http://stacks.iop.org/0266-5611/6/i=4/a=005. 3, 109, 111

C. James and O. Gibson. Temporally constrained ICA: an application to artifact rejection in electromagnetic brain signal analysis. *IEEE Transactions on Biomedical Engineering*, 50(9):1108–1116, 2003. ISSN 0018-9294. doi: 10.1109/TBME.2003.816076. 20

Jean Baptiste Joseph Fourier. *Théorie analytique de la chaleur*. Chez Firmin Didot, père et fils ..., 1822. URL http://archive.org/details/thorieanalytiqu00fourgoog. 25

B. Jeffs, R. Leahy, and M. Singh. An evaluation of methods for neuromagnetic image reconstruction. *IEEE transactions on bio-medical engineering*, 34(9):713–723, Sept. 1987. ISSN 0018-9294. 3, 109, 111

O. Jensen and L. L. Colgin. Cross-frequency coupling between neuronal oscillations. *Trends in Cognitive Sciences*, 11(7):267–269, July 2007. ISSN 1364-6613. doi: 10.1016/j.tics.2007.05.003. 102

O. Jensen, J. Gelfand, J. Kounios, and J. E. Lisman. Oscillations in the alpha band (9–12 hz) increase with memory load during retention in a short-term memory task. *Cerebral Cortex*, 12(8):877–882, Jan. 2002. ISSN 1047-3211, 1460-2199. doi: 10.1093/cercor/12.8.877. URL `http://cercor.oxfordjournals.org/content/12/8/877`. 86

K. Jerbi, S. Baillet, J. C. Mosher, G. Nolte, L. Garnero, and R. M. Leahy. Localization of realistic cortical activity in MEG using current multipoles. *NeuroImage*, 22(2):779–793, June 2004. ISSN 1053-8119. doi: 10.1016/j.neuroimage.2004.02.010. 111

V. K. Jirsa and A. R. McIntosh. *Handbook of Brain Connectivity*. Springer, Berlin ; New York, auflage: 2007 edition, July 2007. ISBN 9783540714620. 2

C. A. Joyce, I. F. Gorodnitsky, and M. Kutas. Automatic removal of eye movement and blink artifacts from EEG data using blind component separation. *Psychophysiology*, 41(2):313–325, Mar. 2004. ISSN 0048-5772. doi: 10.1111/j.1469-8986.2003.00141.x. 20

T. P. Jung, S. Makeig, C. Humphries, T. W. Lee, M. J. McKeown, V. Iragui, and T. J. Sejnowski. Removing electroencephalographic artifacts by blind source separation. *Psychophysiology*, 37(2):163–178, Mar. 2000. ISSN 0048-5772. 20

M. Kaminski and K. J. Blinowska. A new method of the description on information flow. *Biol.Cybern.*, 65:203–210, 1991. 112

E. R. Kandel, J. H. Schwartz, T. M. Jessell, S. A. Siegelbaum, and A. J. Hudspeth. *Principles of Neural Science*. Mcgraw-Hill Publ.Comp., New York, 5th ed. edition, Oct. 2012. ISBN 9780071390118. 1

M. Kawanabe, W. Samek, K.-R. Müller, and C. Vidaurre. Robust common spatial filters with a maxmin approach. *Neural Computation*, 26(2):349–376, Nov. 2013. ISSN 0899-7667. doi: 10.1162/NECO_a_00544. URL `http://dx.doi.org/10.1162/NECO_a_00544`. 95

G. H. Klem, H. O. Lüders, H. H. Jasper, and C. Elger. The ten-twenty electrode system of the international federation. the international federation of clinical neurophysiology. *Electroencephalography and clinical neurophysiology. Supplement*, 52:3–6, 1999. ISSN 0424-8155. 13

T. R. Knösche, E. M. Berends, H. R. Jagers, and M. J. Peters. Determining the number of independent sources of the EEG: a simulation study on information criteria. *Brain topography*, 11(2):111–124, 1998. ISSN 0896-0267. 50

S. P. Koch, C. Habermehl, J. Mehnert, C. H. Schmitz, S. Holtze, A. Villringer, J. Steinbrink, and H. Obrig. High-resolution optical functional mapping of the human

somatosensory cortex. *Frontiers in Neuroenergetics*, 2:12, 2010. ISSN 1662-6427. doi: 10.3389/fnene.2010.00012. 85

Z. J. Koles. The quantitative extraction and topographic mapping of the abnormal components in the clinical EEG. *Electroencephalography and Clinical Neurophysiology*, 79(6):440–447, Dec. 1991. ISSN 0013-4694. 94

M. Krauledat, P. Shenoy, B. Blankertz, R. P. N. Rao, and K.-R. Müller. Adaptation in CSP-based BCI systems. In G. Dornhege, J. del R. Millán, T. Hinterberger, D. McFarland, and K.-R. Müller, editors, *Toward Brain-Computer Interfacing*, pages 305–309. MIT Press, Cambridge, MA, 2007. 94

H. W. Kuhn. The hungarian method for the assignment problem. *Naval Research Logistics Quarterly*, 2(1-2):83–97, Mar. 1955. ISSN 1931-9193. doi: 10.1002/nav.3800020109. URL `http://onlinelibrary.wiley.com/doi/10.1002/nav.3800020109/abstract`. 34

J.-P. Lachaux, E. Rodriguez, J. Martinerie, and F. J. Varela. Measuring phase synchrony in brain signals. *Human Brain Mapping*, 8(4):194–208, Jan. 1999. ISSN 1097-0193. doi: 10.1002/(SICI)1097-0193(1999)8:4<194::AID-HBM4>3.0.CO;2-C. URL `http://onlinelibrary.wiley.com/doi/10.1002/(SICI)1097-0193(1999)8:4<194::AID-HBM4>3.0.CO;2-C/abstract`. 112

M. G. Lacourse, E. L. R. Orr, S. C. Cramer, and M. J. Cohen. Brain activation during execution and motor imagery of novel and skilled sequential hand movements. *NeuroImage*, 27(3):505–519, Sept. 2005. ISSN 1053-8119. doi: 10.1016/j.neuroimage.2005.04.025. 85

L. S. Lasdon. *Optimization Theory for Large Systems*. Courier Dover Publications, 1970. ISBN 9780486419992. 107

S. Lemm, B. Blankertz, T. Dickhaus, and K.-R. Müller. Introduction to machine learning for brain imaging. *NeuroImage*, 56(2):387–399, May 2011. ISSN 1053-8119. doi: 10.1016/j.neuroimage.2010.11.004. URL `http://www.sciencedirect.com/science/article/pii/S1053811910014163`. 11

W. Li. Mutual information functions versus correlation functions. *Journal of Statistical Physics*, 60(5-6):823–837, Sept. 1990. ISSN 0022-4715, 1572-9613. doi: 10.1007/BF01025996. URL `http://link.springer.com/article/10.1007/BF01025996`. 112

F.-H. Lin, T. Witzel, S. P. Ahlfors, S. M. Stufflebeam, J. W. Belliveau, and M. S. Hämäläinen. Assessing and improving the spatial accuracy in MEG source localization by depth-weighted minimum-norm estimates. *NeuroImage*, 31(1):160–171, May 2006. ISSN 1053-8119. doi: 10.1016/j.neuroimage.2005.11.054. URL `http://www.sciencedirect.com/science/article/pii/S1053811905024973`. 3, 109

N. K. Logothetis. What we can do and what we cannot do with fMRI. *Nature*, 453 (7197):869–878, June 2008. ISSN 0028-0836. doi: 10.1038/nature06976. URL http://www.nature.com/nature/journal/v453/n7197/full/nature06976.html. 2

F. H. Lopes da Silva, H. J. Wieringa, and M. J. Peters. Source localization of EEG versus MEG: empirical comparison using visually evoked responses and theoretical considerations. *Brain Topography*, 4(2):133–142, 1991. ISSN 0896-0267. 18

M. Lotze, P. Montoya, M. Erb, E. Hülsmann, H. Flor, U. Klose, N. Birbaumer, and W. Grodd. Activation of cortical and cerebellar motor areas during executed and imagined hand movements: an fMRI study. *Journal of Cognitive Neuroscience*, 11(5): 491–501, Sept. 1999. ISSN 0898-929X. 85

S. J. Luck. *An introduction to the event-related potential technique*. The MIT Press, Cambridge (MA); London, 2005. ISBN 0262122774 9780262122771 0262621967 9780262621960. 10, 11

S. Makeig, S. Debener, J. Onton, and A. Delorme. Mining event-related brain dynamics. *Trends in Cognitive Sciences*, 8(5):204–210, May 2004. ISSN 1364-6613. doi: 10.1016/j.tics.2004.03.008. URL http://www.sciencedirect.com/science/article/pii/S1364661304000816. 20

E. Maris. A resampling method for estimating the signal subspace of spatio-temporal EEG/MEG data. *IEEE Transactions on Biomedical Engineering*, 50(8):935–949, Aug. 2003. ISSN 0018-9294. doi: 10.1109/TBME.2003.814293. 50, 51

L. Marzetti, C. D. Gratta, and G. N. G. Understanding brain connectivity from EEG data by identifying systems composed of interacting sources. *Neuroimage*, 42(1): 87–98, 2008. 100

L. Marzetti, S. Della Penna, A. Snyder, V. Pizzella, G. Nolte, F. de Pasquale, G. Romani, and M. Corbetta. Frequency specific interactions of MEG resting state activity within and across brain networks as revealed by the multivariate interaction measure. *NeuroImage*, 79:172–183, Oct. 2013. ISSN 1053-8119. doi: 10.1016/j.neuroimage.2013.04.062. URL http://www.sciencedirect.com/science/article/pii/S1053811913004096. 4

K. Matsuura and Y. Okabe. Selective minimum-norm solution of the biomagnetic inverse problem. *IEEE transactions on bio-medical engineering*, 42(6):608–615, June 1995. ISSN 0018-9294. doi: 10.1109/10.387200. 110, 111

F. Meinecke. *Identifying Interactions from Superimposed Signals*. PhD thesis, Berlin Institute of Technology, 2012. 97

K. D. Micheva, B. Busse, N. C. Weiler, N. O'Rourke, and S. J. Smith. Single-synapse analysis of a diverse synapse population: Proteomic imaging methods and markers. *Neuron*, 68(4):639–653, Nov. 2010. ISSN 0896-6273. doi: 10.1016/j.neuron.2010.09.024. URL http://www.cell.com/article/S089662731000766X/abstract. 1

R. G. Miller. The jackknife-a review. *Biometrika*, 61(1):1–15, 1974. doi: 10.1093/biomet/61.1.1. URL `http://biomet.oxfordjournals.org/content/61/1/1.abstract`. 30

J. Milton, S. L. Small, and A. Solodkin. Imaging motor imagery: methodological issues related to expertise. *Methods (San Diego, Calif.)*, 45(4):336–341, Aug. 2008. ISSN 1095-9130. doi: 10.1016/j.ymeth.2008.05.002. 85

K.-R. Müller, C. W. Anderson, and G. E. Birch. Linear and nonlinear methods for brain-computer interfaces. *IEEE transactions on neural systems and rehabilitation engineering: a publication of the IEEE Engineering in Medicine and Biology Society*, 11 (2):165–169, June 2003. ISSN 1534-4320. doi: 10.1109/TNSRE.2003.814484. 15

G. Monge. Mémoire sur la théorie des déblais et des remblais. *Histoire de l'Académie Royale des Sciences*, pages 666–704, 1781. 33

J. Mosher and R. Leahy. Source localization using recursively applied and projected (RAP) MUSIC. *IEEE Transactions on Signal Processing*, 47(2):332–340, 1999. 3, 24, 51, 111

J. Mosher, R. Leahy, and P. Lewis. EEG and MEG: forward solutions for inverse methods. *IEEE Transactions on Biomedical Engineering*, 46(3):245–259, 1999a. ISSN 0018-9294. doi: 10.1109/10.748978. 22

J. C. Mosher, S. Baillet, and R. M. Leahy. EEG source localization and imaging using multiple signal classification approaches. *Journal of clinical neurophysiology: official publication of the American Electroencephalographic Society*, 16(3):225–238, May 1999b. ISSN 0736-0258. 3, 111

J. C. d. Munck. The potential distribution in a layered anisotropic spheroidal volume conductor. *Journal of Applied Physics*, 64(2):464–470, July 1988. ISSN 0021-8979, 1089-7550. doi: 10.1063/1.341983. URL `http://scitation.aip.org/content/aip/journal/jap/64/2/10.1063/1.341983`. 12

J. C. d. Munck and B. W. v. Dijk. Symmetry considerations in the quasi-static approximation of volume conductor theory. *Physics in Medicine and Biology*, 36 (4):521, Apr. 1991. ISSN 0031-9155. doi: 10.1088/0031-9155/36/4/009. URL `http://iopscience.iop.org/0031-9155/36/4/009`. 12

T. I. Netoff, T. L. Carroll, L. M. Pecora, and S. J. Schiff. Detecting coupling in the presence of noise and nonlinearity. In B. Schelter, t. Winterhalder, and J. Timmer, editors, *Handbook of Time Series Analysis*, pages 265–282. Wiley-VCH Verlag GmbH & Co. KGaA, 2006. ISBN 9783527609970. URL `http://onlinelibrary.wiley.com/doi/10.1002/9783527609970.ch11/summary`. 112

T. E. Nichols and A. P. Holmes. Nonparametric permutation tests for functional neuroimaging: a primer with examples. *Human Brain Mapping*, 15(1):1–25, Jan. 2002. ISSN 1065-9471. 76

V. V. Nikulin, G. Nolte, and G. Curio. A novel method for reliable and fast extraction of neuronal EEG/MEG oscillations on the basis of spatio-spectral decomposition. *NeuroImage*, 55(4):1528 – 1535, 2011. ISSN 1053-8119. doi: DOI:10.1016/j.neuroimage.2011.01.057. URL `http://www.sciencedirect.com/science/article/pii/S1053811911000930`. 45, 50

G. Nolte. The magnetic lead field theorem in the quasi-static approximation and its use for magnetoencephalography forward calculation in realistic volume conductors. *Physics in medicine and biology*, 48(22):3637–3652, Nov. 2003. ISSN 0031-9155. 13, 89

G. Nolte and G. Dassios. Analytic expansion of the EEG lead field for realistic volume conductors. *Physics in medicine and biology*, 50(16):3807–3823, Aug. 2005. ISSN 0031-9155. doi: 10.1088/0031-9155/50/16/010. 13, 63

G. Nolte and K. R. Müller. Localizing and estimating causal relations of interacting brain rhythms. *Frontiers in Human Neuroscience*, 4(00209), 2010. ISSN 1662-5161. doi: 10.3389/fnhum.2010.00209. 4

G. Nolte, O. Bai, L. Wheaton, Z. Mari, S. Vorbach, and M. Hallett. Identifying true brain interaction from EEG data using the imaginary part of coherency. *Clinical Neurophysiology*, 115(10):2292 – 2307, 2004. ISSN 1388-2457. doi: DOI: 10.1016/j.clinph.2004.04.029. 4, 27, 35, 99, 112

G. Nolte, F. C. Meinecke, A. Ziehe, and K. R. Müller. Identifying interactions in mixed and noisy complex systems. *Phys Rev E*, 73:051913, 2006. 4

G. Nolte, A. Ziehe, V. Nikulin, A. Schlögl, N. Krämer, T. Brismar, and K. R. Müller. Robustly estimating the flow direction of information in complex physical systems. *Physical Review Letters*, 100:234101, June 2008. URL `http://ml.cs.tu-berlin.de/causality/psi.pdf`. 100, 112

P. L. Nunez and R. Srinivasan. *Electric Fields of the Brain: The Neurophysics of EEG*. Oxford University Press, Jan. 2006. ISBN 9780195050387. 10

P. L. Nunez, R. Srinivasan, A. F. Westdorf, R. S. Wijesinghe, D. M. Tucker, R. B. Silberstein, and P. J. Cadusch. EEG coherency. i. statistics, reference electrode, volume conduction, laplacians, cortical imaging, and interpretation at multiple scales. *Electroencephalogr. Clin. Neurophysiol.*, 103:499–515, 1997. 3, 4, 112

P. L. Nunez, R. B. Silberstein, Z. Shi, M. R. Carpenter, R. Srinivasan, D. M. Tucker, S. M. Doran, P. J. Cadusch, and R. S. Wijesinghe. EEG coherency II: experimental comparisons of multiple measures. *Clinical Neurophysiology*, 110(3):469 – 486, 1999. ISSN 1388-2457. doi: DOI:10.1016/S1388-2457(98)00043-1. URL `http://www.sciencedirect.com/science/article/B6VNP-43MKB85-G/2/8d76d5c19888028c181615c315a68fc5`. 4

H. Nyquist. Certain topics in telegraph transmission theory. *Transactions of the AIEE*, 47:617–644, 1928. 85

S. Oh and C. Un. Improved MUSIC algorithm for high-resolution array processing. *Electronics Letters*, 25(22):1523–1525, 1989. ISSN 0013-5194. doi: 10.1049/el:19891023. 23

R. Oostenveld, P. Fries, E. Maris, and J.-M. Schoffelen. FieldTrip: Open source software for advanced analysis of MEG, EEG, and invasive electrophysiological data. *Computational Intelligence and Neuroscience*, 2011, Dec. 2010. ISSN 1687-5265. doi: 10.1155/2011/156869. URL `http://www.hindawi.com/journals/cin/2011/156869/abs/`. 89

A. V. Oppenheim, R. W. Schafer, and J. R. Buck. *Discrete-time Signal Processing (2Nd Ed.)*. Prentice-Hall, Inc., Upper Saddle River, NJ, USA, 1999. ISBN 0-13-754920-2. 25

J. P. Owen, D. P. Wipf, H. T. Attias, K. Sekihara, and S. S. Nagarajan. Performance evaluation of the champagne source reconstruction algorithm on simulated and real m/EEG data. *NeuroImage*, 60(1):305–323, Mar. 2012. ISSN 1095-9572. doi: 10.1016/j.neuroimage.2011.12.027. 111

S. Palva and J. M. Palva. New vistas for alpha-frequency band oscillations. *Trends in Neurosciences*, 30(4):150–158, Apr. 2007. ISSN 0166-2236. doi: 10.1016/j.tins.2007.02.001. URL `http://www.sciencedirect.com/science/article/pii/S0166223607000264`. 86

L. C. Parra, C. D. Spence, A. D. Gerson, and P. Sajda. Recipes for the linear analysis of EEG. *NeuroImage*, 28(2):326–341, Nov. 2005. ISSN 1053-8119. doi: 10.1016/j.neuroimage.2005.05.032. URL `http://www.sciencedirect.com/science/article/pii/S1053811905003381`. 15

R. D. Pascual-Marqui. Standardized low-resolution brain electromagnetic tomography (sLORETA): technical details. *Methods and findings in experimental and clinical pharmacology*, 24 Suppl D:5–12, 2002. ISSN 0379-0355. 3, 109, 111

R. D. Pascual-Marqui. Discrete, 3d distributed, linear imaging methods of electric neuronal activity. part 1: exact, zero error localization. *arXiv:0710.3341 [math-ph, physics:physics, q-bio]*, Oct. 2007a. URL `http://arxiv.org/abs/0710.3341`. 16, 25, 46, 109, 110

R. D. Pascual-Marqui. Instantaneous and lagged measurements of linear and nonlinear dependence between groups of multivariate time series: frequency decomposition. *ArXiv e-prints*, Nov. 2007b. URL `http://arxiv.org/pdf/0711.1455v1`. 4, 41, 112, 114

R. D. Pascual-Marqui, M. Esslen, K. Kochi, and D. Lehmann. Functional imaging with low-resolution brain electromagnetic tomography (LORETA): a review. *Methods and findings in experimental and clinical pharmacology*, 24 Suppl C:91–95, 2002. ISSN 0379-0355. 3, 111

R. D. Pascual-Marqui, D. Lehmann, M. Koukkou, K. Kochi, P. Anderer, B. Saletu, H. Tanaka, K. Hirata, E. R. John, L. Prichep, R. Biscay-Lirio, and T. Kinoshita. Assessing interactions in the brain with exact low-resolution electromagnetic tomography. *Philos Transact A Math Phys Eng Sci*, 369(1952):3768–3784, Oct. 2011. 3, 96, 111

D. P. Pelvig, H. Pakkenberg, A. K. Stark, and B. Pakkenberg. Neocortical glial cell numbers in human brains. *Neurobiology of Aging*, 29(11):1754–1762, Nov. 2008. ISSN 0197-4580. doi: 10.1016/j.neurobiolaging.2007.04.013. URL http://www.sciencedirect.com/science/article/pii/S0197458007001686. 1

R. Penrose. A generalized inverse for matrices. *Mathematical Proceedings of the Cambridge Philosophical Society*, 51(03):406–413, 1955. doi: 10.1017/s0305004100030401. URL http://dx.doi.org/10.1017/s0305004100030401. 108

E. Pereda, R. Q. Quiroga, and J. Bhattacharya. Nonlinear multivariate analysis of neurophysiological signals. *Progress in neurobiology*, 77(1-2):1–37, Oct. 2005. ISSN 0301-0082. doi: 10.1016/j.pneurobio.2005.10.003. 112

P. R. Peres-Neto, D. A. Jackson, and K. M. Somers. How many principal components? stopping rules for determining the number of non-trivial axes revisited. *Computational Statistics & Data Analysis*, 49(4):974–997, June 2005. ISSN 0167-9473. doi: 10.1016/j.csda.2004.06.015. URL http://www.sciencedirect.com/science/article/pii/S0167947304002014. 50, 51

G. Pfurtscheller and C. Neuper. Motor imagery activates primary sensorimotor area in humans. *Neuroscience Letters*, 239(2–3):65–68, Dec. 1997. ISSN 0304-3940. doi: 10.1016/S0304-3940(97)00889-6. URL http://www.sciencedirect.com/science/article/pii/S0304394097008896. 90, 92

G. Pfurtscheller and F. H. L. d. Silva. Event-related EEG/MEG synchronization and desynchronization: basic principles. *Clinical Neurophysiology*, 110(11):1842 – 1857, 1999. ISSN 1388-2457. doi: DOI:10.1016/S1388-2457(99)00141-8. URL http://www.sciencedirect.com/science/article/pii/S1388245799001418. 12

E. J. G. Pitman. Significance tests which may be applied to samples from any populations. *Supplement to the Journal of the Royal Statistical Society*, 4(1):119–130, Jan. 1937. ISSN 1466-6162. doi: 10.2307/2984124. URL http://www.jstor.org/stable/2984124. 31

R. Plonsey and D. B. Heppner. Considerations of quasi-stationarity in electrophysiological systems. *Bull Math Biophys.*, 29(4):657–64, 1967. 12, 27, 105

V. Pravdich-Neminsky. Ein versuch der registrierung der elektrischen gehirnerscheinungen. *Zentralblatt für Physiologie*, 27:951–960, 1913. 1

W. S. Pritchard. The brain in fractal time: 1/f-like power spectrum scaling of the human electroencephalogram. *The International Journal of Neuroscience*, 66(1-2): 119–129, Sept. 1992. ISSN 0020-7454. 60

M. H. Quenouille. Problems in plane sampling. *The Annals of Mathematical Statistics*, 20(3):355–375, Sept. 1949. ISSN 0003-4851, 2168-8990. doi: 10.1214/aoms/1177729989. URL http://projecteuclid.org/euclid.aoms/1177729989. Mathematical Reviews number (MathSciNet) MR32175, Zentralblatt MATH identifier0035.09103. 30

M. H. Quenouille. Notes on bias in estimation. *Biometrika*, 43(3-4):353–360, Jan. 1956. ISSN 0006-3444, 1464-3510. doi: 10.1093/biomet/43.3-4.353. URL http://biomet.oxfordjournals.org/content/43/3-4/353. 30

R. Quian Quiroga, A. Kraskov, T. Kreuz, and P. Grassberger. Performance of different synchronization measures in real data: a case study on electroencephalographic signals. *Physical review. E, Statistical, nonlinear, and soft matter physics*, 65(4 Pt 1): 041903, Apr. 2002. ISSN 1539-3755. 28

M. E. Raichle, A. M. MacLeod, A. Z. Snyder, W. J. Powers, D. A. Gusnard, and G. L. Shulman. A default mode of brain function. *Proceedings of the National Academy of Sciences*, 98(2):676–682, Jan. 2001. ISSN 0027-8424, 1091-6490. doi: 10.1073/pnas.98.2.676. URL http://www.pnas.org/content/98/2/676. 90

S. Ramón y Cajal. *Histologie du système nerveux de l'homme & des vertébrés*. Paris : Maloine, 1909. URL http://archive.org/details/histologiedusyst01ram. 2

V. Reddy, A. Paulraj, and T. Kailath. Performance analysis of the optimum beamformer in the presence of correlated sources and its behavior under spatial smoothing. *IEEE Transactions on Acoustics, Speech and Signal Processing*, 35(7):927–936, 1987. ISSN 0096-3518. doi: 10.1109/TASSP.1987.1165239. 22

A. Rodriguez and A. Laio. Clustering by fast search and find of density peaks. *Science*, 344(6191):1492–1496, June 2014. ISSN 0036-8075, 1095-9203. doi: 10.1126/science.1242072. URL http://www.sciencemag.org/content/344/6191/1492. 102

Y. Rubner, C. Tomasi, and L. J. Guibas. The earth mover's distance as a metric for image retrieval. *International Journal of Computer Vision*, 40:2000, 2000. 33

V. Sakkalis. Review of advanced techniques for the estimation of brain connectivity measured with EEG/MEG. *Computers in Biology and Medicine*, 41(12):1110–1117, Dec. 2011. ISSN 0010-4825. doi: 10.1016/j.compbiomed.2011.06.020. URL http://www.sciencedirect.com/science/article/pii/S0010482511001405. 28

W. Samek, C. Vidaurre, K.-R. Müller, and M. Kawanabe. Stationary common spatial patterns for brain–computer interfacing. *Journal of Neural Engineering*, 9(2):026013, Apr. 2012. ISSN 1741-2552. doi: 10.1088/1741-2560/9/2/026013. URL http://iopscience.iop.org/1741-2552/9/2/026013. 94

C. Sannelli, C. Vidaurre, K.-R. Müller, and B. Blankertz. Common spatial pattern patches - an optimized spatial filter for adaptive BCIs. In *Frontiers in computational neuroscience*, 2010. doi: 10.3389/conf.fncom.2010.51.00107. URL http://dx.

doi.org//10.3389/conf.fncom.2010.51.00107. Conference Abstract: Bernstein Conference on Computational Neuroscience 2010. 94

J. Sarvas. Basic mathematical and electromagnetic concepts of the biomagnetic inverse problem. *Phys. Med. Biol.*,, 32(1):11–22, 1987. 3, 12, 105

M. Scherg and P. Berg. Use of prior knowledge in brain electromagnetic source analysis. *Brain topography*, 4(2):143–150, 1991. ISSN 0896-0267. 111

D. M. Schmidt, J. S. George, and C. C. Wood. Bayesian inference applied to the electromagnetic inverse problem. *Human brain mapping*, 7(3):195–212, 1999. ISSN 1065-9471. 111

J. M. Schoffelen and J.Gross. Source connectivity analysis with MEG and EEG. *Hum Brain Mapp.*, 30(6):1857–65, 2009. 4

T. Schreiber. Measuring information transfer. *Physical Review Letters*, 85(2):461–464, July 2000. doi: 10.1103/PhysRevLett.85.461. URL http://link.aps.org/doi/10.1103/PhysRevLett.85.461. 112

K. Sekihara and S. Nagarajan. Residual coherence and residual envelope correlation in MEG/EEG source-space connectivity analysis. In *2013 35th Annual International Conference of the IEEE Engineering in Medicine and Biology Society (EMBC)*, pages 4414–4417, July 2013. doi: 10.1109/EMBC.2013.6610525. 16

K. Sekihara, D. Poeppel, A. Marantz, H. Koizumi, and Y. Miyashita. MEG spatio-temporal analysis using a covariance matrix calculated from nonaveraged multiple-epoch data. *IEEE transactions on bio-medical engineering*, 46(5):515–521, May 1999. ISSN 0018-9294. 50

F. Shahbazi, A. Ewald, A. Ziehe, and G. Nolte. Constructing surrogate data to control for artifacts of volume conduction for functional connectivity measures. In S. Supek and A. Sušac, editors, *17th International Conference on Biomagnetism Advances in Biomagnetism – Biomag2010*, number 28 in IFMBE Proceedings, pages 207–210. Springer Berlin Heidelberg, Jan. 2010. ISBN 978-3-642-12196-8, 978-3-642-12197-5. 59

C. Shannon. Communication in the presence of noise. *Proceedings of the IEEE*, 86(2): 447–457, Feb. 1998. ISSN 0018-9219. doi: 10.1109/JPROC.1998.659497. 85

M. Siegel, A. K. Engel, and T. H. Donner. Cortical network dynamics of perceptual decision-making in the human brain. *Frontiers in Human Neuroscience*, 5(21), 2011. ISSN 1662-5161. doi: 10.3389/fnhum.2011.00021. 2

W. Singer. Neuronal synchrony: A versatile code for the definition of relations? *Neuron*, 24(1):49–65, Sept. 1999. 3

S. M. Smith. The future of FMRI connectivity. *NeuroImage*, 62(2):1257–1266, Aug. 2012. ISSN 1053-8119. doi: 10.1016/j.neuroimage.2012.01.022. URL http://www.sciencedirect.com/science/article/pii/S1053811912000390. 3

M. Spencer, R. Leahy, J. Mosher, and P. Lewis. Adaptive filters for monitoring localized brain activity from surface potential time series. In *1992 Conference Record of The Twenty-Sixth Asilomar Conference on Signals, Systems and Computers, 1992*, pages 156–161 vol.1, 1992. doi: 10.1109/ACSSC.1992.269278. 21, 111

C. J. Stam and B. W. van Dijk. Synchronization likelihood: an unbiased measure of generalized synchronization in multivariate data sets. *Physica D: Nonlinear Phenomena*, 163(3–4):236–251, Mar. 2002. ISSN 0167-2789. doi: 10.1016/S0167-2789(01)00386-4. URL http://www.sciencedirect.com/science/article/pii/S0167278901003864. 112

C. J. Stam, G. Nolte, and A. Daffertshofer. Phase lag index: Assessment of functional connectivity from multi channel EEG and MEG with diminished bias from common sources. *Human Brain Mapping*, 28(11):1178–1193, 2007. ISSN 1097-0193. doi: 10.1002/hbm.20346. URL http://dx.doi.org/10.1002/hbm.20346. 4, 112

G. W. Stewart. On the early history of the singular value decomposition. *SIAM Rev.*, 35(4):551–566, Dec. 1993. ISSN 0036-1445. doi: 10.1137/1035134. URL http://dx.doi.org/10.1137/1035134. 19

S. Stigler. Fisher and the 5% level. *CHANCE*, 21(4):12–12, Dec. 2008. ISSN 0933-2480, 1867-2280. doi: 10.1007/s00144-008-0033-3. URL http://link.springer.com/article/10.1007/s00144-008-0033-3. 28

J. Stinstra and M. Peters. The volume conductor may act as a temporal filter on the ECG and EEG. *Medical and Biological Engineering and Computing*, 36(6):711–716, 1998. ISSN 0140-0118. URL http://dx.doi.org/10.1007/BF02518873. 10.1007/BF02518873. 27

P. Stoica, P. Handel, and A. Nehoral. Improved sequential MUSIC. *IEEE Transactions on Aerospace and Electronic Systems*, 31(4):1230–1239, 1995. ISSN 0018-9251. doi: 10.1109/7.464347. 23

J. V. Stone. *Independent component analysis: a tutorial introduction*. MIT Press, Cambridge, Mass., 2004. ISBN 0262693151 9780262693158. 20

S. H. Strogatz. *SYNC: how order emerges from chaos in the universe, nature, and daily life*. Theia, New York, 2003. ISBN 0786887214 9780786887217. 3

L. W. Swanson. *Brain Architecture*. Oxford University Press, New York, 2 edition edition, Sept. 2011. ISBN 9780195378580. 2

J. Talairach and P. Tournoux. *Co-Planar Stereotaxic Atlas of the Human Brain: 3-Dimensional Proportional System: An Approach to Cerebral Imaging*. Thieme, Stuttgart ; New York, auflage: 1 edition, Feb. 2008. ISBN 9783137117018. 2

J. Theiler, S. Eubank, A. Longtin, B. Galdrikian, and J. Doyne Farmer. Testing for nonlinearity in time series: the method of surrogate data. *Physica D: Nonlinear Phenomena*, 58(1–4):77–94, Sept. 1992. ISSN 0167-2789. doi:

10.1016/0167-2789(92)90102-S. URL http://www.sciencedirect.com/science/article/pii/016727899290102S. 32, 58

R. Tibshirani. Regression shrinkage and selection via the lasso. *Journal of the Royal Statistical Society, Series B*, 58:267–288, 1994. 110

A. N. Tikhonov and V. I. Arsenin. *Solutions of ill-posed problems*. Winston, 1977. ISBN 9780470991244. 109

R. Tomioka, G. Dornhege, G. Nolte, B. Blankertz, K. Aihara, and K.-R. Müller. Spectrally weighted common spatial pattern algorithm for single trial EEG classification. Technical Report 40, Dept. of Mathematical Engineering, The University of Tokyo, July 2006. 94

A. B. L. Tort, R. Komorowski, H. Eichenbaum, and N. Kopell. Measuring phase-amplitude coupling between neuronal oscillations of different frequencies. *Journal of Neurophysiology*, 104(2):1195–1210, Aug. 2010. ISSN 1522-1598. doi: 10.1152/jn.00106.2010. 102

J. W. Tukey. Bias and confidence in not quite large samples. *Annals of Mathematical Statistics*, 29:614, 1958. ISSN 0003-4851. 30

N. Tzourio-Mazoyer, B. Landeau, D. Papathanassiou, F. Crivello, O. Etard, N. Delcroix, B. Mazoyer, and M. Joliot. Automated anatomical labeling of activations in SPM using a macroscopic anatomical parcellation of the MNI MRI single-subject brain. *NeuroImage*, 15(1):273–289, Jan. 2002. ISSN 1053-8119. doi: 10.1006/nimg.2001.0978. 2

B. D. Van Veen, W. van Drongelen, M. Yuchtman, and A. Suzuki. Localization of brain electrical activity via linearly constrained minimum variance spatial filtering. *IEEE transactions on bio-medical engineering*, 44(9):867–880, Sept. 1997. ISSN 0018-9294. doi: 10.1109/10.623056. 3, 21, 111

B. C. M. van Wijk, P. J. Beek, and A. Daffertshofer. Neural synchrony within the motor system: what have we learned so far? *Frontiers in Human Neuroscience*, 6:252, 2012. doi: 10.3389/fnhum.2012.00252. URL http://journal.frontiersin.org/Journal/10.3389/fnhum.2012.00252/full. 92

S. Vanni, A. Revonsuo, and R. Hari. Modulation of the parieto-occipital alpha rhythm during object detection. *The Journal of neuroscience: the official journal of the Society for Neuroscience*, 17(18):7141–7147, Sept. 1997. ISSN 0270-6474. 12

F. Varela, J.-P. Lachaux, E. Rodriguez, and J. Martinerie. The brainweb: Phase synchronization and large-scale integration. *Nat Rev Neurosci*, 2(4):229–239, Apr. 2001. ISSN 1471-003X. URL http://dx.doi.org/10.1038/35067550. 3

R. Vicente, M. Wibral, M. Lindner, and G. Pipa. Transfer entropy–a model-free measure of effective connectivity for the neurosciences. *Journal of Computational Neuroscience*, 30(1):45–67, Feb. 2011. ISSN 1573-6873. doi: 10.1007/s10827-010-0262-3. 112

J. L. Vincent, A. Z. Snyder, M. D. Fox, B. J. Shannon, J. R. Andrews, M. E. Raichle, and R. L. Buckner. Coherent spontaneous activity identifies a hippocampal-parietal memory network. *J. Neurophysiol.*, 96(6):3517–3531, Dec. 2006. 2

J. L. Vincent, I. Kahn, A. Z. Snyder, M. E. Raichle, and R. L. Buckner. Evidence for a frontoparietal control system revealed by intrinsic functional connectivity. *J. Neurophysiol.*, 100(6):3328–3342, Dec. 2008. 2

M. Vinck, R. Oostenveld, M. van Wingerden, F. Battaglia, and C. M. A. Pennartz. An improved index of phase-synchronization for electrophysiological data in the presence of volume-conduction, noise and sample-size bias. *NeuroImage*, 55(4): 1548–1565, Apr. 2011. ISSN 1095-9572. doi: 10.1016/j.neuroimage.2011.01.055. 4, 47, 112

P. von Bünau, F. C. Meinecke, F. C. Király, and K.-R. Müller. Finding stationary subspaces in multivariate time series. *Physical Review Letters*, 103(21):214101, Nov. 2009. ISSN 1079-7114. 102

J. Vrba and S. E. Robinson. Signal processing in magnetoencephalography. *Methods*, 25(2):249–271, Oct. 2001. ISSN 1046-2023. doi: 10.1006/meth.2001.1238. URL `http://www.sciencedirect.com/science/article/pii/S1046202301912381`. 21, 111

F. Wendling, K. Ansari-Asl, F. Bartolomei, and L. Senhadji. From EEG signals to brain connectivity: A model-based evaluation of interdependence measures. *Journal of Neuroscience Methods*, 183(1):9–18, Sept. 2009. ISSN 0165-0270. doi: 10.1016/j.jneumeth.2009.04.021. URL `http://www.sciencedirect.com/science/article/pii/S0165027009002350`. 28

C. Wernicke. *Der aphasische Symptomencomplex: Eine psychologische Studie auf anatomischer Basis*. Cohn, 1874. URL `http://archive.org/details/deraphasischesy00werngoog`. 1

T. Womelsdorf, J.-M. Schoffelen, R. Oostenveld, W. Singer, R. Desimone, A. K. Engel, and P. Fries. Modulation of neuronal interactions through neuronal synchronization. *Science*, 316(5831):1609–1612, June 2007. ISSN 0036-8075, 1095-9203. doi: 10.1126/science.1139597. URL `http://www.sciencemag.org/content/316/5831/1609`. 6

M.-H. Wu, R. E. Frye, and G. Zouridakis. A comparison of multivariate causality based measures of effective connectivity. *Computers in Biology and Medicine*, 41(12):1132–1141, Dec. 2011. ISSN 0010-4825. doi: 10.1016/j.compbiomed.2011.06.007. URL `http://www.sciencedirect.com/science/article/pii/S0010482511001272`. 28

A. Ziehe and K.-R. Müller. TDSEP — an efficient algorithm for blind separation using time structure. In L. Niklasson, M. Bodén, and T. Z. MSc, editors, *ICANN 98*, Perspectives in Neural Computing, pages 675–680. Springer London, Jan. 1998. ISBN 978-3-540-76263-8, 978-1-4471-1599-1. URL `http://link.springer.com/chapter/10.1007/978-1-4471-1599-1_103`. 20, 59

A. Ziehe, K. R. Müller, G. Nolte, B.-M. Mackert, and G. Curio. Artifact reduction in magnetoneurography based on time-delayed second-order correlations. *IEEE Transactions on Biomedical Engineering*, 47(1):75–87, 2000. ISSN 0018-9294. doi: 10.1109/10.817622. 20